

**RADAR STUDIES OF  
HIGH LATITUDE CONVECTION FLOWS**

**MARK BURRAGE**

Being a dissertation submitted to the Faculty of Science,  
University of Leicester, in candidature for the degree  
of Philosophiae Doctor

Department of Physics,  
University of Leicester,

January, 1988

UMI Number: U008067

All rights reserved

INFORMATION TO ALL USERS

The quality of this reproduction is dependent upon the quality of the copy submitted.

In the unlikely event that the author did not send a complete manuscript and there are missing pages, these will be noted. Also, if material had to be removed, a note will indicate the deletion.



UMI U008067

Published by ProQuest LLC 2015. Copyright in the Dissertation held by the Author.  
Microform Edition © ProQuest LLC.

All rights reserved. This work is protected against  
unauthorized copying under Title 17, United States Code.



ProQuest LLC  
789 East Eisenhower Parkway  
P.O. Box 1346  
Ann Arbor, MI 48106-1346

### ACKNOWLEDGEMENTS

Special thanks are due to my supervisor Professor Tudor Jones and to Dr. Jeff Waldock, Dr. Mark Lester, and Dr. Terry Robinson for their help and encouragement throughout the course of the study and for their constructive criticism of the manuscript.

I would also like to thank the following:

Dr. Jeff Hughes, Alan Rodger, and Ian McCrea for helpful discussions and comments.

Nick Mattin and Nigel Wade for their assistance with computing difficulties.

Dr. Chris Thomas, Chris Stewart, and Roderick Maude for the maintenance of the Wick radar and the SABRE analysis computer.

Dr. Farideh Honary and Angela Wilkinson for proof reading of the manuscript.

Warren Smith and Peter Chapman for their help.

The Max Planck Institut für Aeronomie (MPAE), Lindau, W.Germany in cooperation with the Uppsala Ionospheric Observatory for the operation of the Swedish component of the SABRE system.

Dr. Erling Nielsen of MPAE for providing STARE data.

The NSSDC, Goddard Space Flight Center, Greenbelt, Maryland for supplying satellite data.

The British Geological Survey, Edinburgh for providing magnetograms.

Dr. Bill Bain for his MEM computer program.

Professor J. L. Beeby, Professor E. A. Davis, and Professor K. A. Pounds for the opportunity to work in the Physics Department of the University of Leicester.

The SERC for financial support during the period of the study.

This thesis is dedicated to my parents.

## CONTENTS

### GLOSSARY

#### CHAPTER 1 INTRODUCTION

1.1 The Neutral Atmosphere and the Ionosphere	1
1.2 The Solar Wind	2
1.3 The Magnetosphere	3
1.4 Magnetospheric Substorms	5
1.5 The Auroral Oval	7
1.6 The SABRE System	8
1.7 Aims of the Present Study	8

#### CHAPTER 2 IONOSPHERIC CONVECTION

2.1 Introduction	11
2.2 Solar wind-magnetosphere coupling processes	13
2.2.1 Viscous interaction	13
2.2.2 Magnetic reconnection	14
2.2.3 Open vs. closed	16
2.3 Observational techniques	16
2.4 Observations of the high latitude convection pattern	18
2.4.1 Convection with IMF $B_z < 1$ nT	19
2.4.2 IMF $B_y$ dependent asymmetries	21
2.4.3 Effects associated with IMF $B_x$	24
2.4.4 Convection with northward IMF ( $B_z > 1$ nT)	24
2.4.5 Substorm response of the magnetosphere and ionosphere	26
2.5 Energy coupling	28
2.6 Summary	30

CHAPTER 3	MEASUREMENT TECHNIQUES	
3.1	Introduction	31
3.2	SABRE	31
3.2.1	Antenna configuration	32
3.2.2	Measurement technique	33
3.2.3	Backscatter power	34
3.2.4	Theory of the backscatter mechanism	36
3.2.5	Backscatter statistics	39
3.3	Spacecraft	40
3.4	Summary	41
CHAPTER 4	SOLAR WIND MODULATION OF SABRE BACKSCATTER INTENSITIES	
4.1	Introduction	42
4.2	The first SUNDIAL campaign	43
4.3	Empirical relationship of backscatter power with solar wind parameters	46
4.3.1	Comparison of SABRE with energy coupling parameters	47
4.3.2	Interpretation of the empirical results	48
4.4	Spectral analysis of Wick backscatter intensities	49
4.4.1	Spectra of the backscatter intensity data	50
4.4.2	Interpretation and discussion of the spectra	52
4.5	Summary	54
CHAPTER 5	STATISTICAL STUDIES OF SABRE CONVECTION MEASUREMENTS	
5.1	Introduction	56
5.2	Synoptic survey of the data	56
5.2.1	Dependence on geomagnetic conditions	56
5.2.2	Dependence on the IMF	57
5.3	The Harang discontinuity	59
5.3.1	Structure of the discontinuity	59

5.3.2 Local time of the Harang discontinuity	61
5.4 Harang discontinuity and IMF $B_y$ - discussion	65
5.5 Summary	67

## CHAPTER 6 DAYSIDE CONVECTION OBSERVATIONS

6.1 Introduction	68
6.2 Synopsis of the dayside observations	70
6.3 Observations for inferred $B_y > 0$	72
6.3.1 6 September, 1982	72
6.3.2 16 November, 1984	73
6.3.3 2 March, 1983	74
6.3.4 28 April, 1985	76
6.4 Observations for inferred $B_y < 0$	77
6.4.1 5 February, 1983	77
6.4.2 7 August, 1982	78
6.5 Discussion	80
6.6 Summary	84

## CHAPTER 7 NIGHTSIDE CONVECTION OBSERVATIONS

7.1 Introduction	86
7.2 Observations during southward IMF	86
7.3 Observations during northward IMF	89
7.3.1 Observations for 4-5 February, 1983	89
7.3.2 Four cell interpretation	92
7.3.3 Two cell interpretation	95
7.3.4 Observations for 25 March, 1983	97
7.4 Summary	99

## CHAPTER 8 CONCLUSIONS

8.1 Introduction	101
------------------	-----

8.2 Principal results	101
8.3 Suggestions for further work	103
8.4 Concluding remarks	105

Appendix A Spectral analysis techniques.

A1 Fourier analysis	106
A2 Smoothing techniques	107
A3 Maximum entropy method	108

References	109
------------	-----

## GLOSSARY

Symbols and abbreviations are defined as they occur, but those which appear most frequently are listed below.

AE	auroral electrojet index
B	magnetic induction, interplanetary magnetic field magnitude
$B_x$	Sun-Earth line component of the interplanetary magnetic field
$B_y$	azimuthal component of the interplanetary magnetic field
$B_z$	north-south component of the interplanetary magnetic field
C	ion acoustic speed
$D_{st}$	index of geomagnetic field perturbation due to ring current
E	electric field strength
e	charge on the electron
GG	geographic
GM	geomagnetic
H	horizontal component of the geomagnetic field
i	$\sqrt{-1}$
IMF	interplanetary magnetic field
$K_p$	planetary geomagnetic activity index
LT	local time
MEM	maximum entropy method
MHD	magnetohydrodynamic
MLT	magnetic local time
nT	nano Tesla ( $= 10^{-9}$ T or 1 gamma)
$P_r$	received backscatter power
$R_E$	radius of the Earth
RTV	range time velocity
SABRE	Sweden and Britain auroral radar experiment
SADIE	SABRE altitude determining interferometer experiment

$S_q^p$	quiet time polar diurnal variation of the geomagnetic field
ssc	sudden storm commencement
STARE	Scandinavian twin auroral radar experiment
$T_{HD}$	time of occurrence of the Harang discontinuity
$T_{MR}$	time of occurrence of the morning convection flow reversal
$T_S$	synodic period of the solar rotation
UT	universal time
V	solar wind flow velocity
$v_d$	relative drift velocity between electrons and ions
VHF	very high frequency
X	X coordinate in $R_E$
Y	Y coordinate in $R_E$
Z	Z coordinate in $R_E$ , vertical component of the geomagnetic field
$\epsilon$	energy coupling parameter
$\Phi_{PC}$	cross polar cap potential
$\phi$	radar aspect angle, azimuthal angle of the IMF
$\theta$	radar propagation angle, polar angle of the IMF
$\mu_0$	permeability of free space
$\rho$	density
$\sigma$	irregularity backscatter cross section
$\tau$	time delay, pulse duration
~	approximately

## CHAPTER 1

### INTRODUCTION

#### 1.1 The Neutral Atmosphere and the Ionosphere

The terrestrial atmosphere is comprised of a mixture of gases which form a relatively thin layer enveloping the Earth. The neutral component of the atmosphere may be described by the basic properties pressure ( $p$ ), density ( $\rho$ ), mean molecular weight ( $M$ ) and temperature ( $T$ ). The variation of these parameters as a function of altitude is illustrated in Figure 1.1. Both pressure and density decrease rapidly with height, with the particle number density falling from a value of about  $10^{25} \text{ m}^{-3}$  at sea level to  $10^{19} \text{ m}^{-3}$  at 100 km. The temperature profile is more complicated due to the absorption of different wavelengths of the incident solar radiation at different levels. In the lower atmosphere the gases are mixed by turbulence so that their relative proportions remain constant. The increase in temperature at greater heights produces an atmosphere which is stable to vertical motion and thus there is no turbulence in this region. Consequently, above 100 km, the composition changes with altitude so that the mean molecular weight decreases with increasing height.

In the upper atmosphere oxygen and nitrogen are ionised by solar radiation in the x-ray and extreme ultra-violet bands. The degree of ionisation depends on the balance between the rate of electron-ion production and the rate of electron-ion recombination. The part of the atmosphere above about 60 km, where the concentration of free electrons is sufficient to influence the propagation of radio waves, is known as the ionosphere. The principal electron (ion) density layers have been

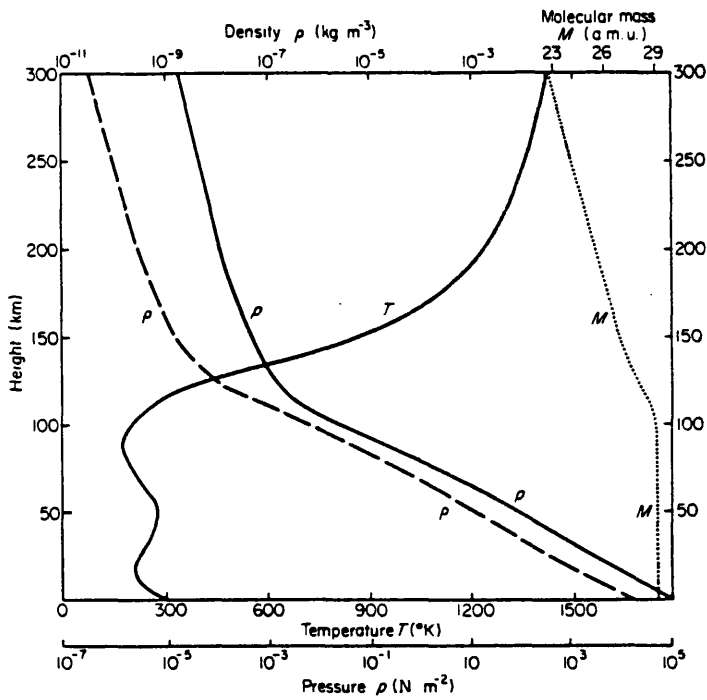


**FIGURE 1.1.** Typical variation with altitude of atmospheric pressure, density, temperature and mean molecular weight. [From Rishbeth and Garriot, 1969.]

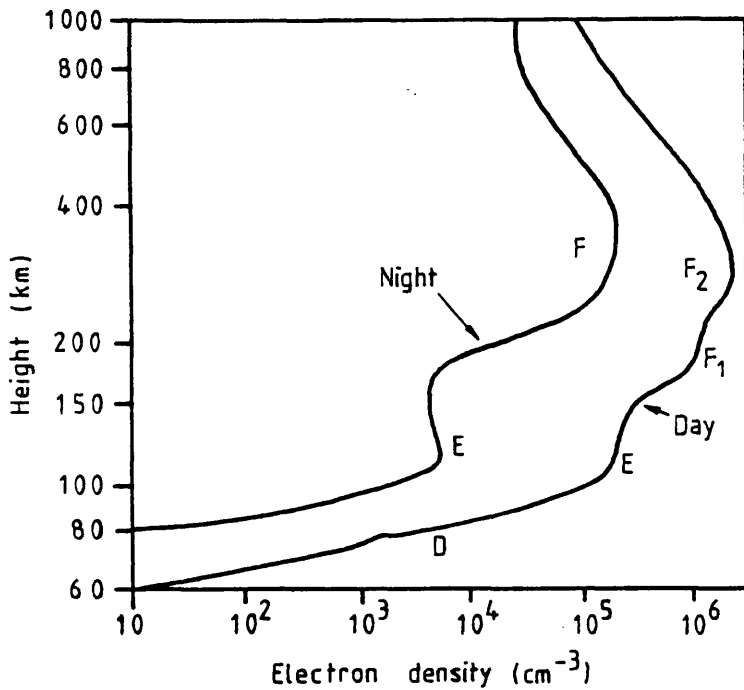


**FIGURE 1.2.** Typical vertical profiles of the mid-latitude ionosphere. [From wallchart Aerospace Environment. W. Swider. Airforce Geophysics Laboratory, Hanscom Air Force Base, Massachusetts.]

labelled, in order of increasing altitude, the D (60–90 km), E (90–120 km) and F (above 150 km) regions. During the daytime the F-region is sometimes divided into two parts, the F1 and F2 layers. Typical electron density profiles with height are depicted in Figure 1.2.

The atmospheric regime above the ionosphere is termed the magnetosphere. There is no physical separation between ionospheric and magnetospheric regions, although a height of 1000 km is commonly defined as the position of the topside of the ionosphere. This thesis is primarily concerned with phenomena observed in the E-region of the ionosphere, which arise from the interaction of the Earth's magnetosphere with the solar wind. There follows a description of these different domains and an overview of the ways in which they affect each other.

## 1.2 The Solar Wind

The solar corona, which is a fully ionised plasma consisting mainly of protons and electrons, is in a continuous state of supersonic expansion, forming a stream of charged particles known as the solar wind. The properties of the solar wind plasma depend upon the level of solar activity. Typical values for the kinetic parameters of the plasma in the vicinity of the Earth and for a quiet Sun are listed in Table 1.1.

In addition to the kinetic properties of the solar wind, there is an associated 'interplanetary' magnetic field (IMF) originating from the Sun which, at the distance of the Earth, usually has a magnitude of only a few nT. The density of magnetic energy ( $= B^2/2\mu_0$ , where  $B$  is the magnetic induction and  $\mu_0$  the permeability of free space), which is typically about  $10^{-12} \text{ J m}^{-3}$ , is considerably less than the particle kinetic energy density (Table 1.1). Consequently, the IMF is 'frozen in' and carried along with the solar wind.

As the wind travels radially outwards, the Sun rotates on its axis once

Particle speed ( $v$ )	$3 \times 10^5 \text{ m s}^{-1}$
Particle flux ( $F$ )	$1.5 \times 10^{12} \text{ m}^{-2} \text{ s}^{-1}$
Particle concentration ( $n$ ) (= $F/v$ )	$5 \times 10^6 \text{ m}^{-3}$
Energy of a proton in the wind ( $E$ )	$8 \times 10^{-17} \text{ J} = 500 \text{ eV}$
Energy of an electron in the wind	0.25 eV (negligible compared with proton energy)
Energy density ( $nE$ )	$4 \times 10^{-10} \text{ J m}^{-3}$
Power flux ( $nvE$ )	$1.2 \times 10^{-4} \text{ W m}^{-2}$

TABLE 1.1. Typical solar wind parameters for a quiet Sun.  
[From Ratcliffe, 1972.]

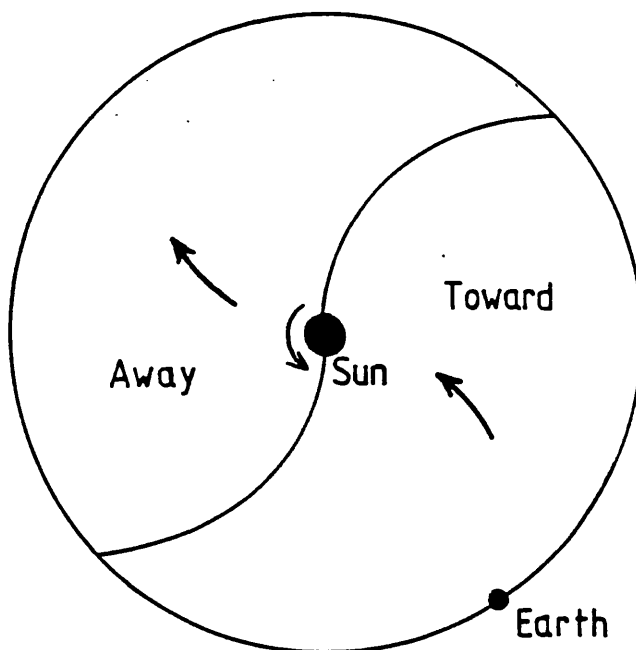


FIGURE 1.3. Two sector structure of the IMF. In one sector the magnetic field is directed away from the Sun and in the other towards the Sun.

in 27 days, so that particles emitted in succession from the same point are later distributed along a spiral. Since the particles carry the IMF with them, the field has the same spiral form. This is sometimes referred to as the 'garden hose effect'. At the orbit of the Earth the angle between the field lines and the radial direction is typically  $45^\circ$ .

The spiral magnetic field is on average divided into roughly equal sectors, the field in alternate sectors being directed either towards or away from the Sun. Although it is possible that a four or even six sector IMF structure may appear, a two sector structure, as illustrated in Figure 1.3, is probably dominant (Burlaga, 1983). The existence of these sectors may be understood in terms of the warped current sheet model of the solar wind (Alfvén, 1977). The current sheet marks the separatrix between toward and away solar magnetic field (IMF) lines. When the Earth is north (south) of the sheet it is located in an away (toward) sector. When the Earth is swept through the current sheet crossing a sector boundary, the local solar wind velocity and density and the magnitude and orientation of the IMF are changed. These variations have periodicities associated with the solar rotation. In addition, sunspots, flares, and coronal mass ejections, lead to irregularities in the solar current sheet which may entirely disrupt the periodic sector structure. Thus, the solar wind is a medium which is both kinetically and magnetically highly variable, and this has a profound impact on the structure and dynamics of the geospace environment.

### 1.3 The Magnetosphere

The magnetosphere is the region of the Earth's atmosphere where the geomagnetic field is the dominant factor in controlling the motion of charged particles. Its shape is greatly distorted from that of a simple dipole magnetic field as a result of the dynamic pressure exerted by the

solar wind, so that the geomagnetic field is compressed in front of the Earth, and stretched out behind it as the magnetotail. Because of its high electrical conductivity, the solar wind plasma cannot enter the geomagnetic cavity but is swept around it forming a region known as the magnetosheath, as illustrated in Figure 1.4. The interface sunward of the Earth, between the free-streaming supersonic solar wind and the more dense, subsonic and hotter magnetosheath plasma, is the bow shock. This feature is analagous to the shock produced around the nose of an aircraft travelling supersonically through the atmosphere.

The boundary of the geomagnetic cavity is called the magnetopause and it is approximately spherical on the sunward side, lying at typically 10 Earth radii ( $R_E$ ) in front of the Earth (Ness, 1964). In the antisunward direction, the magnetopause is roughly cylindrical and extends well beyond the lunar distance ( $\sim 60 R_E$ ), with tail-like plasma having been detected as far as  $1000R_E$  downstream (Villante, 1975). The precise morphology of the magnetopause is governed by the dynamic pressure of the solar wind and by the IMF.

In the representation of the magnetosphere depicted in Figure 1.4, it is evident that there are two regions in the dayside magnetosphere, one in the northern and one in the southern hemisphere, in which magnetic field lines lead up from the Earth and terminate at two neutral points on the magnetopause. In the vicinity of these points the total magnetic field is extremely low, allowing plasma to stream through the magnetopause and down into the ionosphere. These regions of direct particle entry are referred to as 'cusps' or 'clefts'.

The magnetosphere contains several different plasma regions which are populated by particles originating in the solar wind rather than the terrestrial atmosphere. The plasma mantle forms a thick layer of plasma, flowing in the anti-solar direction, just inside the magnetopause. The plasma sheet, which is sometimes referred to as the neutral sheet, is a

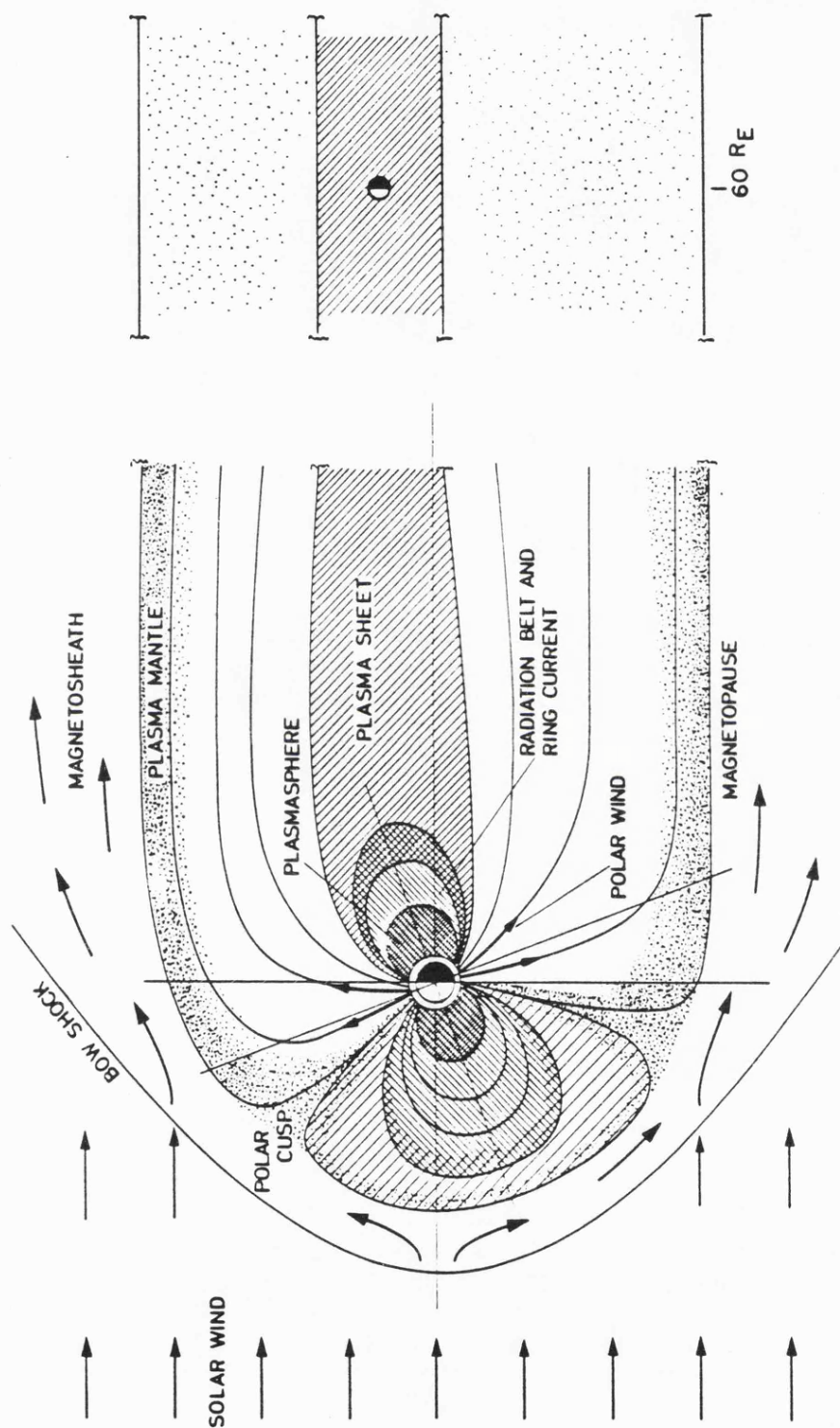


**FIGURE 1.4.** Five domains of magnetospheric plasma: the plasma mantle, the cusp, the plasma sheet, the Van Allen belt and the plasmasphere. [From Akasofu, 1977.]

thin sheet like distribution of charged particles, centred around the midplane of the magnetotail and dividing the two lobes where the geomagnetic field is in opposite directions. Plasma sheet particles carry a current, called the cross-tail current, which flows across the magnetotail from the dawn magnetopause to the dusk magnetopause. The total current carried at geocentric distances from 10 to 60  $R_E$  is typically  $\sim 6 \times 10^6$  Amperes. A further magnetospheric current system, the ring current, consists of a belt of energetic particles encircling the Earth, which are trapped on closed field lines between 3 and 7  $R_E$ , with protons drifting to the west and electrons to the east. The total magnitude of the ring current is  $\sim 10^6 - 10^7$  A. The outer portion of the ring current coincides with the Van Allen radiation belt, where electrons of even higher energy are injected from the plasma sheet and subsequently trapped. The magnetospheric plasma domain which exists within the ring current belt is known as the plasmasphere. The plasma in this region is supplied from the ionosphere and its outer boundary is the plasmopause.

#### 1.4 Magnetospheric Substorms

The Earth's magnetic field is not confined completely to the geomagnetic cavity. In fact the geomagnetic field lines from the polar regions are merged with the IMF lines to produce 'open' field lines. The solar wind plasma 'blows' across the open field lines, creating a magnetohydrodynamic (MHD) dynamo (Akasofu, 1977) which converts the kinetic energy of the solar wind plasma into electrical energy that is stored within the magnetotail. The magnetospheric substorm is a general term for many of the physical phenomena that occur as the magnetosphere extracts and dissipates energy from the solar wind. The IMF can play a crucial role in initiating substorms since it effectively acts as a 'gating' mechanism which controls the efficiency of the energy transfer process.

An IMF dependent substorm mechanism has been described by (Baker et al., 1986). The efficiency of the MHD dynamo is regulated by the north-south ( $B_z$ ) component of the IMF. If the IMF has a large (~5 nT) northward component for a prolonged period (6-12 hours), this efficiency approaches a minimum, and the corresponding state may be considered to be the 'ground state' of the magnetosphere. When the IMF turns south, the dynamo efficiency increases so that excess energy is accumulated in the magnetotail as magnetic energy and the tail grows longer. This is called the 'growth phase'. However, there is a limit to the amount of energy which can be absorbed and the excited magnetosphere tends to sporadically release its accumulated energy in a collapse of the tail towards the Earth. The energy is dissipated in the form of kinetic energy of auroral particles and the joule heat energy of the ionosphere, as well as in the form of kinetic energy of particles in the plasma sheet. This explosive release of energy is termed the magnetospheric substorm, which manifests itself in the disturbances of ground based magnetometer records as the 'geomagnetic substorm' and as the 'expansive phase onset' normally identified with visual auroral intensifications. The return of the magnetosphere to the ground state is known as the 'recovery phase' (Akasofu, 1964).

The successive and frequent occurrence of intense substorms, which is usually associated with a period of sustained southward IMF, is termed the main phase of the geomagnetic storm. In general, the latter is defined as the period during which the magnetic field at the Earth's surface is depressed. This depression is caused by an intensification of the ring current in the inner magnetosphere.

Substorm activity depends not only on the behaviour of the IMF but also on the kinetic energy density of the solar wind. In fact, the sudden commencement storm (denoted ssc), which commonly begins with an increase in the magnitude of the geomagnetic field, is associated with a compression of the magnetosphere due to a sudden enhancement in the dynamic pressure of

the solar wind. Most substorms, however, do not arise simply from a direct impact of the enhanced solar wind stream on the magnetosphere. Rather, the solar wind kinetic energy is first converted to magnetic energy which is stored in the magnetotail, before being released into the ring current and the auroral ionosphere.

### 1.5 The Auroral Oval

The strong modulation of the magnetosphere by the solar wind was briefly described in the previous section. In turn, the magnetosphere has a profound influence on the composition and dynamics of the ionosphere. This coupling involves the transfer of electric fields and particles along the highly conducting geomagnetic field lines. The most conspicuous example of the exchange between the magnetosphere and the ionosphere is the visual aurora, in which high energy electrons enter the high latitude upper atmosphere, colliding with and exciting ions of oxygen and nitrogen. As these metastable species decay, they release visible light of a variety of wavelengths, giving rise to the colourful and often spectacular auroral display. Also, ionisations produced by particle precipitation, and approximately colocated with the luminous aurora, reflect radio waves, the so-called radar aurora. Consequently, radar techniques may be employed to study the morphology and dynamics of these auroral ionisations or plasma irregularities.

Auroral phenomena tend to be highly structured in both space and time and are concentrated into a high latitude zone known as the auroral oval (Figure 1.5), the configuration of which was first established by Feldstein (1963). The oval is eccentric with respect to the dipole pole, with the centre appreciably displaced toward the nightside hemisphere. The magnetic latitude of the statistical maximum is near  $67^\circ$  at local midnight but about  $77^\circ$  at local noon. The poleward edge of the auroral oval is approximately

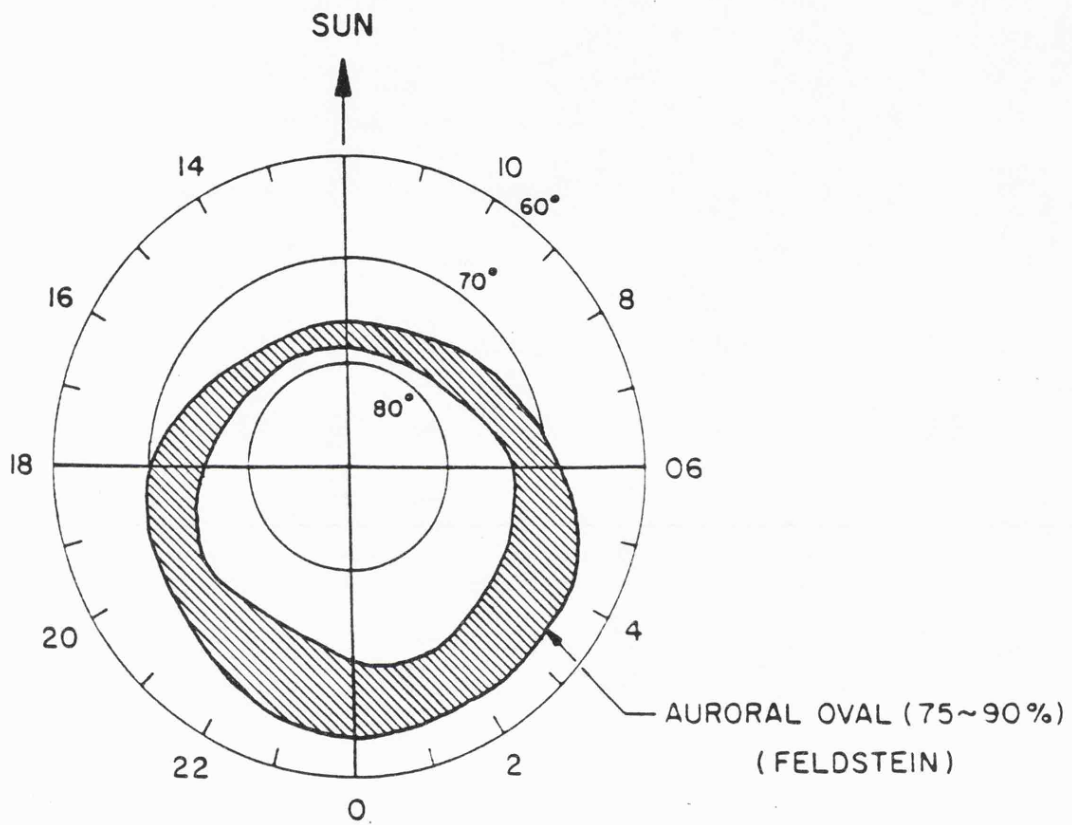


FIGURE 1.5. Auroral oval determined by Feldstein (1963).

coincident with the boundary of the polar cap, which is defined as the region of open geomagnetic field lines.

In addition to particle transfer, electric fields generated in the distant magnetosphere map down the geomagnetic field lines into the high latitude ionosphere, where they drive bulk motions of plasma. This is equivalent to an electrical circuit in which solar wind driven currents in the outer magnetosphere are connected to horizontal currents in the ionosphere by means of field-aligned currents. Thus, the study of ionospheric convection at auroral latitudes yields information on the dynamics of the magnetosphere and on the coupling mechanisms which transfer energy from the solar wind to the atmosphere.

### 1.6 The SABRE system

The Sweden And Britain auroral Radar Experiment (SABRE) is the principal experimental technique employed in this investigation. The system comprises two multi-beam radars each of which measures the line of sight Doppler velocity of plasma irregularities that propagate in the auroral E-region with a phase velocity related to the electron drift velocity. By combining these measurements, the horizontal electron drift vector may be estimated. Between March, 1982 and November, 1986 SABRE operated almost continuously and has provided observations of the high latitude convection electric field with excellent spatial and temporal resolution ( $20 \times 20 \text{ km}^2$  and 20 s, respectively) over a large total viewing area of some 200,000  $\text{km}^2$ . The SABRE system is described in greater detail in Chapter 3.

### 1.7 Aims of the Present Study

The aim of this thesis is to enhance the present knowledge of sun-magnetosphere-ionosphere coupling processes. An improved understanding

of these relationships is of fundamental importance to solar-terrestrial physics, and will have significant practical applications, particularly for high latitude radio communications, military early warning systems, and air and sea navigation. The dependence of the ionosphere on solar activity was first inferred from early studies of geomagnetism. In recent years, the investigation of solar-terrestrial interactions has been revolutionised by the advent of spacecraft and sophisticated ground based radars such as SABRE. These techniques have provided the opportunity to monitor simultaneously all of the constituent regions - the interplanetary medium, the magnetosphere and the ionosphere - of the coupled system.

Following a review of previous observational results in the context of current theories of solar-terrestrial coupling mechanisms, and a description of the SABRE system, an empirical study demonstrates that the backscatter intensity measured by a coherent auroral radar (a parameter which has rarely been employed in geophysical investigations) is modulated by the solar wind. A study of the long term variation in SABRE backscatter intensity for over 4 years of data reveals strong periodicities near 27 and 13.5 days. The results are interpreted in terms of a model of the solar wind and have consequences for both the relative contributions of the kinetic and magnetic properties of the interplanetary medium to the solar-terrestrial interaction and for the long term evolution of the heliospheric sector structure.

The statistical relationship between interplanetary conditions and the average E-region convection flows measured by SABRE is investigated in order to categorise the various effects of the different components of the IMF on the high latitude convection pattern. This demonstrates that the influence of the east-west ( $B_y$ ) component of the IMF is not confined to the noon hours (cusp region), but also affects the convection flow morphology in the vicinity of the Harang discontinuity.

A series of case studies of the convection flows observed by SABRE on

individual days are described, firstly for the dayside and secondly for the nightside. For some of the examples the latitudinal coverage of the convection pattern is extended by employing a technique which combines the SABRE measurements with those obtained by STARE, a radar system located to the north-east of SABRE. The radar observations are compared with high resolution satellite measurements of the solar wind. The dayside studies confirm the firm control of cusp convection flows by the  $B_y$  component of the IMF, while the investigation of nightside flows provides a new insight into the nature of the solar wind-magnetosphere coupling mechanism when the IMF is strongly northward.

These studies represent an attempt to improve on the understanding of the coupled solar-terrestrial system as a whole, and in particular the nature of the high latitude ionospheric response to changes in the solar wind and the Earth's magnetosphere.

## CHAPTER 2

### IONOSPHERIC CONVECTION

#### 2.1 Introduction

Large scale electric fields and corresponding plasma convections are generated throughout the major part of the outer magnetosphere by dynamic coupling with the solar wind. The outer magnetosphere maps magnetically to the high latitude regions of the Earth and the projection of the magnetospheric convection electric fields along geomagnetic field lines produce circulatory motions of plasma in the polar ionosphere. The charged particles move with the lines of force so long as the collision frequency is less than the gyro-frequency. This condition ceases to be valid first for ions at a height of about 140 km, and then for electrons lower down at a height of about 80 km. Consequently, in the E-region (~100-110 km) there is a differential motion between the ions and the electrons and this constitutes a current.

The existence of ionospheric currents was originally inferred from the perturbations which they produce in the geomagnetic field measured at the ground. Both Birkeland (1908) and Chapman (1918) found intense eastward currents (which produce positive excursions or bays in the horizontal or H component of the geomagnetic field) and westward currents (negative bays) in the polar region. Chapman named these horizontal currents the auroral electrojets.

Birkeland suggested that the electrojets are fed from outside the ionosphere by means of field-aligned currents (Birkeland currents), although he realised that there is no way of deducing unambiguously the

vertical current component purely from ground based observations. Direct experimental evidence for the existence of field-aligned currents in the polar region was provided by spacecraft observations of the distribution of field-aligned electron fluxes (Berko, 1973; Berko et al., 1975) and by satellite magnetometer data (Zmuda et al., 1966; Armstrong and Zmuda, 1970). These studies demonstrated that Birkeland currents are a permanent feature, observable even on magnetically very quiet days, and that they are concentrated in two circumpolar belts (Figure 2.1) situated within the auroral oval (Zmuda and Armstrong, 1974; Iijima and Potemra, 1976).

Chapman was concerned with a representation of the magnetic variations observed on the ground in terms of the so-called 'equivalent overhead current system' on a spherical shell concentric to the Earth. The  $S_q$  current system (Chapman and Ferraro, 1932) is related to the periodic magnetic variation over a solar day (S) under geomagnetically quiet conditions (q). The  $S_q$  variation, which is observed at all latitudes, is not thought to be driven by coupling with the magnetosphere, but is considered to originate from the dynamo action of the neutral wind system in the ionosphere and as such is beyond the scope of this discussion.

In polar regions, a particular type of diurnal variation of the geomagnetic field, denoted by  $S_q^P$ , was first recognised by Hasegawa (1940) and later by Nagata and Kokubun (1962), and this may be attributed to the current system illustrated in Figure 2.2. It is now known that this is due to a twin cell pattern of electron drift in the high latitude E-region, with a reversal of the flow direction in the auroral zone near midnight. The change in direction was first observed by Harang (1946) in ground magnetometer data which revealed a discontinuity in current flow. Heppner (1972a) named this feature the Harang discontinuity. The  $S_q^P$  variation, which is always present, is superposed on the  $S_q$  system and at midlatitudes these can be difficult to separate. The polar variation cannot be accounted for in terms of the wind dynamo action since the required wind

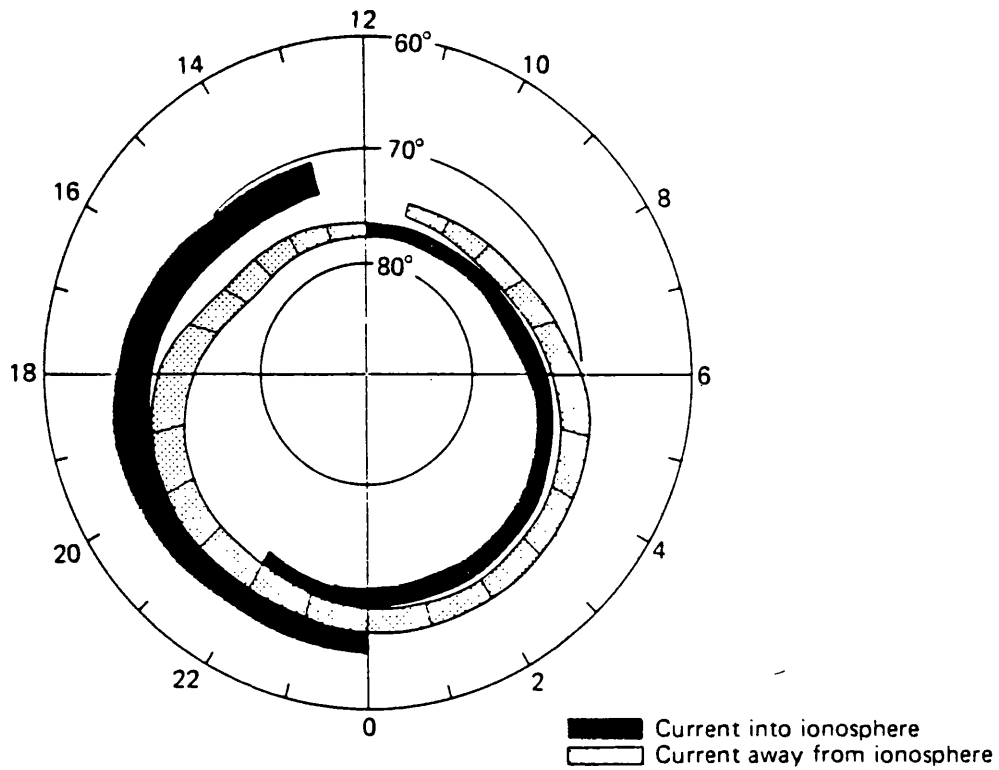


**FIGURE 2.1.** *The distribution and flow directions of large scale Birkeland currents during weakly disturbed conditions. [From Iijima and Potemra, 1978.]*

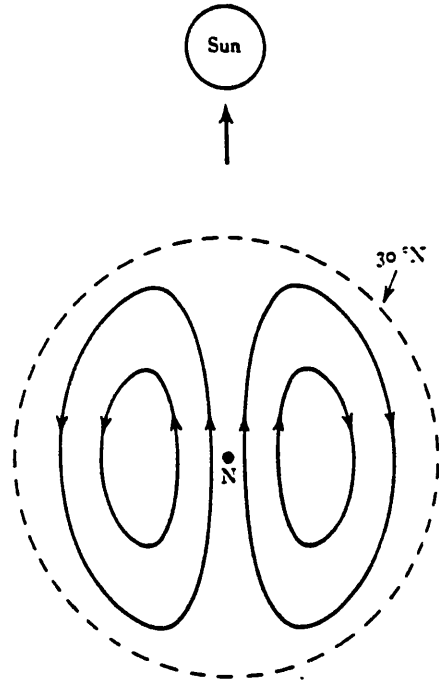


**FIGURE 2.2.** An idealised representation of the current system in the polar region that is responsible for the  $S_q^P$  part of the solar diurnal variation.

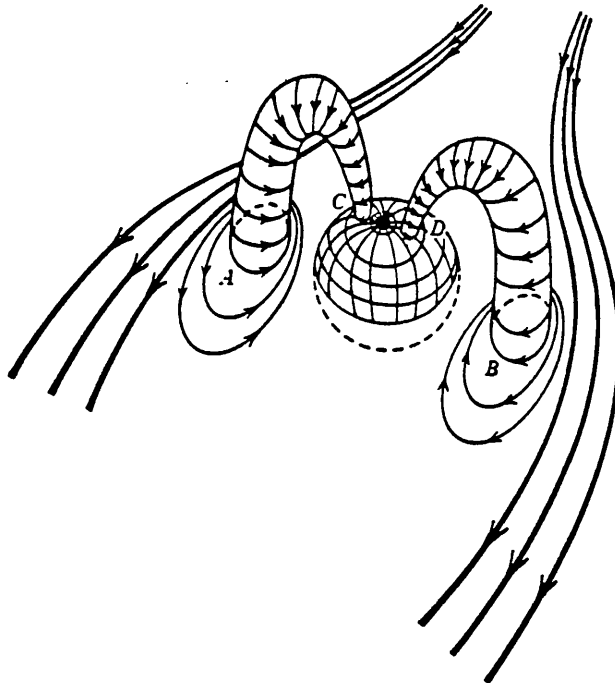


**FIGURE 2.3.** To illustrate the viscous interaction mechanism. The solar wind produces circulatory movements of plasma at A and B. These motions are transferred along the field lines and into the E-region giving rise to circulatory loops of electrons at C and D. [From Ratcliffe, 1972.]

speeds and ionospheric conductivities are far too large to be physically realistic. It appears, therefore, that the  $S_q^P$  current system is generated by the coupling of the high latitude ionosphere to the solar wind driven magnetospheric flows by means of field-aligned currents (e.g. Matsushita and Xu, 1982).

Nishida (1968, 1971) suggested that there is an additional magnetic variation, termed DP-2, which is global in extent and which intermittently grows and decays with a dependency on the north-south component of the IMF. Nishida proposed a further  $B_z$  dependent equivalent current system, the DP-1 variation, which is superposed on  $S_q^P$  and which is associated with the substorm current system localised in the midnight sector (section 2.3.5). Akasofu et al. (1973a) and Leont'yev and Lyatskiy (1974) state that DP-2 and DP-1 fluctuations are not due to new current systems, but arise from IMF modulations of the permanently existing  $S_q^P$  current system.

## 2.2 Solar Wind-Magnetosphere Coupling Processes

### 2.2.1 Viscous Interaction

In 1961, Axford and Hines suggested that magnetospheric flows are driven by a 'viscous like' interaction between the ionised material in the outer 'closed' magnetosphere and the solar wind. The precise mechanism by which momentum is transferred from the solar wind plasma to the magnetospheric boundary layer was physically unspecified. A simple frictional interaction depends on collisions between particles. However, the particle densities in the interaction zone are far too low for collisions to be significant. The coupling could be initiated by some irregularity (such as the Kelvin-Helmholtz instability) or alternatively involve the transport of magnetosheath particles onto closed geomagnetic field lines either by classical magnetic (gradient and curvature) drift or anomalous (non-collisional) cross-field diffusion (Hill, 1983 and references

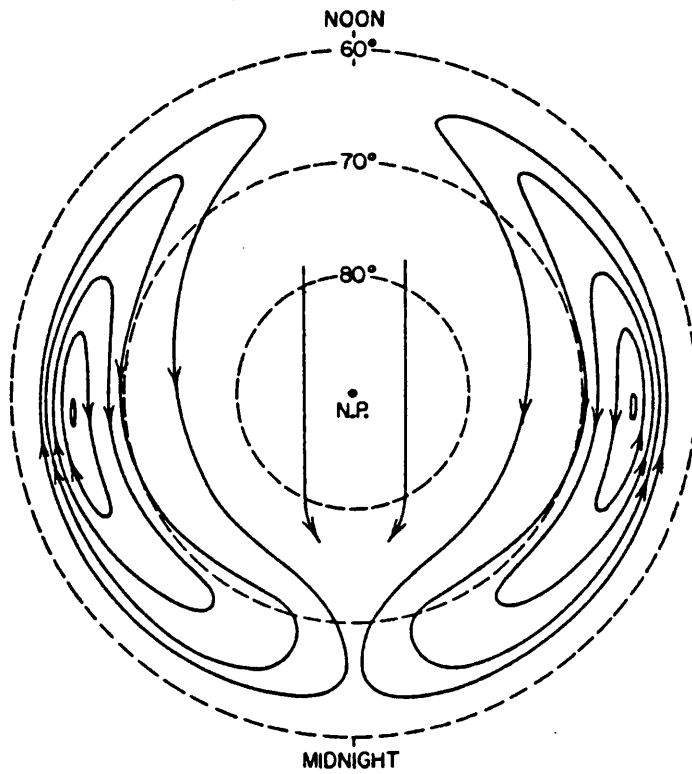


**FIGURE 2.4.** The symmetric two cell ionospheric convection pattern predicted by the viscous interaction model. [From Axford and Hines, 1961.]

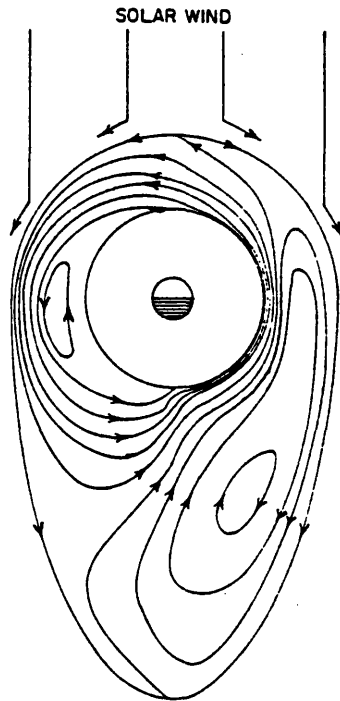


**FIGURE 2.5.** Plasma motion in the equatorial plane of the magnetosphere driven by viscous interaction and incorporating the effect of the Earth's rotation. [From Axford and Hines, 1961.]

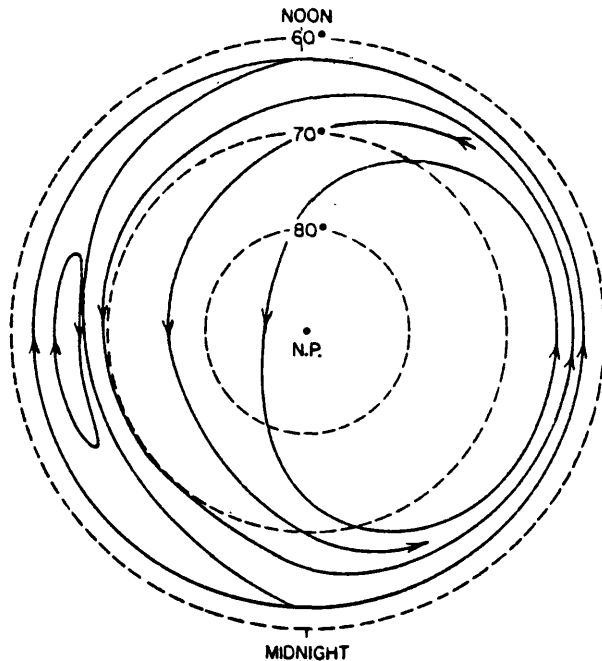


**FIGURE 2.6.** Asymmetric two cell convection pattern obtained by mapping the motions of Figure 2.5 along the geomagnetic field lines down to ionospheric levels. [From Axford and Hines, 1961.]

therein).

As a result of the transfer of momentum across the magnetopause, the magnetospheric plasma is carried away from the sun towards the geomagnetic tail. Because the plasma is 'frozen' onto closed geomagnetic field lines and the build up of material in the tail cannot persist in the steady state, a return flow of ionisation is set up in the interior of the magnetosphere. Circulatory loops are established in which the ionisation convects continuously. Since the lines of magnetic force are constrained to move with the plasma, these motions are transferred along the field lines and into the ionosphere in the manner depicted in Figure 2.3. Consequently, this simple model gives rise to a symmetric two cell pattern of convection in the E-region of the ionosphere illustrated in Figure 2.4, in which electrons flow over the poles in an antisunward direction, with a return flow at middle latitudes. The ion motion is collision dominated, and thus the ions drift with the neutral species. The general features of the predicted E-region electron convection pattern are in agreement with the  $S_q^P$  current system derived from magnetometer measurements.

As a consequence of the rotation of the Earth and its ionosphere, the geomagnetic field lines are carried round by the conducting ionosphere at their base and transport the magnetospheric plasma with them. When this rotation of the plasma is incorporated into the viscous interaction model, the resulting motion in the equatorial plane of the magnetosphere has the form depicted in Figure 2.5. If these flows are mapped down the field lines, the resulting ionospheric convection is an asymmetric two cell pattern (Figure 2.6).

### 2.2.2 Magnetic Reconnection

Dungey (1961) introduced the concept of solar wind interaction with an open magnetosphere through the interconnection of magnetic field lines between the Earth and the interplanetary medium. The Dungey model involves the

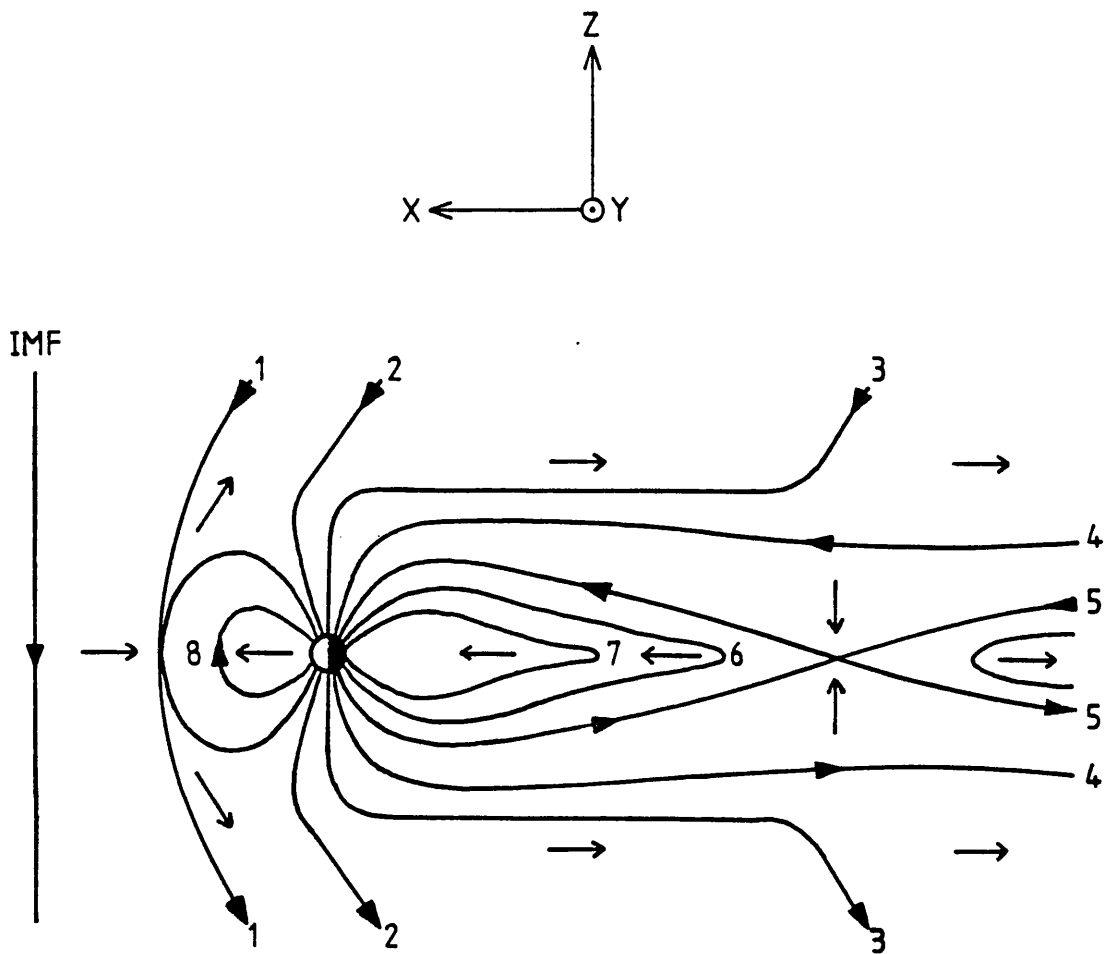
merging of geomagnetic field lines on the dayside of the Earth's magnetopause with the IMF. Since the IMF is frozen into the solar wind, the opened field lines are 'dragged' across the poles, transporting plasma in an antisunward direction. The field lines reconnect in the magnetospheric tail and the return flow is on closed field lines around the flanks of the magnetosphere.

Figure 2.7 is a schematic illustration of the process in the noon-midnight meridian plane, for a purely southward IMF. The merging takes place where the interplanetary and geomagnetic field lines are initially antiparallel (Crooker, 1979), which in two dimensions occurs at a single point where the net field is zero (neutral). In the merging process, the two antiparallel field lines form an X-type configuration which, extending the picture to three dimensions, occurs in the equatorial plane along the dayside half of the neutral line. Dayside merging is complemented by the reconnection of the IMF and geomagnetic field lines along the nightside half of the neutral line. The ionospheric image of the resultant magnetospheric convection cycle is again a two cell flow pattern consistent with the  $S_q^P$  current system.

The above convection mechanism has been described in terms of the bulk motion of ions and electrons in the presence of the geomagnetic induction  $\underline{B}$ . If this 'magnetoplasma' moves with a velocity  $\underline{V}$ , then according to the MHD approximation (e.g. Siscoe, 1983) an electric field is established given by

$$\underline{E} = -\underline{V} \times \underline{B}$$

Since the conductivity along the magnetic field lines is very high, the circulation of the magnetosphere is equivalent to an electric field which maps from the magnetosphere into the ionosphere. In the tail and in the polar cap the electric field is directed from the dawn side to the dusk



**FIGURE 2.7.** Schematic representation of the convection cycle proposed by Dungey (1961) initiated by dayside reconnection between the geomagnetic field and a purely southward-directed IMF ( $B_x = 0$ ,  $B_y = 0$ ). The numbers indicate the successive positions of a flux tube in the cyclic flow. [From Cowley, 1982.]

side. The corresponding potential drops across these regions are important quantities to measure since they depend on the efficiency of the solar wind magnetosphere coupling process and, in turn, govern the magnitude of the ionospheric convection flows.

### 2.2.3 Open vs. closed

Both the open (Dungey) model and the closed (Axford and Hines) model predict the two cell circulation topology of the  $S_q^P$  current system observed in the high-latitude ionosphere. Measurements from satellites positioned in the magnetosphere suggest that both mechanisms contribute to high latitude electrodynamics. The experimental evidence indicates that the magnetosheath plasma exerts tangential stresses on closed field lines through the low latitude boundary layer (Eastman et al., 1976). Direct evidence for dayside merging as steady (Gosling et al., 1982) and sporadic processes (Russel and Elphic, 1979) has been provided by the ISEE 1 and ISEE 2 satellites.

However, the observed IMF dependence of the ionospheric flow pattern (section 2.4) has provided a strong indication that the Dungey magnetic reconnection process is normally the dominant mechanism in the generation of magnetospheric convection. Statistical studies (Reiff, 1983; Cowley, 1984 and references therein) have indicated that the polar cap potential drop responds to IMF  $B_z$  as expected in the Dungey model, and that on average less than 20% of this potential drop can be attributed to viscous interaction.

## 2.3 Observational Methods

Geomagnetic investigations with ground based magnetometers laid the foundations of the study of the high-latitude ionospheric convection pattern, and these continue to be important today. By combining

simultaneous measurements from stations at different longitudes, it is possible to infer an instantaneous picture of global convection (e.g. Kamide et al., 1982). However, this method has the disadvantage that there are only a limited number of observing stations and many assumptions are required in order to deduce the current system.

Electric fields have been measured by stratospheric balloon borne sensors (Mozer and Serlin, 1969) but this technique suffers from its dependency on the mapping of the ionospheric electric field to the altitude of the balloon (typically 25 km), an assumption which may not always be valid (Park, 1976). Several balloons must be employed simultaneously to achieve any degree of spatial coverage.

Injun 5 (Cauffman and Gurnett, 1971) and OGO 6 (Heppner, 1972b) were the first of the high inclination satellites which have probed the large scale electric field distribution. The Atmosphere-Explorer C spacecraft measured ion drifts directly (Heelis et al., 1976). The advantage of satellite measurement techniques is that they provide complete and nearly instantaneous (typically 10 minutes is required for one pass over the auroral zones and polar cap) cross-sections of the convection pattern. The principal disadvantage is that the measurements are restricted to the path of the satellite.

High latitude convection flows have also been measured by both incoherent and coherent ground based radars. The first auroral zone incoherent scatter radar was installed in 1972 at Chatanika, Alaska (Banks et al., 1973). In both the incoherent and coherent radar methods, the Doppler shift of the echo gives one component of the convection drift velocity. In the case of monostatic radars like Chatanika, the velocity vector is determined by combining the measurements from three different successive antenna pointing directions. This requires the assumption of spatial and temporal homogeneity of the velocity field. The incoherent technique suffers from the disadvantage that the scattered signal is very

weak. As a result, incoherent radars need very high transmitter powers and large receiving antennas and can only probe comparatively small volumes of plasma at a time. The lack of instantaneous spatial coverage is the most serious disadvantage of the incoherent scatter technique for convection studies.

The coherent radar technique (Greenwald et al., 1978) depends on the scattering of radio waves by plasma density irregularities which propagate perpendicular to the magnetic field with a phase velocity related to the electron drift velocity. These radars can provide large spatial coverages together with high spatial and temporal resolutions. As with all ground based measurements, the effective global temporal resolution for a single system is 24 hours. One disadvantage of the coherent technique is that echoes are received only when the electric field threshold for the production of ionospheric irregularities (about  $15 \text{ mV m}^{-1}$ , Greenwald et al., 1978) is exceeded. The large coherent radar data bases have proved particularly useful for both statistical investigations of the gross long term features of the convection flow pattern, and for the study of short time scale structures such as those associated with substorms.

#### 2.4 Observations of the High Latitude Convection Pattern

In general the IMF does not point purely southward ( $B_z < 0$ ), but has components in the solar equatorial plane (Sun-Earth direction,  $B_x$ , and east-west direction,  $B_y$ ). In addition, the IMF can be directed northward ( $B_z > 0$ ). The different effects of these components on the steady merging and reconnection process have specific consequences for the observed high latitude ionospheric convection flows. During substorms, reconnection tends to occur in bursts, and this also has a particular ionospheric convection signature. The influence of substorms can be difficult to distinguish from the quiet steady state reconnection effects. Thus, the

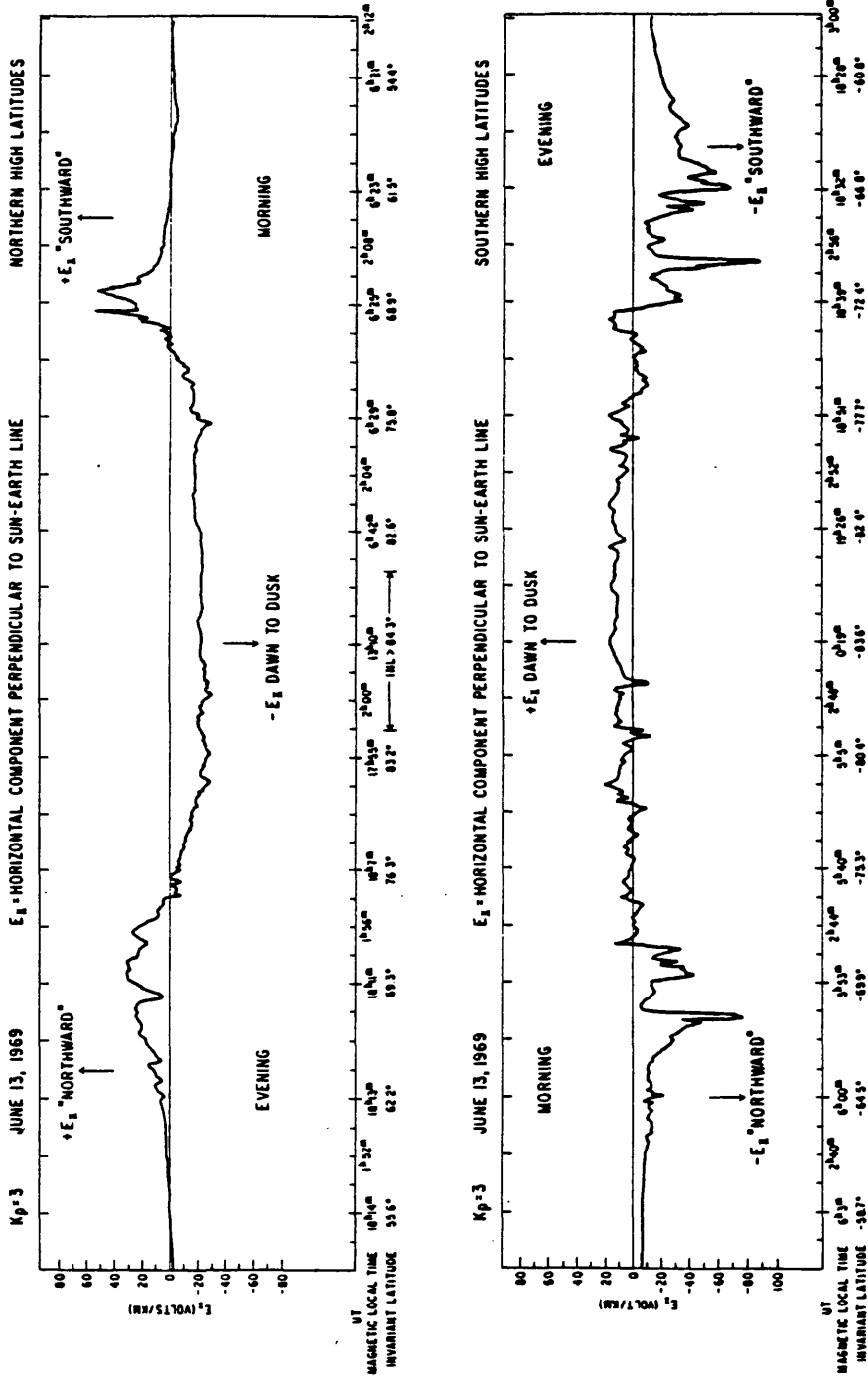
influence of the IMF on substorm dynamics must be incorporated into the convection flow models.

#### 2.4.1 Convection with IMF $B_z < 1$ nT

Under conditions of negative or weakly positive IMF  $B_z$ , the gross features of the plasma convection pattern are as depicted in Figure 2.6. The OGO-6 satellite gave the first complete cross-section of the ionospheric electric field from mid-latitudes and across the polar caps. Electric field profiles measured for two OGO-6 traverses, one of the northern polar region and the other of the southern polar region, are reproduced in Figure 2.8 (Heppner, 1972b). The north pole signature indicates that the satellite passed successively over the northern evening auroral belt (northward E), the polar cap (dawn-dusk E) and the morning auroral belt (southward E). A similar E-field profile was obtained for the south pole traversal and the results are consistent with the existence of the two cell pattern over both poles.

The gross characteristics of the average two cell convection pattern have now been well established, particularly as a result of investigations with ground based incoherent (Foster et al., 1982; Alcaydé et al., 1986) and coherent (Zi and Nielsen, 1982; Waldock et al., 1985) radars. These systems are able to provide complete (but not instantaneous) representations of the large scale auroral convection flow system. A typical example of the large scale pattern observed over a 24 hour period (Figure 2.9) reveals several important features. The auroral portions of the morning and evening convection cells are very prominent, as is the reduction in velocities resulting from an attenuation of the electric field toward the equatorward edge. In the noon sector, convection flows associated with the cusp region are weak and the dayside flow reversal is ill defined. In the midnight sector, however, there is a clear reversal from westward to eastward directed flow at the Harang discontinuity.

FIGURE 2.8. Dawn-dusk components of the electric field along a dawn-dusk traverse across the northern and southern polar regions. [From Heppner, 1972b.]



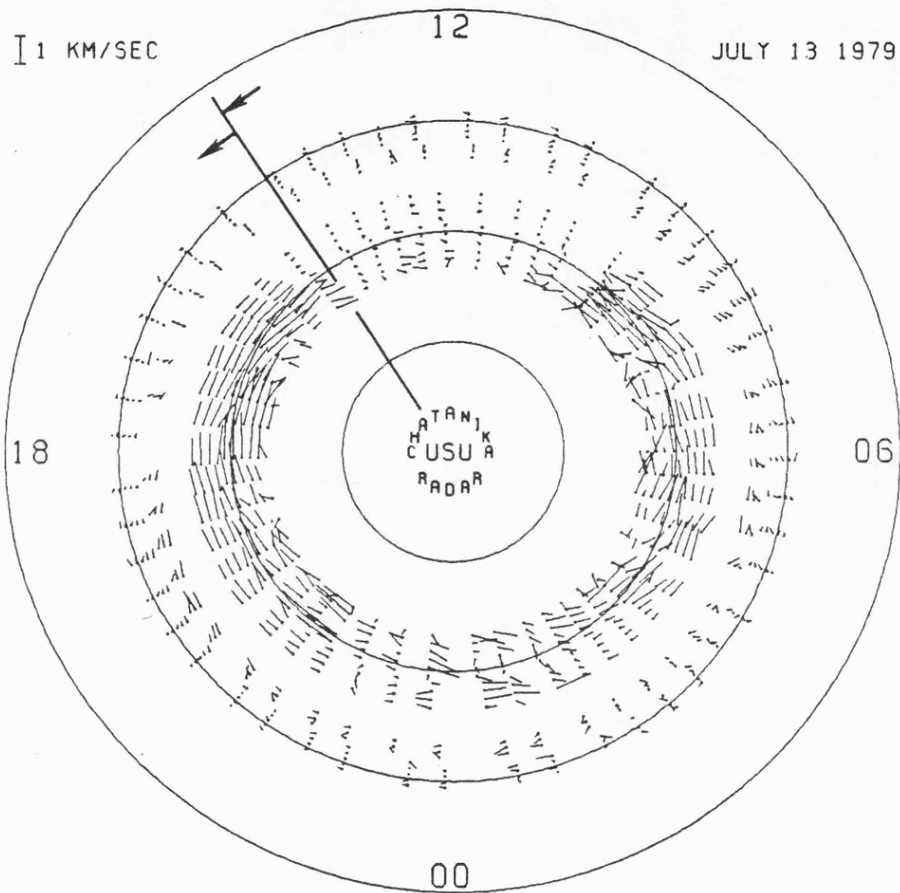


FIGURE 2.9. Plasma convection velocities observed with the Chatanika incoherent radar over 24 hours. A two cell pattern is apparent. [From Foster et al., 1982.]

There have been many investigations of  $B_z$  dependent variations in the convection pattern, but these have not been entirely definitive since negative  $B_z$  components lead to substorm activity. After the onset of substorm activity, it can be difficult to separate the substorm induced phenomena from normal steady reconnection driven flows. Nonetheless, several  $B_z$  effects have been established. Studies of the size of the polar cap, which gives a measure of the extent of the convection pattern, have indicated a correlation with  $B_z$ . Using DMSP satellite observations of the visual aurora made during quiet auroral displays, Holzworth and Meng (1975) found a linear relation between the radius of the auroral circle (ie., the size of the polar cap) and the hourly averaged magnitude of the interplanetary  $B_z$  component (Figure 2.10). This relation appeared to extend to conditions when the IMF had a substantial northward component ( $B_z > 1$  nT). Meng (1980) obtained an empirical expression for the radius of the auroral circle given by

$$R = 20.5^\circ - 1.25 B_z$$

where  $R$  is in units of co-latitude and  $B_z$  is in nT. An empirical relationship derived from balloon measurements by Mozer et al. (1974), has suggested that the polar cap electric field  $E$  is also proportional to  $B_z$ . The product of  $E$  and  $R$  in the dawn-dusk meridian is the cross polar cap potential  $\phi_{PC}$ . This parameter has been determined by the integration of electric field or plasma flow data obtained from low altitude spacecraft which cross the polar regions in the 1800 to 0600 local time meridian (Burke and Doyle, 1986, and references therein).  $\phi_{PC}$  is perhaps the most direct parameter for quantifying the solar wind/IMF coupling with the magnetosphere since it measures the rate at which newly merged magnetic flux is transferred from the dayside to the nightside of the Earth (Siscoe, 1982). The potential drops across the auroral oval (in the dawn-dusk

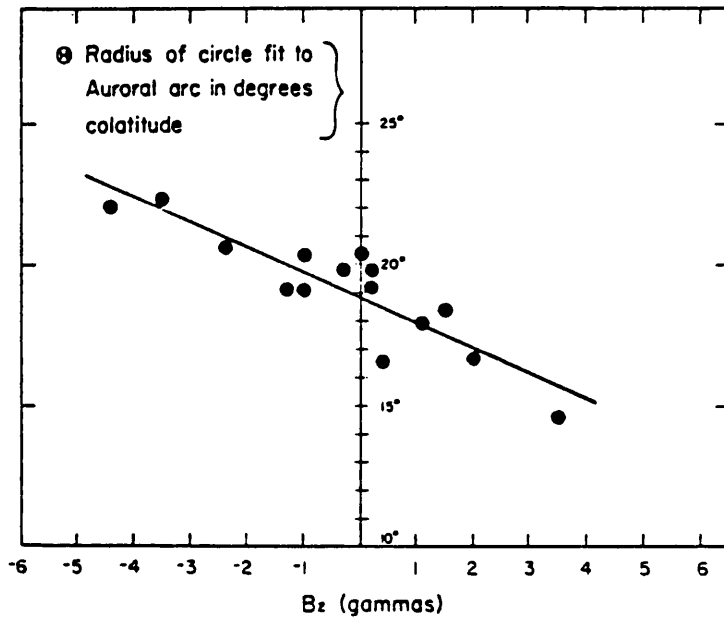


FIGURE 2.10. The relationship between the radius of the auroral circle and IMF  $B_z$ . [From Holzworth and Meng, 1975.]

meridian) give the rates of reconnected flux return. The sum of potential drops across the two auroral belts is on average approximately equal to the potential drop across the polar cap (Burke and Doyle, 1986). The polar cap potential drop, which ranges from 20 kV to 100 kV, has been found to increase as  $B_z$  becomes more negative (Reiff et al., 1981; Cowley, 1984).

The  $B_z$  effect on the convection flow pattern has also been investigated by studying field-aligned currents both with ground based (Rostoker et al., 1982) and satellite magnetometers (Kamide et al., 1976; Reiff and Burch, 1985). The ground based measurements indicated that the downward field-aligned currents across the noon sector, and the auroral eastward and westward electrojets which they feed, are intensified in response to southward turnings of the IMF. Satellite observations have demonstrated that the field-aligned currents associated with the dayside polar cusp move equatorward with increasingly negative  $B_z$  (Burch, 1973). The location of the cusp indicates the latitudinal extent of the large scale convection pattern.  $B_z$  dependent polar cusp motions have also been inferred from satellite measurements of the characteristics of particles and fields in the dayside magnetosphere (Russel et al., 1971; Burch, 1972, 1973; Meng, 1983) and by observations of the cusp aurora (Sandholt et al., 1985).

To summarize the observational evidence, there is a strong trend toward larger convection electric fields and an equatorward expansion of the convection flow pattern when  $B_z$  becomes more negative. These are the DP-2 variations in the  $S_q^P$  current system and they are consistent with the Crooker (1979) antiparallel merging model. The latter indicates that the length of the dayside merging line increases as the IMF turns south. This enhances the production rate of open flux tubes, thus increasing both the magnitude of the antisunward convection flow and the size of the polar cap.

#### 2.4.2 IMF $B_y$ -dependent asymmetries

The concept of a spiral configuration of the interplanetary magnetic field,

introduced in section 1.2, implies that the IMF usually has significant components in both the x and y directions. The first observational evidence for the modulation of the high latitude convection flow pattern by the  $B_y$  component was provided by Svalgaard (1968) and Mansurov (1969). They noticed differences in the daily magnetic variations measured by ground based magnetometers which had an apparent dependence on whether the Earth was located in a 'toward' or 'away' IMF sector. This change in the magnetic signature measured on the ground has been termed the Svalgaard-Mansurov effect or DPY disturbance.

Svalgaard (1973) proposed that the effect could be explained by an additional circular current superposed on the  $S_q^P$  current, and flowing about the magnetic pole at a magnetic latitude near  $80^\circ$  in an anticlockwise direction (viewed from above the north polar region) when the IMF was directed away and a clockwise direction when it was directed toward the Sun. Friis-Christensen et al. (1972) confirmed that IMF  $B_y$ , which is positive for away and negative for toward sectors, is responsible for the DPY disturbance.

The ground based magnetometer results were supported by the OGO-6 polar cap electric field measurements of Heppner (1972c, 1973), who observed that the electric field profile, obtained for dawn-dusk traversals of the polar cap, became asymmetric when the  $B_y$  component had a non-zero value, and that the sense of the asymmetry depended on the sign of  $B_y$ . The conclusion of Heppner was that positive (dawn to dusk) IMF  $B_y$  components produce convection electric field maxima on the dawn side of the northern polar cap and on the dusk side of the southern polar cap. These maxima are reversed for negative IMF  $B_y$  components. The results suggest a  $B_y$  dependent dawn-dusk shift of the large scale convection electric field pattern. In addition, DMSP satellite images of the visual aurora (Meng, 1980) have indicated a dawnward shift of the centre of the northern hemisphere auroral oval for  $B_y > 0$  and a duskward shift for  $B_y < 0$ .

Ion drift velocities measured in the vicinity of the cusp by the low altitude Atmosphere Explorer C satellite have suggested the existence of a confined 'throat' region (the dayside equivalent of the Harang discontinuity) through which the flow direction undergoes a rotation from sunward to antisunward (Heelis et al., 1976). Poleward of the cleft, the ion convection appeared to have a strong azimuthal flow directed toward dawn or dusk depending on whether  $B_y$  was positive or negative, respectively. These results were consistent with the convection pattern generated by Crooker's (1979) dayside merging model, in which two cells are formed for negative IMF  $B_z$ , one crescent shaped, the other oval. The crescent cell overlaps the oval cell on the dayside and lies on the morning (evening) side for positive (negative)  $B_y$ . Heelis (1984) presented empirical models of the flow geometries in the dayside northern hemisphere for different magnitudes of  $B_y$ . The inferred convection patterns (Figure 2.11) indicate that the dusk and dawn cells change their relative sizes and shapes depending on  $B_y$ . Also, it is evident that the antisunward flow maximum is shifted to the dawn side of the noon-midnight meridian for positive values of  $B_y$  and to the dusk side for negative  $B_y$ . Similar  $B_y$  modulations of the convection flow pattern have been deduced from spacecraft measurements of Birkeland currents (McDiarmid et al., 1978; Iijima et al., 1978; Burch et al., 1985), Millstone Hill incoherent scatter radar data (Holt et al., 1987) and SABRE cusp flow observations (Waldock et al., 1984).

The  $B_y$  dependent features may be explained in terms of an extension of the antiparallel merging concept out of the x-z plane in the y direction. Merging is favoured in regions where the vector magnetic fields of the interplanetary medium and the Earth are antiparallel, or at least very nearly so (Crooker, 1979). Figure 2.12 schematically illustrates the IMF and geomagnetic field geometries viewed from the sun and the location of the favoured merging regions for different IMF orientations. The  $B_x$

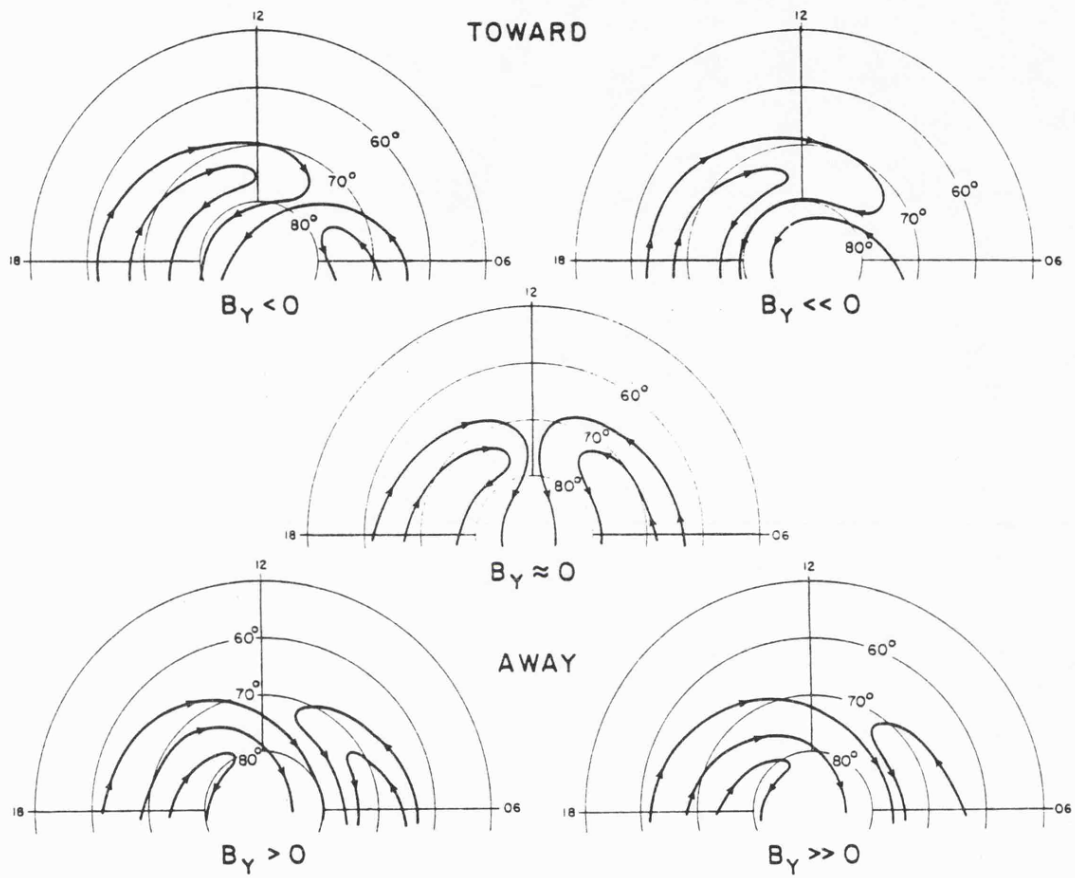


**FIGURE 2.11.** Schematic representation of the flow geometries in the dayside northern hemisphere, inferred from AE-C satellite observations, for different  $B_Y$  conditions.  $B_Z$  is negative and  $|B_X|$  is constant in all cases. [From Heelis, 1984.]

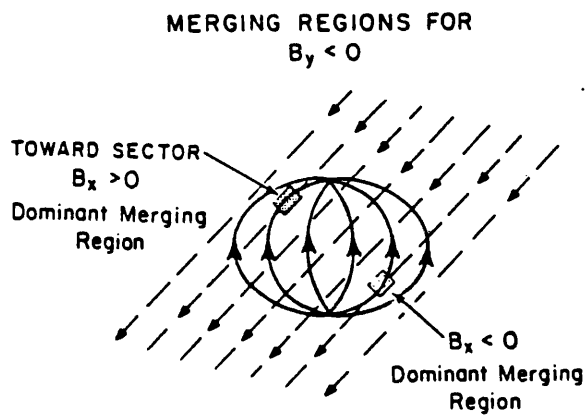
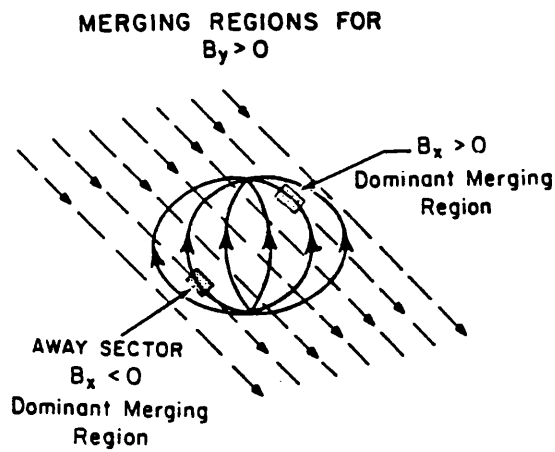


**FIGURE 2.12.** Schematic view of the IMF and geomagnetic field geometries viewed from the Sun. Regions of preferred merging for different orientations of the IMF are indicated by the shaded boxes. [From Heelis, 1984.]

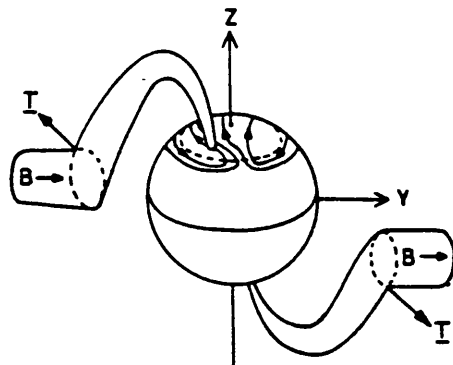


**FIGURE 2.13.** Schematic view of newly opened flux tubes on the dayside, illustrating the field line tension  $T$  arising from IMF  $B_y > 0$ , which results in oppositely directed azimuthal flows in northern and southern cusp regions. The flows reverse for  $B_y < 0$ . [From Cowley, 1982.]

component determines whether merging is promoted in the northern or southern hemisphere. If  $B_y$  is negative (positive), merging takes place in the pre-noon (post-noon) sector in the northern hemisphere.

According to Cowley (1981, 1982), provided  $B_y$  is not zero, the tension on newly opened flux tubes has a net east-west component, which is oppositely directed in northern and southern hemispheres (Figure 2.13). These oppositely directed forces constitute a torque exerted by the IMF on the magnetosphere, which drives the observed oppositely directed azimuthal flows in the dayside cusp. This torque may be considered to arise from a 'penetration' of the IMF  $B_y$  component into the magnetosphere (Alexeev, 1986).

#### 2.4.3 Effects associated with IMF $B_x$

The principal effect of  $B_x$  variations on the high-latitude ionospheric convection pattern appears to be sunward-tailward shifts of the flows. The analysis of DMSP auroral images has indicated that the northern auroral oval is shifted tailward for positive  $B_x$  and sunward for negative  $B_x$  and vice versa in the southern hemisphere (Meng, 1980).

Cowley (1982) suggests that this result is a consequence of the appearance of a  $B_x$  component within the magnetosphere whose sign depends on the IMF  $B_x$ . The shift of the oval is oppositely directed to the net x-directed flux in the northern hemisphere, and in the same direction in the southern hemisphere. The possible appearance of  $B_x$  within the magnetosphere is analagous to the  $B_y$  effect described above, and may be considered as being due to inter-hemispheric differences in the flux tube tension on newly opened dayside field lines.

#### 2.4.4 Convection with northward IMF ( $B_z > 1$ nT)

During periods of northward IMF, the electrodynamics of the high latitude ionosphere are observed to be radically different from the normal two cell

system. The first evidence for this was provided by OGO 6 electric field data (Heppner, 1972c) which indicated that a region of dusk-to-dawn electric field occasionally appeared in a localised region of the central polar cap when magnetic activity was low. Heppner (1977) and Heppner and Maynard (1987) interpreted these results as arising from localised distortions of the two cell pattern.

However, Maezawa (1976) demonstrated that magnetic field deflections observed at four high latitude stations during the summers of 1966 and 1968 when  $IMF B_z > 1$  nT could only be explained if convection was directed sunward across the central polar cap. This conclusion was supported by S3-2 satellite (Burke et al., 1979) and MAGSAT satellite observations (Iijima et al., 1984). An example of S3-2 measurements of the dawn-to-dusk electric field component, obtained over the southern hemisphere when the hourly averaged value of  $B_z$  was 4.9 nT, is depicted in Figure 2.14. Regions of positive (negative) electric field correspond to regions of antisunward (sunward) convection. The figure illustrates how the data may be interpreted as evidence for the existence of a four cell pattern for northward IMF, with antisunward flow along the flanks of the polar cap and sunward flow in the auroral oval and in the central polar cap.

Consideration of the simple Dungey model indicates that a magnetically open magnetosphere can occur for all orientations of the IMF except due north, when a closed magnetosphere is predicted (e.g. Stern, 1973; Cowley, 1973). To explain the formation of a four cell pattern, it has been assumed (Maezawa, 1976; Burke et al., 1979; Cowley, 1982) that the two polar cap cells are driven by magnetic merging between the northward directed IMF and tail lobe field lines poleward of the dayside cusp, leading to the formation of closed field line 'boundary layers'. This process, schematically depicted in Figure 2.15, results in the removal of flux from the tail and the addition of closed field lines containing magnetosheath plasma to the dayside, and gives rise to the 'reverse'

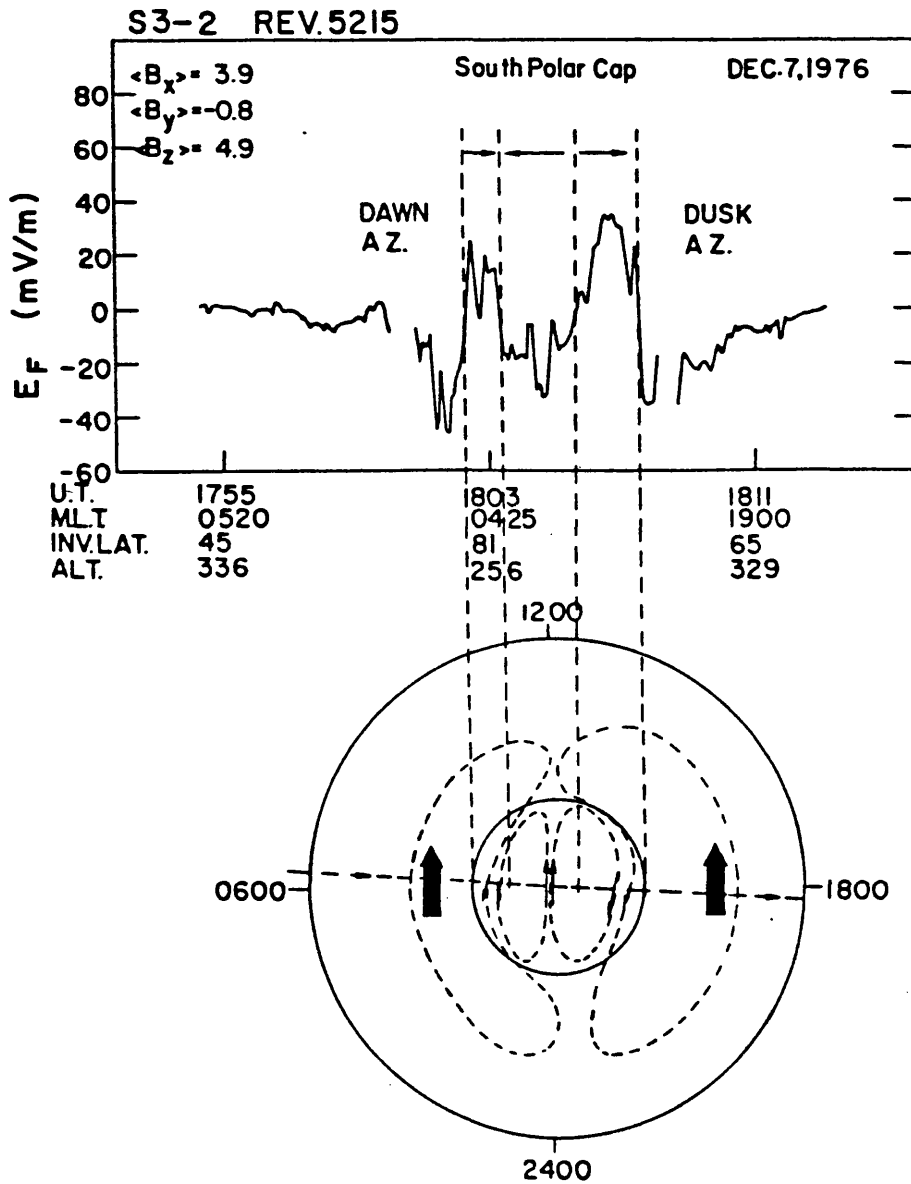


**FIGURE 2.14.** Dawn-dusk component of the convection electric field measured by the S3-2 satellite when the IMF had a 4.9 nT northward component. A four-cell convection pattern consistent with the electric field data is sketched in the lower panel. [From Burke and Doyle, 1986.]

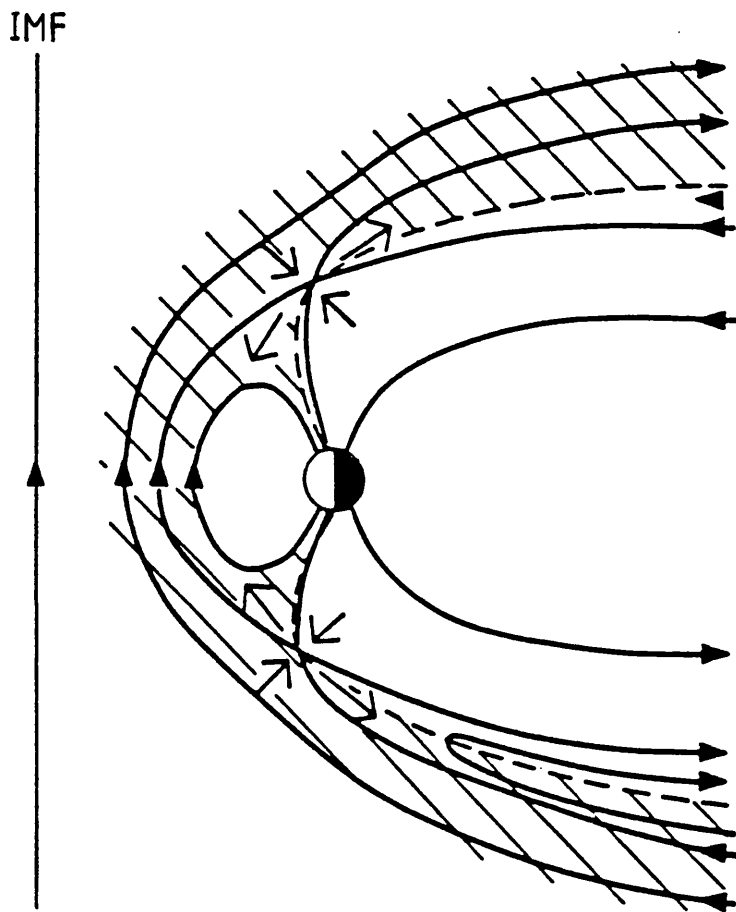


FIGURE 2.15. Sketch of the formation of closed field line boundary layers at the dayside magnetopause by the reconnection process for northward IMF. The arrows indicate the directions of field line motion near to the reconnection sites while the hatching indicates the region occupied by magnetosheath plasma. [From Cowley, 1986.]

convection cells at very high latitudes with sunward flow in the central polar cap. The two cells at lower latitudes are generated by the circulation of closed field lines driven by viscous forces acting on the low latitude magnetopause boundary layers (Cowley, 1982; Mozer, 1984).

The observational evidence for a four cell model of ionospheric convection with northward IMF is not conclusive. The convection velocities are generally smaller, and thus less easy to measure accurately, than those observed when the IMF has a southward component. This fact, coupled with a considerable degree of structure or turbulence in the nightside hemisphere during northward IMF (Heppner et al., 1972c; Bythrow et al., 1985; Heelis et al., 1986), make characterization of the convection pattern extremely difficult. Heppner and Maynard (1987) reject the concept of a multi-cell pattern maintaining that the observations can be interpreted in terms of a rotationally distorted two cell system.

#### 2.4.5 Substorm response of the magnetosphere and ionosphere

During relatively quiet conditions, steady nightside reconnection occurs far down the tail. The expansive phase onset of a magnetospheric substorm is triggered by the sudden 'explosive' reconnection of tail magnetic flux, which takes place at a position much closer to the Earth (typically 10-20  $R_E$ ) (Baker et al., 1987). The resultant formation of a near-Earth neutral line pinches off a tailward portion of the plasma sheet, producing a magnetically closed bubble of plasma called the plasmoid which travels rapidly tailward (Hones et al., 1984; Baker et al., 1984).

On the Earthward side of the neutral line, initially tail-like field lines rapidly collapse toward the Earth, reverting to a more dipolar configuration. In the process they carry hot plasma and energetic particles onto trapped orbits near 7  $R_E$ , causing an enhancement in the ring current and the near-Earth cross tail current (Wolf, 1983; Baker et al., 1987). The ionospheric response to a substorm is azimuthally localised in

the midnight sector and is characterised by particle precipitation which causes both a sudden brightening of auroral arcs (Baumjohann et al., 1981) and a large increase in ionospheric conductivities (Horwitz et al., 1978). As a result, a part of the enhanced cross-tail current is diverted down the collapsing field lines, where it is closed in an intensified westward electrojet (Kamide, 1982; Baumjohann, 1983). This three dimensional current system, known as the substorm current wedge and illustrated in Figure 2.16, was introduced by McPherron et al. (1973) to explain the geomagnetic signature of a substorm.

The main consequence of a substorm for the high latitude convection pattern is a rapid westward expansion ( $1-2 \text{ km s}^{-1}$ ) of the substorm enhanced westward electrojet (Kamide et al., 1982; Baumjohann and Glassmeier, 1984), the magnetic signature of which is the DP-1 disturbance. This is consistent with coherent radar observations which have indicated that the Harang discontinuity moves to earlier local times as substorm activity increases (Zi and Nielsen, 1982; Waldock et al., 1985). The growth and decay of the horizontal ionospheric current system during a typical substorm, as inferred from a global network of magnetometers by Kamide et al. (1982), is reproduced in Figure 2.17.

The question of how substorm activity is influenced by the interplanetary medium must be addressed in order to understand the solar wind modulation of the high latitude convection pattern under disturbed conditions. Magnetospheric substorms result from the sudden release of energy which has been steadily accumulated in the magnetosphere by its interaction with the solar wind. The energy transference is most efficient when the IMF is directed southward (Fairfield and Cahill, 1966; Rostoker and Fälthammer, 1967). Investigations of the relationship between solar wind parameters and geomagnetic activity have emphasised both  $B_z$  and the solar wind velocity (e.g. Clauer et al., 1981; Holzer and Slavin, 1982).

The triggering of substorms by the step-like turning of the IMF to the

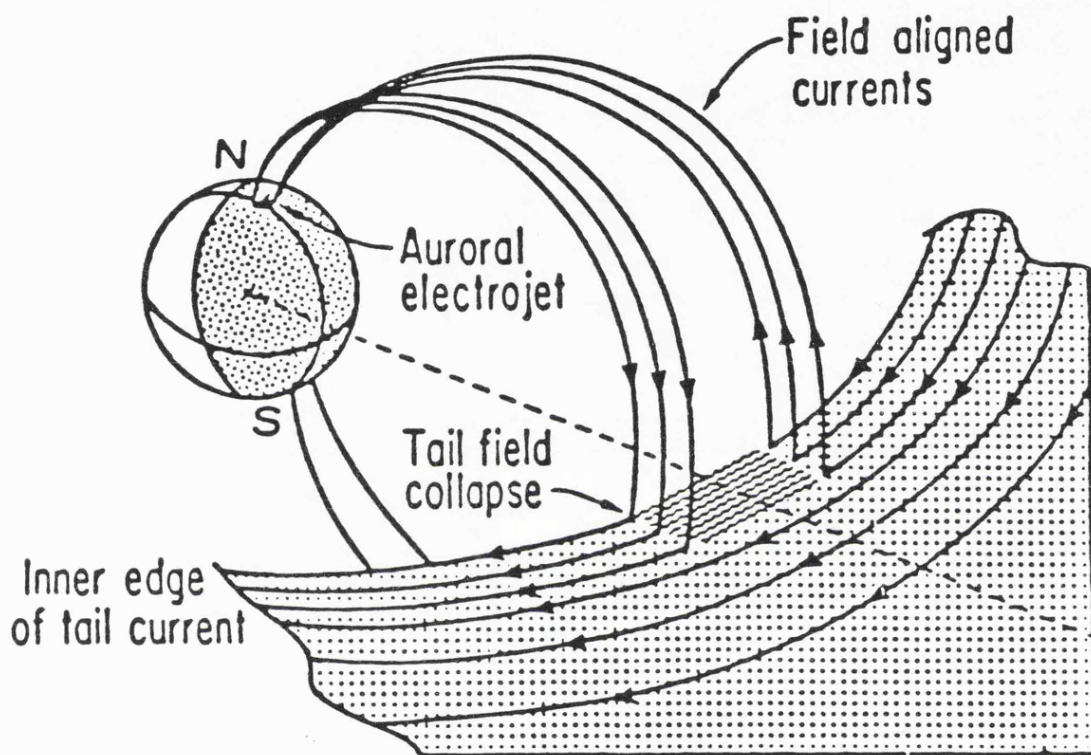


*FIGURE 2.16. The substorm current system introduced by McPherron et al. (1973). Part of the cross-tail current is diverted down geomagnetic field lines and closes via a westward electrojet in the auroral ionosphere.*

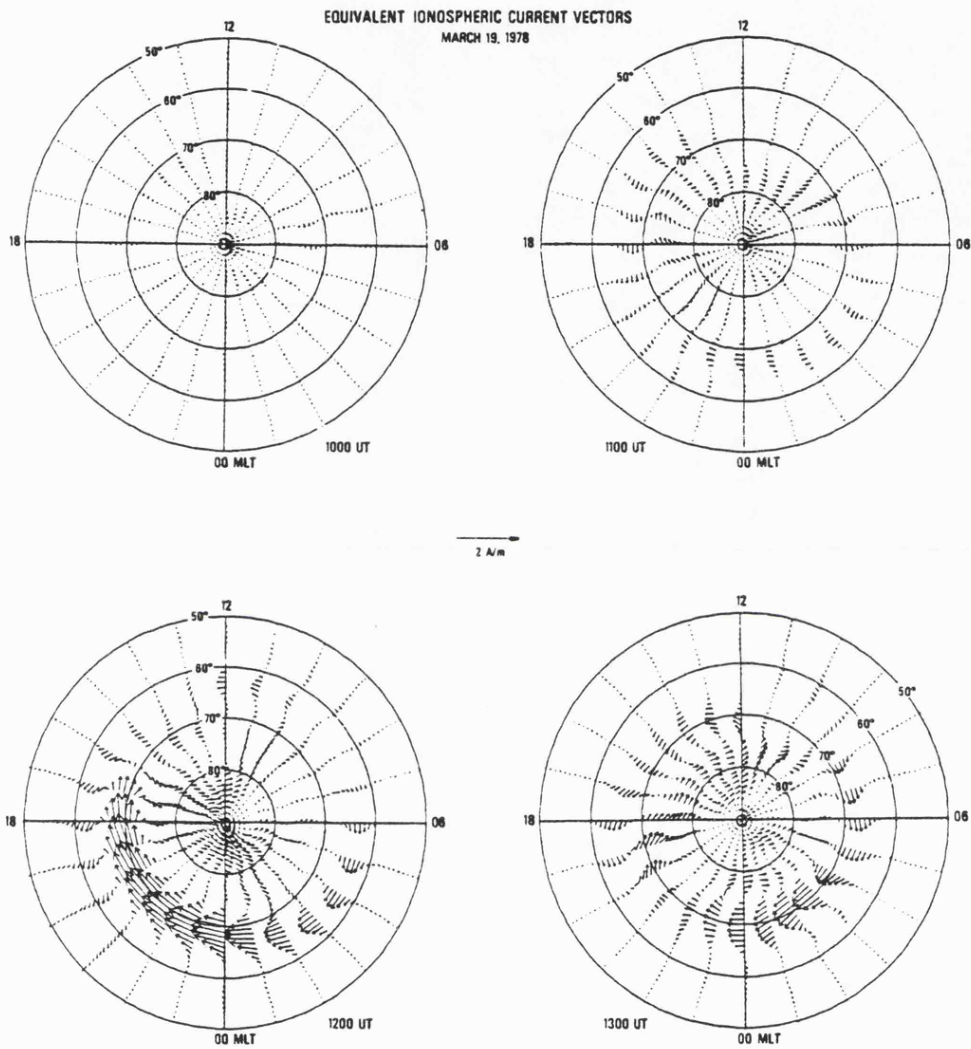


FIGURE 2.17. Equivalent ionospheric current vectors inferred from measurements provided by a global network of magnetometers during a substorm. [From Kamide et al., 1982.]

north (Caan et al., 1977; Rostoker, 1983) or by sudden changes in the solar wind dynamic pressure leading to an ssc (Kawasaki et al., 1971; Kokubun et al., 1977) is well established. A substorm onset requires the formation of a neutral line, which in turn should depend on the magnitude of the component of the magnetic field perpendicular to the neutral sheet (Galeev et al., 1978). Both an ssc and a northward turning could alter this component. McPherron et al. (1986) concluded that triggering by northward turnings appears to be much more common than ssc triggering. In addition, they found that not all sudden expansion onsets are obviously correlated with changes in the interplanetary medium, suggesting that some may be due to a process internal to the magnetosphere. This conclusion has been supported by recent observations by Eather (1985) of the dayside aurora, which, contrary to the result of most earlier studies (see section 2.3.1), indicated that the position of the dayside cusp does not depend strongly on  $B_z$ . Eather found a close dependence on the auroral electrojet (AE) index suggesting that the position of the cusp may be largely controlled by substorm processes internal to the magnetosphere rather than by the direct merging of the geomagnetic field with the IMF.

## 2.5 Energy Coupling

Present understanding of solar wind-magnetosphere coupling has been enhanced by empirical studies which attempt to develop an energy coupling function. Such a parameter is likely to depend on the velocity of the solar wind and the orientation of the IMF and should correlate well with quantities which measure substorm activity. There has been considerable disagreement as to the most appropriate form for the energy input parameter or function. Arnoldy (1971) suggested simply the product of the solar wind velocity with the southward IMF component ( $vB_s$ ), while Rostoker et al. (1972) employed the very similar expression  $-vB_z$ . This quantity, which has

units of Volts  $m^{-1}$ , is equivalent to the east-west (dawn-dusk) component of the interplanetary electric field and implies an electrostatic coupling with the magnetosphere. The expression  $VB_s$  allows no energy transfer for northward IMF, and has therefore been termed the half-wave rectifier model (Burton et al, 1975).

Perreault and Akasofu (1978) proposed that the most suitable parameter is the power developed by the solar wind-magnetosphere dynamo  $\epsilon$ . Now the total solar wind kinetic energy flux incident upon the magnetosphere is given by (e.g. Schwenn, 1981)

$$K = \frac{1}{2}\rho V^3 l_0^2$$

where  $\rho$  is the density of the solar wind,  $V$  is the flow velocity and  $l_0$  is a dimension of the magnetosphere ( $\sim 7 R_E$ ). Since little direct relationship appears between  $K$  and the energy dissipated within the magnetosphere as indicated by geomagnetic activity, the energy coupling function  $\epsilon$  was expressed in the form of the solar wind magnetic energy flux. An estimate of  $\epsilon$  was obtained in terms of the Poynting flux ( $\underline{E} \times \underline{B}/\mu_0$ ) incident on the front of the magnetosphere and this yielded

$$\epsilon = V(B^2/\mu_0)\sin^4(\theta/2)l_0^2$$

where  $B$  is the IMF magnitude, and  $\theta$  is the polar angle of the IMF projected on the Y-Z plane ( $= \tan^{-1}(|B_Y|/B_Z)$  for  $B_Z > 0$  or  $\pi + \tan^{-1}(|B_Y|/B_Z)$  for  $B_Z < 0$ ). Unlike  $VB_s$ , the  $\epsilon$  parameter is a 'leaky' function which predicts a weak solar wind-magnetosphere interaction for northward IMF.

Murayama et al. (1980) suggested the parameter  $V^2B_s$  as a coupling function. Baker et al. (1981a, 1983) evaluated the correlative behaviour of the  $VB_s$ ,  $V^2B_s$  and  $\epsilon$  parameters with the level of geomagnetic activity as measured by the AE index. They found the parameters to have virtually

identical correlation properties with AE during quiet times, but that of the three  $\epsilon$  was less well correlated under disturbed conditions. Nonetheless, it has been observed that weak substorm activity occurs even when the IMF has been northward for several hours (Akasofu et al., 1973b; Akasofu, 1974) whereas the half-wave rectifier coupling functions  $VB_s$  and  $V^2B_s$  predict zero energy transfer for positive  $B_z$ . However, if the time taken for the tail to dissipate all of its stored energy and return to the ground state is sufficiently long, the  $VB_s$  and  $V^2B_s$  parameters may still be valid.

## 2.6 Summary

Observations of high latitude ionospheric convection flows and the resulting advances in the understanding of the solar wind-magnetosphere interaction have been reviewed. Although progress in recent years has been particularly rapid, there remain many unanswered questions. The present view of the IMF dependent behaviour of the convection flows is based mainly on low altitude satellite measurements, which provide only one dimensional profiles of the pattern. Consequently, some of the features of the interaction mechanism are only qualitatively understood. Also, the coupling for northward IMF is still a subject of great controversy and no completely satisfactory energy transfer function has yet been proposed. Until these problems have been resolved, it will not be possible to develop a self consistent model capable of predicting the detailed ionospheric response to a given set of interplanetary conditions.

## CHAPTER 3

### MEASUREMENT TECHNIQUES

#### 3.1 Introduction

SABRE (the Sweden And Britain Radar aurora Experiment) was constructed by the University of Leicester and the Max Planck Institut für Aeronomie (MPAE), Lindau, W. Germany. Commencing bistatic operation in March, 1982, SABRE was a development of STARE (Scandinavian Twin Auroral Radar Experiment) which was built by MPAE in 1977. SABRE, whose operational characteristics are very similar to those of STARE, was designed to make measurements of E-region electron flows in a viewing area located to the south-west of that of the older STARE system. Together, the two facilities provide a large latitudinal coverage over an L shell range of 4 to 8.

SABRE observations of the high latitude convection pattern, and to a lesser extent those of STARE, have provided the bulk of the observations presented in this thesis. However, an investigation of the solar wind control of E-region convection flows would be incomplete without simultaneous observations of the interplanetary medium. Thus, the following discussion of experimental techniques concludes with a brief description of the two spacecraft, ISEE-3 and IMP-8, from which the solar wind data have been obtained.

#### 3.2 SABRE

SABRE and STARE are bistatic VHF auroral backscatter radar systems, which can detect the backscattered signals from field aligned plasma

irregularities present in the auroral E-region (Greenwald et al., 1978). From the measured Doppler shifts of these signals, the high latitude convection flow pattern may be deduced. The two components of SABRE are located at Wick, Scotland and Uppsala, Sweden, while those of STARE are at Malvik, Norway and Hankasalmi, Finland. The coordinates of the radars and their viewing areas are given in Table 3.1 and their relative locations illustrated in Figure 3.1.

### 3.2.1 Antenna configuration

Each of the component radars of the SABRE and STARE systems employs a broad beam transmitting antenna and a narrow beam receiving antenna. A 50 kW peak pulsed transmitter feeds the transmitting array consisting of two vertical stacks of 4 eight element Yagi antennas, which provide a forward gain of 17 dB, resulting in an effective radiated power in excess of 1 MW. With a half power beam width of 25°, the transmitting antenna illuminates the entire viewing area.

The receiving array comprises 16 vertical stacks, each of four 8 element Yagi antennas, resulting in a gain of 28 dB. The combined signal from each stack is amplified and all 16 signals are fed to a Butler matrix. The latter is a passive phasing network which provides the necessary combinations of phase shifts to form 16 antenna lobes. Each of these lobes has a half power beam width of 3.2° and an angular separation of 3.6°. Thus, in principle the radar may 'look' in 16 different directions simultaneously. In practice, the outer beams suffer from poor sidelobe isolation, and in order to avoid any significant backscatter from directions other than those of the main beams, only the 8 central beams are utilised. The beam geometries of the two SABRE radars are illustrated in Figure 3.2. The common viewing area formed from the overlap of the beam patterns of the two separate radars covers an area of  $\sim 200,000 \text{ km}^2$ .

**STARE**

Station	Location		Viewing Area		Frequency (MHz)
	GG Lat. (°N)	GG Long. (°E)	GG Lat. (°N)	GG Long. (°E)	
Norway	63.4	10.7	67.6-72.6	14.0-26.0	140.0
Finland	62.3	26.9			143.8

**SABRE**

Station	Location		Viewing Area		Frequency (MHz)
	GG Lat. (°N)	GG Long. (°E)	GG Lat. (°N)	GG Long. (°E)	
Scotland	58.4	-3.1	63.6-68.6	0.0-12.0	153.2
Sweden	59.9	17.7			142.6

**TABLE 3.1.** The locations, and frequencies of the STARE and SABRE radars and the viewing areas of the bistatic systems.

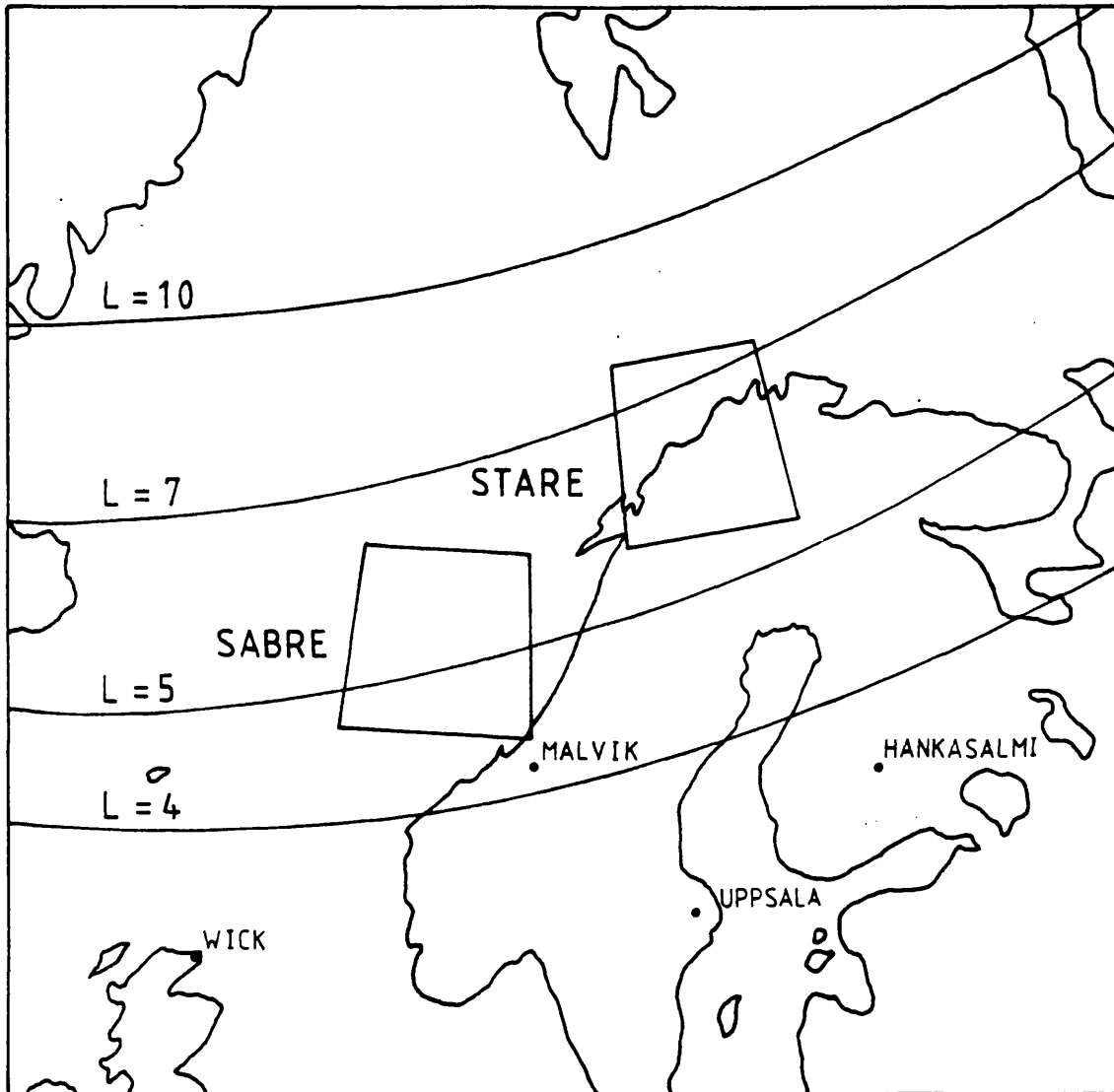


**FIGURE 3.1.** Illustrating the locations of the SABRE and STARE viewing areas with respect to magnetic L shells.

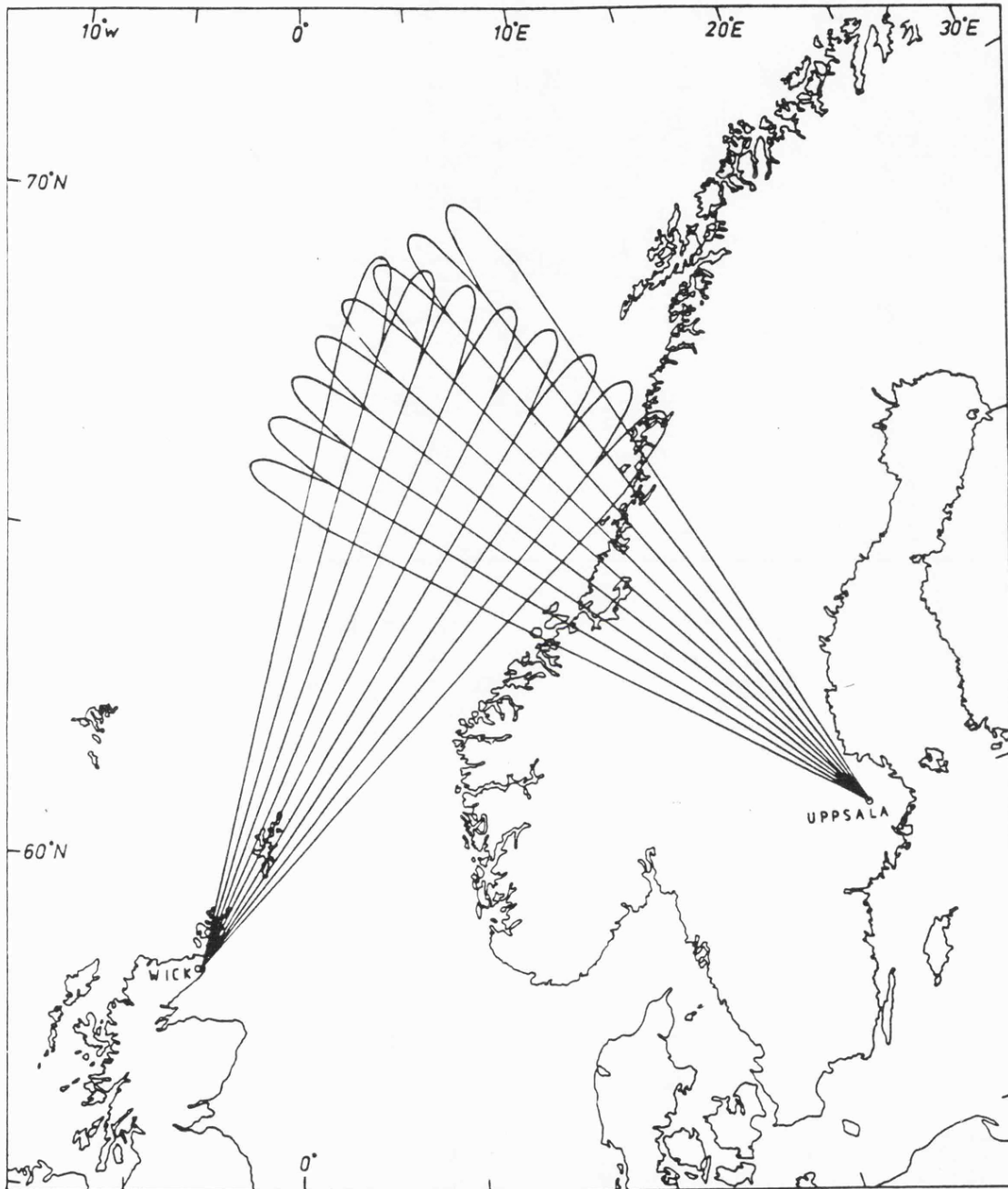
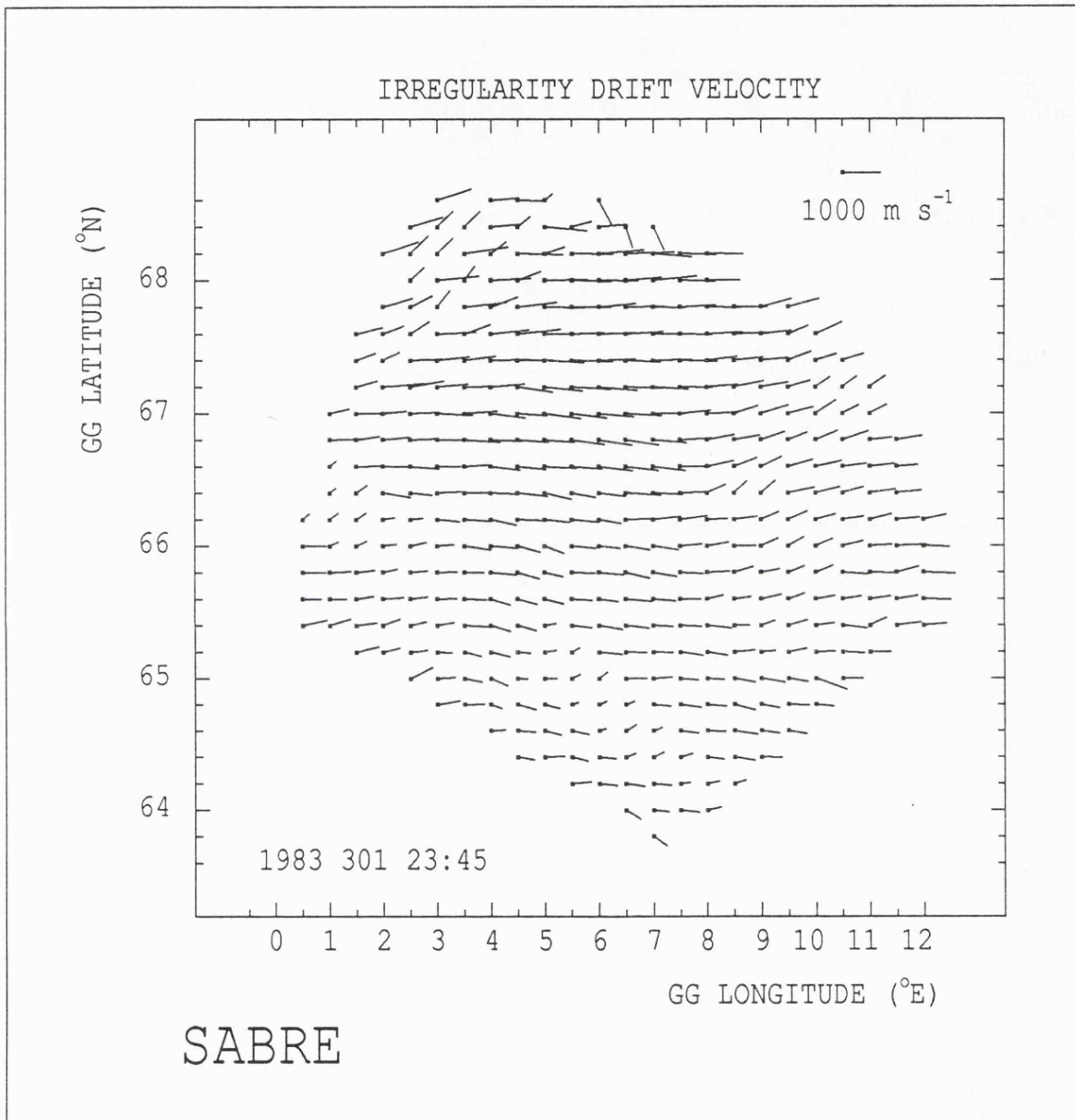


FIGURE 3.2. The beam geometry of the Wick and Uppsala radars.

### 3.2.2 Measurement technique

The backscatter power and line of sight Doppler velocity are measured in 50 range gates from 495 km to 1230 km, for each of the 8 central beams simultaneously, with an integration time of 20 seconds. An additional measurement is also taken at a range beyond the maximum range for auroral backscatter, and this provides a value of the noise level for each of the beams. The measurement procedure involves the alternate transmission of a single pulse to obtain the backscatter power, and a double pulse to determine the Doppler velocity of irregularities, in each of the range-beam cells (Greenwald et al., 1975; Greenwald et al., 1978).

According to simple linear theory (Fejer and Kelley, 1980), an estimate of the two dimensional electron drift vector may be obtained by combining the line of sight determinations of the irregularity drift velocity of the two radars. The relationship between the electron drift velocity and the measured irregularity drift velocity is discussed in section 3.2.4. The velocity data is mapped from range-beam coordinates onto a geographic grid of 26 x 26 points, providing a spatial resolution of 0.5° in longitude and 0.2° in latitude (equivalent to 20 x 20 km). An example of the flow velocities measured by SABRE, as a function of latitude and longitude and integrated over 20 seconds, is reproduced in Figure 3.3 for 23:45 UT, 28 October, 1983, when predominantly eastward flows (westward electrojet) were observed. Each vector in the figure depicts the flow magnitude and flow direction measured for the corresponding grid point. In addition, if it is assumed that the irregularity drift velocity equals the electron drift velocity, the electric field vector  $\underline{E}$  can be determined from the flow measurement by means of the MHD approximation ( $\underline{E} = -\underline{v} \times \underline{B}$ , section 2.2.2). The minimum field strength required to produce detectable backscatter is about 15 mV m<sup>-1</sup>.



**FIGURE 3.3.** A typical example of the irregularity drift flows measured by SABRE as a function of geographic latitude and longitude and with a temporal resolution of 20 seconds. The observation is for 23:45 UT, 28 October, 1982 when SABRE viewed predominantly eastward flows associated with the westward electrojet.

### 3.2.3 Backscatter power

There are many factors which determine the received backscatter power  $P_r$  measured by the SABRE radars. A consideration of the radar equation (Farley et al., 1981) for backscatter in the plane perpendicular to the magnetic field, and assuming that each of the range-beam cells is uniformly filled with backscatterers, indicates the following expression for  $P_r$

$$P_r = P_t \cdot G_t(\chi, \xi) \cdot G_r(\chi, \xi) \cdot \eta_t \eta_r \sigma c \tau \lambda^2 / 2(4\pi R)^3 \quad (3.1)$$

where  $P_t$  is the transmitted power, and  $G_t$  and  $G_r$  are the gains of the transmitter and receiver antennae, respectively, which are functions of the azimuth angle,  $\chi$ , and elevation angle,  $\xi$ , of the backscatterers with respect to the radar.  $\eta_t$  is the ohmic loss factor of the transmitted pulse,  $\eta_r$  the ohmic loss factor for the received pulse,  $\sigma$  is the backscatter cross section of the irregularities,  $c$  is the velocity of light,  $\tau$  is the pulse duration,  $\lambda$  is the radar wavelength, and  $R$  is the range.

Now, because the receiver azimuthal beam widths are very narrow (see previous section) the azimuth angle for a given beam is constant. If the height of the backscattering irregularities does not change, then the elevation angle for a given range is also constant. However, recent results from the SABRE Altitude Determining Interferometer Experiment (SADIE) has indicated that the backscatter height may vary by ~20 km (Thomas and Jones, 1988). For a range of 800 km, for example, this corresponds to a variation in the elevation angle of  $\sim 1.5^\circ$ , which results in a change in the transmitter and receiver antenna gains of  $< 2$  dB (Thomas, 1988). Other factors which affect the antenna gains include weather conditions (the accumulation of water or ice on the antennae changes their physical dimensions) and variations in ground conductivity (which determines the strength of the ground reflected signal with respect to the

direct signal). However, it has been estimated that these effects amount to less than 0.1 dB (Thomas, 1988).

Thus, changes in the gains of the antennae are small compared to the typical range of backscatter powers which are observed of 0-50 dB. Considering the other terms in equation (3.1), ohmic losses at the SABRE frequency are very small and variations in them are negligible, the change in power with range is corrected for (inverse cube law), and the parameters  $P_t$ ,  $c$ ,  $\tau$ , and  $\lambda$  are all constants. Variations in backscatter power must, therefore, be almost entirely due to fluctuations in the irregularity cross section, which according to Uspensky et al. (1983) and Starkov et al. (1983) can be expressed in a simplified form as

$$\sigma = kN^2 \cdot \langle (\Delta N/N)^2 \rangle \cdot F(\phi, \theta) \quad (3.2)$$

where  $k$  is a constant,  $N$  is the ambient electron density and  $\langle (\Delta N/N)^2 \rangle$  is the mean square of the electron density fluctuations associated with the irregularities observed by the radar.  $F(\phi, \theta)$  is a function of the radar aspect angle  $\phi$ , which is measured between the incident radar wave vector  $\underline{k}$  and the geomagnetic field  $\underline{B}$ , and the propagation angle  $\theta$  between the radar wave vector and the electron drift direction.

Experimental results at VHF indicate an attenuation of the backscatter power of 1-10 dB/deg. as the aspect angle deviates from 90° (Koehler et al., 1985; Ruohoniemi and Moorcroft, 1985). Moreover, the height of the irregularities are confined to an altitude range of ~100-130 km (Ruohoniemi and Moorcroft, 1985; Thomas and Jones, 1988). Thus, there are severe geometrical constraints on the possible location of a coherent auroral radar. The aspect angles of the Wick and Uppsala radar, calculated utilising the 1980 IGRF magnetic field model for a height of 110 km, are found to be orthogonal to within  $\pm 2^\circ$  inside the viewing area (Figure 3.4).

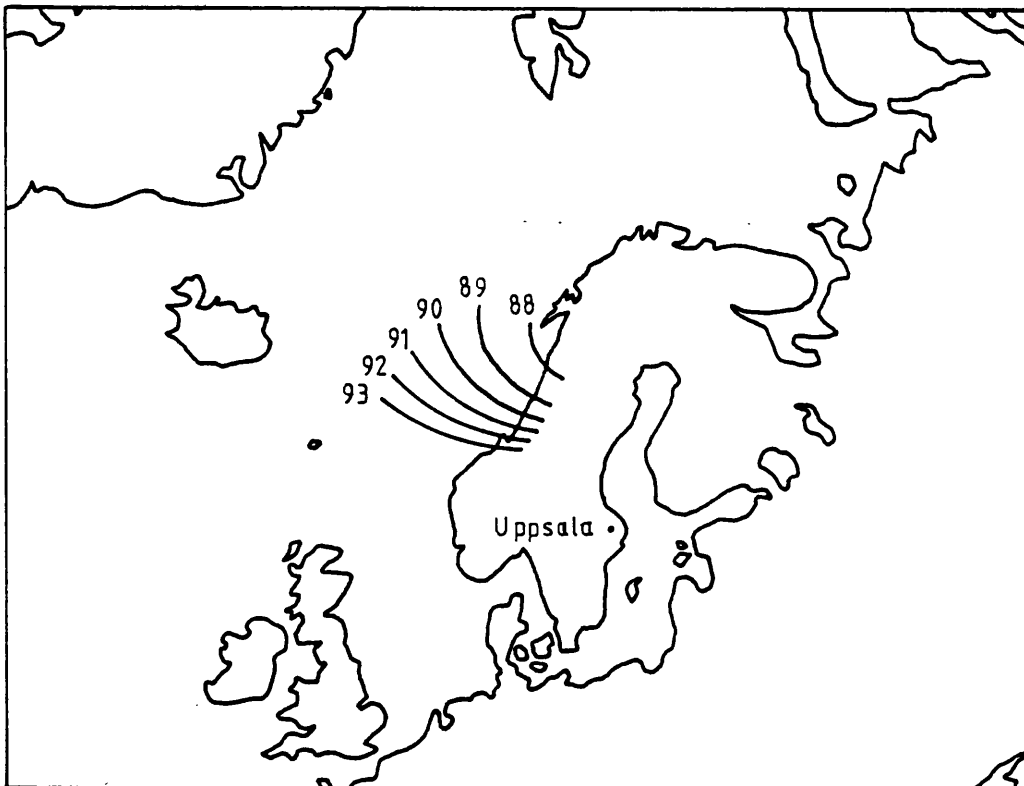
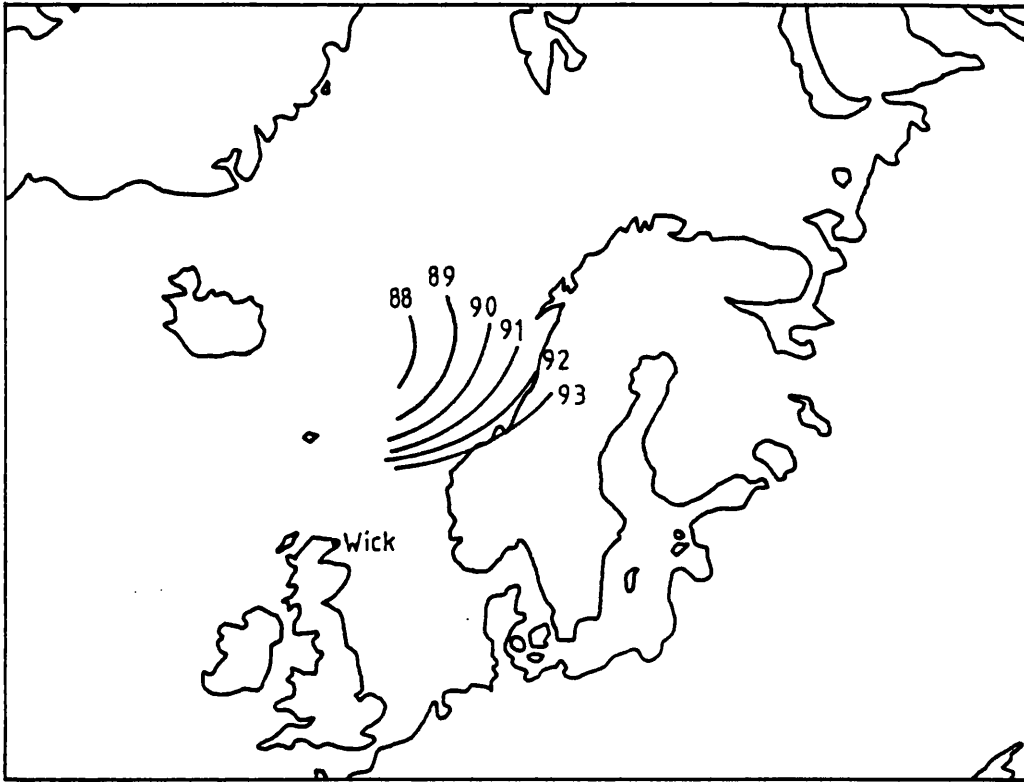


**FIGURE 3.4.** Aspect angle contours for the Wick radar (upper panel) and the Uppsala radar (lower panel). [From Burrage, 1986.]

#### 3.2.4 Theory of the backscatter mechanism

Two processes are believed to produce the irregularities responsible for coherent auroral radar backscatter. When the relative electron-ion drift in the plane perpendicular to the magnetic field exceeds the ion acoustic velocity, the E-region plasma becomes unstable and ion acoustic waves are generated. This process, proposed by Farley (1963) and Buneman (1963), is referred to as the two stream instability. The second process, termed the gradient drift instability, occurs if an electrostatic potential gradient exists in the direction of the ambient ionospheric electric field (Maeda, 1963). In this case, relative electron-ion drift velocities below the ion acoustic velocity can create plasma waves with wavelengths of the order of 100 m, and these structures cascade into shorter wavelength irregularities due to nonlinear processes.

The two stream and the gradient drift plasma instability mechanisms give rise to irregularities which propagate approximately in a plane perpendicular to the geomagnetic field, with a phase velocity which depends on the electron drift velocity. The SABRE/STARE systems are sensitive to irregularities with scale sizes ( $\sim 1$  m), equal to half of the radar wavelength, which travel along the line of sight. Given that the threshold for the generation of two stream instabilities is exceeded, the two stream mechanism dominates the gradient drift process for the production of 1 m irregularities (Fejer and Kelley, 1980).

The measured line of sight Doppler velocities from the two radars are routinely combined according to the so-called 'cosine relation', to estimate the electron drift velocity (Nielsen et al., 1983). However, comparisons between STARE and EISCAT (European Incoherent SCATer) radar measurements indicate that the cosine rule analysis causes the coherent radars to increasingly underestimate the higher drift speeds, although there is little error ( $< \pm 10^\circ$ ) in the directions (Nielsen and Schlegel, 1983). The reason for this is that the irregularity drift phase velocity

( $v_{ph}$ ) is limited to the ion acoustic speed  $C$  by nonlinear effects (Sudan, 1983; Prindahl and Bahnsen, 1985). Robinson (1986) finds that  $C$  is a nonlinear and monotonically increasing function of the electron drift speed  $v_e$  (Figure 3.5). Robinson and Honary (1987) propose a new theory which suggests that for  $\sim 1$  m irregularities,  $v_{ph}/C$  is greater than unity and varies in the range 1.06–1.24 over altitudes of 100–115 km. Thus, the electron drift velocity is a complex function of the measured irregularity phase velocity. An empirical correction factor has been proposed (Nielsen and Schlegel, 1985) which enables STARE to provide estimates of  $v_e$  which are in good agreement with EISCAT measurements. The validity of this technique has yet to be established for SABRE, and no correction has been applied to the measurements presented in this thesis.

A recent theoretical argument (Robinson, 1987) has demonstrated that SABRE backscatter power observations may also provide useful measurements for the study of high latitude electrodynamics. In the previous section, it was shown that the backscatter power depends principally on the backscatter cross section, suggesting the following approximation

$$P_r = k_1 \cdot \sigma \quad (3.3)$$

where  $k_1$  is a constant. If daily averages of the backscatter power are employed, then changes in power due to fluctuations in the aspect angle (arising from distortions of the geomagnetic field) and variations in the propagation angle (which are largely diurnal) are removed. Therefore, equations (3.2) and (3.3) imply the following approximation for the daily average power

$$P_r = k_2 N^2 \cdot \langle (\Delta N/N)^2 \rangle \quad (3.4)$$

where  $k_2$  is a constant. In addition, from plasma irregularity theory

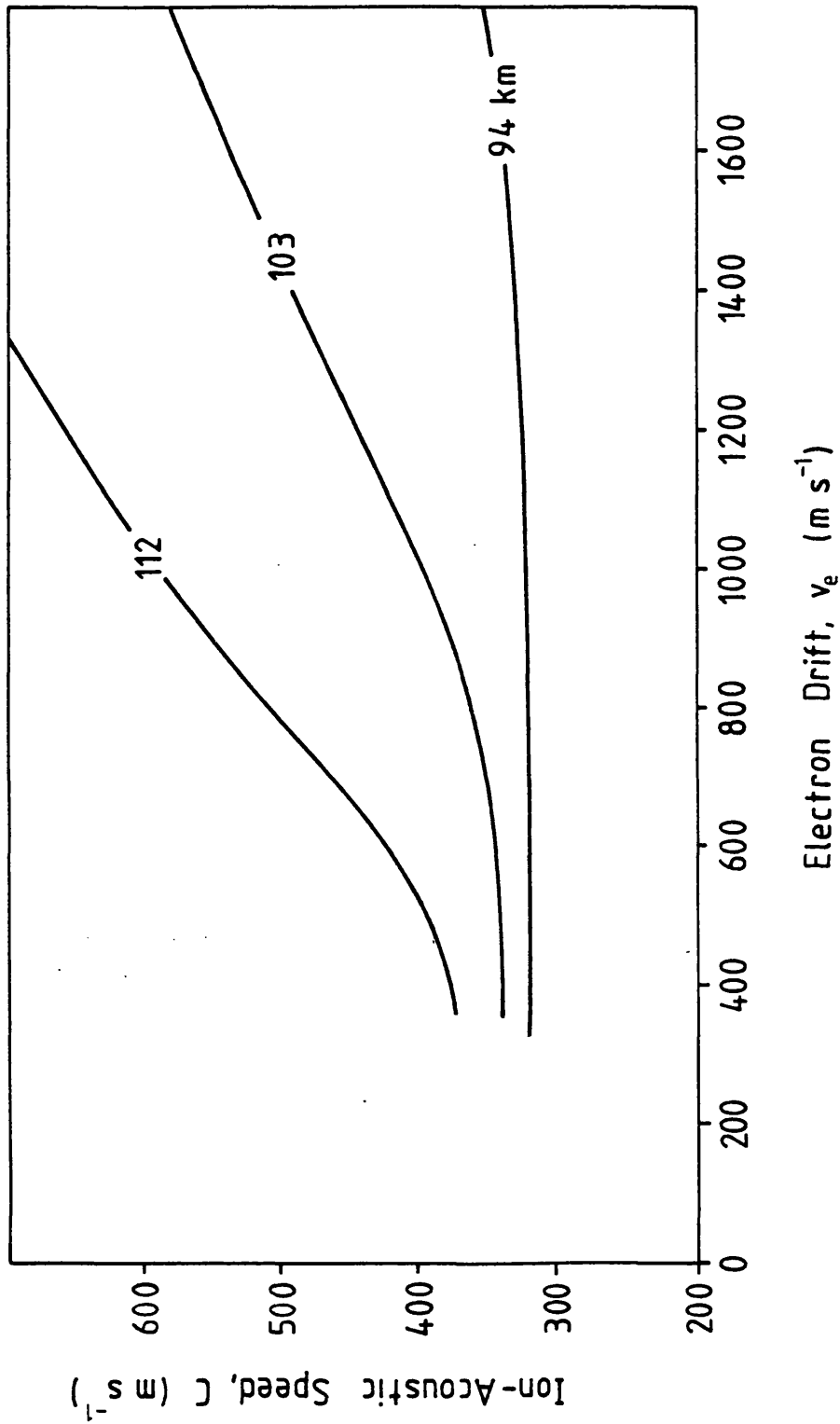


**FIGURE 3.5.** Theoretical curves of ion acoustic speed against electron drift for altitudes of 94, 103 and 112 km. [From Robinson, 1986.]

(Farley, 1985), Robinson (1987) has obtained the following simplified expressions for the mean square of the electron density fluctuations and the anomalous collision frequency  $\nu_e^*$

$$\langle (\Delta N/N)^2 \rangle = \nu_e^* (\nu_e + \nu_e^*) / \Omega_e^2 \quad (3.5)$$

$$\nu_e^* = \nu_e ((v_d/C) - 1 - \psi) / \psi \quad (3.6)$$

where  $v_d (= v_e - v_i)$  is the relative drift velocity between the electrons and the ions and  $\psi$  is given in terms of the electron and ion collision frequencies ( $\nu_e$  and  $\nu_i$ ) and gyro frequencies ( $\Omega_e$  and  $\Omega_i$ ) by  $\psi = (\nu_e \nu_i) / (\Omega_e \Omega_i)$ . Physically,  $\nu_e^*$  represents the anomalous scattering of electrons by the plasma wave field (Robinson, 1986). Substituting (3.6) into (3.5) yields

$$\langle (\Delta N/N)^2 \rangle = k_3 (v_d - C) (v_d - C(1 + \psi)) / C^2 \quad (3.7)$$

where  $k_3$  is a constant ( $= \nu_e^2 / (\Omega_e^2 \psi^2)$ ). In the E-region,  $\psi \sim 0.01$  (André, 1983), and thus equation (3.7) approximates to

$$\langle (\Delta N/N)^2 \rangle = k_2 (v_d - C)^2 / C^2 \quad (3.8)$$

Substituting (3.8) into (3.4), multiplying the RHS by  $e^2/e^2$  where  $e$  is the charge on the electron, and rearranging yields

$$P_r = (k_2 k_3 / C^2 e^2) (N e v_d - N e C)^2 \quad (3.9)$$

Now since the current density  $J = N e v_d$ , it follows that

$$P_r = k_4 (J - J_0)^2 \quad (3.10)$$

where  $k_4 (= k_2 k_3 / C^2 e^2)$  is a constant and  $J_0$  is a threshold current for the generation of the instabilities responsible for the radar backscatter. This argument suggests a strong sensitivity of the radar backscatter power to variations in the intensity of the auroral electrojets, which is in agreement with the conclusions of Uspensky et al. (1983) and Starkov et al. (1983).

### 3.2.5 Backscatter statistics

The production of irregularities by the two stream instability requires  $v_d$  to exceed a threshold of around  $300\text{--}400 \text{ m s}^{-1}$ , a condition which is regularly satisfied within the auroral electrojets. The latter are approximately colocated with the statistical auroral oval and Figure 3.6 depicts the path of the SABRE viewing area through the oval (as determined by Feldstein, 1963) as the Earth rotates once in 24 hours. Due to the displacement of the auroral oval towards midnight, the SABRE field of view is usually outside the oval on the dayside, but intersects it for most of the nightside sector. The expansion of the oval during intervals of geomagnetic disturbance increases the probability of SABRE observing backscatter at a given local time.

Figure 3.7 illustrates the Wick radar backscatter intensity as a function of geomagnetic latitude and local time, averaged over  $100^\circ\text{--}102^\circ \text{ E}$  geomagnetic longitude, for the entire data set of 1875 days available at the time of writing. A diurnal variation arising from the two cell structure of the high latitude current system is evident. Strongest backscatter occurs between 13:00 and 19:00 and between 22:00 and 04:00, while weak backscatter is observed in the morning sector when the SABRE field of view is farthest from the statistical oval. The significant reduction in the mean backscatter intensity between 19:00 and 22:00 coincides with the Harang discontinuity. Figure 3.8 illustrates the mean plasma convection pattern observed by SABRE as a function of geomagnetic

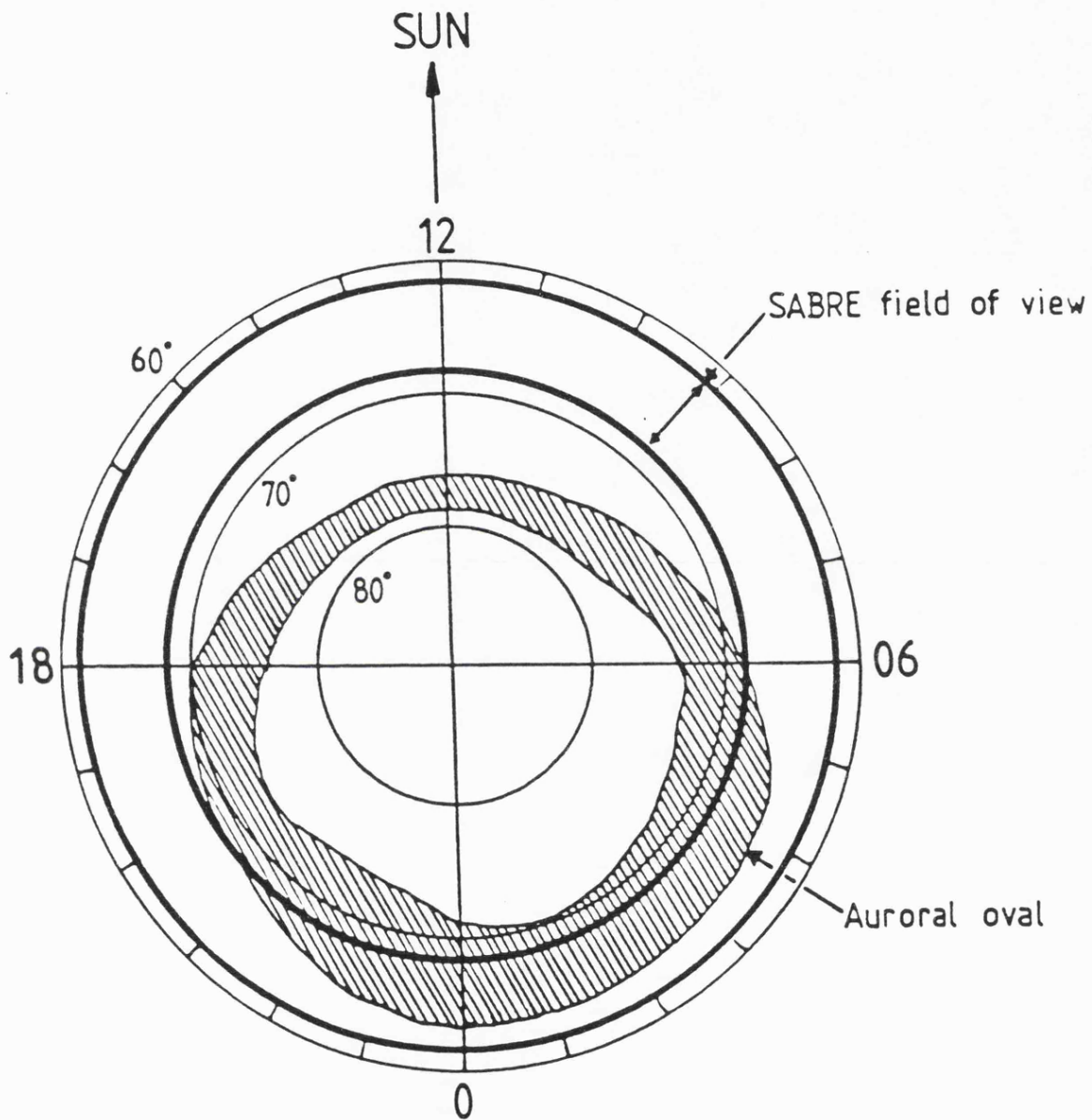


*FIGURE 3.6. Illustrating the path of the SABRE viewing area as the Earth rotates under the statistical auroral oval in a 24 hour period.*

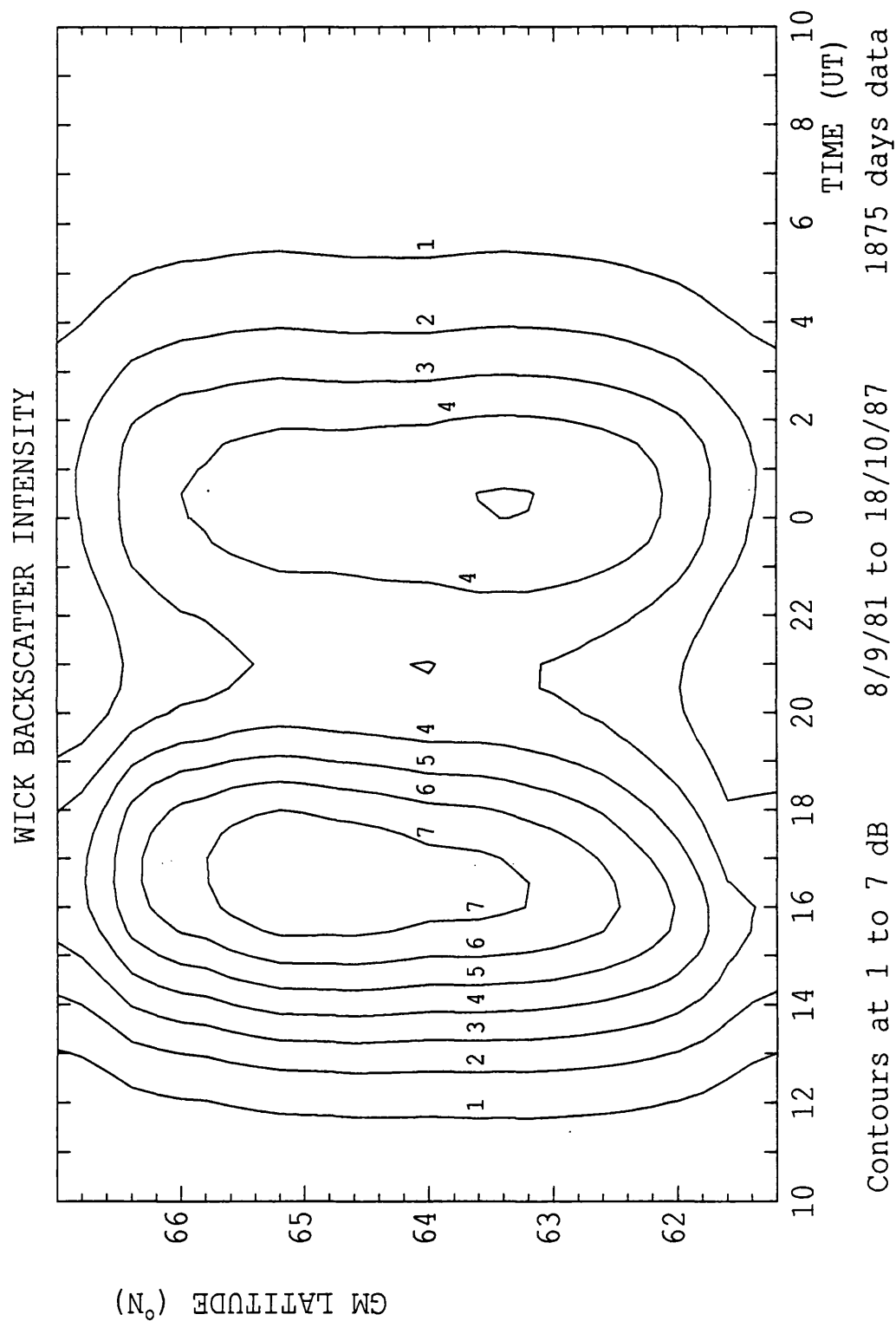
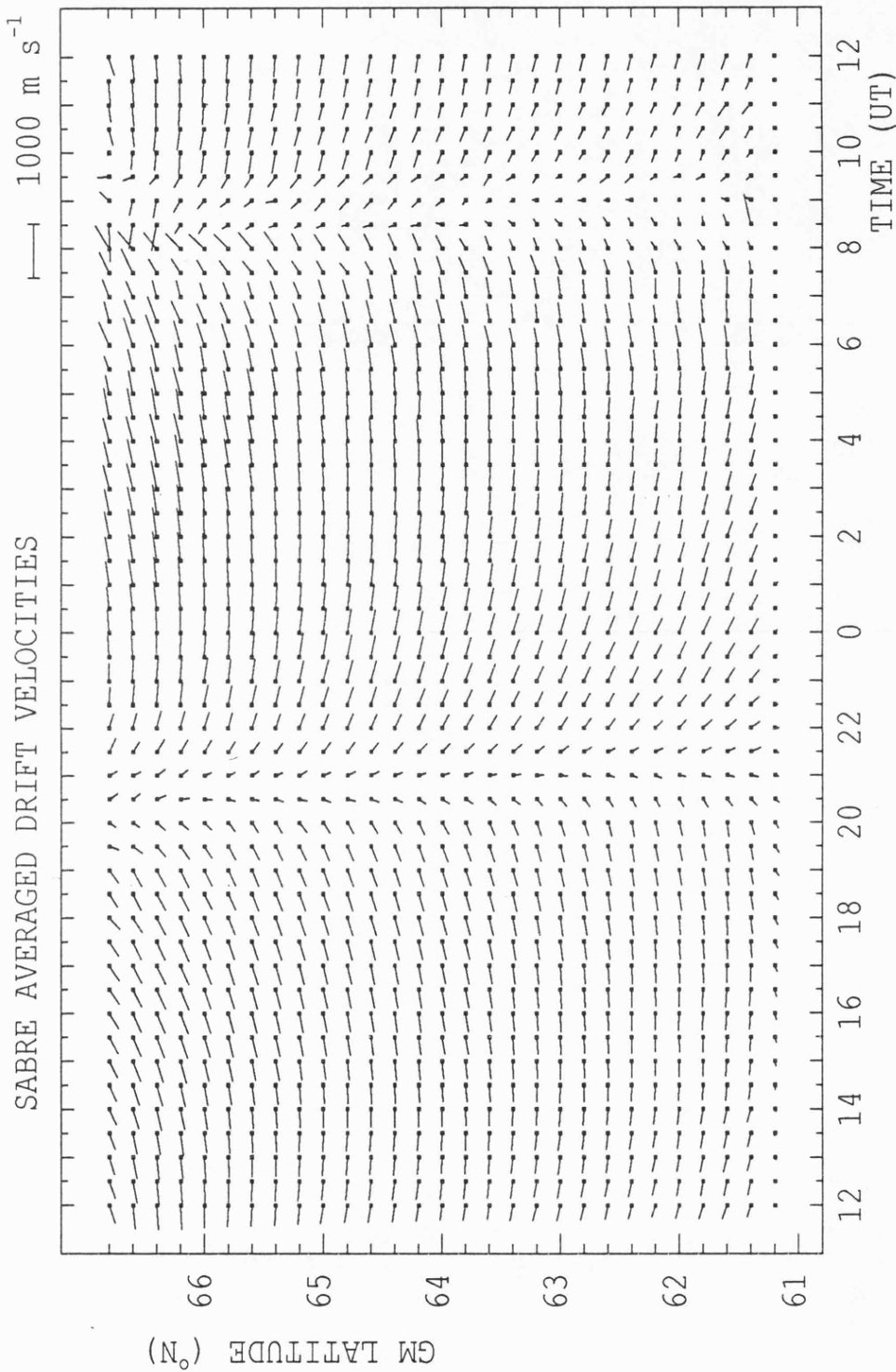


**FIGURE 3.7.** Contours of Wick backscatter intensity as a function of universal time and geomagnetic latitude averaged over 100°-102° E geomagnetic longitude, for the complete 1875 day Wick data set.



All data 22/3/82 to 27/10/86 1013 days

**FIGURE 3.8.** The mean convection pattern measured by SABRE as a function of universal time and geomagnetic latitude averaged over geomagnetic longitudes  $100^{\circ}$ - $102^{\circ}$  E, for the complete 1013 day SABRE data set.

latitude and time, averaged over a  $100^{\circ}$ - $102^{\circ}$  E longitudinal strip. The main features are the westward flows (eastward electrojet) and eastward flows (westward electrojet), which are separated by the morning discontinuity at about 09:00 UT and the evening (Harang) discontinuity at approximately 21:00 UT.

### 3.3 Spacecraft

ISEE-3 was launched on 12 August, 1978, initially into an approximately elliptical orbit about the sunward libration point, making a complete circuit around the Earth-Sun line every 6 months. This orbit allowed the spacecraft to maintain a stable position  $\sim 200 R_E$  up-stream of the Earth, and to observe the solar wind approximately 1 hour before it encountered the outer magnetosphere. The agreement between upstream ISEE-3 measurements and IMP-8 observations in front of the Earth's bowshock indicated that on average the solar wind characteristics were reasonably constant over the distance between ISEE-3 and the nose of the magnetosphere (von Rosenvinge, 1982). In September, 1982, ISEE-3 was redeployed into an orbit which periodically intersected the distant magnetotail. Thereafter, ISEE-3 observations of the solar wind were subject to frequent and extended interruptions. The ISEE-3 data employed in this thesis were obtained from data pool tapes, containing plasma parameters and magnetic data of  $\sim 5$  minute and 1 minute resolution, respectively, and from a magnetic tape containing hourly averages of these parameters, all of which were supplied by the National Space Science Data Center (NSSDC). The solar wind bulk flow velocities, temperatures and densities were measured by the Los Alamos plasma analyser on board ISEE-3 (Bame et al., 1978). The Cartesian components of the magnetic field were measured in the spacecraft coordinate system (within  $\sim 1^{\circ}$  of the GSE system) by the Jet Propulsion Laboratory vector helium magnetometer (Frandsen et al., 1978). The hourly averages of

the magnetic data have been transformed into the GSM frame.

IMP-8 was launched on 26 October, 1973 into an approximately circular orbit of radius  $35 R_E$  and period 12.6 days (Figure 4.4 illustrates a typical IMP-8 orbit). The spacecraft spends 6-8 days per orbit monitoring the solar wind and 4-6 days per orbit measuring magnetosheath and magnetotail plasmas (King, 1982). The IMP-8 data employed in the present investigation comprise hourly averages of bulk flow velocity and density, and Cartesian components of the magnetic field in GSM coordinates, obtained from a magnetic tape provided by NSSDC. The plasma parameters were measured by the Los Alamos electrostatic analyser (Feldman et al., 1975) and the magnetic quantities by the Goddard Space Flight Center triaxial fluxgate magnetometer (King, 1982, and references therein).

### 3.4 Summary

SABRE is able to provide very high temporal and spatial resolution maps of the auroral convection flows. On a statistical basis SABRE observations reproduce the mean large scale (two cell) convection pattern. Although the flow magnitudes are probably underestimated for higher speeds, the flow directions are accurate. Thus, the morphology of the large scale convection pattern is accessible to the SABRE system. In addition, recent theories have demonstrated that the backscatter power measurements provide an indication of the intensities of the electrojets.

The ISEE-3 and IMP-8 satellites have provided high quality measurements of the interplanetary medium, although interruptions in coverage by ground based tracking stations, together with the frequent intersection of the magnetosphere by IMP-8, and since 1982 by ISEE-3, has resulted in a relatively incomplete solar wind data set.

## CHAPTER 4

### SOLAR WIND MODULATION OF WICK BACKSCATTER INTENSITIES

#### 4.1 Introduction

Inspection of long intervals of SABRE backscatter intensities reveals several periodicities. The most obvious is the diurnal variation (section 3.2.5), which results from the daily rotation of the Earth under the two cell convection pattern. Superposed on the diurnal variation are universal time effects due to the modulation of convection flows by changes in the interplanetary medium. The convection flow response to changes on time scales of hours or less are investigated in chapters 5, 6 and 7. This chapter deals with longer term changes, with periods considerably greater than a day, which appear in the backscatter intensities as a consequence of gross structures in the solar wind. In order to appreciate the implications of the periodicities observed in the radar data, an empirical study is also presented of the relationship between the backscatter power and various solar wind parameters.

A prerequisite of a study of long time scale effects is that the data set should be continuous (or nearly so) and at least twice as long as the longest changes to be detected. Most radars which probe the high latitude ionosphere are operated on an intermittent or campaign basis, and consequently these have not provided data bases which are suitable for detecting effects with periodicities longer than about a day. The Wick radar is exceptional in that it has been operated continuously, apart from a few short breaks, since September, 1981. The Uppsala station, which operated between March, 1982 and November, 1986, was less reliable; data

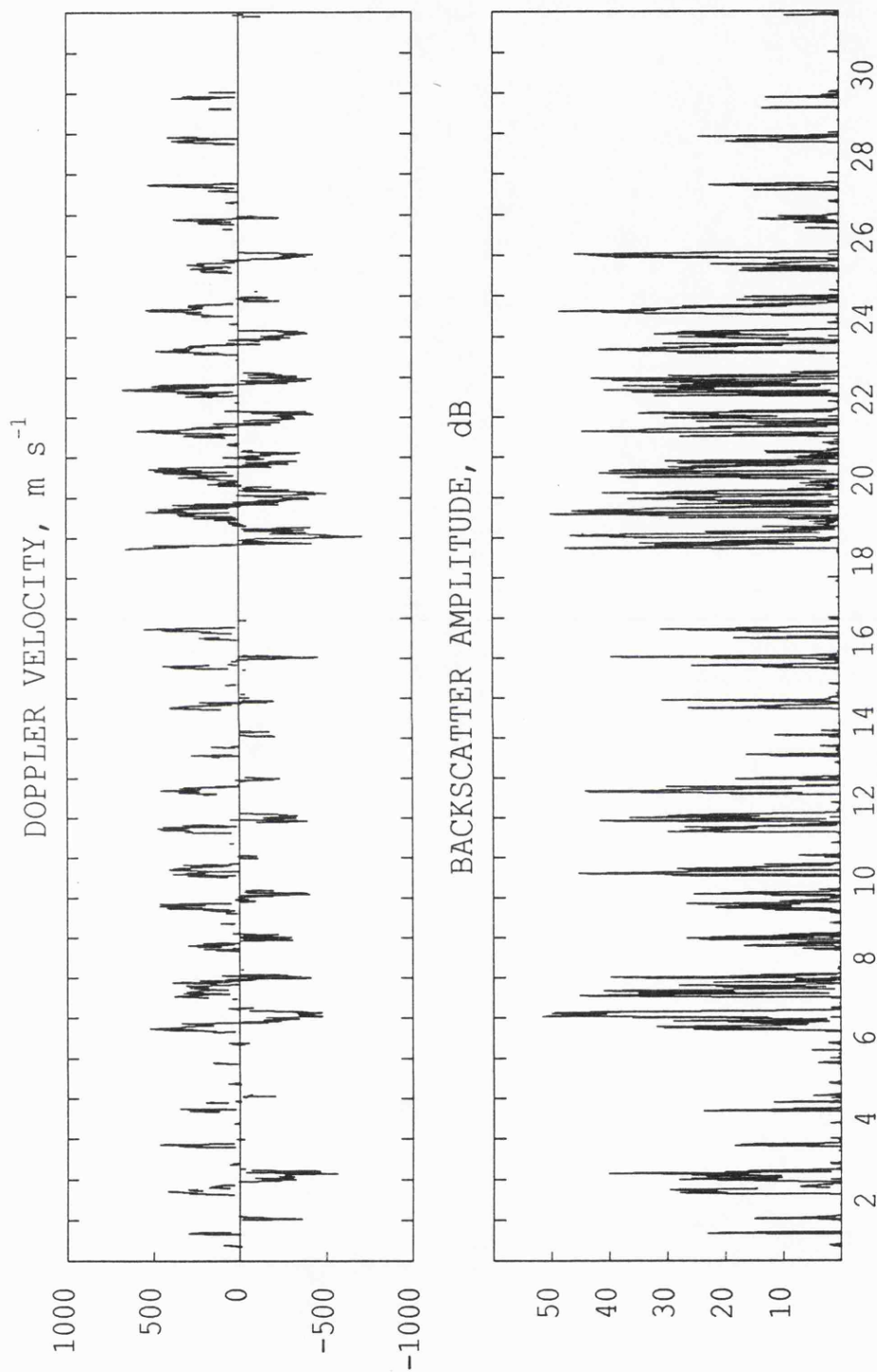
from this radar has therefore not been employed in the present investigation.

#### 4.2 The first SUNDIAL campaign

The first SUNDIAL campaign (Robinson et al., 1987), which occurred between 5 October and 13 October, 1984, provided the first indication that Wick radar backscatter intensity data contains long term variations induced by perturbations in the solar wind. In the present work, the features detected in the campaign interval have been further investigated by considering the data for the whole month of October, 1984.

The line of sight irregularity drift velocity and the backscatter power for Wick, for October, 1984, are illustrated in Figure 4.1. The data are averaged over the geographic area  $66^{\circ}$ - $67^{\circ}$  N,  $4^{\circ}$ - $6^{\circ}$  E, with a time resolution of 1 minute. The velocities and intensities exhibit variations on several different time scales. Firstly, there is the obvious diurnal variation, which is particularly evident in the velocities. In addition, there are more rapid variations due to transient fluctuations in electrojet current intensities and conductivities. There also exists a cyclic variation on a time scale much longer than the diurnal period, as is evident from the envelope of the shorter period fluctuations. There are two cycles of enhancement in both the velocity and backscatter power measured by the Wick radar, one of which commenced on the 6 October, 1984, and the other on 18 October, 1984. Both periods lasted for approximately 11 days and were preceded by about 2 days of minimal auroral activity, indicated by reduced radar backscatter.

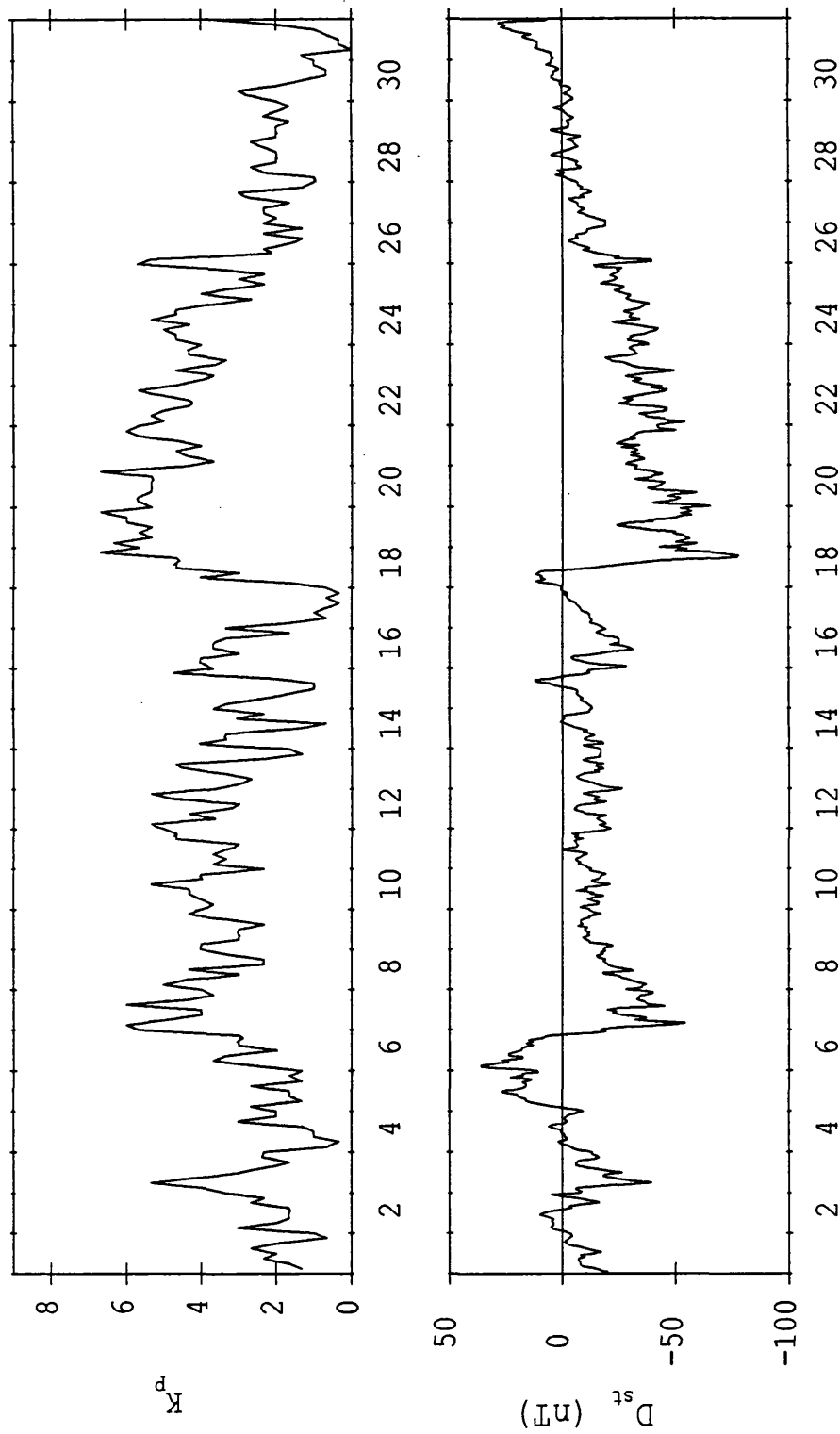
The geomagnetic indices  $D_{st}$  and  $K_p$  (Figure 4.2) exhibit two periods of increased disturbance at approximately the same times as the enhancements in velocity and power measured by the Wick radar. The  $D_{st}$  index for October, 1984 clearly exhibits the signatures of the main phases of two



WICK  
1 TO 31 October, 1984

**FIGURE 4.1.** Line of sight Doppler velocities and backscatter amplitudes for the Wick radar, for 1-31 October, 1984, averaged over geographic latitudes 66-67° N, and longitudes 4-6° E.

$K_p$  (upper panel) and  $D_{st}$  (lower panel) vs. time



1 to 31 October, 1984

**FIGURE 4.2.** Geomagnetic indices  $K_p$  and  $D_{st}$  for 1-31 October, 1984.

geomagnetic storms (defined in section 1.4). In each case, the peak depression of  $D_{st}$  (due to the intensified storm time ring current) is preceded by an interval of increased  $D_{st}$  (growth phase), presumably arising from an initial compression of the magnetosphere. The peak depression of  $D_{st}$  for the storm commencing on October 6 is  $-54$  nT (indicative of a weak to moderate storm) and for the storm commencing on 18 October it is  $-77$  nT (a moderate storm). The growth phase of the second storm is much less prominent than that for the first storm, and yet the main phase of the second is more intense. The latter point is also apparent in the increased levels of  $K_p$  and Wick backscatter intensity.

Hourly means of the magnitude of the IMF and the velocity and calculated kinetic energy flux density of the solar wind for October, 1984, obtained from IMP-8 satellite measurements, are reproduced in Figure 4.3. The equatorial projection of the orbit of IMP-8 relative to the magnetopause is depicted in Figure 4.4. This indicates that the satellite was never more than  $10 R_E$  upstream of the nose of the magnetosphere or  $5 R_E$  downstream of the Earth, and since the flow speed was in the range  $300-800 \text{ km s}^{-1}$ , the time lag which must be applied to compare the solar wind measurements with the ground based observations is only 1-4 minutes. Since the temporal resolution of the solar wind data is 1 hour, this time lag is negligible.

Because of the numerous data gaps, coinciding with intervals when the satellite was inside the magnetosphere, it is not possible to establish an exact correlation with the ground based data. However, the interplanetary parameters (Figure 4.3) appear to exhibit a similar long term behaviour, with enhancements apparently associated with those observed on the ground. A comparison of the times of the enhancements in the data sets suggests that it is the increase in the magnitude of the magnetic field  $B$ , rather than the solar wind velocity  $V$ , which is more closely correlated with the enhancements in the ionospheric parameters. This is particularly noticeable during the period of enhancement which commenced on 6 October,

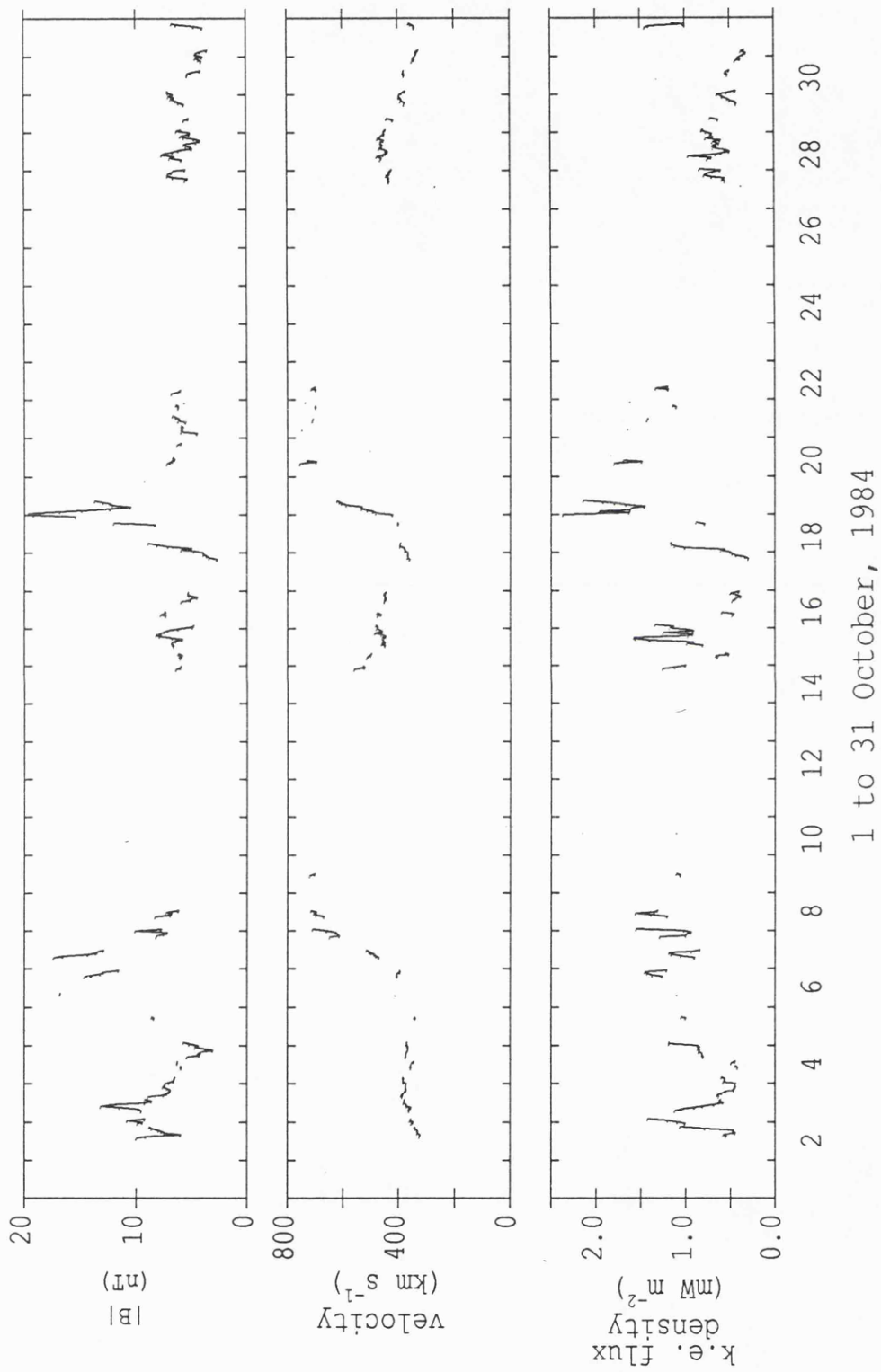


**FIGURE 4.3.** Magnitude of the IMF (upper panel), solar wind velocity (middle panel) and solar wind kinetic energy flux density (lower panel) for 1-31 October, 1984.

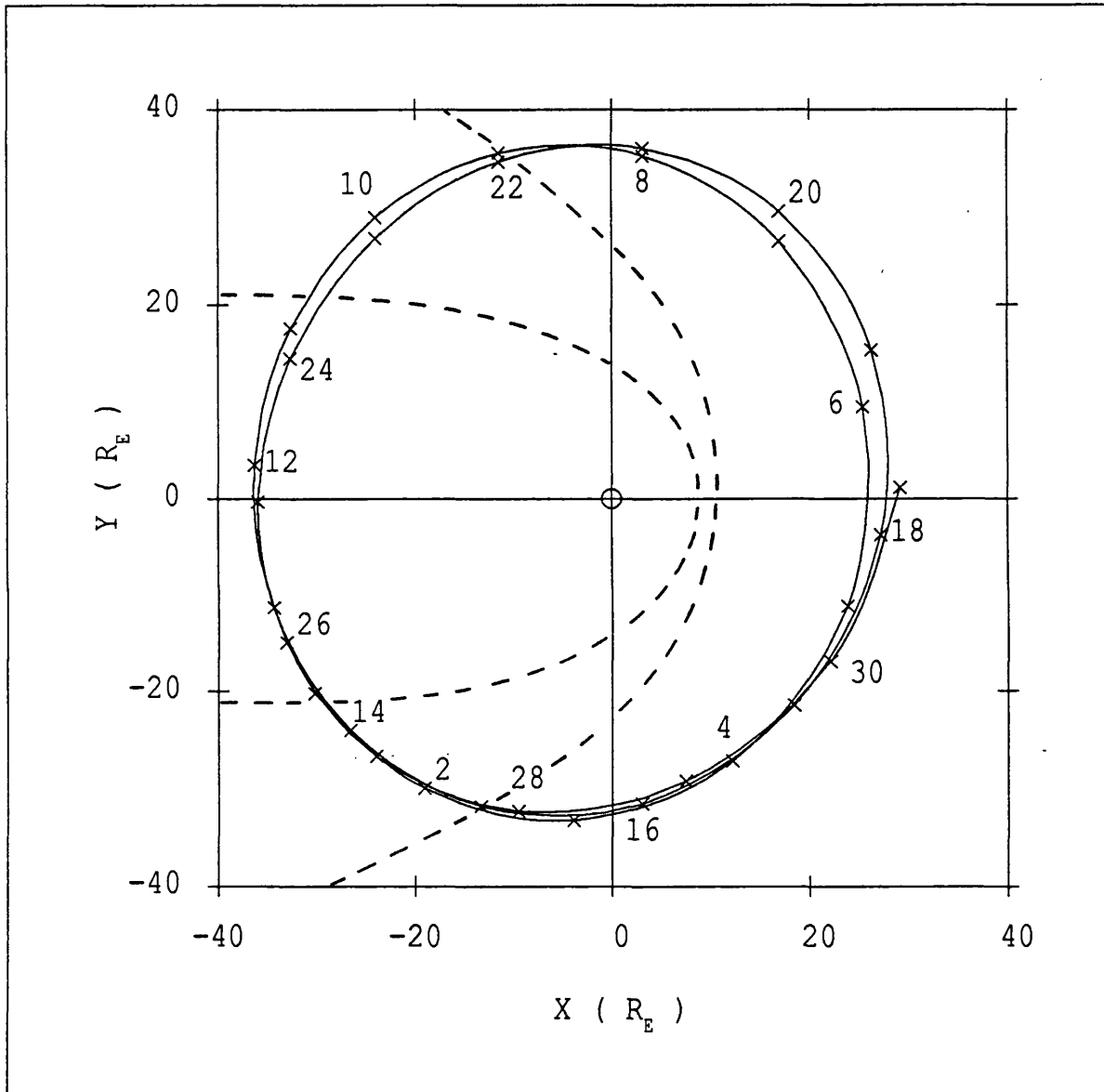


**FIGURE 4.4.** The orbit of IMP-8 projected into the solar ecliptic X-Y plane for 1-31 October, 1984. The numbers indicate dates and the dashed lines represent model bow shock and magnetopause locations [provided by J. H. King, NSSDC].

where the rise in the magnitude of the IMF correlates with the ionospheric parameters, while the rise in the solar wind speed maximises a day or so later. In addition, B has a higher peak value ( $\sim 20$  nT) for the enhancement commencing on 18 October, than for the 6 October enhancement ( $\sim 17$  nT). On the basis of a comparison of interplanetary quantities with AE and  $D_{st}$  indices, Perrault and Akasofu (1978) suggest that B is often the dominant term in determining the level of substorm activity. Akasofu (1981) suggests that this is a natural consequence of the form of the solar wind-magnetosphere energy coupling parameter  $\epsilon$  (section 2.5), which is linear in  $V$  (range  $300\text{--}1000$  km s $^{-1}$ ) but a function of  $B^2$  ( $9$  nT $^2$ – $900$  nT $^2$ ). This argument could explain the greater intensity of the second of the two storms.

The observed lag of about a day between the enhancements in the ionospheric quantities and the increase in  $V$  may nonetheless be explained by an expression for the solar wind energy transferred to the magnetosphere-ionosphere system which is kinetic ( $\rho V^3/2$ ) in character rather than magnetic ( $VB^2$ ). Referring again to Figure 4.3, it is evident that the solar wind kinetic energy flux density rises to a peak on 6 October at about the same time as B and the ionospheric parameters. Large particle densities were sufficient to compensate for the initially weak solar wind speeds on this day. A very similar relationship between the ground based and interplanetary parameters is apparent during the enhancements which commence around 18 October, and the smaller enhancement on 2–3 October, 1984. Significantly, the increase in kinetic energy flux density is considerably greater for the 18 October storm than for the 6 October storm (the weaker of the two).

These observations are consistent with the current sheet model of the heliosphere, (section 1.2). This model predicts that observations made at the Earth should exhibit a number of recurrent enhancements, with a periodicity related to the 27 day rotation of the Sun. In the simplest

case, when the solar current sheet has a structure corresponding to two equal sectors, two identical periods of enhancement would occur for each solar rotation. This structure would account for the two approximately 13 day cycles of activity described above, although the amplitude differences between the two cycles suggests an asymmetry between the sectors.

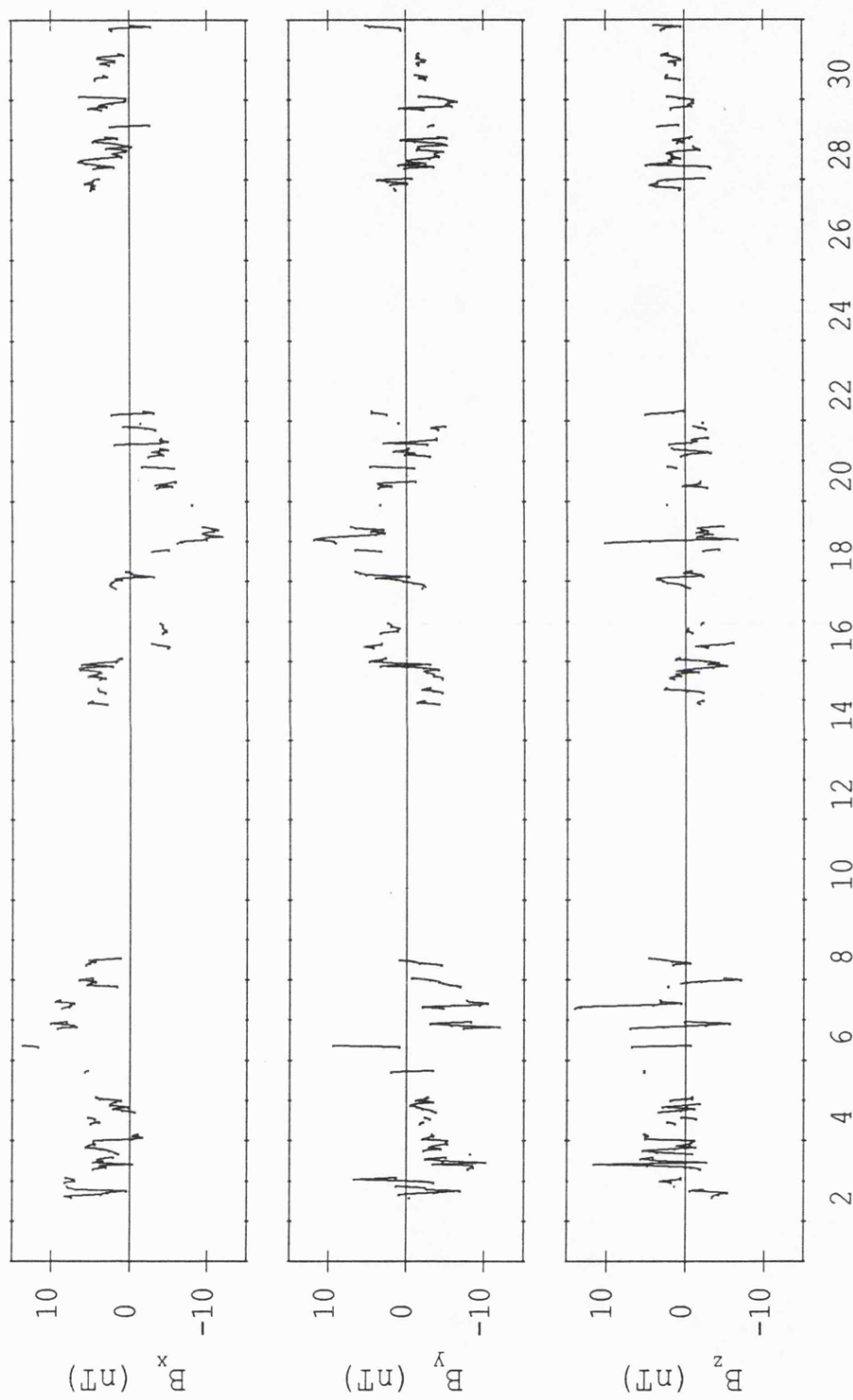
More direct evidence for the existence of the two sector form of the current sheet during October, 1984 is provided by the measurements of the IMF components  $B_x$ ,  $B_y$  and  $B_z$ , illustrated in Figure 4.5.  $B_x$  was generally positive from 2 October until 15 October, when it turned negative. By 27 October,  $B_x$  was positive again. In addition,  $B_x$  is approximately anticorrelated with the  $B_y$  component, and together they indicate that the Earth was in a 'toward' sector at the beginning of the month, in an 'away' sector during the middle of the month, and had returned to a 'toward' sector by the end of the month. However, because of the large breaks in the data, this can only be regarded as a tentative conclusion. It is difficult to discern a two sector signature in the  $B_z$  component, presumably due to the fact that the IMF sector structure is essentially confined to the x-y plane.

#### 4.3 Empirical relationship of backscatter power with solar wind parameters

Previous empirical studies (section 2.5) of the relationship between solar wind parameters and the ionospheric response have usually employed satellite data and geomagnetic indices, respectively. In the present study, the daily mean of the Wick radar backscatter intensity is adopted as a direct measurement of the ionospheric response. The Wick mean backscatter power is determined for a spatial average over an area ( $66^\circ$ - $67^\circ$  N,  $4^\circ$ - $6^\circ$  E, geographic) in the centre of the field of view, and a temporal average of 24 hours.

On average, the Wick radar observes zero backscatter for a significant

IMF components  $B_x$  (upper panel)  $B_y$  (middle panel)  $B_z$  (lower panel) vs. time



1 to 31 October, 1984

**FIGURE 4.5.**  $B_x$ ,  $B_y$  and  $B_z$  components of the IMF for 1-31 October, 1984.

fraction of the day (section 3.2.5), this fraction depending on the level of geomagnetic activity. A large value for the daily average backscatter intensity is only obtained when the backscatter occurrence probability is high, and vice versa. The relationship between the daily average value of the backscatter intensity and the probability of occurrence of backscatter in a day is illustrated in Figure 4.6. Either of these parameters is expected to indicate the level of auroral ionospheric activity.

#### 4.3.1 Comparison of SABRE with energy coupling parameters

The solar wind values, velocity  $V$ , IMF magnitude  $B$ , and IMF components  $B_y$  and  $B_z$ , required for calculating the coupling parameters were obtained from a composite omni-tape of hourly average ISEE-3 and IMP-8 satellite data provided by NSSDC. The coupling parameters which are now tested against the response of the Wick radar are  $-VB_z$ ,  $\epsilon$  and  $-V^2B_z$  (section 2.5). The range of each calculated parameter is split into bins of equal width, and the mean value and standard error of the daily mean radar backscatter power in each bin are determined. The results for the  $-VB_z$ ,  $-V^2B_z$  and  $\epsilon$  parameters are represented graphically in Figures 4.7, 4.8 and 4.9, respectively, and a curve denoting the number of data points within each bin is superposed on all of the plots.

In Figure 4.7, the daily average Wick power displays an almost linear increase as the  $-B_zV$  parameter becomes increasingly positive (positive  $-B_zV$  corresponds to negative  $B_z$  or southward IMF). The growing spread in the data as  $-B_zV$  increases may be simply due to the decreasing number of points for the higher values. The backscatter power changes little for negative values of  $-B_zV$ , corresponding to positive  $B_z$  or northward IMF. (There is perhaps a slight indication that as  $-B_zV$  becomes increasingly negative, the radar power increases, suggesting that high solar wind speeds may compensate for the expected reduction of the solar wind-magnetosphere coupling efficiency by northward IMF conditions.) The dependence of the

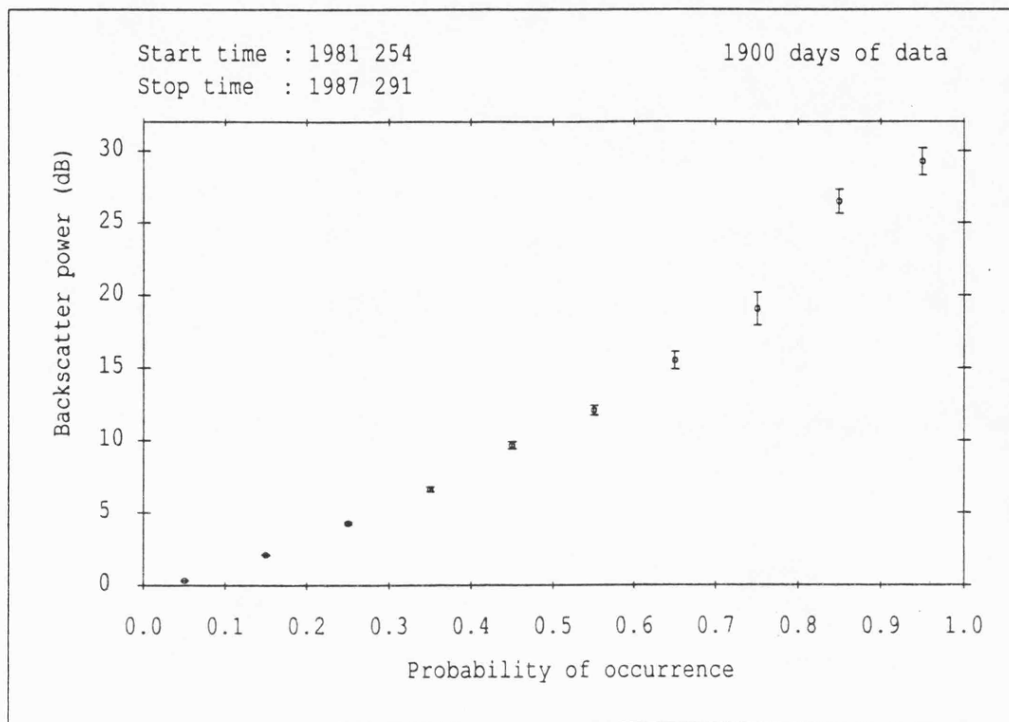
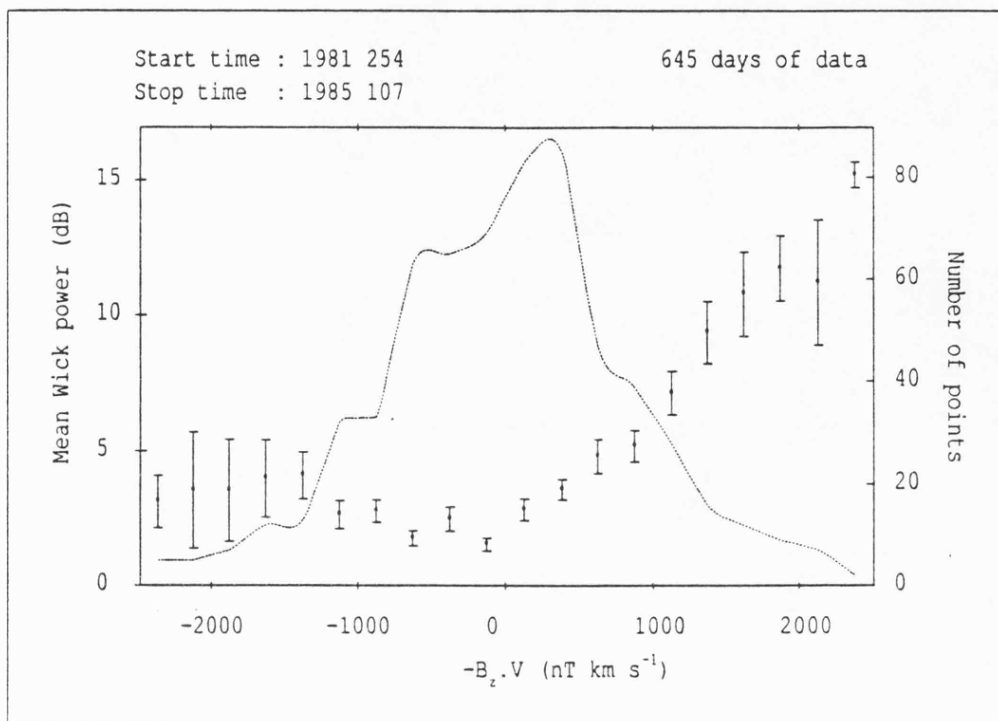
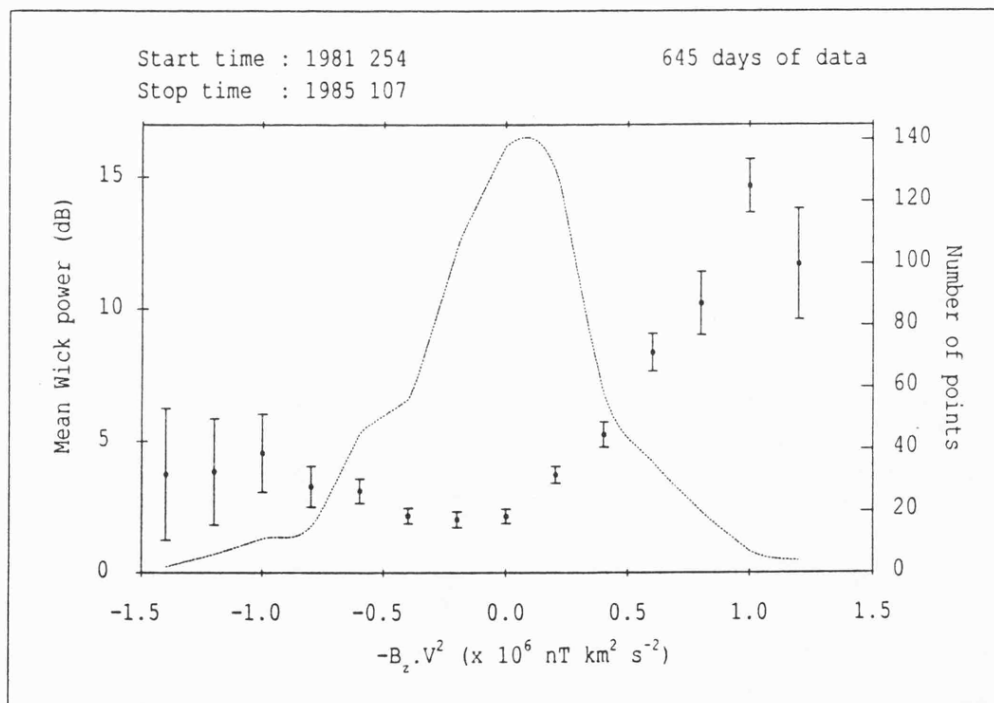


FIGURE 4.6. Plot of daily average backscatter power as a function of the occurrence probability of backscatter.



**FIGURE 4.7.** Dependence of Wick backscatter power on the  $-B_zV$  coupling parameter.



**FIGURE 4.8.** Dependence of Wick backscatter power on the  $-B_zV^2$  coupling parameter.

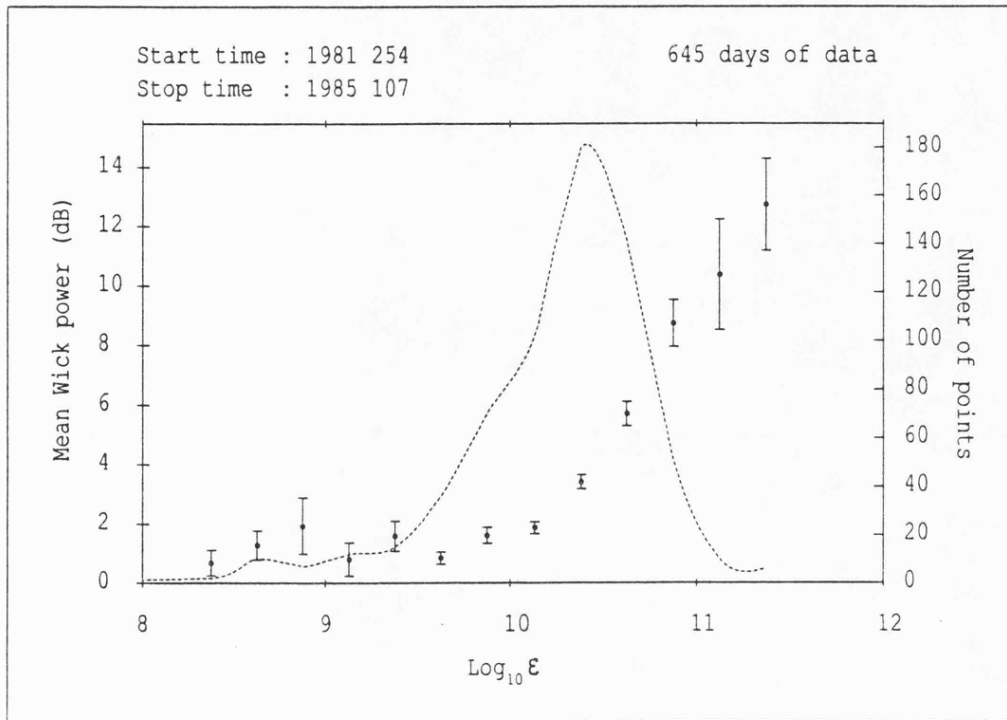


**FIGURE 4.9.** Dependence of Wick backscatter power on the  $\epsilon$  coupling parameter.

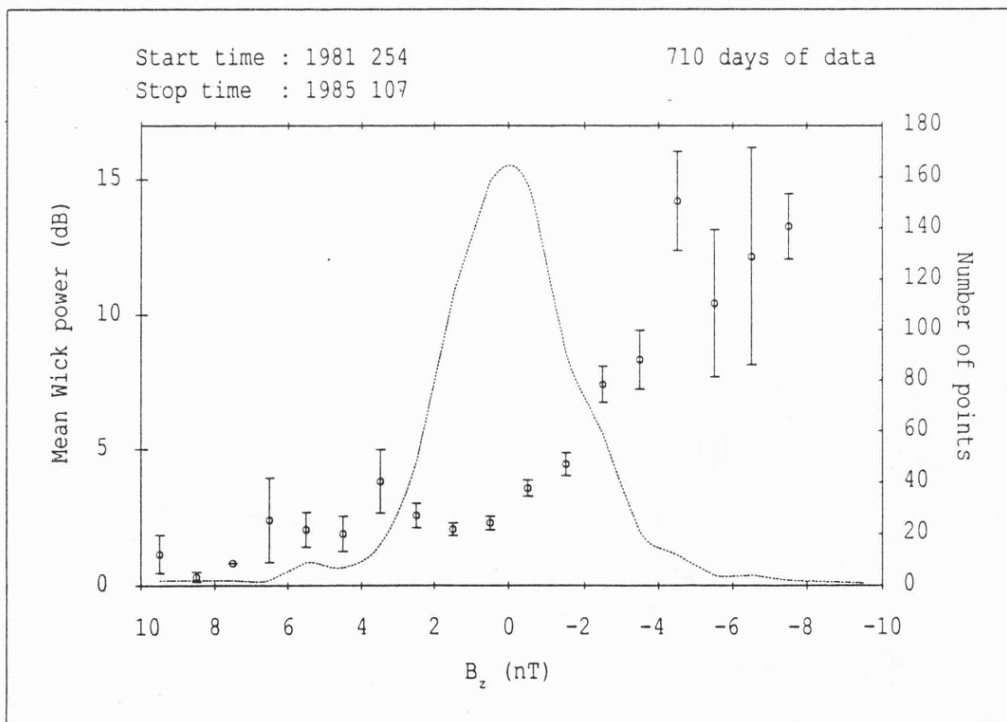


**FIGURE 4.10.** Dependence of Wick backscatter power on the IMF  $B_z$  component.

average Wick power on the  $B_z$  component alone (Figure 4.10) provides a more direct demonstration of the dominance of the reconnection process in the solar wind-magnetosphere interaction. In Figure 4.10, the backscatter power is approximately constant for positive  $B_z$ , while for  $B_z < 0$ , the power increases rapidly as  $B_z$  becomes more negative.

The comparison of the radar data with the  $-B_z V^2$  parameter (Figure 4.8) again suggests the existence of a threshold in the coupling parameter above which the backscatter power is increasingly enhanced (as is the scatter of the data) and generally the relationship is very similar to that for  $-B_z V$ . The dependence of the radar power on  $\epsilon$  (Figure 4.9) is again nonlinear, with the mean backscatter power remaining relatively constant until a threshold value for  $\epsilon$  of about  $10^{10}$  W is exceeded.

#### 4.3.2 Interpretation of the empirical results

The relationship between the daily mean backscatter power and the solar wind parameters is now considered in more detail. In section 3.2.4, a close relationship between the daily average backscatter power and the electrojet intensity (equation (3.10)) was demonstrated. The ultimate energy source for the electrojet system is the solar wind ( $V$  dependency) and the dominant mechanism for transferring this energy to the magnetosphere is reconnection ( $B_z$  dependency). Since the geomagnetic index  $K_p$  is known to respond to average electrojet intensities, the dependence of backscatter power on  $K_p$  should provide a test of the above argument. This relationship is illustrated in Figure 4.11, in which the values of the Wick daily mean backscatter power have been binned for each possible value of the daily average  $K_p$  ( $=K_p \text{ sum}/8$ ). The error bars indicate standard errors and the figure demonstrates that the backscatter power is a smoothly increasing function of  $K_p$ . Thus, a single coherent auroral radar which measures backscatter power monitors the average electrojet intensity and on a statistical basis may provide a scalar parameter which quantifies the

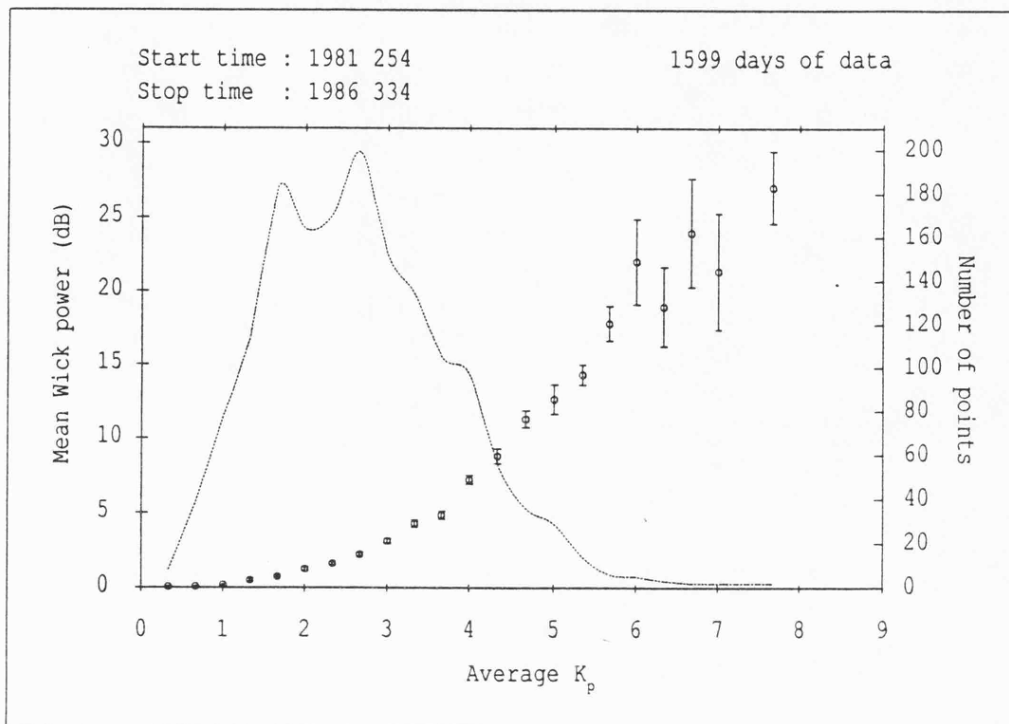


**FIGURE 4.11.** Daily mean Wick backscatter power against daily mean  $K_p$ . The broken curve indicates the distribution of the data.

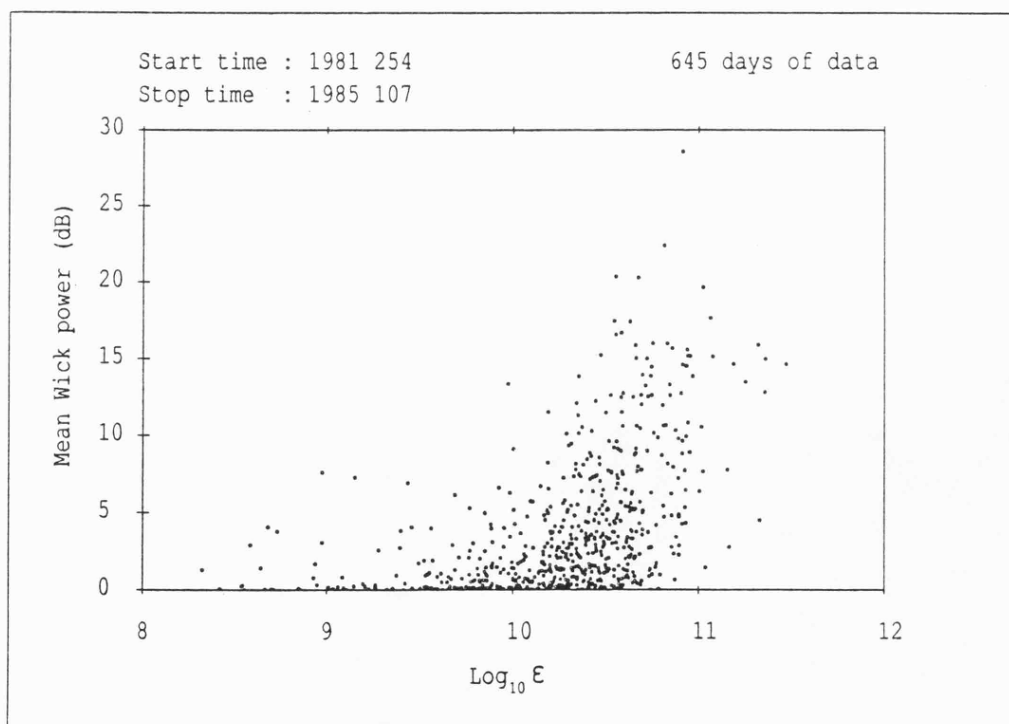


**FIGURE 4.12.** Scatter plot of Wick daily average backscatter power against  $\epsilon$ .

solar wind-magnetosphere interaction.

An examination of a scatter plot of the mean Wick backscatter power against  $\epsilon$  (Figure 4.12) reveals an additional feature of the interaction mechanism. For all values of  $\epsilon$ , the mean Wick backscatter power ranges from zero to a maximum which is dependent on  $\epsilon$ . Thus, a high value of  $\epsilon$  does not guarantee a strong radar response. This is because the ionospheric response is not solely determined by the characteristics of the solar wind, but depends also on the existing ionospheric conditions, for example the conductivity. Fedder and Lyon (1987) predict substantial modifications of the solar wind-magnetosphere-ionosphere interaction by variations in the latter parameter alone.

#### 4.4 Spectral analysis of Wick backscatter intensities

Spectral analysis techniques have been applied to the daily means of the backscatter power in order to investigate the longer term ( $> 1$  day) periodicities. Both the backscatter power and levels of geomagnetic activity are strongly influenced by the electrodynamic properties of the solar wind, as discussed in sections 4.2 and 4.3. In the long term, the geomagnetic field is modulated by the 27 day ( $T_s$ ) solar rotation synodic period, an effect first recognised by Chapman and Bartels (1940), the semiannual and annual variations (Russell and McPherron, 1973), and the 11 year and 90 year solar cycles (Delouis and Mayaud, 1975).

Spectral studies of very long intervals of various magnetic indices (Courtilot et al., 1977; Arora and Rangarajan, 1981) and magnetometer data (de Meyer and de Vuyst; de Meyer, 1986) have been most successful in establishing the semiannual, annual and solar cycle variations. However, higher frequency components, such as  $T_s$ , have appeared less prominently in these studies due to their lower power and the fact that they have become smeared out as a result of non-stationarities which occur in the data over

the very long intervals (30–100 years) typically employed. The sensitivity of the coherent radar technique and the length and continuity of the Wick data base render it very suitable for the detection of periodicities in the 10–30 day range.

The coherent radar technique has certain advantages over a magnetometer for the study of long term variations in electrojet intensity. For example, the Wick radar is directly sensitive to currents at one location, while magnetometers respond to currents over a (variable) range of latitudes. Also, compared to the radar data, magnetometer measurements require considerable processing to be of use in this type of investigation. Geomagnetic indices provide a suitable reduced data set. However, there is a time delay of ~3–4 years in the supply of AE (auroral electrojet) indices, while  $K_p$ , which is an average obtained from 12 mid-latitude stations, is relatively less sensitive to the electrojets.

#### 4.4.1 Spectra of the backscatter intensity data

Figure 4.13 depicts the spectrum, normalised to the total spectral power, derived from a Fourier transform (Appendix A1) of the Wick daily average powers, for the time interval 11 September, 1981 to 20 April, 1986. During this period, the radar operated for 1441 days out of a total possible 1683 days. Prior to calculating the Fourier transform, the backscatter powers within these data gaps were assigned the mean value of the complete data set and, in order to reduce end effects, a 10% cosine bell was applied (Appendix A2), before subtracting the mean. The resulting spectrum displays two prominent lines or clusters of lines, labelled  $R_1$  and  $R_2$ , centered on frequencies corresponding to periods of approximately 26 ( $\sim T_S$ ) and 14 days ( $\sim T_S/2$ ), respectively. The  $R_1$  cluster is dominated by a doublet, whereas the  $R_2$  cluster is dominated by a single, stronger, peak. The appearance of doublets or clusters in the spectrum, rather than single lines, may arise from a modulation of these periods by longer term

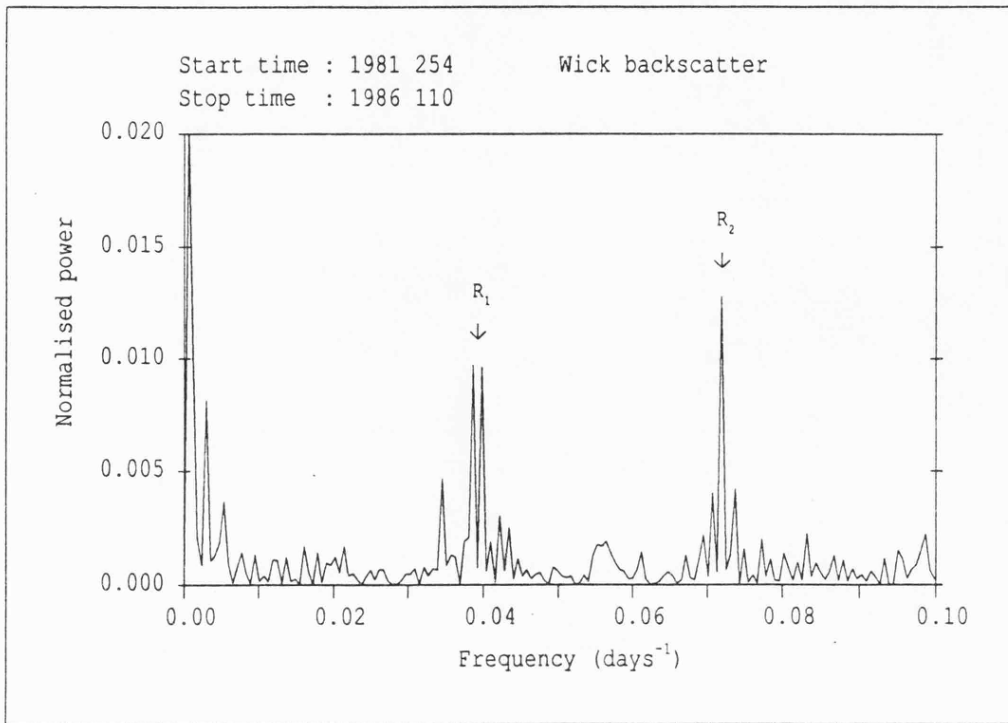


**FIGURE 4.13.** *Fourier spectrum of over 4.5 years of Wick daily mean backscatter intensity data.*

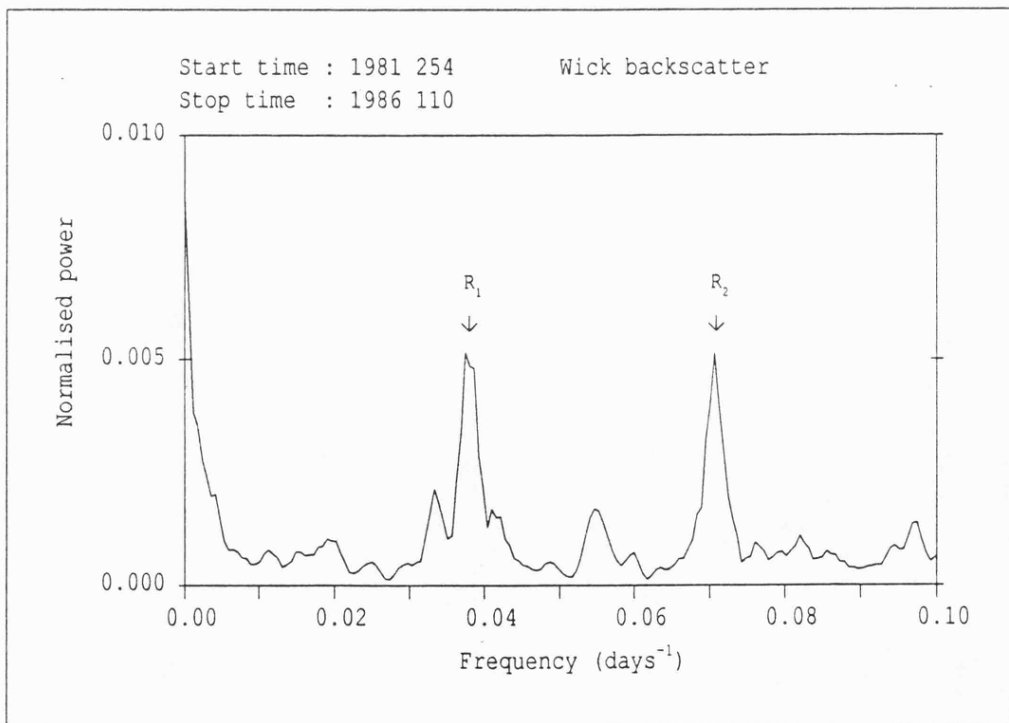


**FIGURE 4.14.** *Same as Figure 4.13 but smoothed with 5 point triangular running mean.*

variations. Other lines, which are less prominent but which are significant compared to the noise, exist at the low frequency end of the spectrum, and these may be associated with longer periodicities such as the semiannual and annual variations. However, the length of the data set provides insufficient resolution at these low frequencies to confirm this conjecture.

An estimate of the uncertainties in the periodicities derived from the frequency analysis is obtained by smoothing the Fourier spectrum with a simple triangular 5 point running mean technique (Appendix A2). The error in the determination of the period corresponding to each peak was obtained from the half power width of the peak. The smoothed spectrum is illustrated in Figure 4.14, which indicates values of  $26.4 \pm 1.2$  and  $14.0 \pm 0.4$  days for the  $R_1$  and  $R_2$  peaks, respectively.

To support the results of the radar data analysis, a comparison was made with the spectrum obtained from the daily sum of the  $K_p$  index for the same time period. The  $K_p$  spectrum (Figure 4.15) is similar to that of the radar backscatter power (Figure 4.13), with two clusters of lines  $R_1$  and  $R_2$  again close to periods of 27 and 13.5 days, respectively. The smoothed spectrum (Figure 4.16) yields values for the periods, corresponding to  $R_1$  and  $R_2$ , of  $27.5 \pm 3.5$  days and  $14.1 \pm 0.6$  days, respectively. The  $R_1$  peak, in particular, is considerably weaker and broader than for the Wick radar spectrum, suggesting that the  $K_p$  index is a less sensitive indicator of the long term variations. The appearance of periods close to  $T_s$  and  $T_s/2$  in the aa geomagnetic index has also been reported (Villante and Francia, 1986), although in that case the  $T_s$  line was the dominant spectral peak.

The SUNDIAL data presented in section 4.2 forms part of the longest continuous operational interval of the radar, from 17 September, 1984 to 17 January, 1985. This is, therefore, particularly suitable for demonstrating the nature of the variation in a subset of the complete database. A time series of the daily average backscatter intensity for this 123 day interval

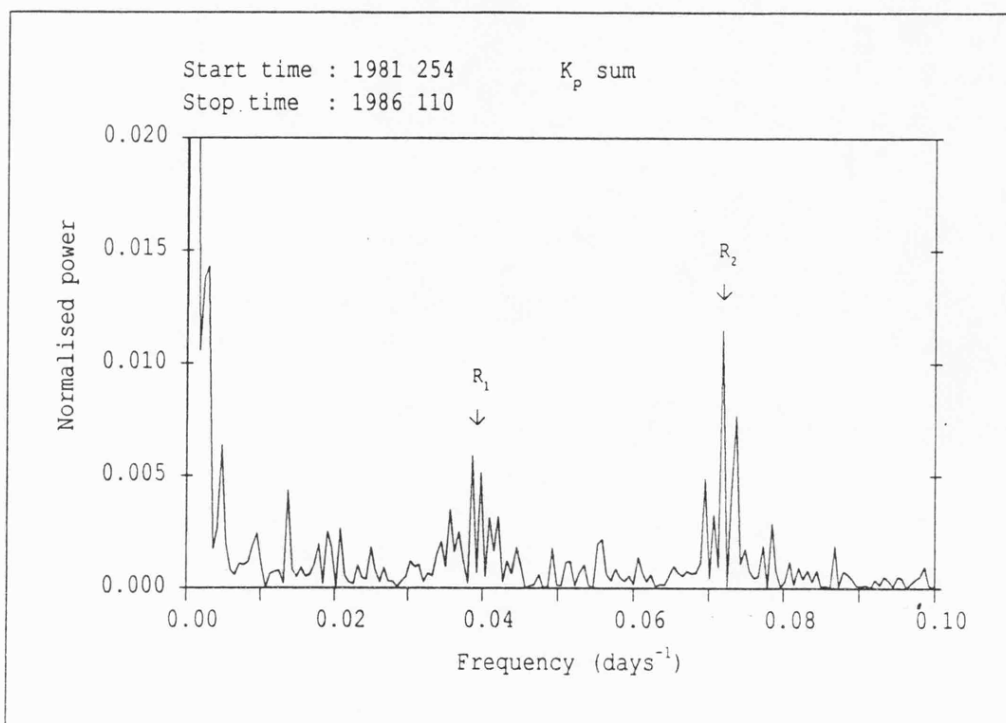


FIGURE 4.15. Fourier spectrum for the same period as Figure 4.13 but for  $K_p$  sum.

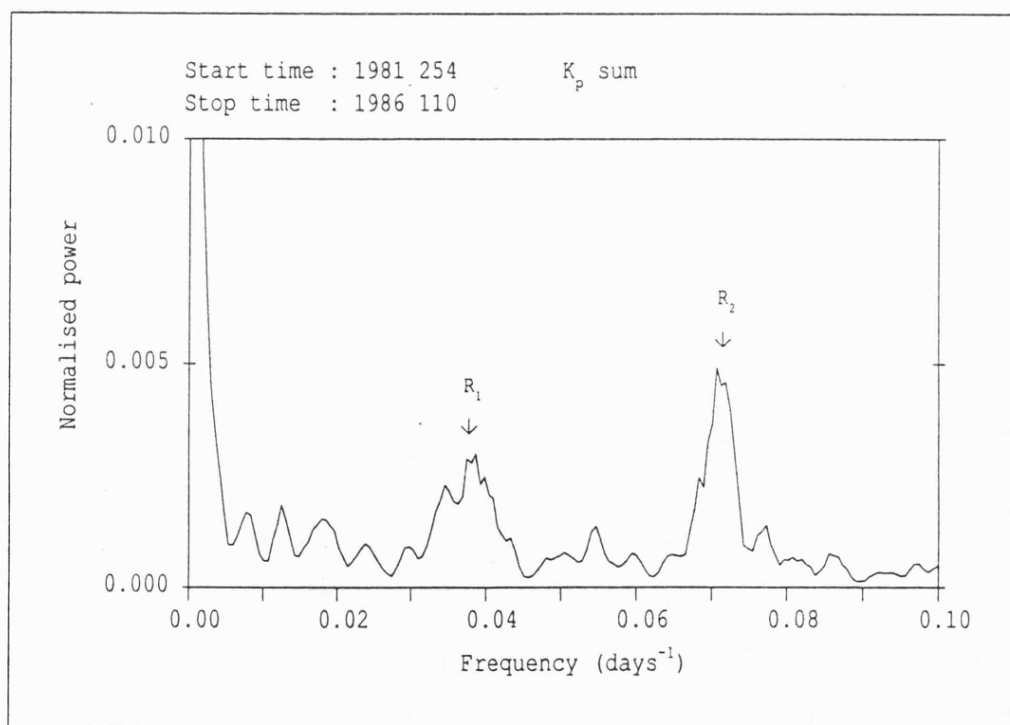


FIGURE 4.16. Same as Figure 4.15 but smoothed with 5 point triangular running mean.

(Figure 4.17) appears to exhibit about 9 cycles of activity. After smoothing the data (Appendix A2), a maximum entropy analysis method (Appendix A3), which is particularly suitable for smaller data sets, was applied (Figure 4.18). The peaks  $R_1$  and  $R_2$  correspond to periods of  $25.0 \pm 2.0$  days and  $13.2 \pm 0.5$  days, respectively, with  $R_1$  the broader spectral peak and  $R_2$  the more prominent and clearly defined line.

#### 4.4.2 Interpretation and discussion of the spectra

The prominent  $T_s$  and  $T_s/2$  periodicities in the ionospheric data may be interpreted in terms of a warped current sheet model of the heliosphere (Alfvén, 1977), in which the Earth periodically crosses the current sheet from one solar hemisphere to the other as the Sun rotates. For a two sector solar wind structure, the model predicts two enhancements of the solar wind flow in the vicinity of the Earth per solar rotation. It is generally accepted that changes in solar wind velocity can influence both geomagnetic activity (Akasofu, 1977) and coherent radar observations (McDiarmid and Nielsen, 1987a, b). In addition, the Fourier spectra of long periods of solar wind speed data usually display broad bands of power centered on periods of 27 and 13.5 days, of which the latter is much more prominent (Fenimore et al., 1978). Consequently, the perturbations in the solar wind flow encountered by the Earth should give rise to an ionospheric signature with a periodicity of  $T_s/2$ .

For the two sector heliospheric structure, the period of recurrence of the same IMF orientation is  $T_s$  (as opposed to  $T_s/2$  for the flow speed). By assuming that the strength of the interaction between the solar wind and the Earth's magnetosphere is determined by the orientation of the IMF alone, Villante et al. (1983) predicted that the power spectra of geomagnetic indices would contain a strong peak at a period close to  $T_s$  and only a very weak peak at a period of  $T_s/2$ . The radar backscatter power spectra, in which the strength of the  $T_s/2$  line exceeds that of the  $T_s$

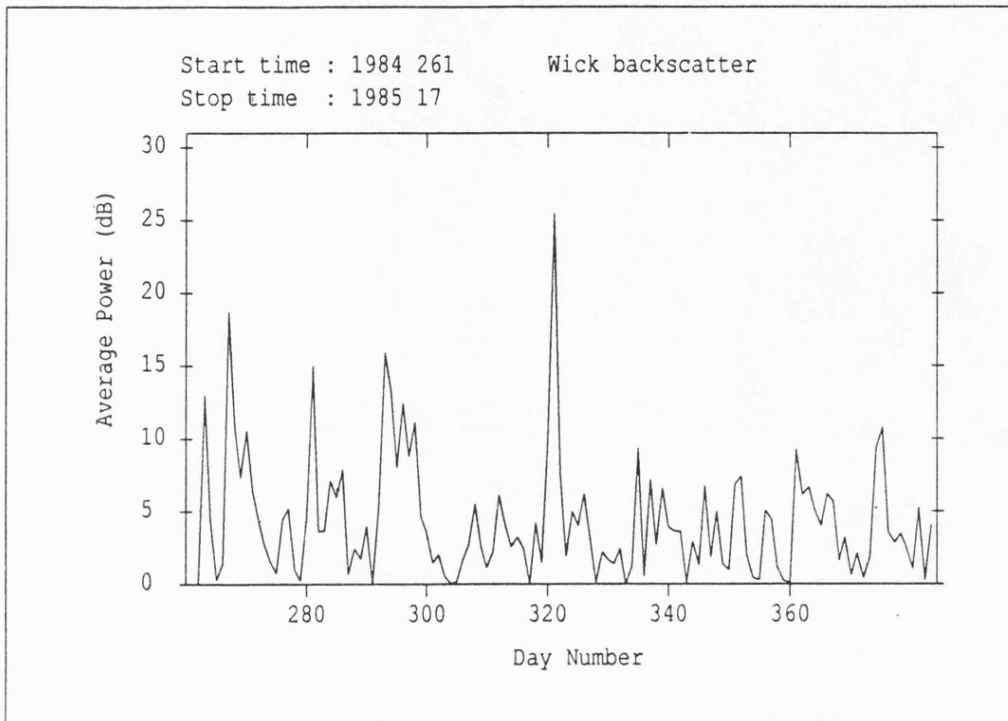


FIGURE 4.17. Wick backscatter power time series for a continuous interval of 123 days.

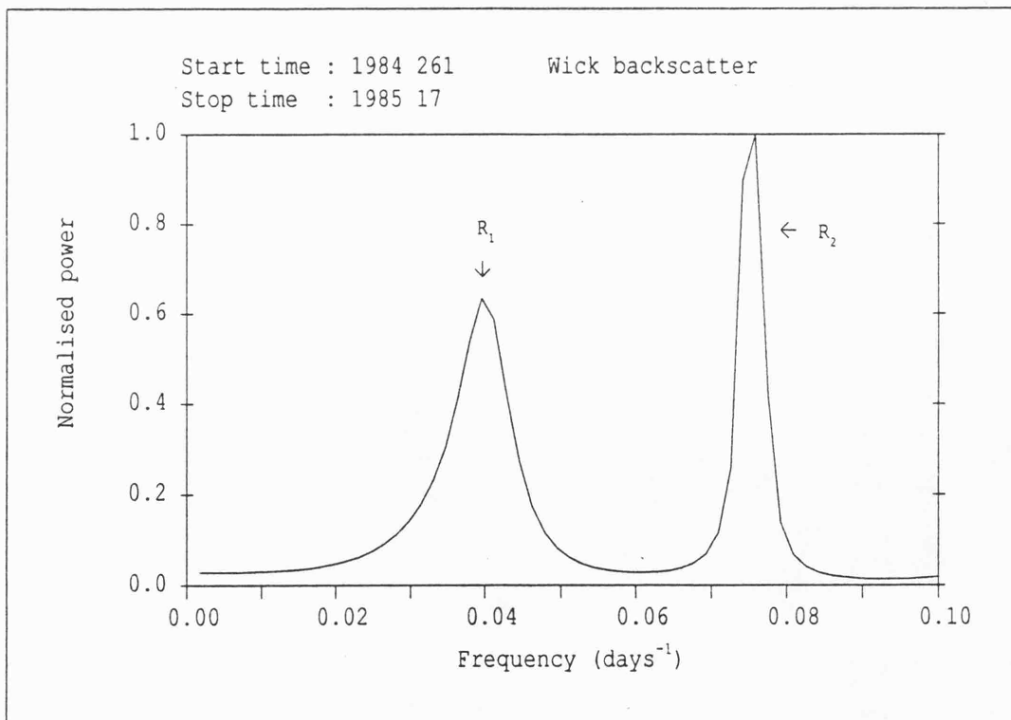


FIGURE 4.18. Maximum entropy spectrum for the data of Figure 4.17.

line, could be explained if the ionospheric response was modulated by a  $T_s$  periodicity in the IMF and, more strongly, by a  $T_s/2$  periodicity in the solar wind velocity. The spectra, which display no significant lines for periods shorter than  $T_s/2$ , imply that on average the heliospheric current sheet maintained a relatively stable two sector structure throughout the interval of 1981 to 1986.

If the sectors of the solar current sheet model are exactly equivalent, then  $V$  and  $B$  should each experience two equal enhancements per solar rotation. However, the  $T_s$  periodicity requires a sector dependent bias of either a magnetic or a kinetic parameter of the solar wind.  $B_z$  does not appear to exhibit an obvious IMF sector dependency, as is illustrated by a scatter plot of  $B_z$  against  $B_y$  (Figure 4.19) in which the points are symmetrically distributed in all four quadrants. This is in distinct contrast with a scatter plot of  $B_y$  against  $B_x$  (Figure 4.20), in which most of the points are confined to two diagonally adjacent quadrants, consistent with the IMF sector structure (the top left quadrant corresponds to a toward sector and the bottom right to an away sector). This conclusion does not conflict with the well established IMF  $B_z$  dependency responsible for shorter period ( $< T_s/2$ ) variations. Since the mean IMF sector structure is largely confined to the x-y plane (Matsushita and Trotter, 1980), the  $B_z$  component is not expected to exhibit the strong  $T_s$  variation which is evident in  $B_x$  and  $B_y$ . In fact, the poor understanding of the causes of changes in IMF  $B_z$  is one of the most serious hinderances to the development of a predictive capability for geomagnetic storms (Akasofu and Fry, 1986).

The lack of an obvious magnetic asymmetry between sectors is further demonstrated by the relationship between  $B$  and  $B_y$  (Figure 4.21) which is almost symmetric about the  $B_y = 0$  axis over a  $3\frac{1}{2}$  year period. This symmetry is also apparent in similar plots for much shorter intervals. It then remains to investigate the possibility of a kinetic asymmetry between

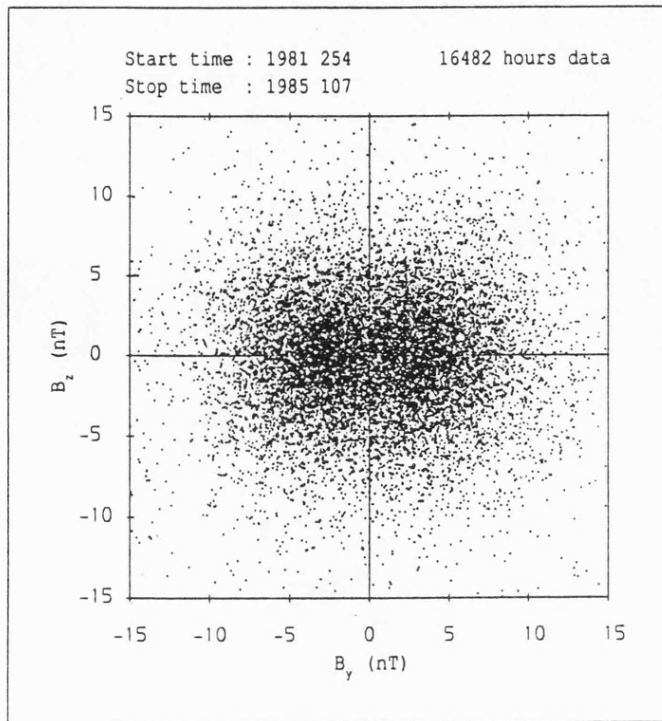


FIGURE 4.19. Scatter plot of IMF  $B_y$  against  $B_z$ .

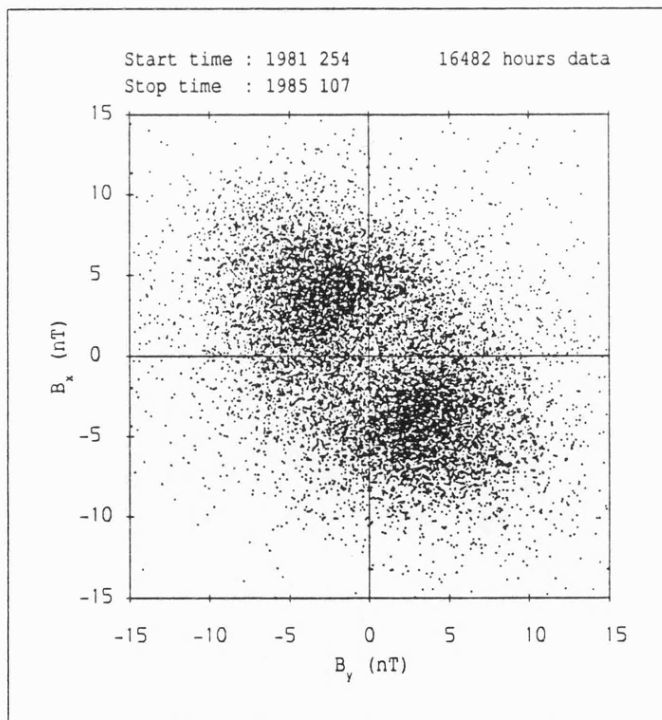
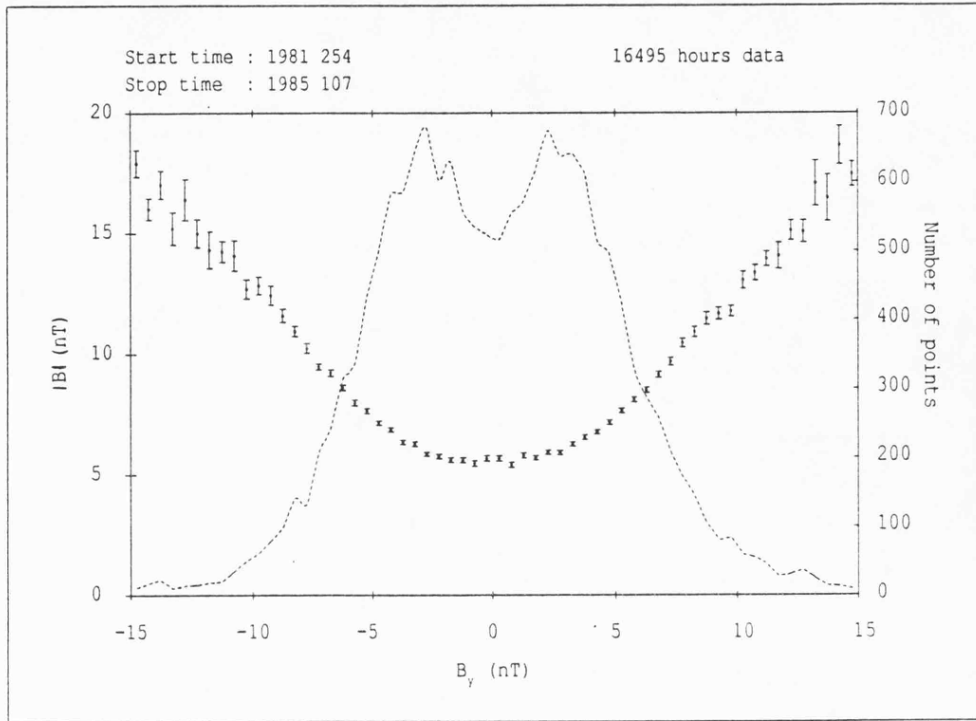
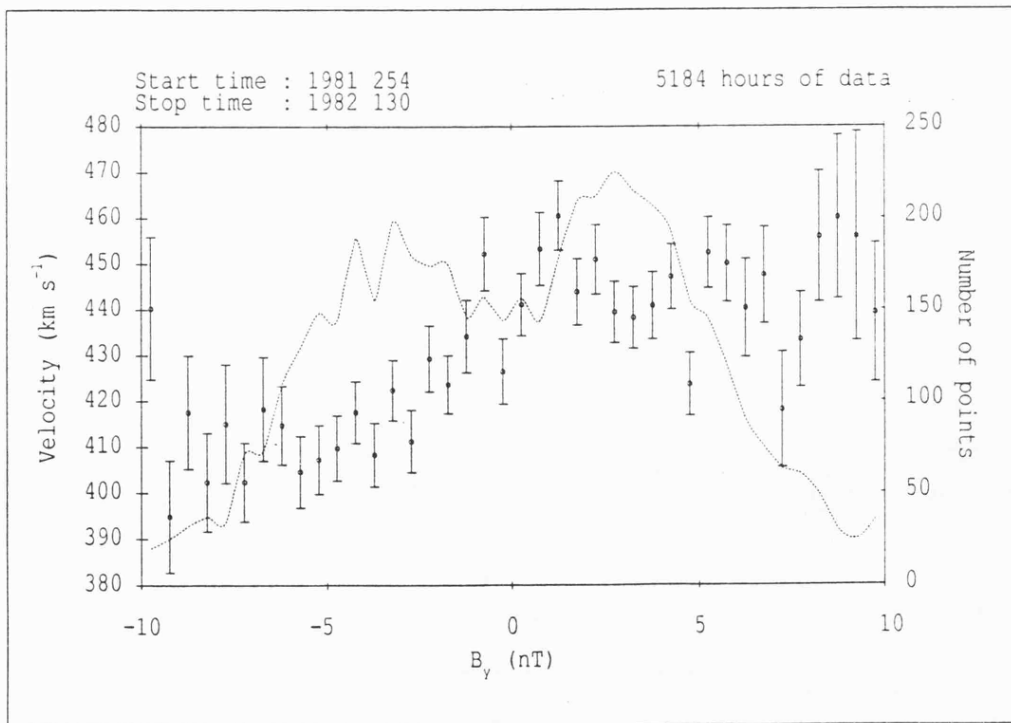


FIGURE 4.20. Scatter plot of IMF  $B_y$  against  $B_x$ .



**FIGURE 4.21.** Plot of the magnitude of the IMF  $|B|$  against  $B_y$ .



**FIGURE 4.22.** Plot of solar wind velocity against  $B_y$ .

the two sectors. In Figure 4.22, the solar wind flow velocity is plotted against  $B_y$ , and despite the appreciable scatter of the points, it is evident that there is a tendency for the velocity to be higher for positive values of  $B_y$  than for negative values, the average difference being some  $40 \text{ km s}^{-1}$ . This implies a sector dependent flow velocity bias, with higher (lower) speed streams being associated with away (toward) sectors for the interval of Figure 4.22. Such an asymmetry in the two sector solar current sheet structure could explain the  $T_s$  variation observed by the Wick radar.

Fenimore et al. (1978) noted that the solar wind speed power spectra differed considerably from year to year, indicating that the time series was nonstationary. In particular, the  $T_s$  and the  $T_s/2$  peaks were much more significant in the descending phase of solar cycle 20 (1965–1976) than in the ascending phase. This result supported the conclusion of Gosling et al. (1976), who had suggested that the solar wind stream structure was considerably less chaotic during the descending phase of solar cycle 20. It is perhaps significant that the very clear peaks at  $T_s$  and  $T_s/2$  detected by the Wick radar were observed during the descending phase of solar cycle 21 (1976–1987).

#### 4.5 Summary

In the past, the backscatter intensity measured by a coherent auroral radar has rarely been employed in geophysical studies. As a result of the present investigation, a strong empirical relationship between the Wick radar backscatter intensity and solar wind parameters such as  $\epsilon$  has been established. The sign of  $B_z$  exerts a crucial influence on the backscatter power. However, the SUNDIAL study indicated that the long term envelope of the radar response correlated with the solar wind velocity  $V$ , not with  $B_z$ . To summarise, the backscatter power is governed in the long term by  $V$ , but is 'gated' by a coupling efficiency factor which depends strongly on  $B_z$ .

The close relationship between the backscatter intensity and the solar wind parameters is consistent with theories which relate backscatter power to electrojet intensities (Uspensky et al., 1983; Starkov et al., 1983; Robinson, 1987).

Because of its high sensitivity and continuous operation, the Wick radar is an excellent tool for the investigation of long term (~10-30 days) variations in the ionosphere and their relationship with structures in the solar wind. A preliminary study has demonstrated the existence of perturbations in the high latitude ionosphere with periodicities of approximately  $T_S$  and  $T_S/2$ . The  $T_S/2$  periodicity in the ionospheric data probably arises from the existence (over the interval of the study) of a temporally stable two sector heliospheric structure, resulting in the enhancement of both kinetic and magnetic parameters of the interplanetary medium twice per solar rotation. The  $T_S$  periodicity indicates that the two sectors are not equal and it is tentatively suggested that the asymmetry manifests itself as a difference in the average solar wind velocity between sectors.

## CHAPTER 5

### STATISTICS OF SABRE CONVECTION FLOWS

#### 5.1 Introduction

A statistical study of Wick backscatter power data was presented in the previous chapter. A statistical approach is now applied to the SABRE irregularity drift velocity measurements, and the dependence of the average convection flows on  $K_p$  and on the orientation of the IMF is investigated. A useful parameter for quantifying the large scale convection pattern is found to be the time of occurrence of the Harang discontinuity ( $T_{HD}$ ) in the centre of the SABRE field of view. The Harang discontinuity is a distinctive feature of the pattern which is frequently observed by SABRE, and its variation with various geomagnetic indices and with the components of the IMF has been studied.

#### 5.2 Synoptic survey of the data

High latitude ionospheric perturbations are induced both directly by the solar wind and indirectly via the storage and subsequent release of energy by the geomagnetic tail (section 2.4). It is therefore important to investigate the correlations of the high latitude convection flows (as measured by SABRE) with IMF parameters and also with geomagnetic indices (which indicate the level of substorm activity).

##### 5.2.1 Dependence on geomagnetic conditions

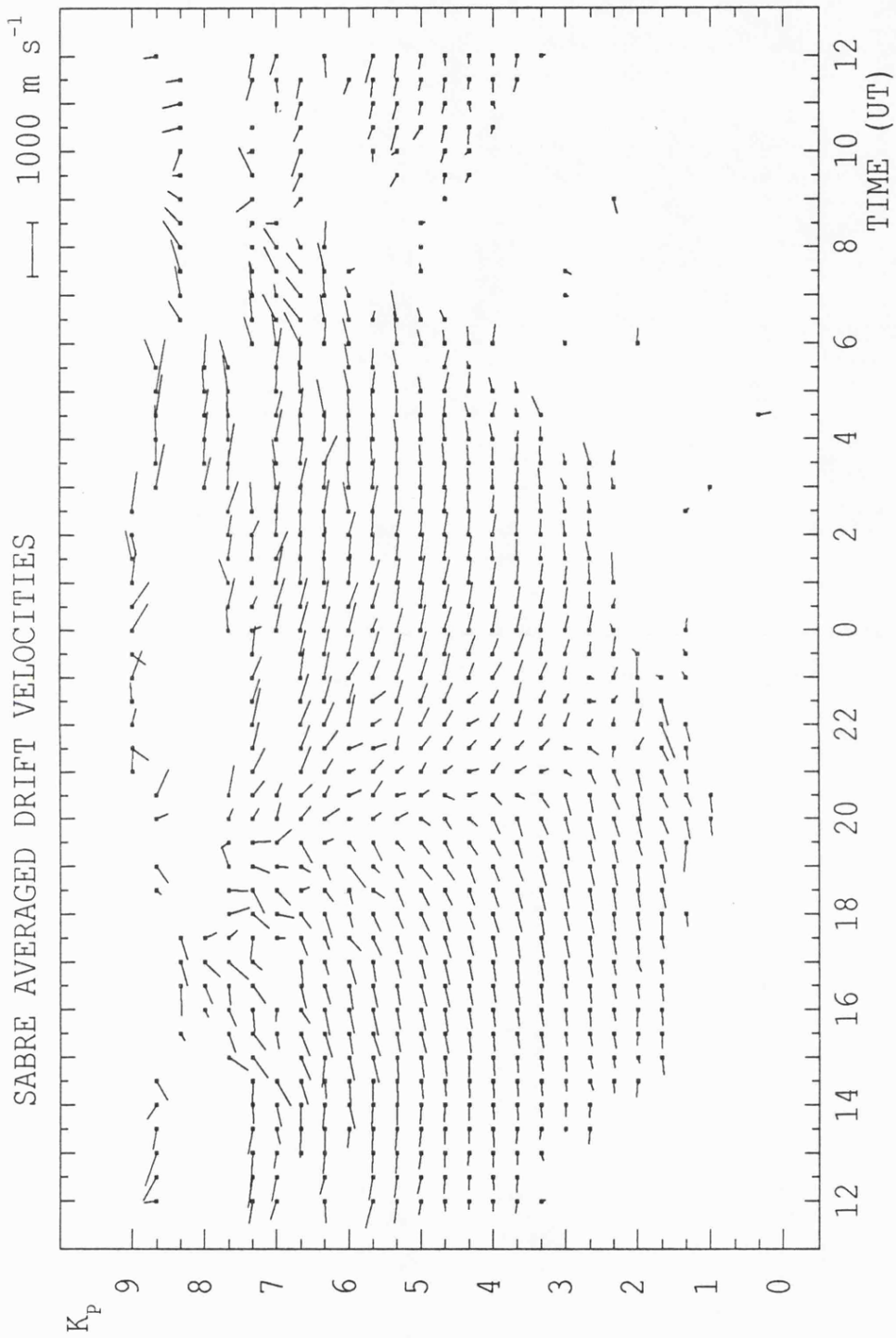
The dependence of the mean SABRE measured convection flow pattern on the

geomagnetic index  $K_p$  was first described by Waldock et al. (1985), for a sample of 384 days observations. In this study, 30 minute averages of the SABRE convection flow velocities measured in the centre of the viewing area (geomag. lat. 64.0–64.2° N, long. 100–102° E) were grouped according to the  $K_p$  value. The same method has now been applied to a larger SABRE data set of 1016 days (22 March, 1982 to 27 October, 1986). The resulting average convection flow velocities, grouped according to  $K_p$ , are plotted, as a function of time over a 24 hour period, in Figure 5.1. The most obvious feature is the shift to earlier times of the Harang discontinuity with increasing activity, from between 21:00 and 21:30 UT at a  $K_p$  of 2 to 19:30–20:00 UT at a  $K_p$  of 6. Also, strong flows are observed in the vicinity of the morning reversal only for high values of  $K_p$ . Both of these effects are consistent with the equatorward expansion of the large scale convection pattern with increasing geomagnetic activity.

### 5.2.2 Dependence on the IMF

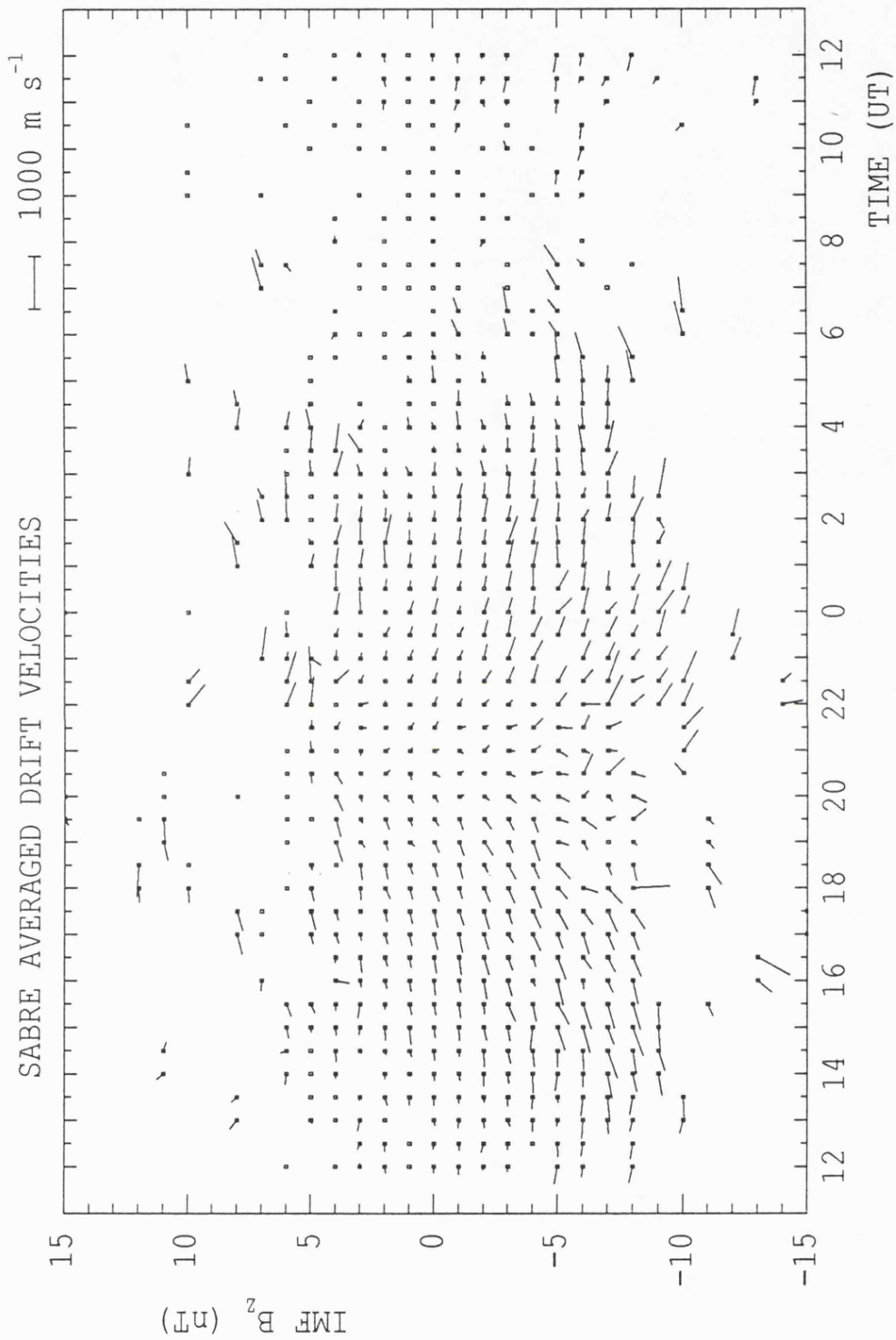
The variation of the convection pattern with the orientation of the IMF has been investigated utilising 1500 hours of simultaneous SABRE and IMF measurements, collected over the period from 22 March, 1982 to 22 March, 1985. For this purpose, hourly averaged IMF data (section 3.3) were compared with 15 minute means of the convection flows measured by SABRE, spatially averaged over a region in the centre of the viewing area (64.0–64.2° N, 100° to 102° E, geomagnetic).

Figure 5.2 illustrates the average SABRE flow pattern as a function of IMF  $B_z$  and the 24 hour time period from 12 to 12 UT, at intervals of 30 minutes. Figure 5.2 clearly indicates that there are less data for positive values of  $B_z$  than for negative values, despite the statistically equal probability of either  $B_z$  polarity (Figure 4.19). This is consistent with the  $B_z$  dependence of the radar backscatter power presented in the previous chapter (Figure 4.10) and is in agreement with the reconnection



GM Lat.  $64.0^{\circ}$ - $64.2^{\circ}$  N      22/3/82 to 27/10/86      1013 days

**FIGURE 5.1.** Mean convection flow velocities measured by SABRE, as a function of universal time and  $K_p$ , averaged over the geomagnetic latitude range  $64.0^{\circ}$ - $64.2^{\circ}$  N and longitude  $100^{\circ}$ - $102^{\circ}$  E.



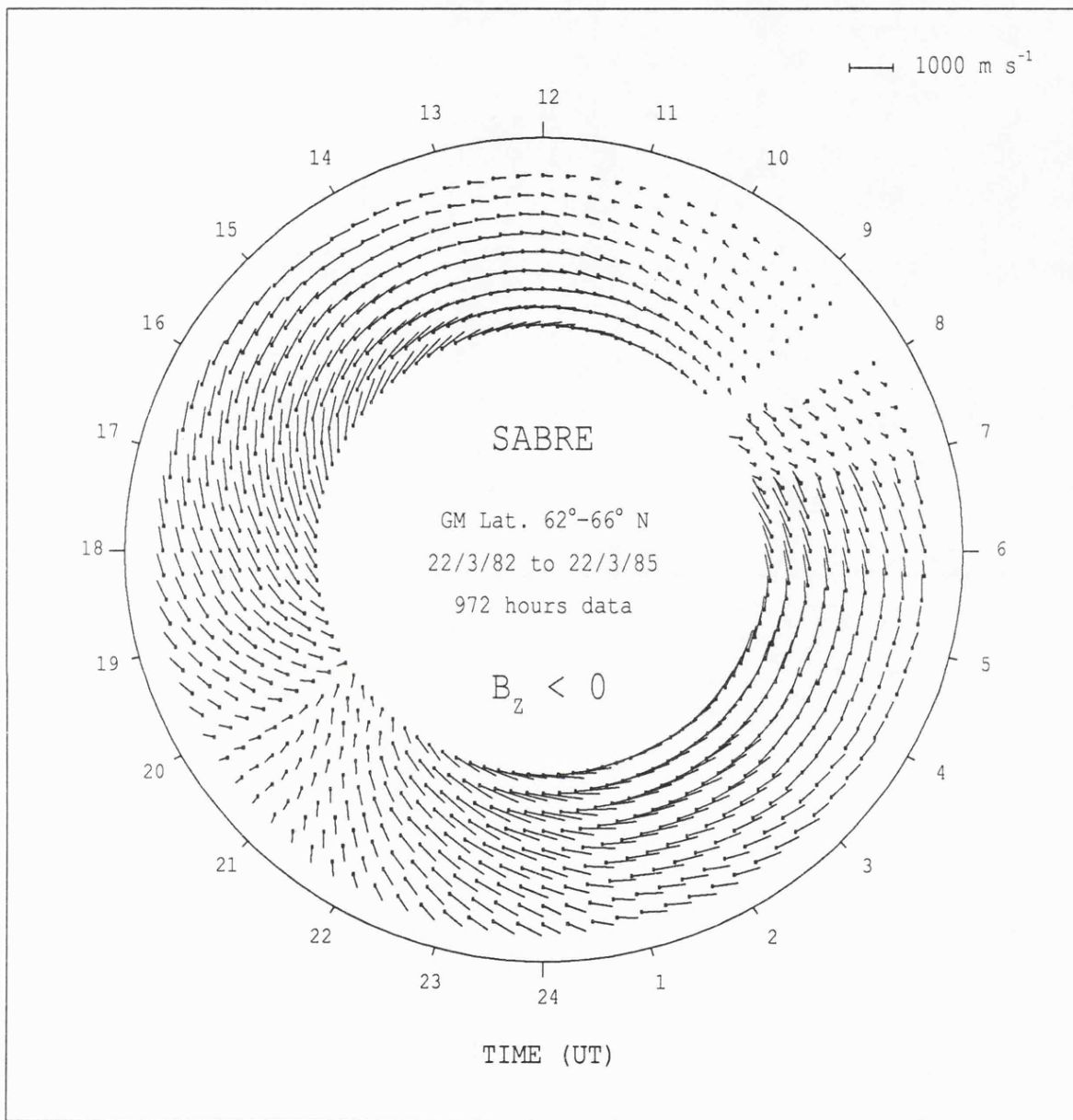
GM Lat. 64.0°-64.2° N 22/3/82 to 22/3/85 1500 hours data

FIGURE 5.2. Mean convection flow velocities measured by SABRE, as a function of universal time and IMF  $B_z$ , averaged over geomagnetic latitude 64.0°-64.2° N and longitude 100°-102° E.

model for the generation of the large scale convection pattern (section 2.4.1). The flows are mainly confined to the  $-10$  to  $+5$  nT  $B_z$  range, and are strongest in the range  $-10$  to  $-5$  nT. The lack of any appreciable backscatter for  $B_z < -10$  nT is due to the relatively low incidence of such strongly southward IMF conditions.

In Figures 5.3 and 5.4, the SABRE statistical convection flows are presented as annular plots, for 9 latitudes from  $62^\circ$  to  $66^\circ$  N, for all values of  $B_z < 0$  and for all values of  $B_z > 0$ , respectively. This indicates that the Harang discontinuity occurs later and that the convection flows are generally weaker, particularly on the dayside, for positive  $B_z$  than for negative  $B_z$ . Both of these effects are consistent with the reconnection mechanism, which predicts stronger flows and the expansion of the convection pattern for increasingly negative  $B_z$ . The change in the time of occurrence of the Harang discontinuity as the convection pattern expands or contracts is due to the latitudinal variation in the location of the discontinuity.

Figure 5.5 illustrates the statistical convection flow pattern observed by SABRE as a function of IMF  $B_y$ . In contrast to the  $B_z$  dependence of Figure 5.2, observations of convection flows are equally distributed between positive and negative  $B_y$ . There is some evidence in Figure 5.5 that the Harang discontinuity occurs earlier for positive values of  $B_y$ , and this trend is more apparent if the SABRE vectors at each time are averaged for all positive and for all negative values of  $B_y$ . These vectors are presented in annular plots as a function of geomagnetic latitude in Figure 5.6 for  $B_y < 0$  and in Figure 5.7 for  $B_y > 0$ . The annular plots indicate that the average time of occurrence of the Harang discontinuity in the centre of the SABRE field of view ( $64^\circ$  N, geomagnetic) is approximately 20:00 UT for positive  $B_y$  and about 1 hour later at 21:00 UT for negative  $B_y$ . A more quantitative investigation of this effect is presented in the next section. These results support the conclusion of de la Beaujardière



**FIGURE 5.3.** Mean convection flow velocities measured by SABRE as a function of geomagnetic latitude and universal time for IMF  $B_z < 0$ . For the sake of clarity, the latitude range is not to scale.

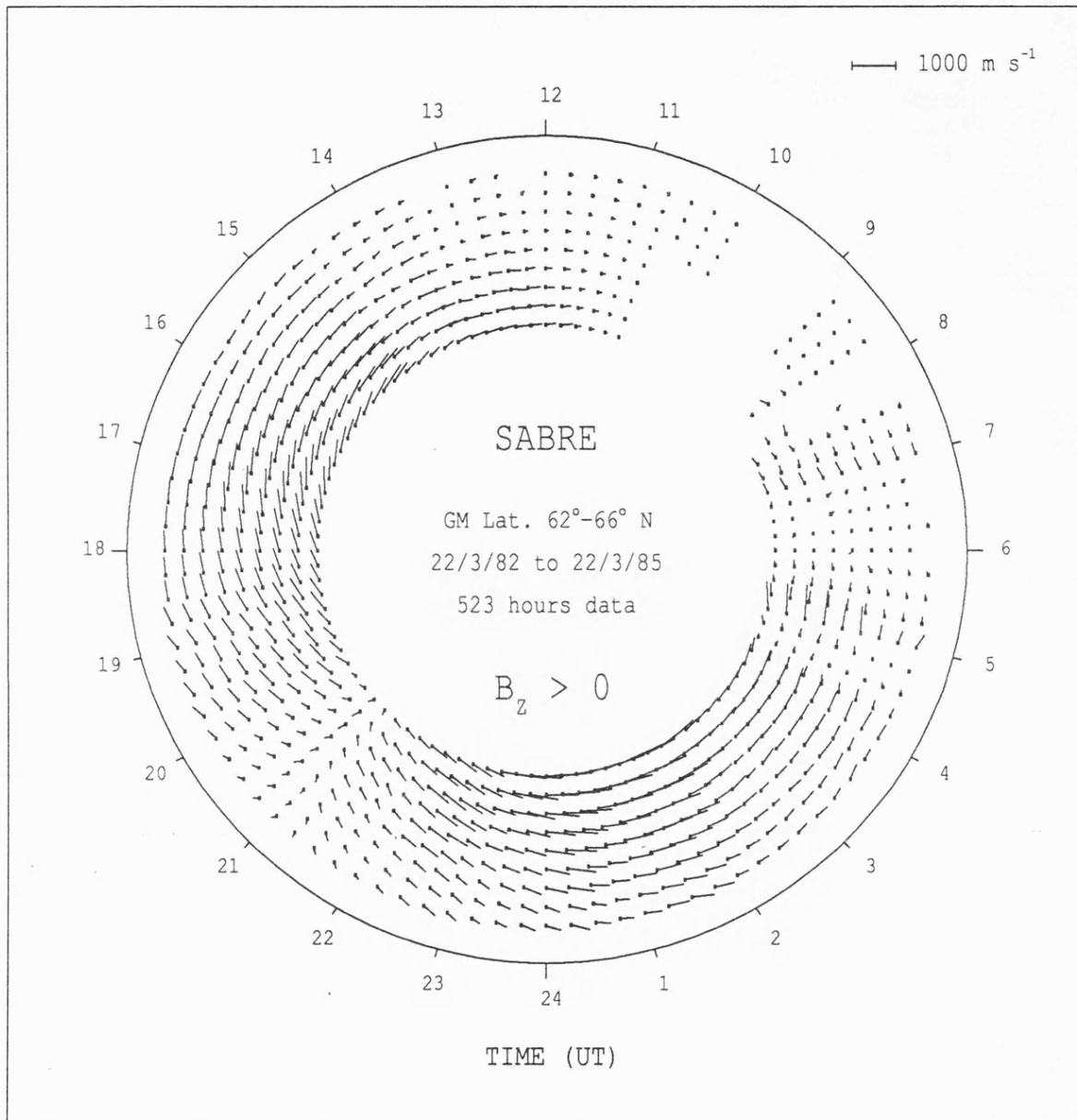
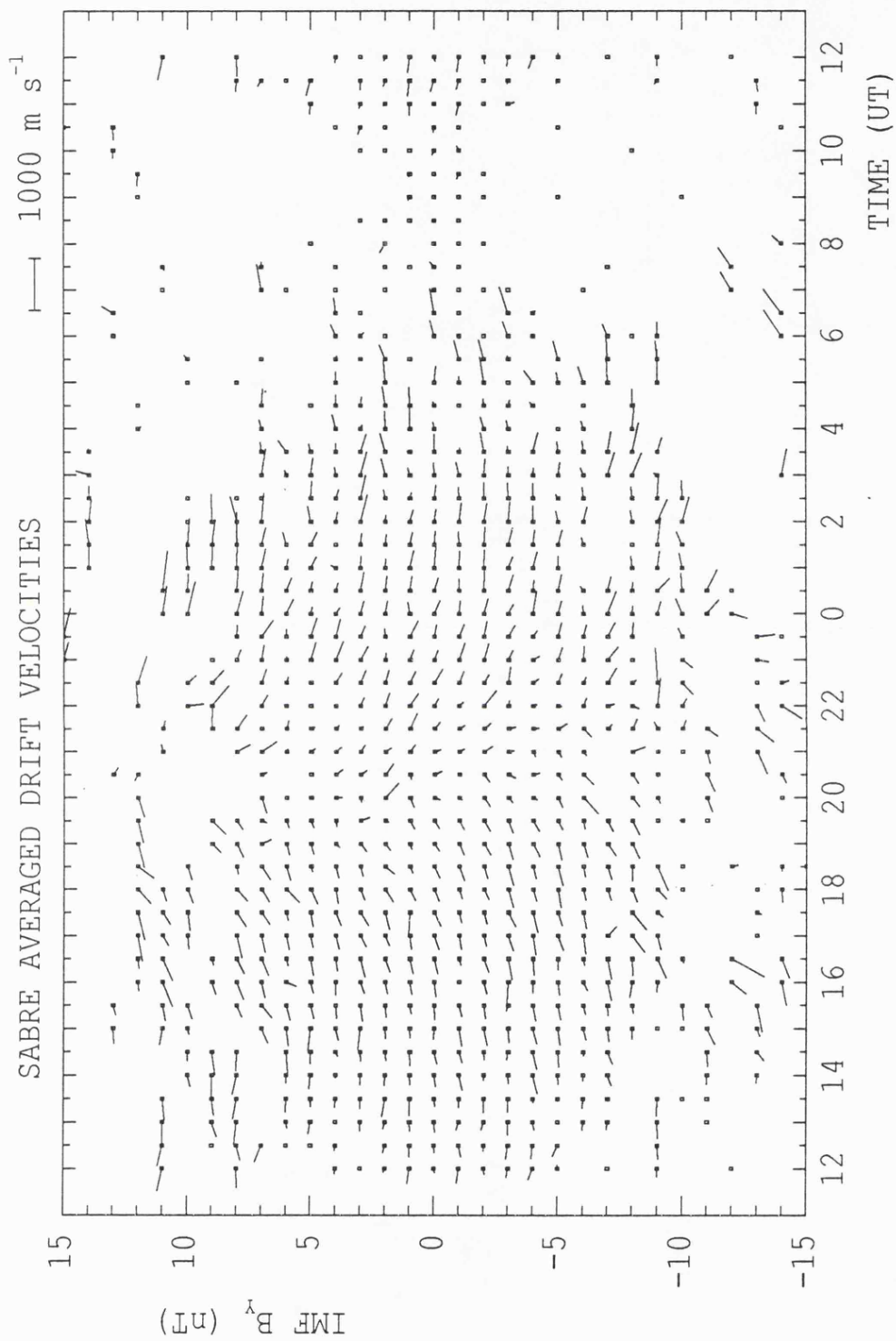


**FIGURE 5.4.** Same as figure 5.3 but for IMF  $B_z > 0$ .



GM Lat. 64.0°-64.2° N 22/3/82 to 22/3/85 1500 hours data

**FIGURE 5.5.** Mean convection flow velocities measured by SABRE, as a function of universal time and IMF  $B_y$ , averaged over geomagnetic latitude 64.0°-64.2° N and longitude 100°-102° E.

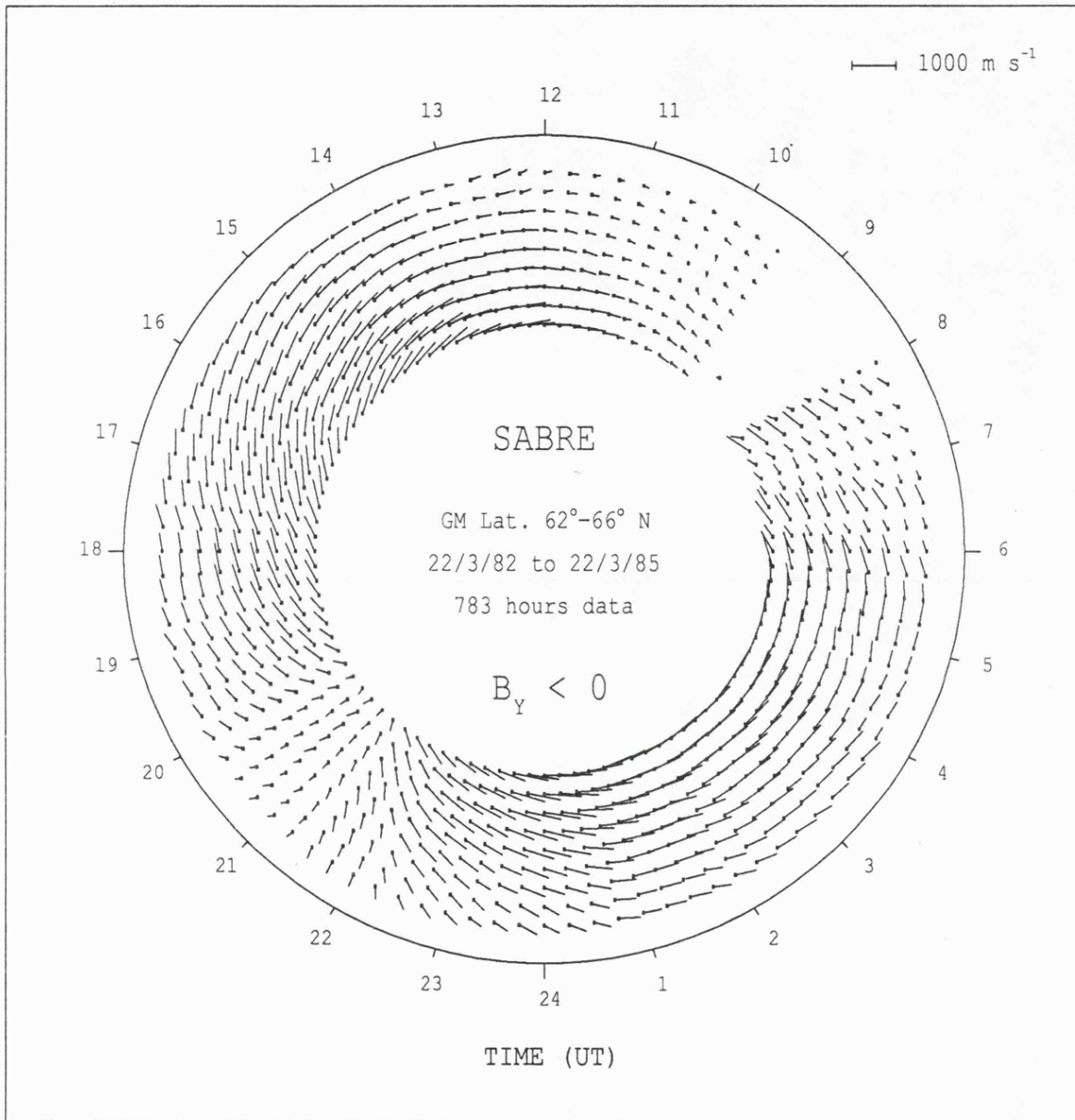


**FIGURE 5.6.** Mean convection flow velocities measured by SABRE as a function of geomagnetic latitude and universal time for IMF  $B_y < 0$ .

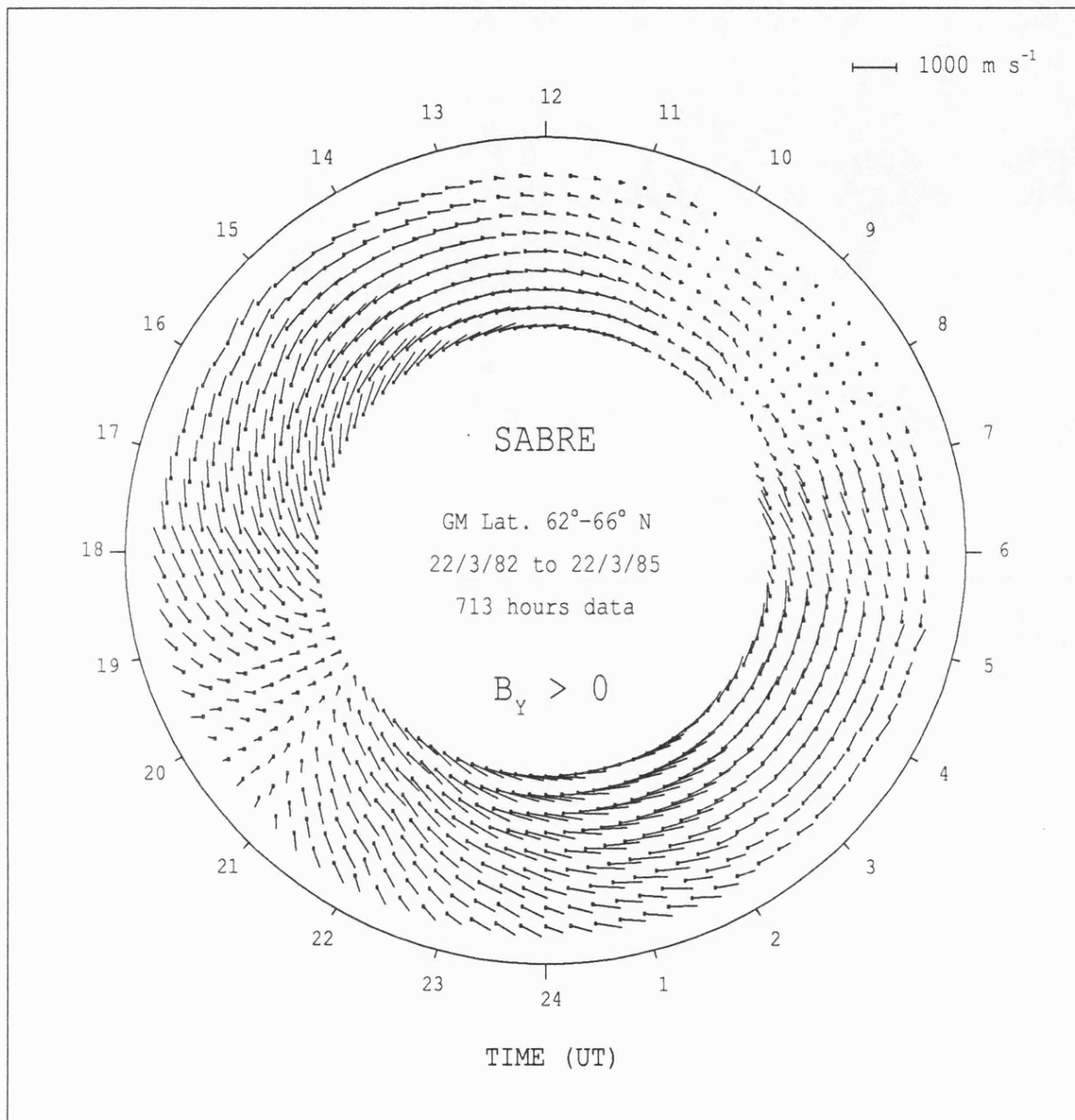


FIGURE 5.7. Same as figure 5.6 but for IMF  $B_y > 0$ .

et al. (1985), whose Sondrestrom incoherent radar observations indicated that the effect of the  $B_y$  component is not limited to the noon hours.

Figures 5.6 and 5.7 suggest one further trend. The time interval in the vicinity of the discontinuity for which the southward flow component is larger than the east-west component is twice as long for negative  $B_y$  (20:00–22:00 UT) than for positive  $B_y$  (19:30–20:30 UT). This point is discussed further in section 5.4. Unfortunately, with the present statistical approach, there are insufficient simultaneous SABRE and IMF data in the morning sector to detect the predicted  $B_y$  dependent cusp flow asymmetries (section 2.4.2). Such asymmetries have been observed by SABRE on a few individual days and these events are presented as case studies in the next chapter.

In Figure 5.8, the average SABRE flows, for  $64^\circ$ – $64.2^\circ$  N, geomagnetic, are illustrated as a function of IMF  $B_x$ . The predicted effect of a positive (negative) value of  $B_x$  on the convection pattern is a tailward (sunward) shift (section 2.4.3). Consequently, flows should be preferentially observed on the nightside for positive  $B_x$  and on the dayside for negative  $B_x$ . No such effect is apparent in Figure 5.8. Moreover, no  $B_x$  dependence of the time of the Harang discontinuity is evident.

### 5.3 The Harang discontinuity

The local time of occurrence of the Harang discontinuity can be a difficult parameter to measure, due to the temporal variability and often complex latitudinal structure of the feature. Some of the SABRE observed characteristics of the discontinuity are now considered.

#### 5.3.1 Structure of the discontinuity

A typical example of the convection flows in the vicinity of the Harang discontinuity was observed on 6 September, 1982, by both the SABRE and the

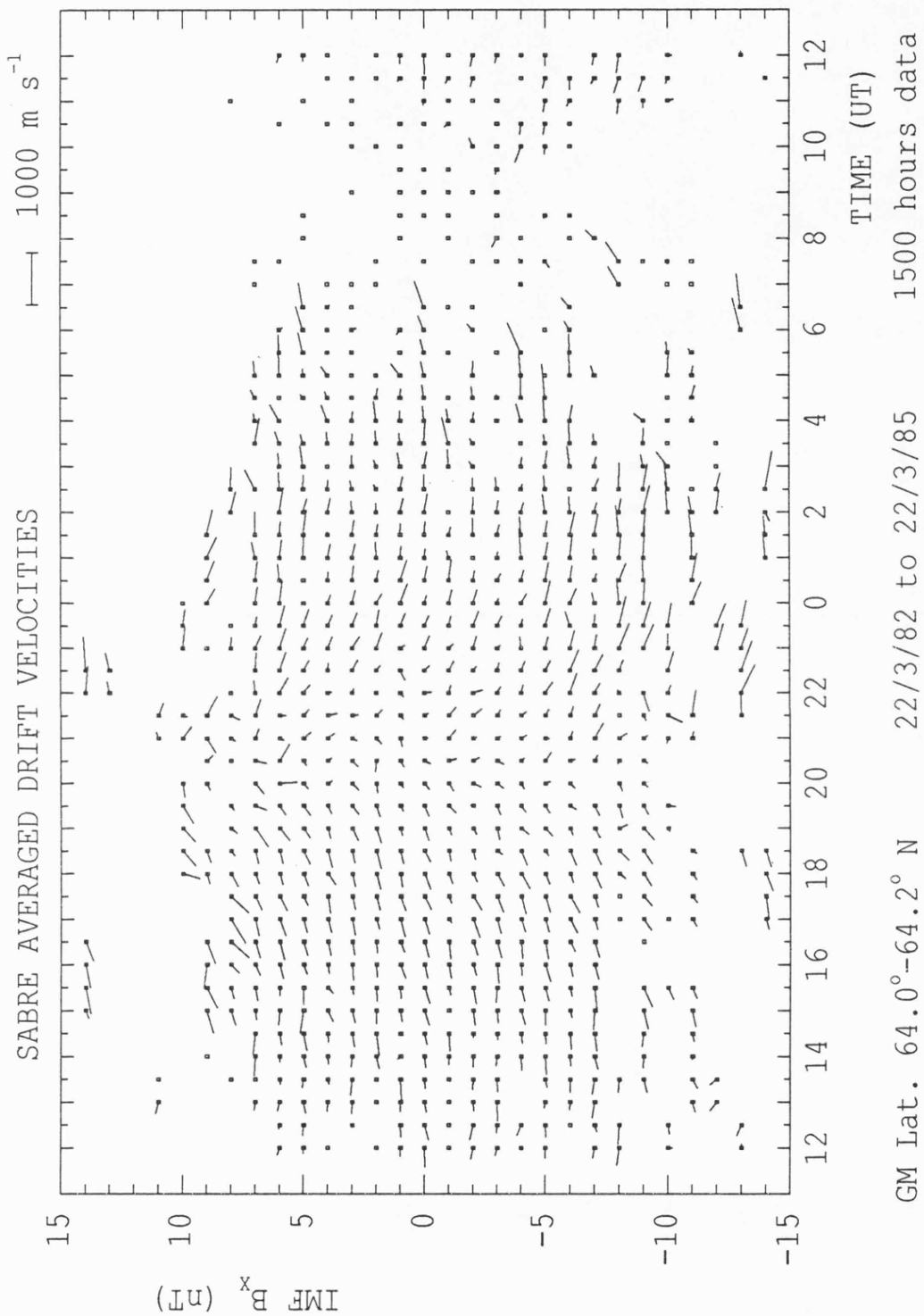


**FIGURE 5.8.** Mean convection flow velocities measured by SABRE, as a function of universal time and IMF  $B_x$ , averaged over geomagnetic latitude  $64.0^\circ$ - $64.2^\circ$  N and longitude  $100^\circ$ - $102^\circ$  E.

STARE systems. Figure 5.9 represents the convection flow vectors at 19:11 UT (6 September, 1982) in the two viewing areas, with the SABRE field of view located to the south-west. The flows in the STARE field of view are directed predominantly south-eastward, while those in the SABRE viewing area are south-westward. At this time the viewing areas lay either side of the Harang discontinuity, with SABRE and STARE observing the dusk and dawn cells, respectively.

Figure 5.10 illustrates the convection flow velocities as a function of latitude and time (a Range Time Velocity or RTV plot), averaged over the longitudinal interval  $8^{\circ}$ - $18^{\circ}$  E, for the same event as Figure 5.9. The longitudinal interval is chosen to include both the eastern edge of the SABRE viewing area and the western edge of the STARE viewing area. The technique for combining SABRE and STARE measurements, in order to double the effective latitudinal coverage of the convection pattern, has been described by Burrage et al. (1985). When the convection flow is not spatially uniform, the averaging process is subject to a limitation due to the longitudinal displacement between the two viewing areas. Figure 5.10 covers the period 18:30 to 20:00 UT, during which time the Harang discontinuity passed through both viewing areas. The discontinuity moves equatorward with time throughout the entire latitude range, although the penetration speed of the eastward flow is latitudinally dependent. In the STARE viewing area, the Harang discontinuity moves equatorward with a speed of approximately  $250 \text{ m s}^{-1}$ , while in the SABRE viewing area this speed has risen to  $1000 \text{ m s}^{-1}$ . The sudden change between the two areas arises from the longitudinal resolution limitation mentioned above. Owing to the high level of geomagnetic activity at this time ( $K_p = 7$ ), the convection pattern had expanded equatorwards, and strong auroral zone flows were located within the latitude range covered by SABRE, while the STARE system observed generally weaker flows. During quiet geomagnetic conditions, the Harang discontinuity would be expected to occur between 22:00 and 23:00 UT for the

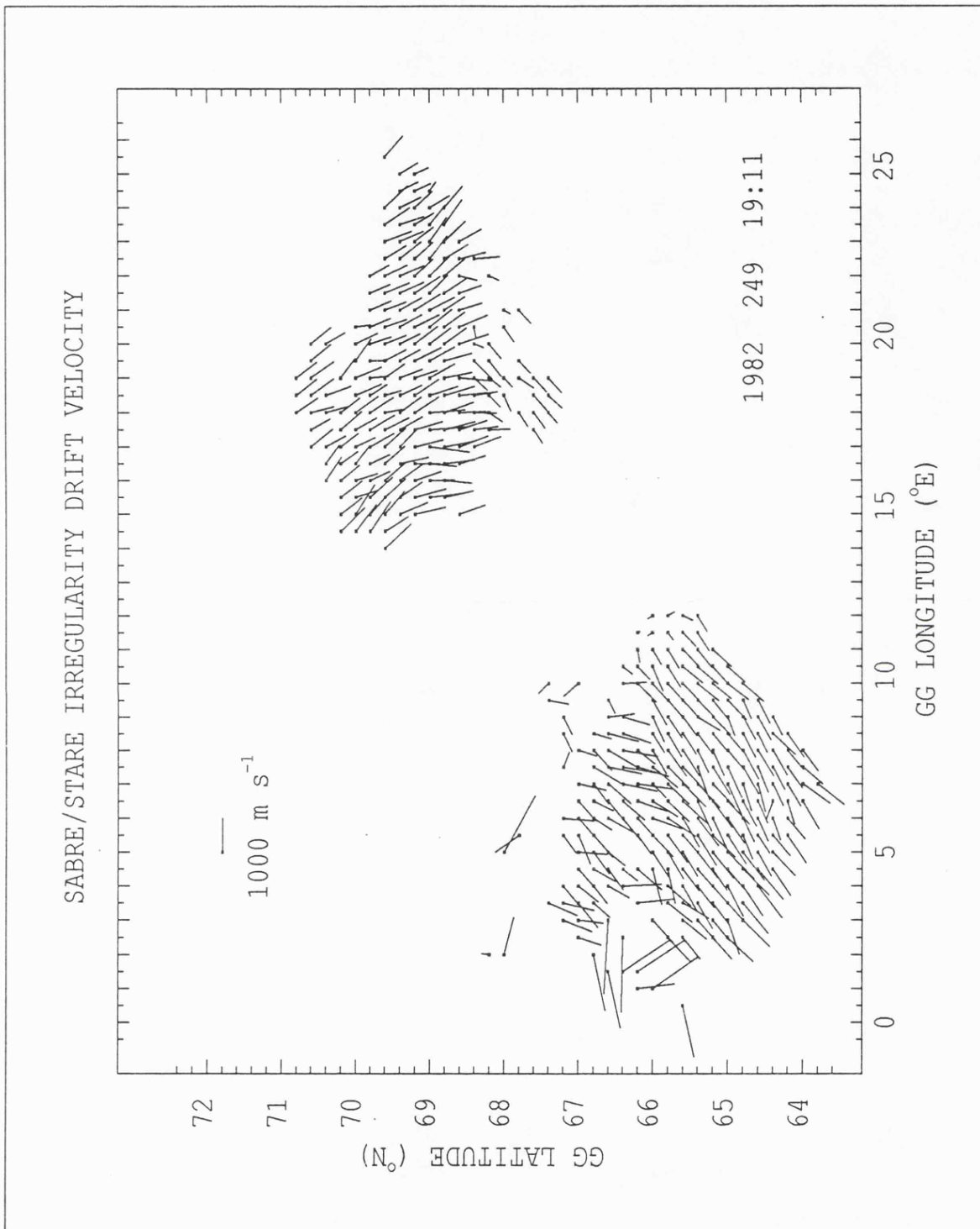


**FIGURE 5.9.** Simultaneous STARE and SABRE flow velocity observations made at 19:11 UT, 6 September, 1982 in the Harang discontinuity region. The velocities are given as a function of geographic latitude and longitude.

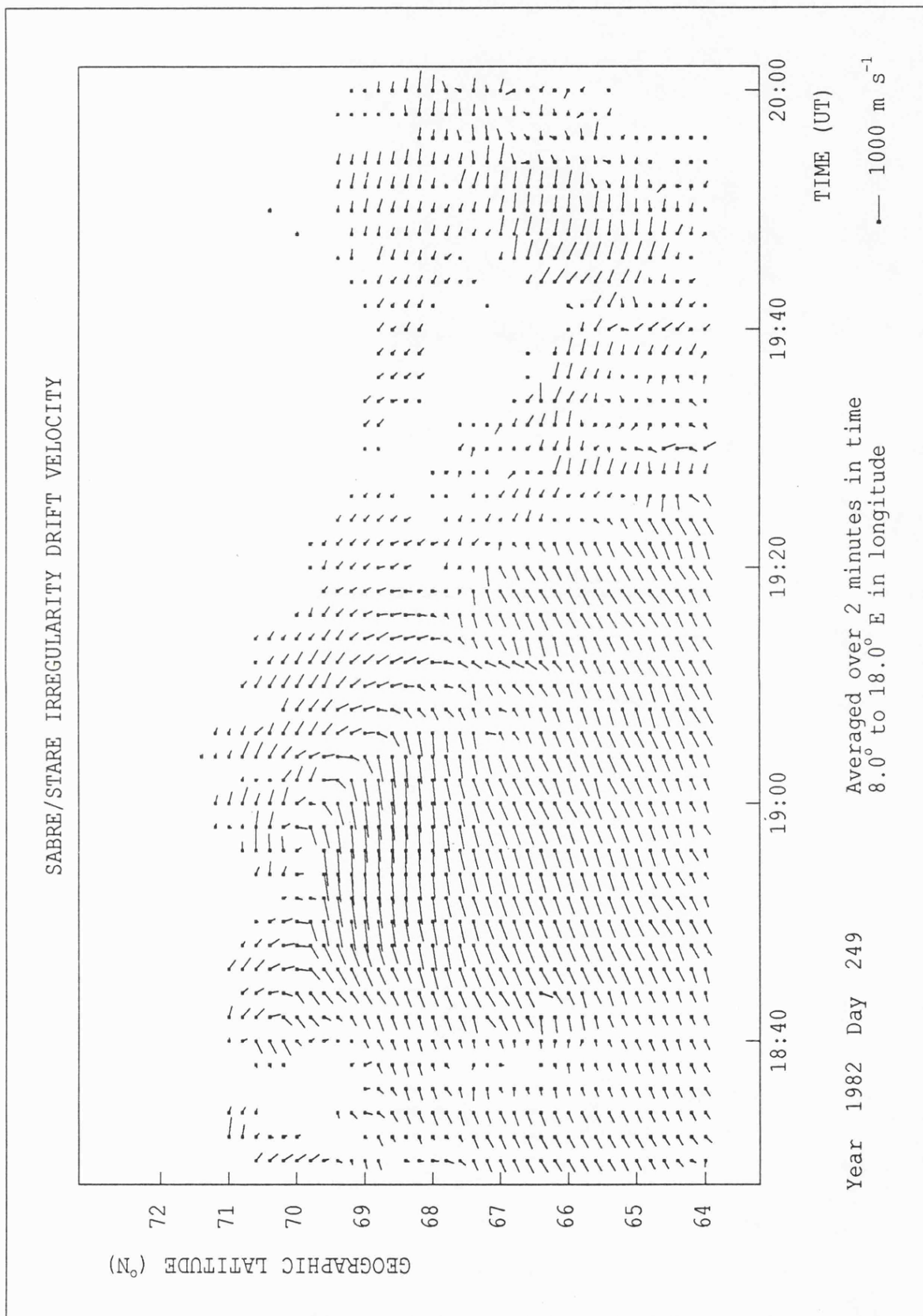


**FIGURE 5.10.** Combined SABRE and STARE flow velocity measurements for 18:30 - 20:00 UT, 6 September, 1982. The velocities are given as a function of geographic latitude and time, averaged over the longitude range 8°-18° E.

STARE and SABRE viewing areas (Nielsen and Greenwald, 1979; Zi and Nielsen, 1982). On 6 September, 1982, the reversal took place between 18:50 and 19:40 UT, over the latitude range  $64^{\circ}$  to  $72^{\circ}$  N, geographic. Despite the highly disturbed conditions, the gross features of the observed flows are in good agreement between the two systems, demonstrating that SABRE and STARE may be usefully combined to provide increased latitudinal coverage of the convection pattern.

In the SABRE statistical convection patterns presented in the previous section, the Harang discontinuity is a distinctive and well defined feature, although its relationship with the various geomagnetic and IMF parameters is not clear. In order to make a quantitative comparison with these parameters, it is necessary to employ a data set consisting of the occurrence times of the Harang discontinuity measured by SABRE in the centre of the viewing area ( $66^{\circ}$  N,  $6^{\circ}$  E, geographic). On a given day, it may be impossible to resolve the discontinuity if there is little backscatter in the appropriate local time sector, or if the nightside convection flows are so turbulent that they disrupt the 'normal' two cell pattern. An example of the latter case, in which it is very difficult to distinguish the Harang discontinuity in the pre-midnight convection pattern, is illustrated in Figure 5.11 as an RTV plot for 19:30 to 20:50 UT, 25 April, 1983. A flow reversal from west to east is observed between 19:50 and 20:00 UT, followed by a return to a westward direction at about 20:20. After 20:40 UT, the convection flow turns eastward again. There are considerable latitudinal variations and the flows are generally highly irregular. A further example of nightside convection flows observed by SABRE for which it is very difficult to distinguish the Harang discontinuity is presented in section 7.3.1.

### 5.3.2 Local time of the Harang discontinuity

In compiling the  $T_{HD}$  data set, the criterion has been that the flows in the

SABRE IRREGULARITY DRIFT VELOCITY

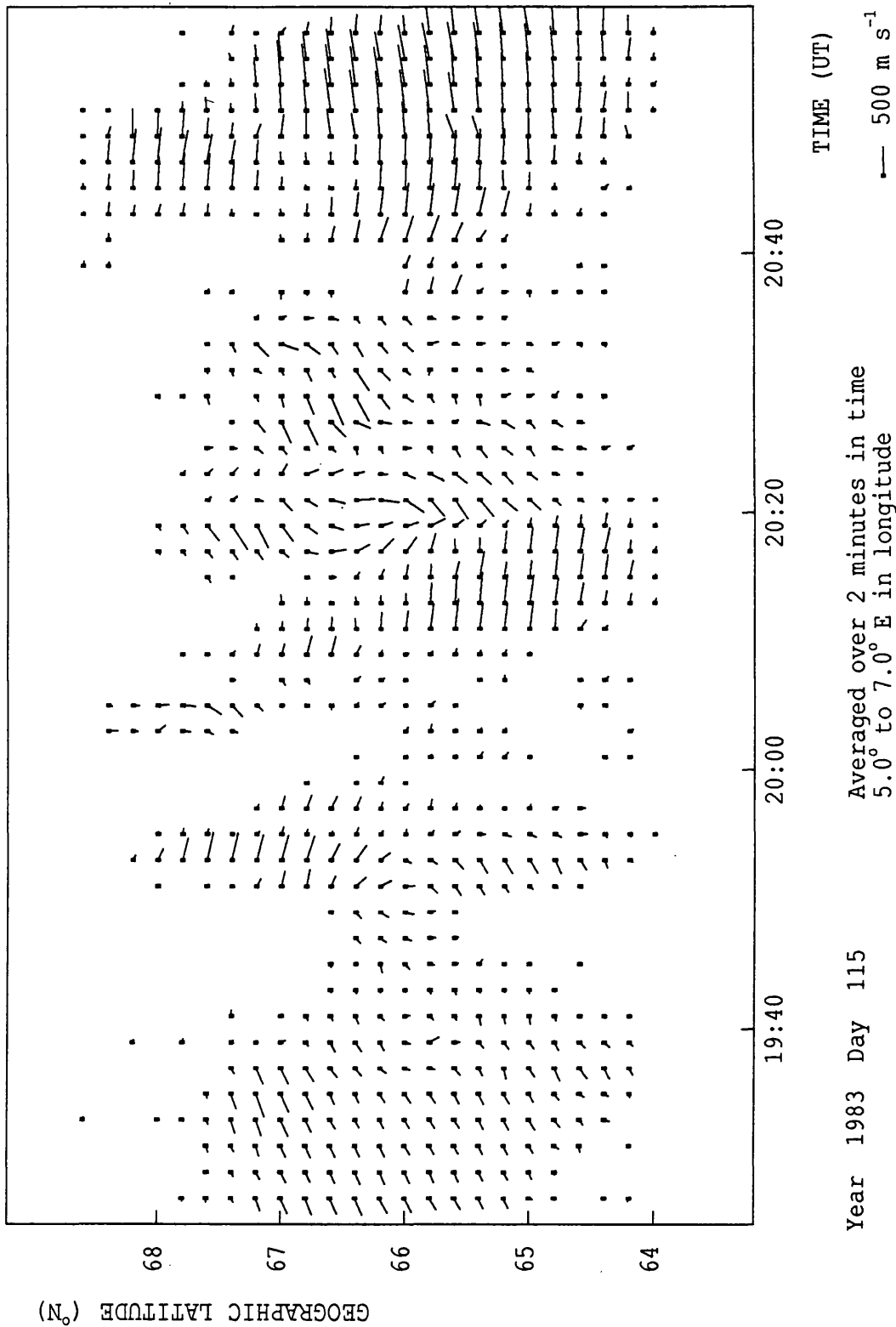


FIGURE 5.11. SABRE flow velocity measurements averaged over the geographic longitude range 5°-7° E for 19:30 - 20:50 UT, 25 April, 1983.

vicinity of the discontinuity should be reasonably well behaved, with only one reversal observed, and that the backscatter 'gap' associated with the discontinuity itself (usually a region of low electric fields) should be no wider than 60 minutes. Thus, the maximum permissible error in  $T_{HD}$  ( $\Delta T_{HD}$ ) is  $\pm 30$  minutes, a requirement which is very selective. As a result, despite a total of over 1000 days of bistatic SABRE operation, the  $T_{HD}$  data set consists of just 63 days. Nonetheless, this compares favourably with earlier STARE investigations of the Harang discontinuity by Scourfield and Nielsen (1981) and Zi and Nielsen (1982) who employed only 14 and 18 examples, respectively. The method of determining  $T_{HD}$  with SABRE consists of measuring the time at which there is a clear change in sign of the east-west velocity component averaged over a geographic latitude range  $65.5^\circ$  to  $66.5^\circ$  N and a longitude range  $5.0^\circ$  to  $7.0^\circ$  E, (ie. the centre of the viewing area).

Rodger et al. (1984) determined the local time of the Harang discontinuity from ground based magnetometer data. If the electrojets are considered as simple line currents, an enhanced eastward electrojet (westward convection flow) lying poleward of a northern hemisphere observatory causes the Z-component of the geomagnetic field to become more positive. After the Harang discontinuity crosses the meridian, a negative perturbation or bay is observed in the Z-component due to the westward electrojet (eastward flow). The time at which the discontinuity passes the observatory is when the Z-component is equally affected by the westward and eastward electrojets.

A magnetometer is susceptible to currents flowing over a wide range of latitudes and, as pointed out by Rodger et al., the technique assumes that the eastward and westward electrojets have equal, but opposite, effects on the Z-component of the geomagnetic field. By contrast, the SABRE method observes the flow reversal directly and can determine  $T_{HD}$  at a single latitude. If, however, the temporal location of the discontinuity exhibits

a latitudinal dependency, it is difficult to distinguish an azimuthal shift of the discontinuity from an expansion or contraction of the convection pattern. In contrast, a magnetometer measures the average temporal location over a large latitude range, provided the observatory remains well equatorward of the electrojet system. The two techniques have been compared by plotting  $T_{HD}$  as measured by SABRE against values of  $T_{HD}$  derived from the Z-component magnetogram of the Lerwick observatory ( $60.0^\circ$  N,  $1.2^\circ$  W, geographic), and they are found to be in excellent agreement (Figure 5.12). SABRE tends to measure lower UT values of  $T_{HD}$  (by ~30 minutes), which is consistent with the south-westward displacement of the Lerwick station from the centre of the SABRE viewing area.

$K_p$  and  $D_{st}$  indices have been obtained for all 63 SABRE  $T_{HD}$  values, but AE was available for only 39 days. In addition, hourly averages of the IMF were available for only 29 of the days. The comparison of  $T_{HD}$  and  $K_p$  indicates a trend for the discontinuity to move to earlier times with increasing  $K_p$  (Figure 5.13), but the scatter is considerable. Some discrepancy is to be expected since the Harang discontinuity is an auroral feature, whereas  $K_p$  is a subauroral index based on a 3 hour average, which may not be sufficiently well resolved for such a comparison. When  $T_{HD}$  is plotted against  $D_{st}$ , which is a 1 hour average, the scatter is even greater (Figure 5.14). However,  $D_{st}$  is an equatorial parameter which indicates the intensity of the ring current, and its response is known to lag behind auroral activity by several hours (e.g. Meng, 1983). The relationship between  $T_{HD}$  and the hourly average AE index is illustrated in Figure 5.15. The AE values are those for the hour closest to the corresponding values of  $T_{HD}$ . AE and  $T_{HD}$  are clearly well correlated, and the linear regression of the data (Figure 5.15) suggests the following empirical expression for the local time occurrence of the Harang discontinuity;

$$T_{HD}(LT) = (23.9 \pm 0.5) - (0.005 \pm 0.001)AE$$

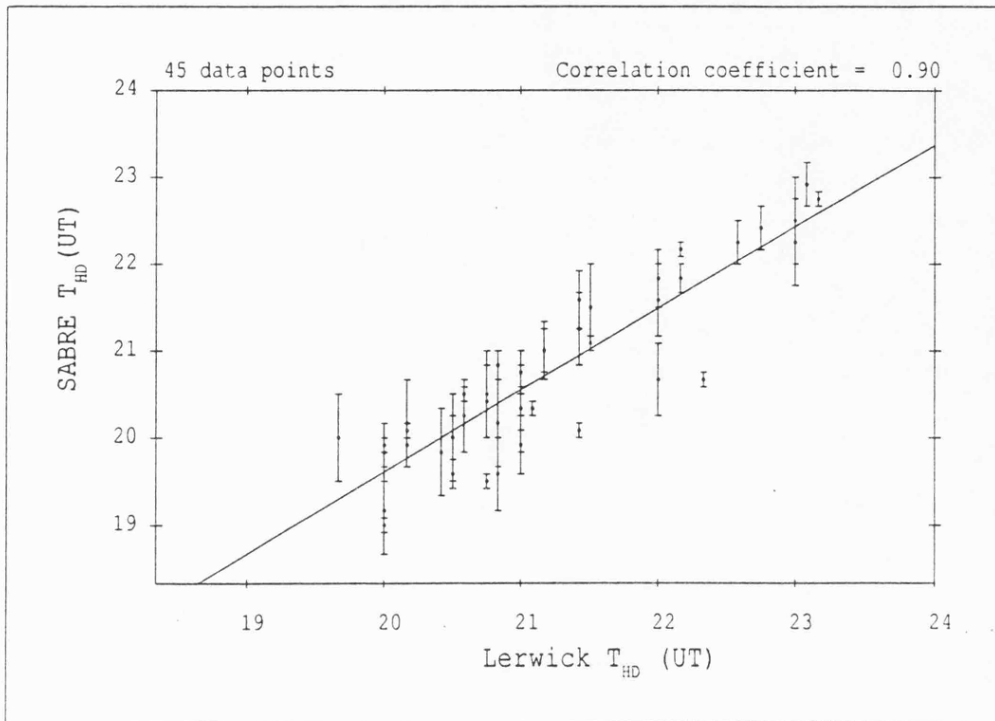


**FIGURE 5.12.** A comparison of the times of occurrence of the Harang discontinuity ( $T_{HD}$ ) as measured by SABRE and by the Lerwick magnetometer.

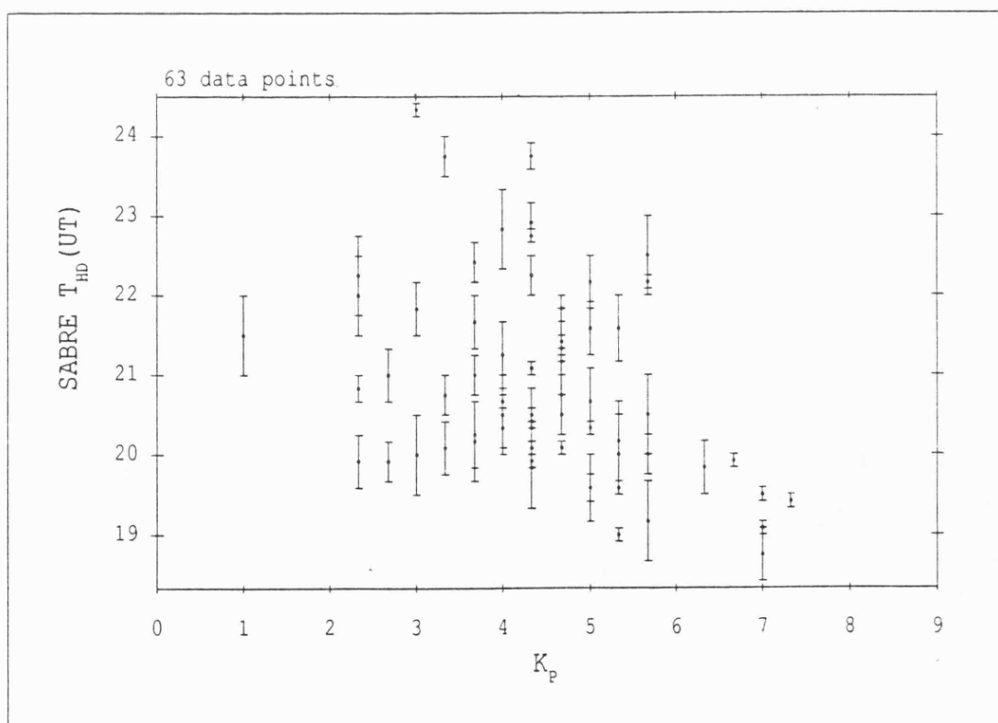


**FIGURE 5.13.**  $T_{HD}$  measured by SABRE as a function of the  $K_p$  index.

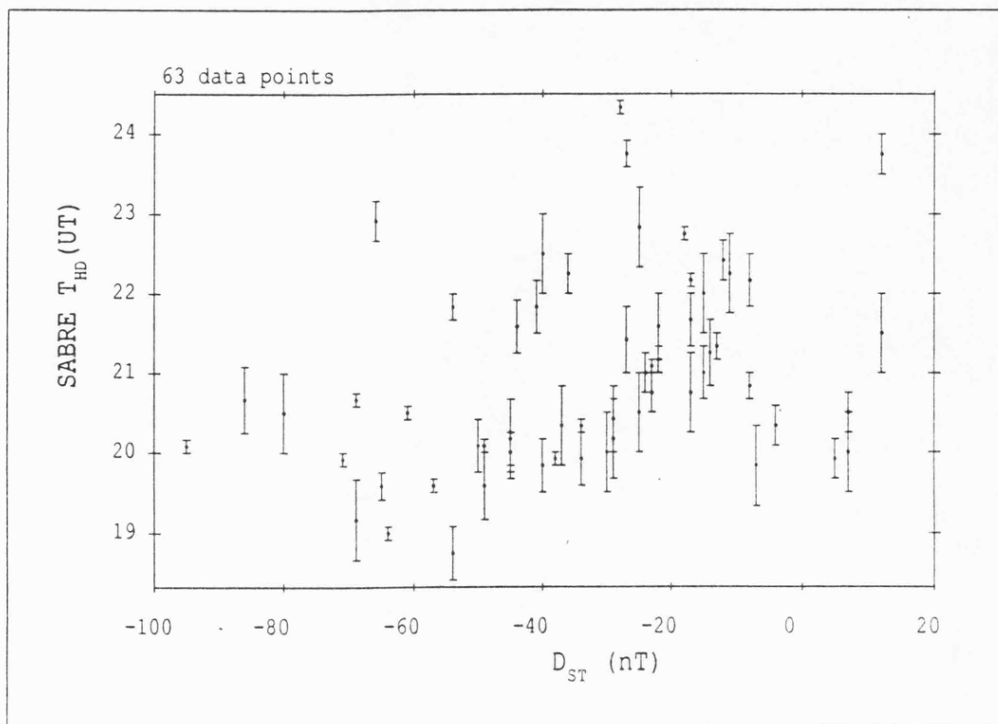


FIGURE 5.14.  $T_{HD}$  measured by SABRE as a function of the  $D_{ST}$  index.

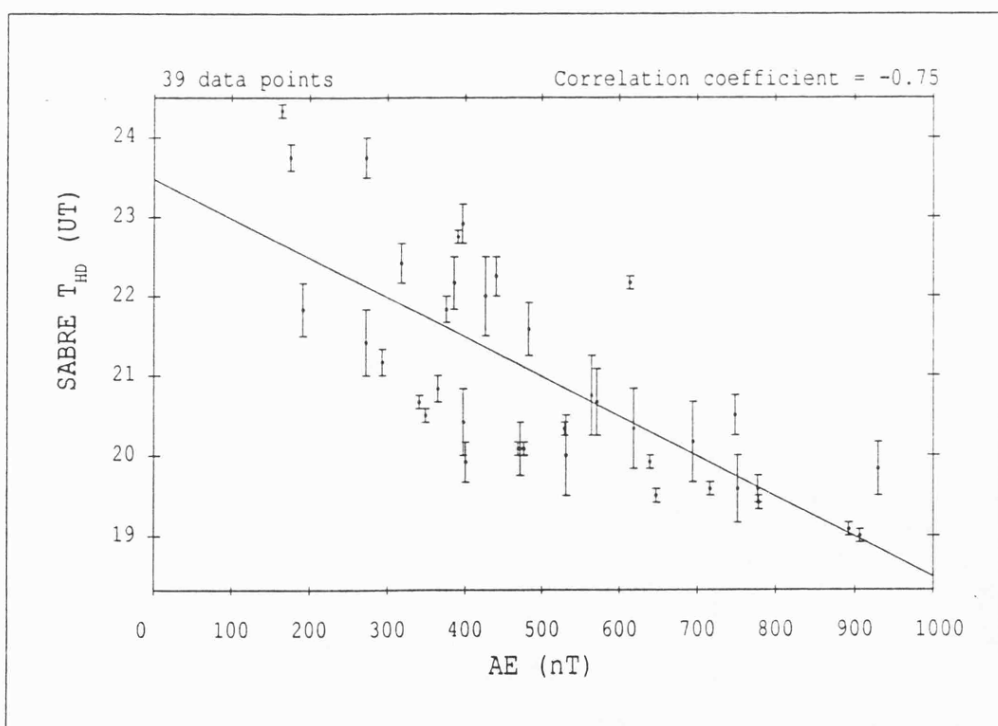


FIGURE 5.15. Same as for figure 5.14 but for the AE index.

where  $T_{HD}(LT)$  is in hours, AE in nT, and assuming that the difference between universal time and local time at the centre of the SABRE field of view is about 25 minutes. 3 hour average values of AE yield a similar relationship, although the scatter is somewhat larger.

The AE index is a measure of the electrojet enhancement, and the close relationship between AE and  $T_{HD}$  implies a strong dependence of the location of the nightside convection flow reversal on the level of substorm activity. Zi and Nielsen (1982) interpreted a similar trend as arising from a clockwise rotation of the entire large scale convection pattern with increasing activity. Since both SABRE and STARE indicate a later local time occurrence of the Harang discontinuity with decreasing latitude (e.g. Figure 5.10, and see section 5.4), the shift of the discontinuity to earlier local times with increasing activity is probably explained by an equatorward expansion of the convection pattern.

Figures 5.16, 5.17 and 5.18 are plots of  $T_{HD}$  against IMF  $B_x$ ,  $B_y$  and  $B_z$ , respectively. There is little correlation between  $T_{HD}$  and  $B_x$ , and more surprisingly, no obvious relationship with  $B_z$ . Like substorm activity,  $B_z$  is expected to affect the latitudinal extent of the convection pattern (section 2.4.1), and therefore increasingly negative  $B_z$  should move the discontinuity to earlier local times. The results reproduced in Figure 5.17 suggest that the discontinuity occurs earlier for positive  $B_y$  than for negative  $B_y$ , a result which is also evident in Figures 5.6 and 5.7. A linear regression yields a correlation coefficient of  $-0.54$ , with a probability that the observed variation is due to chance of  $\sim 0.2\%$  (obtained from tables in Bevington, 1969), and suggests the following relationship between  $T_{HD}(LT)$  and  $B_y$ ;

$$T_{HD}(LT) = -(0.13 \pm 0.4)B_y + (21.3 \pm 0.5)$$

This is very similar to the relationship obtained by Rodger et al. (1984)

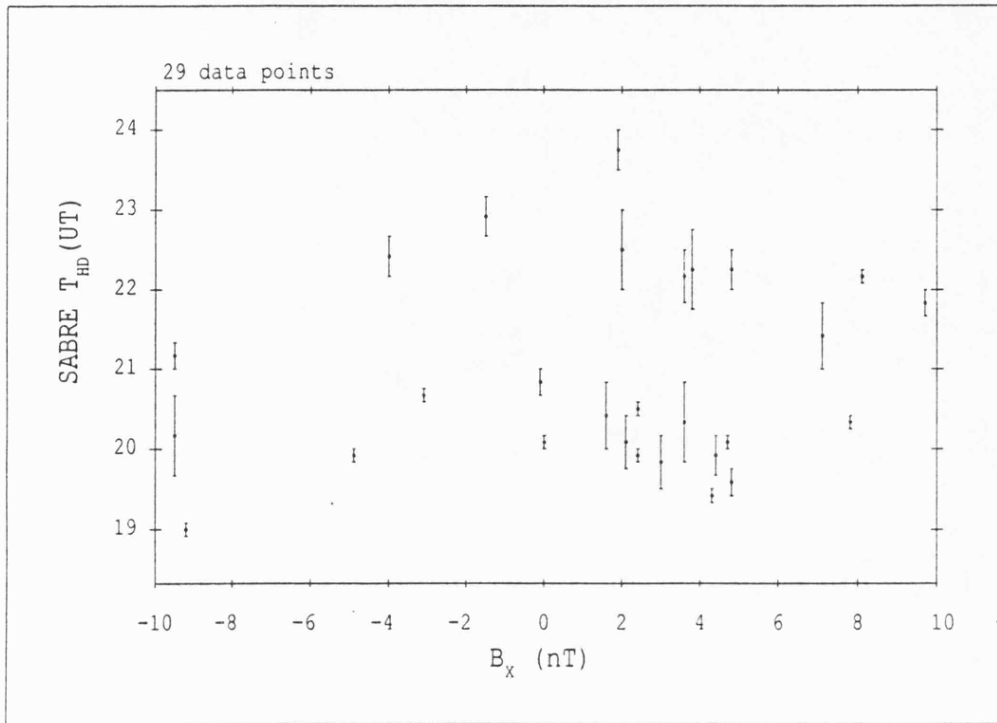


FIGURE 5.16.  $T_{HD}$  measured by SABRE as a function of IMF  $B_x$ .

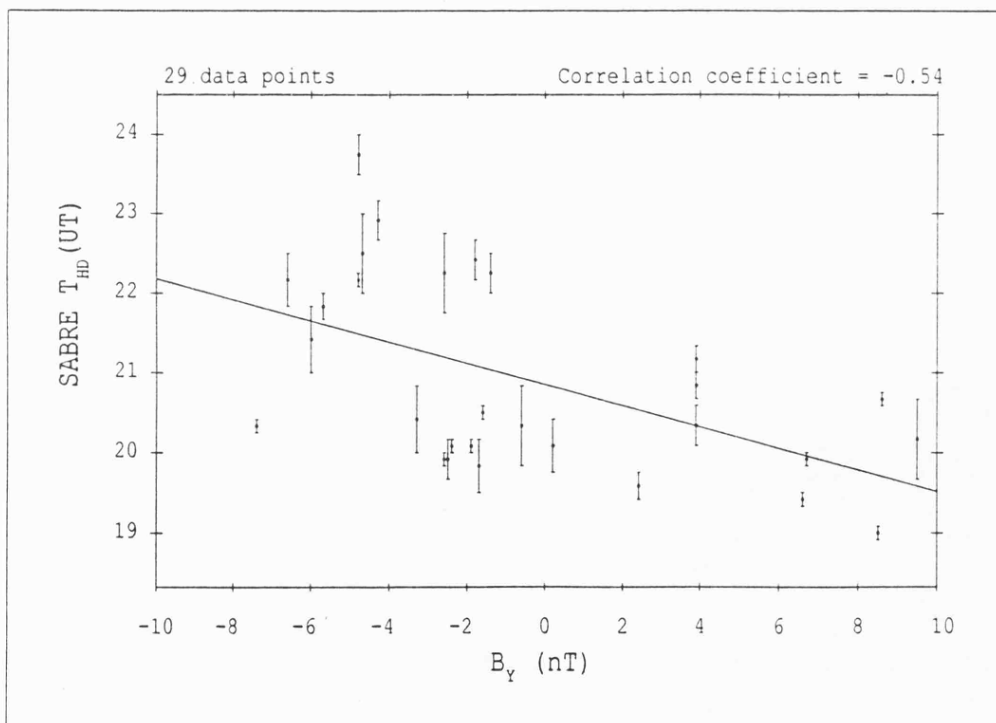


FIGURE 5.17.  $T_{HD}$  measured by SABRE as a function of IMF  $B_y$ .

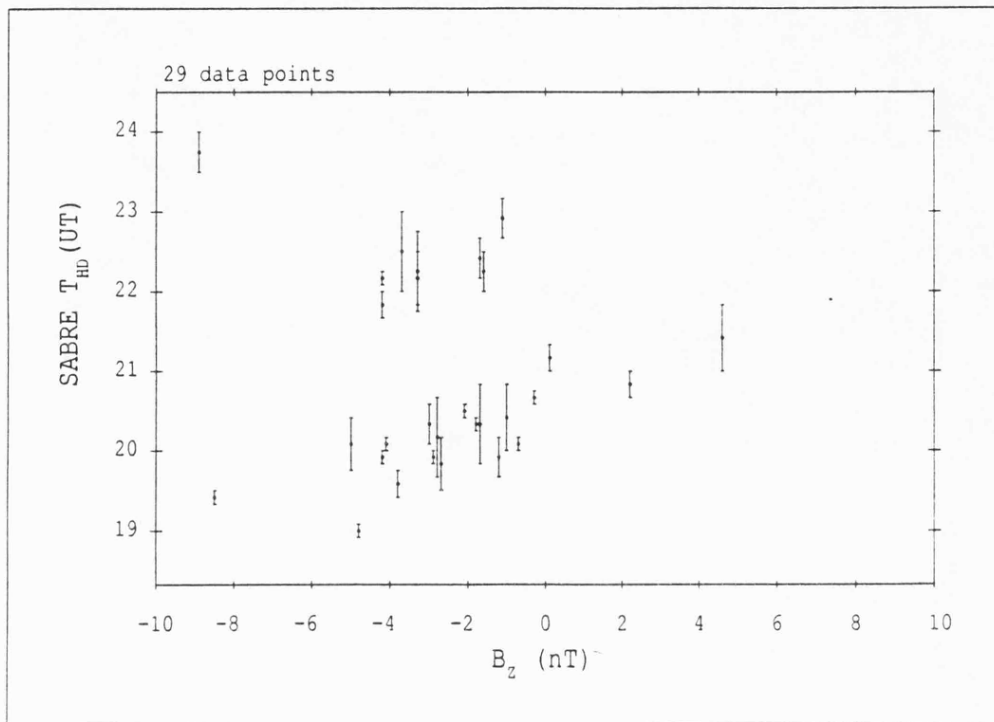


FIGURE 5.18.  $T_{HD}$  measured by SABRE as a function of IMF  $B_z$ .

from Lerwick magnetometer data, and implies an azimuthal displacement of the auroral electrojet current system, as observed in the centre of the SABRE field of view (geomagnetic latitude  $64^\circ$  N), of approximately  $2^\circ$  per nT of IMF  $B_y$ .

#### 5.4 Harang discontinuity and IMF $B_y$ - discussion

The focus of most studies of the  $B_y$  effect on high latitude convection flows has been on the noon local time sector (section 2.4.2). The present investigation indicates that  $B_y$  also effects the nightside. In particular, the Harang discontinuity moves to earlier local times for positive  $B_y$  and later times for negative  $B_y$ . This confirms the conclusion of Rodger et al. (1984), but is at variance with the STARE investigation of Scourfield and Nielsen (1981), which suggested that the discontinuity occurs earlier for negative  $B_y$ . However, the data sample of Scourfield and Nielsen was very small and, as pointed out by Rodger et al., the STARE comparison relied on IMF polarities inferred from ground based magnetograms, rather than on satellite data. Inferred IMF polarities can be erroneous, as discussed in the next chapter. Scourfield and Nielsen (1981) concluded that their results could be interpreted in terms of a simple azimuthal shift of the large scale convection pattern by IMF  $B_y$ . They stated that the shift of the two cell convection pattern toward dawnside for positive  $B_y$  would move the Harang discontinuity to later local times, without considering a change in the shape of the displaced pattern. According to Cowley (1981), who modelled the  $B_y$  effect by the addition of a uniform  $B_y$  field to a dipole field (Figure 5.19), the polar cap boundary shifts dawnward while the evening and morning discontinuities in the auroral zone move duskward to earlier and later local times, respectively, for positive  $B_y$ .

The influence of  $B_y$  on the statistical SABRE convection flows suggest that southward flows in the discontinuity region may be a temporally more

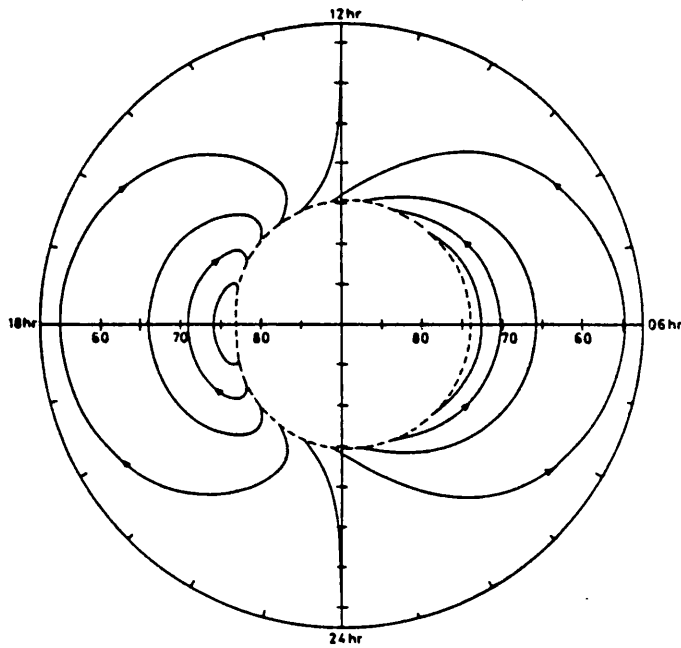


**FIGURE 5.19.** Cowley (1981) theoretical model for the high latitude convection pattern for  $B_y > 0$ , obtained by the addition of a uniform  $B_y$  field to the Earth's dipole field.

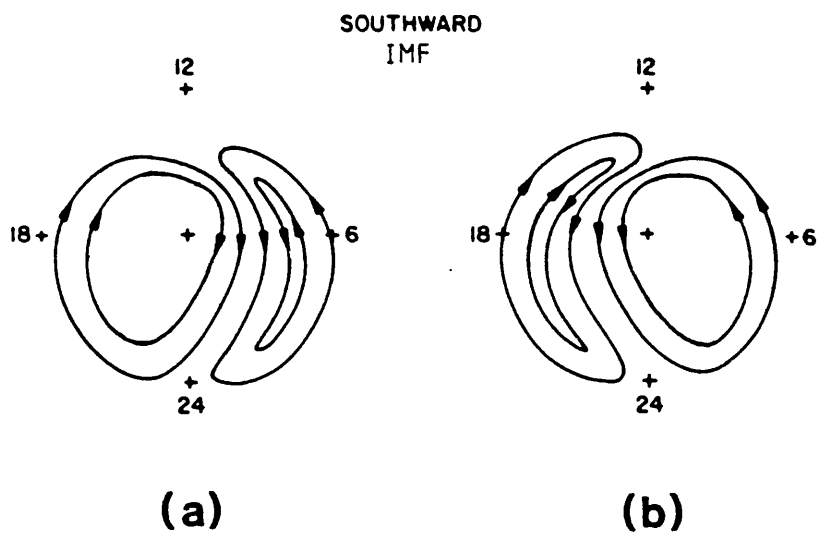


**FIGURE 5.20.** Burch et al. (1985) empirical model for the high latitude convection pattern for (a)  $B_y > 0$  and (b)  $B_y < 0$ .

persistent feature for negative  $B_y$  than for positive  $B_y$  (Figures 5.6 and 5.7, respectively). This implies that the gradient of the discontinuity (defined by its change in latitudinal location with local time) for negative  $B_y$  is different from that for positive  $B_y$ , although they are not 'mirror images'. When  $B_y > 0$ , the Harang discontinuity occurs earlier at higher latitudes. Cowley (1981) predicts that the opposite asymmetry should occur for  $B_y < 0$ , and cites the observational results of Heelis (1979) as evidence that the reversal can appear at later local times at higher latitudes. However, examination of SABRE observations of the Harang discontinuity for 63 days has revealed only one clear example (presented in section 7.2) where such an asymmetry occurs. In fact, the former asymmetry (earlier Harang discontinuity occurrence at higher latitudes) prevails in the absence of any  $B_y$  influence as a result of the corotation electric field, an effect predicted by Axford and Hines (1961) (section 2.2.1). Since the corotation electric field is always in the same direction, a net  $B_y$  component is likely to change the degree of this asymmetry but not the sense. If the SABRE field of view traverses a reversal which changes slowly in its latitudinal location with local time (shallow gradient), as expected for  $B_y > 0$ , the observed flows should be predominantly east-west aligned. For a steeper gradient, as predicted for  $B_y < 0$ , stronger southward components would be expected. This interpretation is consistent with the results of Figures 5.6 and 5.7.

The sense of the  $B_y$ -dependent Harang discontinuity asymmetry remains controversial. The empirical model of Burch et al. (1985) for  $B_y > 0$  (reproduced in simplified form in Figure 5.20a), for example, predicts an asymmetry of the opposite sense to that of Cowley's theoretical model (Figure 5.19) and the experimental results of this chapter. In addition, the present experimental results are in qualitative agreement with Cowley (1981), but in common with the experimental results of Rodger (1984), the magnitude of the observed azimuthal shift in the auroral flows is much

greater than predicted.

### 5.5 Summary

$K_p$  and IMF dependent empirical models of the auroral convection pattern have been developed from the large SABRE data base of convection flow velocities. The time of occurrence of the Harang discontinuity is usually difficult to locate precisely, but nonetheless SABRE data provide values of  $T_{HD}$  which are in close agreement with those determined from Lerwick magnetograms. The much closer dependence of  $T_{HD}$  on AE than on  $B_z$  suggests an indirect solar wind control, via substorm processes, of the latitudinal extent of the large scale convection pattern. However, the poor correlations between  $T_{HD}$  and  $B_z$  and  $B_x$  could result from the competing effects of  $B_z$  induced latitudinal expansions and contractions (section 2.4.1) and  $B_x$  controlled sunward-tailward shifts of the pattern (section 2.4.3).

Of the 3 IMF components,  $B_z$  determines whether flows are observed by SABRE (ie. the latitudinal extent of the large scale convection pattern), while  $B_y$  is found to exert a strong control on the convection flow morphology in the Harang discontinuity region. Statistically, SABRE very seldom observes polar cap flows, and thus the present results confirm the prediction of Cowley (1981) that IMF  $B_y$  associated asymmetries appear on closed (auroral zone) field lines, as well as on open field lines. The SABRE observations are in agreement with the sense of the asymmetry predicted by Cowley, but at variance with the results of Burch et al. (1985). The techniques applied above failed to discern any  $B_x$  effect on the observed SABRE flows, suggesting that  $B_x$  is the component of the IMF which has the least influence on the convection pattern in the SABRE latitude range.

## CHAPTER 6

### DAYSIDE CONVECTION FLOWS OBSERVED BY SABRE

#### 6.1 Introduction

Observations of the dayside ionospheric convection pattern, particularly in the vicinity of the morning flow reversal, which is the ionospheric footprint of the magnetospheric cusp, are of considerable interest since this is a region of direct coupling with the interplanetary medium. The topology of the geomagnetic field in this region permits the direct entry of magnetosheath particles into the inner magnetosphere and ionosphere. In the present study, the cusp zone is defined as the region where sunward (electrojet) dayside convection flows turn antisunward to flow across the polar cap. Studies of the convection flows in this zone indicate the evolution of newly opened flux tubes, which enable the merging process at the dayside magnetopause to be investigated.

Because of the displacement of the auroral oval towards the nightside, observations of cusp flows by the SABRE and STARE radars are extremely rare (section 3.2.5). Indeed, under quiet conditions the cusp is located at about  $76^\circ$  N geomagnetic (Burch, 1979), whereas the latitudinal coverages of SABRE and STARE are  $61.5^\circ$ – $66.5^\circ$  N and  $64^\circ$ – $69^\circ$  N geomagnetic, respectively. It is generally accepted that the polar cusp is shifted equatorward during times of southward IMF (see section 2.4.1), due to the increased rate of merging at the dayside magnetopause between the IMF and the geomagnetic field. During periods of strongly negative  $B_z$ , substorm activity increases, and thus the latitudinal location of the cusp depends on the level of geomagnetic disturbance (Kamide et al., 1976; Horwitz and Akasofu,

1977). However, some observations have suggested that cusp movements are caused solely by variations in substorm magnetospheric current systems, and that the apparent correlation with IMF  $B_z$  results merely from an increased probability of substorms for negative  $B_z$  (Eather et al., 1979). Irrespective of whether equatorward shifts of the cusp are driven directly by increasingly negative  $B_z$  or via a substorm mechanism, it is well established that strong flows enter the STARE and SABRE viewing areas in this local time sector (6:00–12:00 LT) only during very disturbed geomagnetic conditions. Scourfield and Nielsen (1981) found 14 examples of the morning reversal, of which 10 were well defined, during 800 days of STARE observations. In over 1000 days of two station SABRE operation, the morning discontinuity was observed on only 9 occasions, of which 5 were well defined.

Previous observations of the effect of  $B_y$  on dayside convection flows have been reviewed in section 2.4.2. For negative  $B_y$ , the cusp region DPY current flows in the same direction as the ambient westward electrojet (eastward convection flow). For positive  $B_y$ , the DPY current is directed east, which is expected to result in the appearance of westward convection flow poleward of the ambient eastward flow normally observed prior to the morning discontinuity (Friis-Christensen and Wilhelm, 1975; Heelis, 1984). The predicted cusp flow patterns are reproduced in Figure 2.11.

Most experimental studies of cusp flows have relied on the one dimensional profiles provided by satellites and incoherent scatter radars, with the exception of one observation by SABRE (Waldock et al., 1984) and one by STARE (Zi et al., 1987) of a positive  $B_y$  modulated flow pattern. The events presented in this chapter have provided the first opportunity to construct high resolution two dimensional maps representing the ionospheric projection of the dayside merging process for both positive and negative polarities of IMF  $B_y$ .

## 6.2 Synopsis of the Dayside Observations

The 9 days during which the appearance of the morning discontinuity was identified with SABRE are listed in Table 6.1, together with an estimate, accurate to within 5 minutes, of the time of the east to west flow reversal ( $T_{MR}$ ) measured in the middle of the viewing area at a geographic latitude of  $66^\circ$  N. Where the reversal is ill-defined or there is a loss of backscatter between the end of the eastward flows and the commencement of westward flows, a time interval indicating the uncertainty in the time of the reversal ( $\Delta T_{MR}$ ) is quoted. Also included in table 6.1 are the corresponding values of  $K_p$ ,  $D_{st}$ , and where available, the AE index. The generally very large values of these geomagnetic indices (for example, the mean  $K_p$  for the 9 events is 7) are indicative of the unusually active conditions required for SABRE to observe cusp associated convection flows.

Also presented in table 6.1 for each event is the inferred polarity of the IMF (given in Solar-Geophysical Data), based on magnetograms from Vostok, Antarctica. An IMF polarity denoted by A (away from the Sun) corresponds to a positive  $B_y$  component, while T (towards the Sun) indicates a negative  $B_y$  component. The abbreviations AT and TA indicate that the inferred polarity displayed a clear change during the 0-12 hour UT interval from an away to a toward and from a toward to an away sector, respectively. The inferred polarity is at best only a very rough guide to the true azimuthal orientation of the IMF, particularly if the latter is changing on a time scale of less than 6 hours. More direct measurements of the IMF are obviously highly desirable. Unfortunately, IMP-8 hourly mean data (GSM coordinates) were available for only two of the days listed in table 6.1. ISEE-3 satellite measurements (GSE coordinates) have been obtained for four of the days, and these will be presented with the SABRE observations in sections 6.3 and 6.4. Great care must be taken in utilising ISEE-3 data for these intervals since two of them occurred after the spacecraft was

YEAR	DAY	$T_{MR}$ (UT,hr)	$\Delta T_{MR}$ (mins)	$D_{st}$ (nT)	$K_p$	AE (nT)	Inf. IMF
1982	219	9:00	60	-137	7+	764	Def. T
1982	249	9:30	< 5	-236	8+	1036	Def. A
1982	355	8:50	40	-83	5-	204	Def. A
1983	36	8:10	5	-168	7+	650	A T
1983	38	8:40	40	-85	5+	268	Def. T
1983	61	8:20	< 5	-149	7	679	T A
1984	321	8:00	< 5	-133	7	-	A
1985	118	9:00	< 5	-99	7	-	T A
1986	255	7:30	30	-166	7+	-	-

TABLE 6.1. Morning discontinuity occurrence times ( $T_{MR}$ ) with uncertainties ( $\Delta T_{MR}$ ) measured by SABRE together with corresponding values of geomagnetic indices and inferred IMF polarity [T - towards the Sun, A - away, Def. - definitely].

moved from its upstream solar wind position into a new orbit which periodically intersected the magnetosphere (section 3.3). Consequently, it is necessary to establish that the ISEE-3 data is characteristic of solar wind plasma before attempting to compare it with the SABRE observations.

There is tentative observational evidence for a  $B_y$  dependent local time shift about noon of the location of the dayside cleft (Cowley, 1981, and references therein) so that the morning convection flow reversal should appear later (earlier) for positive (negative)  $B_y$ . In table 6.1, the values of  $T_{MR}$  range from 7:30-9:30 UT (8:00-10:00 LT), with no obvious dependence on the inferred IMF polarity. In contrast to the investigation of the Harang discontinuity presented in the previous chapter, the present data sample is much too small and the IMF information of insufficient quality to establish any kind of statistical relationship. In addition, as pointed out by Scourfield and Nielsen (1981), the time of the reversal should also be a function of the level of substorm activity, which is affected by  $B_z$  and indicated by the geomagnetic indices (particularly AE), and which strongly influences the latitudinal extent of the convection pattern (section 2.4.1). If the local time position of the discontinuity has a latitudinal dependence, then the reversal should appear at different times as geomagnetic activity varies. Thus,  $T_{MR}$  is likely to be a complex function of both  $B_y$  and  $B_z$ . It may also involve the  $B_x$  component, which is expected to produce shifts in the convection pattern in the noon-midnight direction (section 2.4.3).

A statistical investigation with SABRE of the geomagnetic and IMF dependence of  $T_{MR}$  is further hindered by the fact that data points could only be obtained for a range of geomagnetic parameters associated with very disturbed conditions and thus limited to very high values. The values of  $T_{MR}$  in table 6.1 suggest that, for such conditions, the reversal occurs some 2-4 hours before local noon. The six best defined SABRE events, for which, with one exception, the cusp region reached the lower latitudinal

boundary of the viewing area, have been selected for a more detailed examination. For this purpose, they are divided into two categories, one for days when the inferred IMF polarity is away from the Sun, indicating positive  $B_y$  (section 6.3), and the other for days when the inferred polarity is towards the Sun, indicating negative  $B_y$  (section 6.4). For two of the events, the latitudinal range has been increased by combining SABRE measurements with those of STARE, to provide simultaneous coverage of the convection flow pattern over  $8^\circ$  of geographic latitude. This technique was described in the previous chapter.

### 6.3 Observations for inferred $B_y > 0$

#### 6.3.1 6 September, 1982

Geomagnetic conditions on this day were the most highly disturbed of all the events presented in this chapter. At 12:00 UT,  $D_{st}$  attained the exceptional value of  $-303$  nT, while the mean value of AE for 0:00–12:00 UT was nearly 1100 nT. An RTV for the interval 7:45 to 10:15 UT, 6 September (day 249), 1982, with a 3 minute integration time, is presented in Figure 6.1. The essential feature of the pattern observed by SABRE is the rotation at 9:30 UT of the eastward flows associated with the westward electrojet, through north, to westward flows associated with the eastward electrojet.

Prior to the reversal, between about 8:30 and 9:25 UT, the eastward flow is interrupted by a region of 'anomalous' westward flow poleward of about  $66^\circ$  N geographic latitude. There are also westward flows at the extreme poleward edge of the viewing area from 8:10 to 8:30 UT. The westward flow incursion is terminated by a region of north-east directed flow associated with the main east-west flow reversal which occupies the entire latitudinal extent of the viewing area. The temporal location of the eastern boundary or trailing edge of the wedge of westward flow exhibits a latitudinal

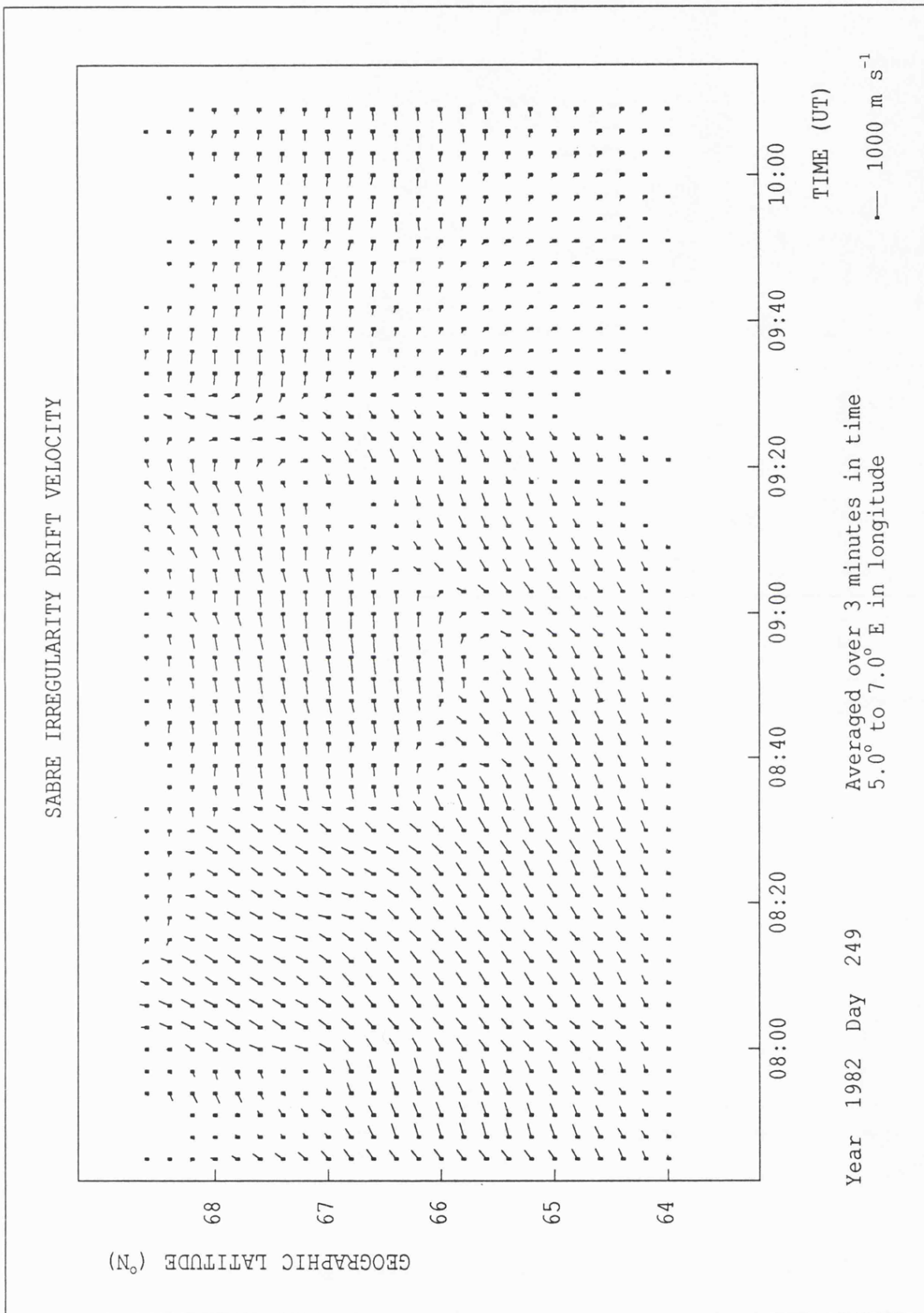


FIGURE 6.1. SABRE Range Time Velocity (RTV) plot for the interval 7:45 to 10:15 UT, 6 September (day 249), 1982.

variation. The boundary is observed at 9:05 UT for a latitude of  $66^\circ$  N, geographic, but not until 9:25 UT for a latitude of  $68^\circ$  N.

Waldock et al. (1984) presented this event (6 September, 1982) as a classic example of a positive  $B_y$  modulated cusp pattern, although these authors did not support their suggestion with satellite IMF data. The ISEE-3 measurements now available and reproduced in Figure 6.2 for the period 0:00 to 12:00 UT, 6 September, 1982 do, however, confirm this interpretation. At this time, the spacecraft was located upstream of the Earth at approximately  $X = 197$ ,  $Y = -85$ ,  $Z = 1 R_E$ . Except for a large but brief enhancement shortly before 9:00 UT, the average solar wind flow velocity  $V$  between 7:00 and 9:30 UT was  $600 \text{ km s}^{-1}$ . Assuming that the solar wind remains uniform from the location of ISEE-3 to the Earth, the time delay  $\tau$  for changes measured by the satellite to reach the Earth is approximately given by

$$\tau = X/V$$

and corresponds to  $\sim 35$  minutes. Taking account of this delay, the ISEE-3 magnetometer data indicate that in the vicinity of the Earth, from 5:00 until 10:00 UT,  $B_x$  and  $B_z$  were predominantly negative and  $B_y$  was almost exclusively positive, with an average value in excess of  $+10 \text{ nT}$ .

### 6.3.2 16 November, 1984

A further example of a morning sector flow pattern consistent with the DPY current system for positive  $B_y$  was observed by SABRE on 16, November (day 321), 1984. This is illustrated in Figure 6.3 by an RTV plot, again with a 3 minute integration time, for the interval from 6:30 to 9:00 UT. The peak  $D_{st}$  depression, attained at 9.00 UT, was  $-133 \text{ nT}$ , so that again the geomagnetic conditions were very highly disturbed. The gross features of the pattern are very similar to those of the previous example and again the

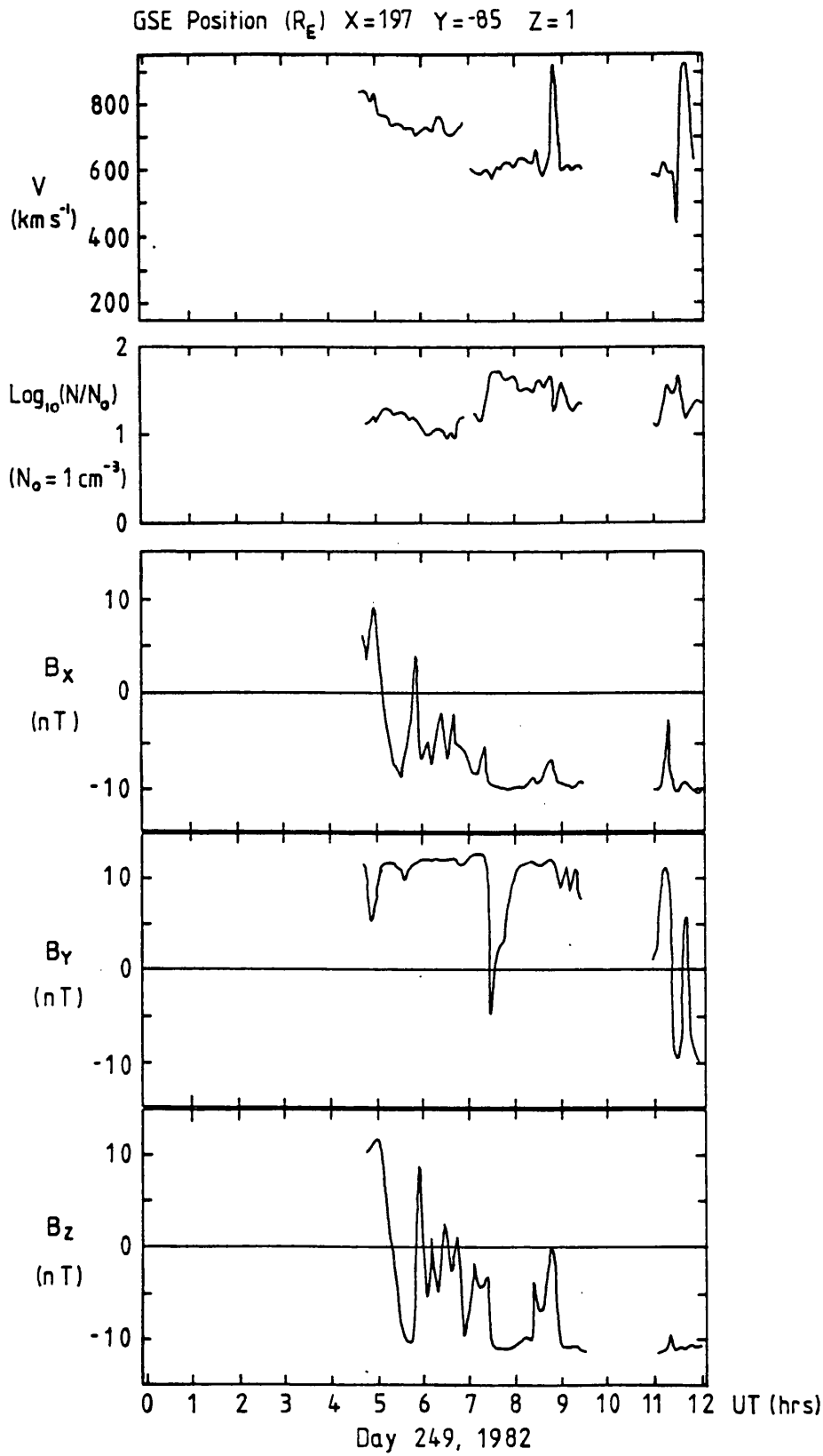


**FIGURE 6.2.** ISEE-3 measurements of the solar wind flow speed and density and the  $B_x$ ,  $B_y$  and  $B_z$  components of the IMF for the period 0:00 to 12:00 UT, 6 September, 1982.

SABRE IRREGULARITY DRIFT VELOCITY

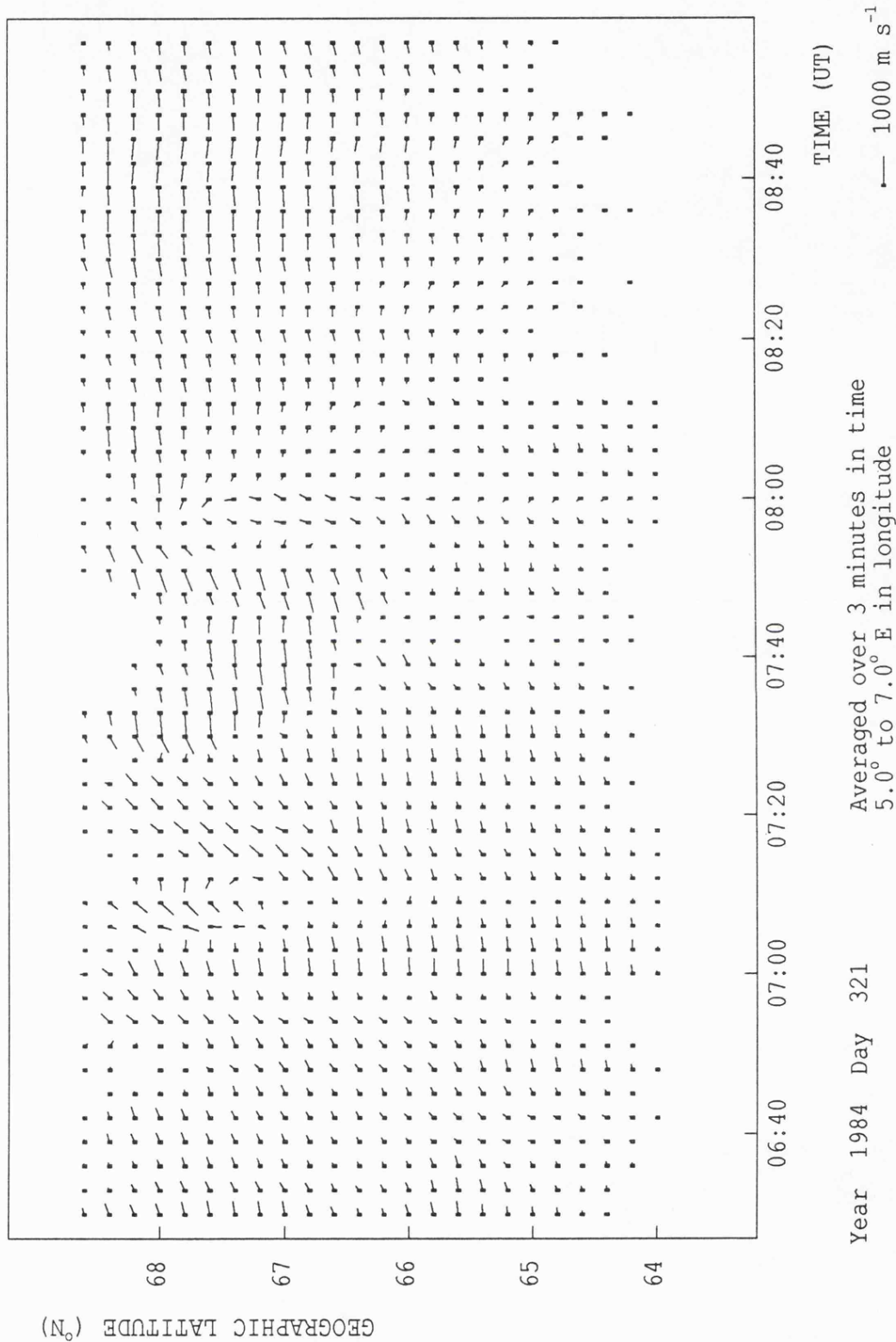


FIGURE 6.3. SABRE RTV plot for the interval from 6:30 to 9:00 UT, 16 November (day 321), 1984.

inferred  $B_y$  polarity was positive. Initially, the convection flow direction is predominantly eastward over the whole latitude range. The principal east-west flow reversal occurs in the middle of the viewing area ( $66^\circ$  N geographic latitude) at about 8:00 UT., and thereafter the flow direction is generally westward.

A westward flow incursion, penetrating from the poleward edge of the field of view to approximately  $66^\circ$  N geographic latitude, appears from about 7:30 until 7:50 UT. In contrast to the previous example, it is the location of the leading (western) edge rather than the trailing (eastern) edge of the westward flow incursion which displays a latitudinal variation. The western boundary occurs at 7:30 UT for  $68^\circ$  N, geographic and at about 7:45 UT for  $66^\circ$  N. In addition, there is a brief interval of westward flow from 7:05 to 7:10 poleward of  $67^\circ$  N.

### 6.3.3 2 March, 1983

The final example of a cusp flow observation which exhibits a positive  $B_y$  modulation effect occurred on 2 March (day 61), 1983. The peak depression of  $D_{st}$  of  $-154$  nT, which occurred at 9:00 UT, and the value of AE at the time of the east-west flow reversal which was  $679$  nT, are once again indicative of the extremely disturbed geomagnetic conditions required to shift the convection flows associated with the cusp into the latitudes viewed by SABRE.

In this case, STARE data extends the latitudinal coverage of the pattern by combining these with the SABRE measurements for the interval from 5:00 to 11:00 UT and averaging over  $8^\circ$  to  $18^\circ$  E geographic longitude, with an integration time of 6 minutes (Figure 6.4). The principal east-west convection flow reversal occurs over most of the joint SABRE/STARE latitude range at about 8:30 UT. Prior to this, the westward flow incursion is particularly prominent, penetrating almost to the equatorward edge of the SABRE field of view. The weak and intermittent flows measured by SABRE

SABRE/STARE IRREGULARITY DRIFT VELOCITY

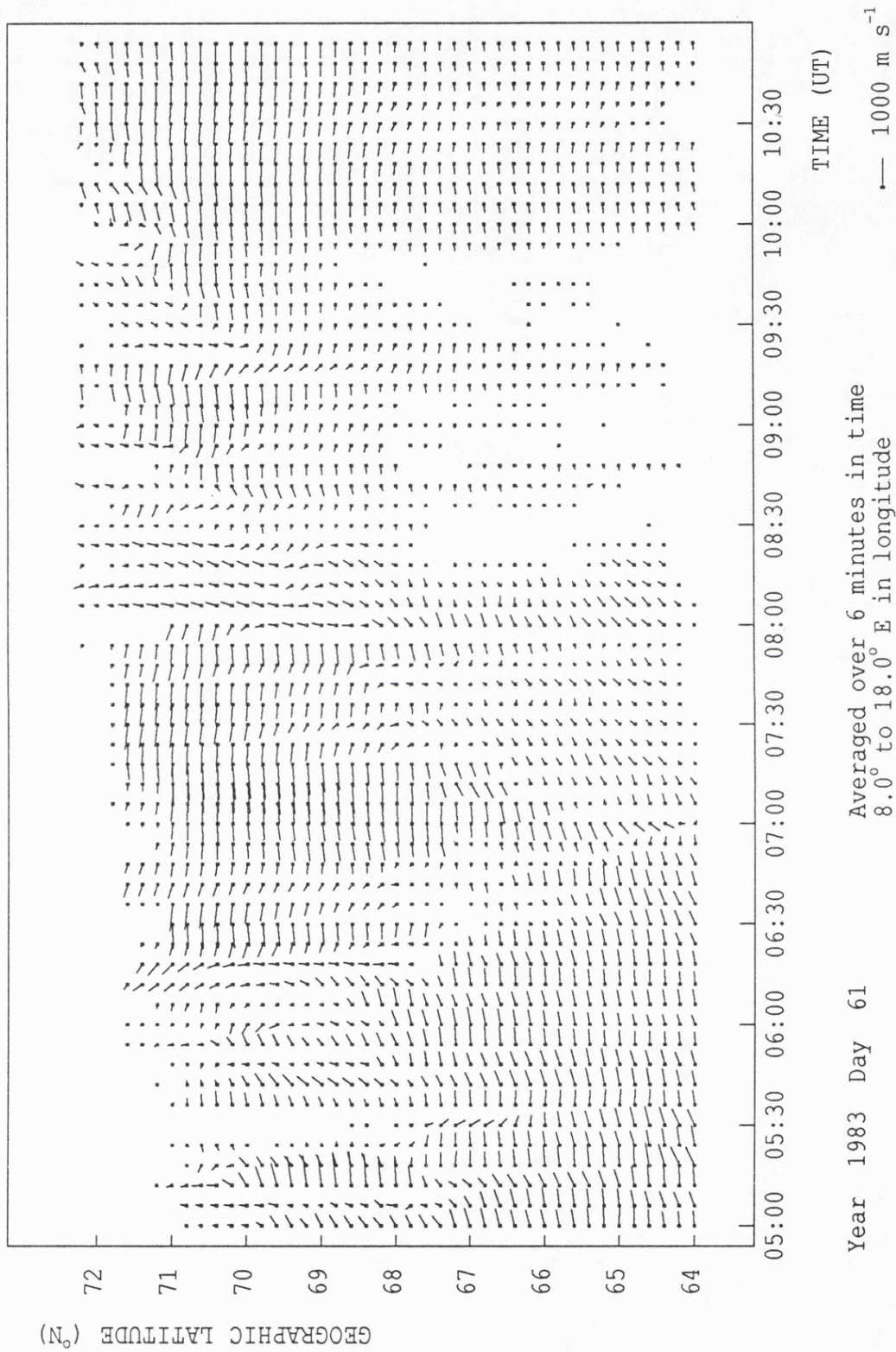
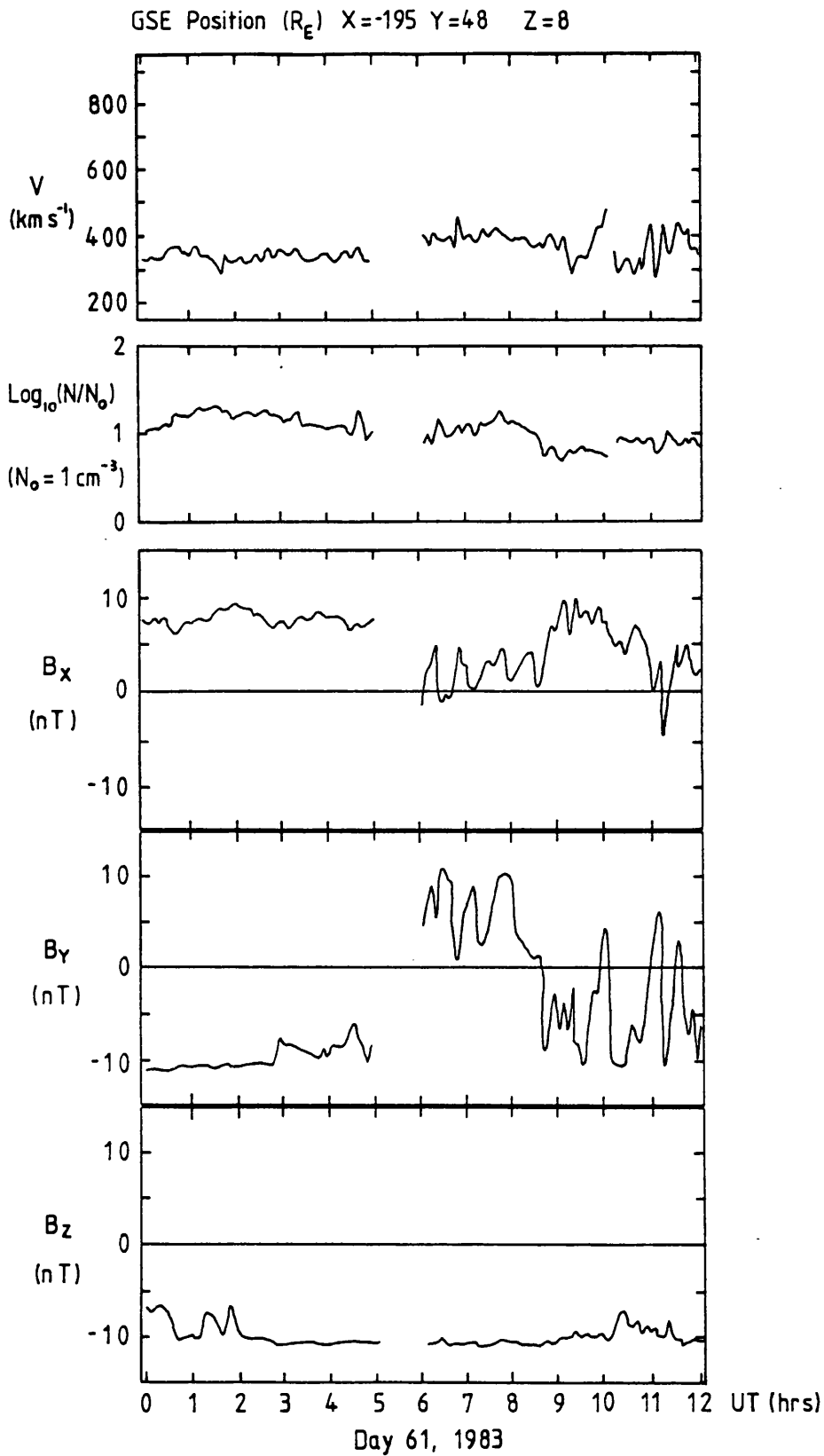


FIGURE 6.4. SABRE/STARE data RTV plot for the interval from 5:00 to 11:00 UT, 2 March (day 61), 1983.

between 8:00 and 10:00 UT are probably indicative of the low electric fields normally associated with the equatorward edge of the cusp region. Intermittent flows are observed by STARE from 5:00 to 6:30 UT, at which time the SABRE flows are strong and continuous, suggesting that during this interval the convection pattern had expanded to bring the STARE field of view into a region of weak polar cap electric fields. Moving south, the temporal extent of the westward incursion decreases, from a duration of nearly 100 minutes (6:20 - 8:00 UT) at a latitude of  $71.6^\circ$  N geographic, to only about 5 minutes at  $64.4^\circ$ . The changes in temporal locations with latitude of the western and eastern boundaries of the incursion are approximately equal (but of opposite sign). This was not the case for the previous two examples of positive  $B_y$  modulated cusp flows (sections 6.3.1 and 6.3.2). In addition to the 'wedge' of westward flow, there is also a brief interval of westward flow at 7:55 UT over the entire latitude range of Figure 6.4.

The cusp convection flow signature of a positive  $B_y$  condition is unmistakable, which is consistent with the recorded IMF polarity which turned away from the Sun in the second half of the 6:00 to 12:00 UT interval. The change of  $B_y$  from negative to positive during the morning sector is confirmed by ISEE-3 data. On 2 March, 1983 ISEE-3 was located at  $X = -195$ ,  $Y = 48$ ,  $Z = -8 R_E$  and the measurements for the interval from 0:00 to 12:00 UT are illustrated in Figure 6.5. These reveal that  $B_z$  was on average about  $-10$  nT and that the mean solar wind flow speed was about  $400 \text{ km s}^{-1}$ . The latter implies an  $\sim -50$  minute time delay between SABRE and ISEE-3 measurements (the minus sign denotes that the satellite is downstream). Until the 1 hour data gap commencing at 5:00 UT,  $B_x$  was in the  $+7$  to  $+9$  nT range, while  $B_y$  was  $< -7$  nT. After the data gap and until approximately 8:40 UT,  $B_x$  fluctuated between  $-1$  and  $+5$  nT, while  $B_y$  varied over the range from  $+2$  to  $> +10$  nT. After 8:40 UT,  $B_x$  was mainly positive and  $B_y$  predominantly negative. Thus  $B_y$  was strongly positive for the



**FIGURE 6.5.** ISEE-3 measurements of the solar wind flow speed and density and the  $B_x$ ,  $B_y$  and  $B_z$  components of the IMF for the interval from 0:00 to 12:00 UT, 2 March, 1983.

duration of the westward flow incursion observed by SABRE and STARE (Figure 6.4).

#### 6.3.4 28 April, 1985

Observations of the dayside flow pattern on 28 April (day 118), 1985, occurred when the inferred IMF polarity for the morning sector indicated that  $B_y$  was at first negative but then turned positive.  $D_{st}$  attained a value of  $-99$  nT at 11:00 UT, again indicative of highly active conditions although it is a somewhat lower value than for the other events. SABRE measurements of the flows are presented as an RTV plot with 3 minute integration in Figure 6.6, for the interval 7:45 to 10:15 UT. This demonstrates that the flow reversed from an eastward to a westward direction in the middle of the latitude range, with the reversal slanted in local time in the sense that the westward flow developed from the south as the eastward flow retreated poleward. There is no evidence of a westward flow incursion from the poleward edge of the viewing area. In the region of the flow discontinuity, the magnitudes of the eastward flows in the northern portion of the viewing area were evidently much larger than the magnitudes of the westward flows occupying the southern part of the area. In addition, the sequence of spatial plots in Figure 6.7 illustrates a rotation of some of the westward flow to a north-east direction, suggesting that SABRE was viewing antisunward flows in the 'throat' between the convection cells.

In summary, the gross features of the cusp flow pattern observed on 28 April, 1985 are very different from those of the previous three examples. An explanation for this is proposed in section 6.5.

SABRE IRREGULARITY DRIFT VELOCITY

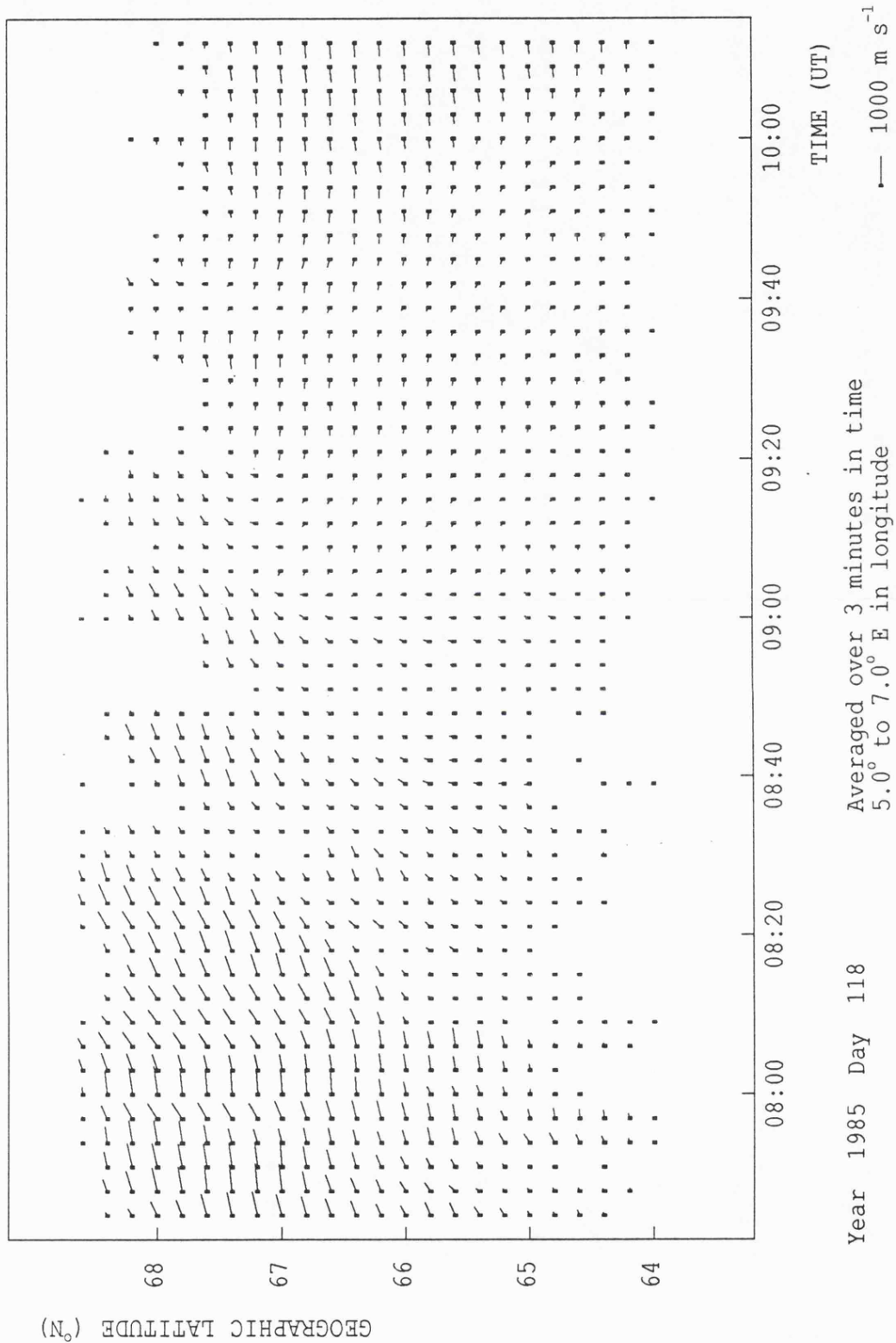


FIGURE 6.6. SABRE RTV plot for the interval 7:45 to 10:15 UT, 28 April (day 118), 1985.

SABRE IRREGULARITY DRIFT VELOCITIES

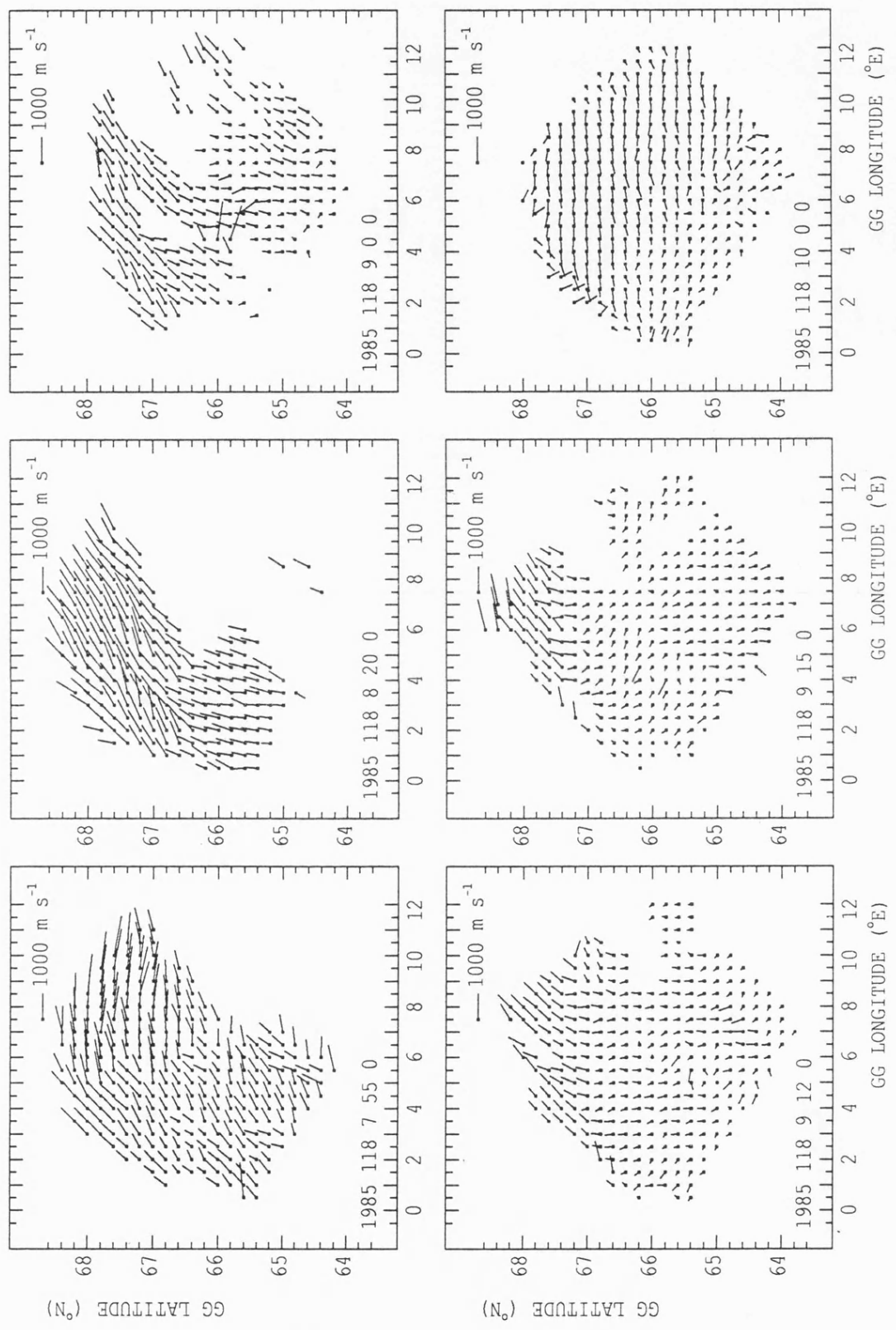


FIGURE 6.7. Sequence of SABRE spatial plots for the morning of 28 April, 1985.

## 6.4 Observations for inferred $B_y < 0$

### 6.4.1 5 February, 1983

Cusp flows observed on 5 February (day 36), 1983, and illustrated in Figure 6.8, are less complex than the positive  $B_y$  signatures described in sections 6.3.1-6.3.3. The flow reversal occurs at about 8:10 UT with no obvious latitudinal dependence, and the time interval from 7:30 to 8:30 UT (in the vicinity of the discontinuity) is characterised by weak flows. The absence of any pre-reversal westward flow incursion is consistent with the inferred  $B_y$  polarity which was negative for the 6:00 to 12:00 UT sector. Meng (1983) finds that the lowest cusp latitude precedes the maximum depression in  $D_{st}$  by between 3 and 7 hours. On 5 February, 1983, the value of  $D_{st}$  attained a peak depression of -169 nT at 11:00 UT, which would suggest that the flow reversal was observed in the SABRE viewing area at a time (approximately 8:20 UT) when the cusp may have reached its lowest latitude. The hourly values of AE in the morning sector were in the range 650-900 nT.

Again, the ground based observations are supported by ISEE-3 satellite measurements. However, this event occurred when the spacecraft was located at approximately  $X = -220$ ,  $Y = 16$ ,  $Z = -13 R_E$ , ie. close to the magnetopause of the far tail. Considerable caution must therefore be exercised in attempting to infer the orientation of the IMF. The plasma and IMF parameters for the period 0:00 to 12:00 UT, 5 February, 1983 are reproduced in Figure 6.9. Until about 3:40 UT, the flow velocity was in the range  $700-900 \text{ km s}^{-1}$ , which is indicative of very high speed solar wind plasma. For several brief intervals thereafter, the velocity dropped sharply by almost  $500 \text{ km s}^{-1}$  and then recovered equally suddenly. This suggests that ISEE-3 repeatedly crossed the magnetopause, sampling successively tail lobe and solar wind plasma. The IMF orientation in the vicinity of the Earth can, therefore, be deduced from ISEE-3 when the flow speeds are very high. Allowance is made for a time delay of -30 minutes,

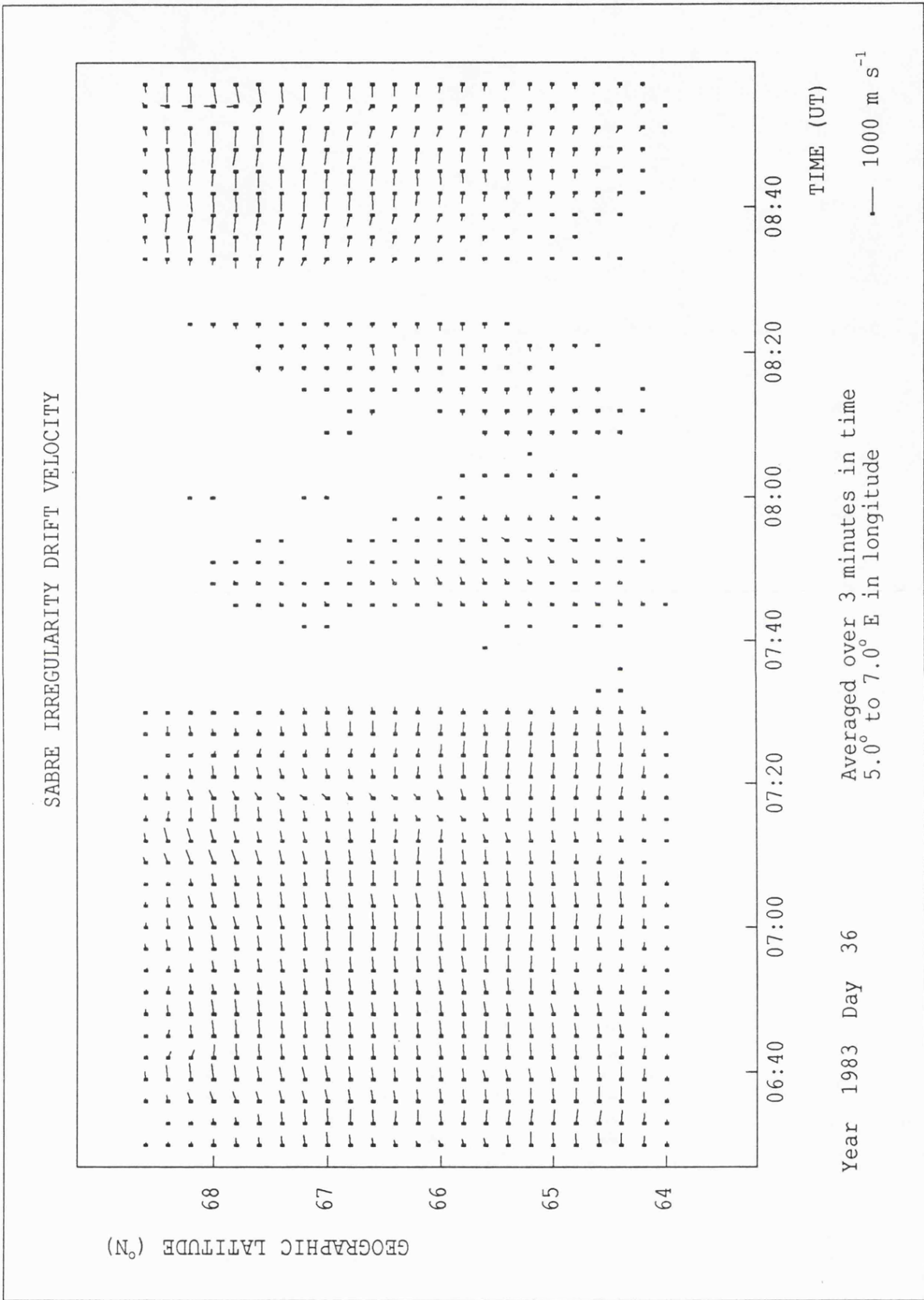


**FIGURE 6.8.** Cusp flows observed by SABRE on 5 February (day 36), 1983.

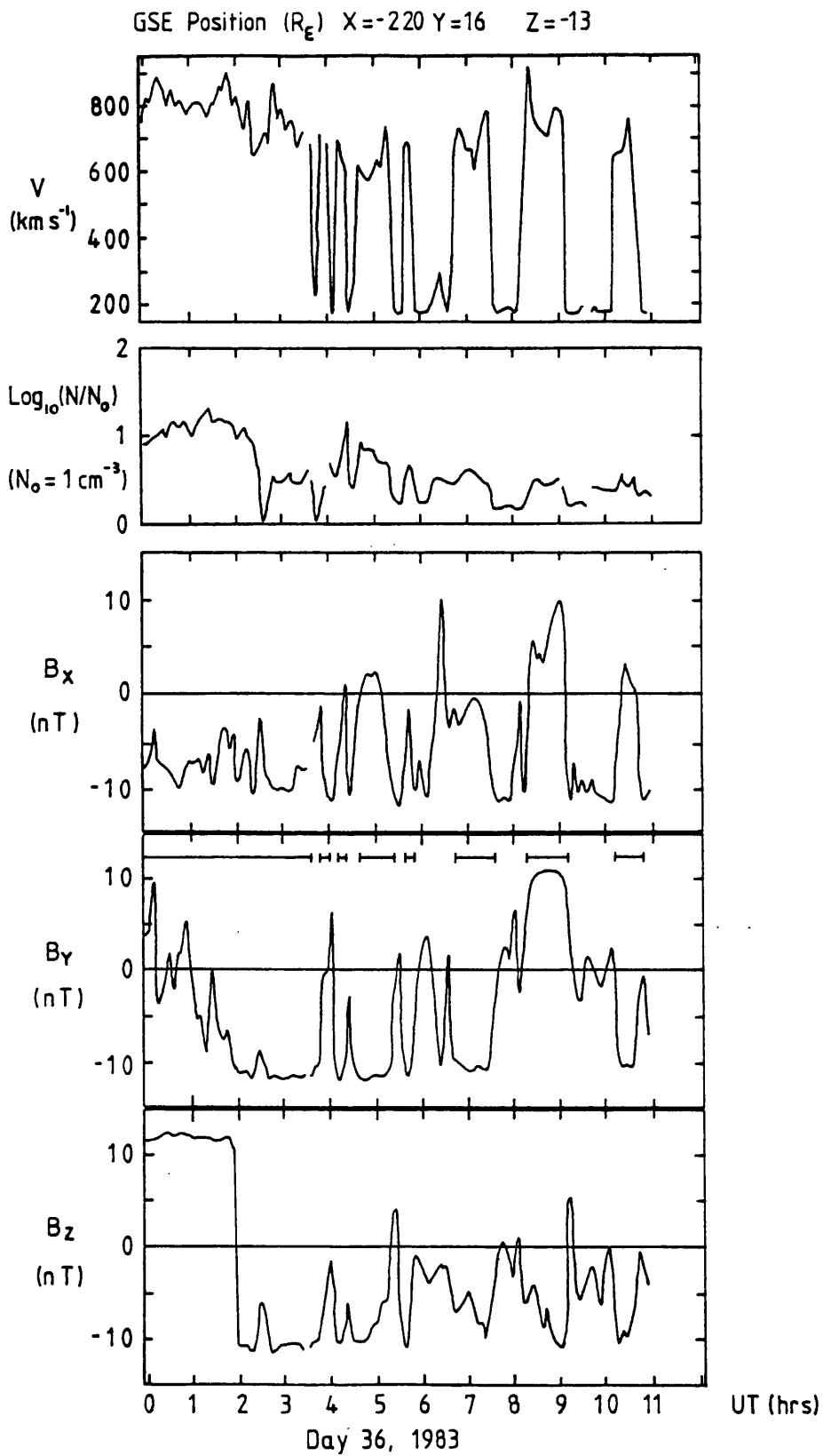


**FIGURE 6.9.** Plasma and IMF parameters measured by ISEE-3 for the period 0:00 to 12:00 UT, 5 February, 1983. The horizontal bars on the  $B_y$  plot indicate the intervals when the spacecraft is inferred to be located in the solar wind.

which assumes an average flow speed of  $800 \text{ km s}^{-1}$ . Accordingly, the ISEE-3 magnetic data reveal that  $B_x$ ,  $B_y$  and  $B_z$  were all, in general, strongly negative for the duration of the ground based measurements of Figure 6.8, with the exception of the 8:00-9:00 UT interval, when  $B_y$  was strongly positive. The latter interval corresponds with the period when SABRE observed weak flows characteristic of the 'throat' region near the equatorward boundary of the convection pattern (7:30-8:30 UT). This suggests that during the interval when  $B_y$  was positive, the polar cap boundary was to the north of the SABRE viewing area, so that it is impossible to determine whether this temporary change in IMF orientation perturbed the large scale pattern.

The  $B_z$  component was on average  $\sim -10 \text{ nT}$ , which is consistent with the observation of cusp flows within the latitude range covered by SABRE. (The step-like turning of  $B_z$  from positive to negative at 02:00 UT falls within the period of a case study presented in the next chapter.) In addition, the  $B_y$  polarity is generally consistent with the absence of a pre-cleft westward flow incursion in the observed convection pattern.

#### 6.4.2 7 August, 1982

Cusp flows in the SABRE field of view which occurred on 7 August (day 219), 1982, are poorly defined compared with the other observations, but the event has been selected by virtue of the availability of simultaneous STARE data. The flow pattern (Figure 6.10) displays a region of weak or zero backscatter separating the electrojets, which widens with decreasing latitude from about one hour at  $72^\circ \text{ N}$  to nearly three hours at  $64^\circ \text{ N}$  geographic. This throat-like structure in the cusp convection pattern is consistent with the AE-C satellite observations of flows into the dayside polar cap (Heelis et al., 1976). The value of  $D_{st}$  reached a peak depression of  $-173 \text{ nT}$  at 8:00 UT, 7 August, 1982, which according to Meng (1983) would suggest that the cusp reached its lowest latitude some hours

SABRE/STARE IRREGULARITY DRIFT VELOCITY

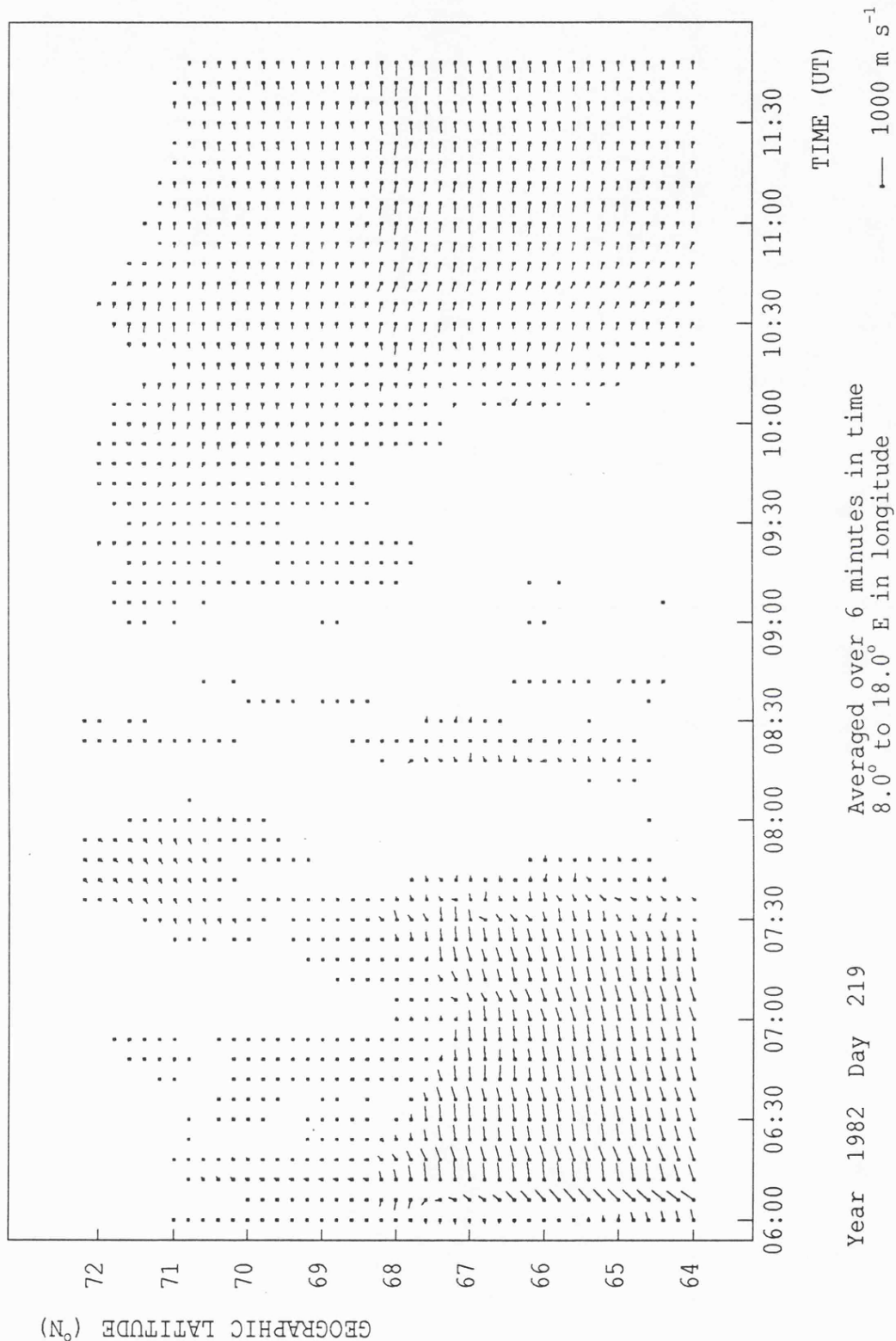


FIGURE 6.10. Combined SABRE/STARE RTV plot, covering the latitudinal range from 64° to 72° N geographic for the time interval 6:00 to 12:00 UT, 7 August (day 219), 1982.

before it was observed by SABRE.

According to the inferred IMF polarity, which is recorded as being towards the Sun, this event ought to be consistent with a negative value of the  $B_y$  component. The absence of any obvious positive  $B_y$  signature in the SABRE flows would tend to confirm this supposition. In contrast, however, the pre-reversal convection flows in the STARE field of view, though intermittent, are predominantly westward, particularly towards the poleward edge of the viewing area and close to the 'throat'. The STARE measurements in this region are of insufficient quality to conclusively identify this as a positive  $B_y$  modulation effect. The latter interpretation is supported, however, by ISEE-3 spacecraft measurements of the upstream solar wind at GSE coordinates  $X = 247$ ,  $Y = -60$ , and  $Z = 16 R_E$  (Figure 6.11). There are several data gaps, but nonetheless it is possible to deduce the general behaviour of the interplanetary medium during this event. The flow speed fluctuates between 450 and 550  $\text{km s}^{-1}$ .  $B_x$  is predominantly negative and  $B_y$  mainly positive until shortly after 8:00 UT, when both reverse direction. From 4:00 to 10:00 UT  $B_z$  is strongly negative, except for the period from 6:30 to 8:30 UT when it is strongly positive.

Assuming an average solar wind flow speed of 500  $\text{km s}^{-1}$  yields a time delay for changes measured by the satellite to reach the Earth of about 1 hour and suggests that  $B_y$  was positive in the vicinity of the Earth until 9:00 UT, which would explain the westward flows observed by STARE prior to the reversal. In addition, the interval of positive  $B_z$  measured by ISEE-3 correlates with the period when SABRE and STARE observed almost no backscatter, suggesting that the convection pattern contracted, due to a reduction in the dayside merging rate, while the IMF was northward. A condition of  $B_z < -10$  nT was apparently required in order to maintain strong flows throughout the joint viewing area. This interpretation is supported by the hourly values of AE. The mean value of AE over the interval from 0:00 to 12:00 UT was over 900 nT, but fell to 300 nT at 8:00

GSE Position ( $R_E$ ) X=247 Y=-60 Z=16

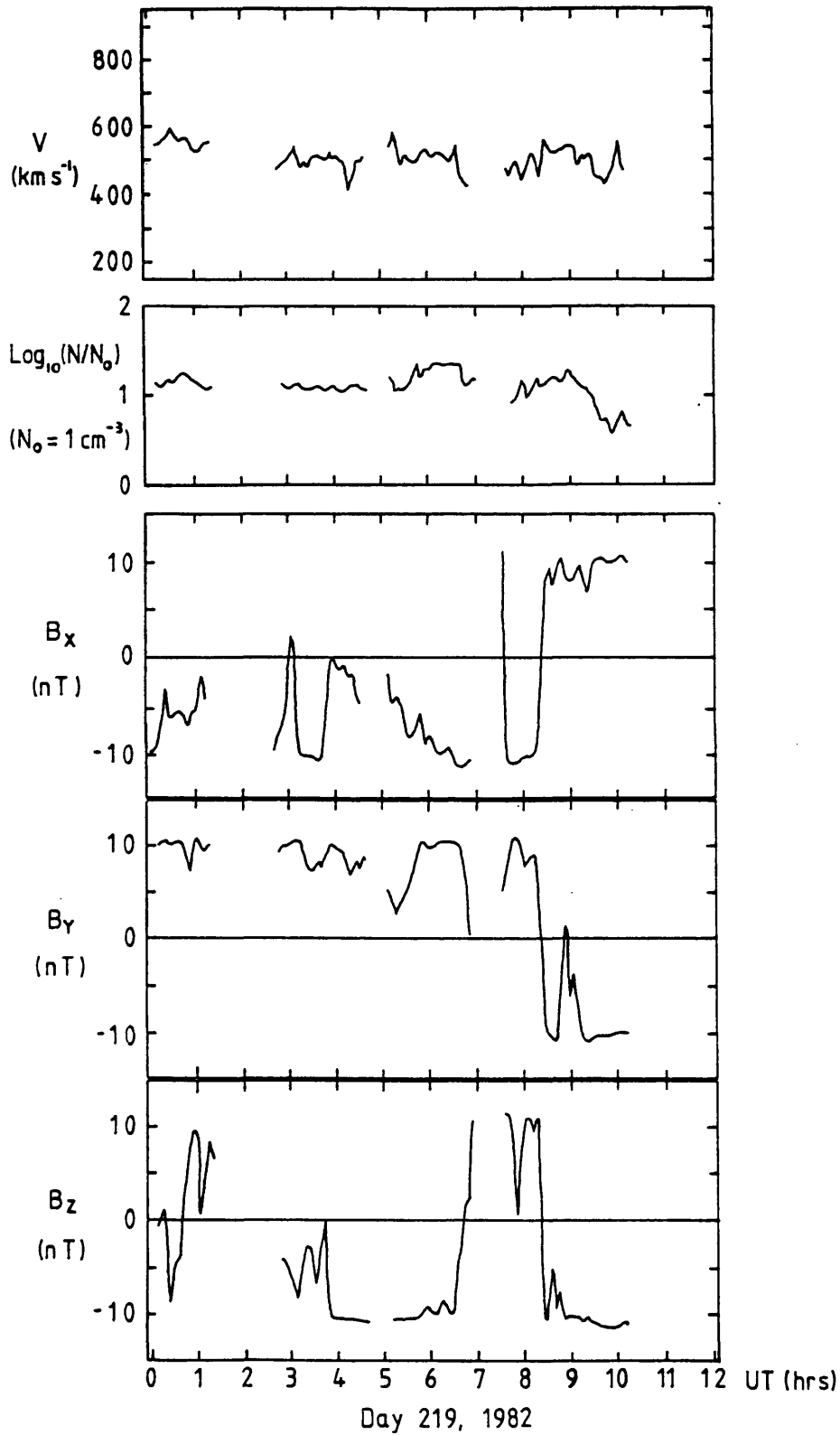


**FIGURE 6.11.** ISEE-3 measurements of the solar wind flow speed and density and the  $B_x$ ,  $B_y$  and  $B_z$  components of the IMF for the interval 0:00 to 12:00 UT, 7 August, 1982.

UT, a time when SABRE was in the 'throat'. Since AE is a global index, it is likely that the loss of backscatter in the SABRE field of view was the manifestation of a temporal change in the large scale convection pattern, specifically a contraction initiated by the northward turning of the IMF. The IMF measurements of the ISEE-3 spacecraft are in general agreement with the IMP-8 data, for which the hourly mean values of  $B_y$  and  $B_z$  changed from negative to positive during the intervals from 6 to 9 UT and 7 to 9 UT, respectively.

### 6.5 Discussion

The observations presented in sections 6.3 and 6.4 suggest that an equatorward motion of the ionospheric footprint of the cusp as far south as  $61.5^\circ$  N geomagnetic (the equatorward boundary of the SABRE viewing area) normally requires very extreme geomagnetic activity. Meng (1983) reports a latitudinal location of the cusp as low as  $61.7^\circ$  N geomagnetic for very active conditions with a  $D_{st}$  of  $-150$  nT. For one of the present events (28 April, 1985), however, a cusp shift to  $61.5^\circ$  N occurred when the peak depression in  $D_{st}$  was only  $-99$  nT. This represents a somewhat lower activity threshold (as indicated by the ring current intensity) than has been reported previously for a cusp movement of this magnitude.  $D_{st}$  may not be a suitable index to compare with the SABRE measurements in attempting to evaluate the likely mechanism for the observed cusp shifts, since, as mentioned earlier, the peak intensity of the ring current lags the maximum cusp displacement by several hours. The AE index appears to exhibit a closer relationship with the latitudinal location of the cusp, especially on 7 August, 1982, when AE decreased considerably as the cusp retreated poleward, although the latter phenomenon was probably triggered directly by the northward turning of the IMF rather than via a substorm process.

While increasingly negative  $B_z$  is expected to produce equatorward expansions of the large scale convection pattern, the  $B_x$  component ought to cause Sun-Earth shifts of the pattern (section 2.4.3). ISEE-3 observations of strongly negative  $B_x$  for three out of four SABRE cusp observations is consistent with the expected sunward shift of the pattern for  $B_x < 0$ . The strongly southward character of the IMF presumably compensated for the effect of a predominantly positive  $B_x$  component on 2 March, 1983.

The observations for 28 April, 1985 are inconsistent with a positive  $B_y$  cusp flow structure but may be easily interpreted in terms of the Heelis (1984) dayside convection pattern for negative  $B_y$ . Figure 6.12 is a schematic representation of the large scale dayside convection patterns for positive, zero and negative  $B_y$ , incorporating simple diagrams to depict the expected flow directions in the SABRE viewing area in the cusp region. The model for negative  $B_y$  predicts that as SABRE rotates under the discontinuity, westward flow associated with the dusk cell would penetrate from the equatorward direction, which is in agreement with the observations (the positive  $B_y$  model predicts that the westward flow penetrates from the poleward direction). The observed rotation of the westward flow to a north-east direction (Figure 6.7) can be explained as the turning of the dusk cell associated westward flows to antisunward flows across the pole.

The above interpretation implies that between about 8:50 and 9:20 UT, at least part of the SABRE viewing area was inside the polar cap, and indicates a very substantial equatorward displacement of the cusp (which is at the equatorward boundary of the polar cap). Also, it appears that the cusp flows observed on 16 November, 1985 were modulated by a negative  $B_y$  condition (unfortunately no satellite data was available to confirm this), a conclusion which is at variance with the inferred IMF polarity. More direct evidence for the unreliability of the latter parameter for these studies was presented in section 6.4.2.

For 6 September, 1982, 2 March, 1983 and 16 November, 1984, SABRE

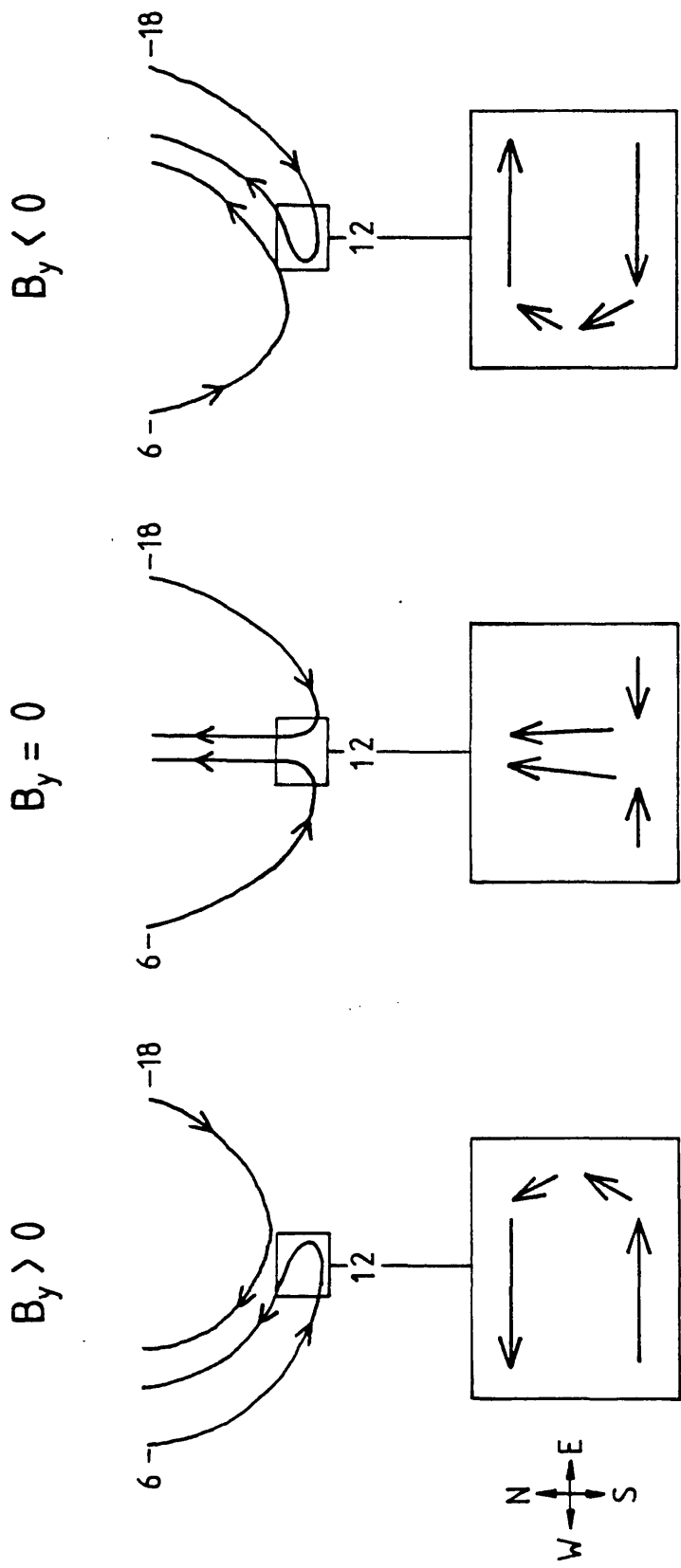


**FIGURE 6.12.** Schematic representation of the predicted large scale dayside convection patterns for positive, zero and negative  $B_y$ , incorporating simple diagrams that depict the expected flow directions in the SABRE viewing area in the vicinity of the cusp.

observed convection flows in the vicinity of the morning reversal which are clearly consistent with a positive  $B_y$  modulated cusp flow pattern. The flow signatures for the three days are qualitatively similar, with a wedge of westward flow penetrating from the poleward edge of the viewing area into the region of ambient eastward flow, prior to the principal east-west flow reversal. However, there are quantitative differences in the structures of the respective westward flow incursions for the three events, particularly in their widths and the temporal locations of their boundaries.

To explain these differences, it is necessary to consider the convection flows which would be observed by SABRE as the viewing area traversed a temporally stable, positive  $B_y$ , perturbed cusp flow pattern for negative  $B_z$ . Figure 6.13 is a schematic representation of the successive positions of the viewing area with respect to a model cusp flow pattern for positive  $B_y$  (after Heelis, 1984). The dashed curve indicates the approximate location of the polar cap boundary, the separatrix between regions of sunward flows at the feet of closed flux tubes and regions of antisunward flows at the feet of open flux tubes. At position 1, predominantly eastward (sunward) flows are expected. As the polar cap boundary is gradually traversed, westward (antisunward) flows are expected to enter from the poleward edge of the field of view (position 2). At the boundary between the dawn and dusk cells (position 3), which is expected to be characterised by low electric fields, the flows ought to be weak, with a generally northward direction. When position 4 is reached, the flows should be predominantly westward (sunward).

The sequence of SABRE spatial plots for the morning sector of 6 September, 1982, presented in Figure 6.14, are in broad agreement with the scenario described above. At 7:39 UT, predominantly eastward flows are observed throughout the field of view, which is consistent with position 1 on the schematic diagram (Figure 6.13). By 8:33 UT, there are indications

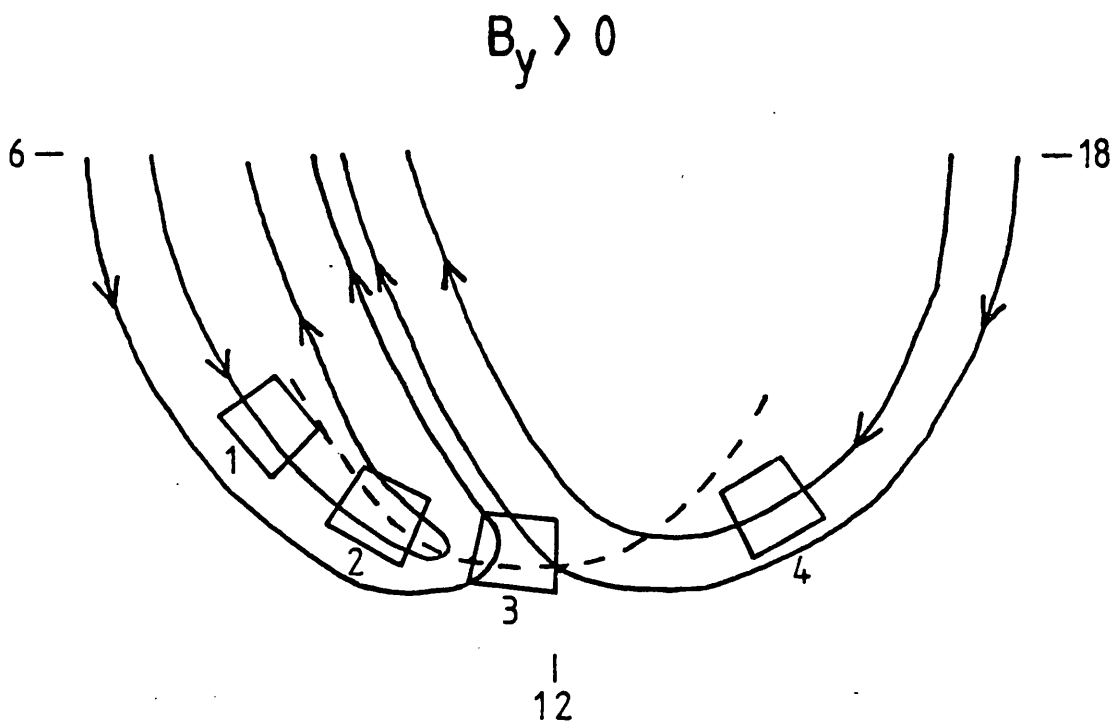


FIGURE 6.13. Schematic representation of the predicted large scale dayside convection pattern for positive  $B_y$ , indicating the successive positions of the SABRE viewing area as the Earth rotates under the pattern. The dashed line denotes the polar cap boundary.

SABRE IRREGULARITY DRIFT VELOCITIES

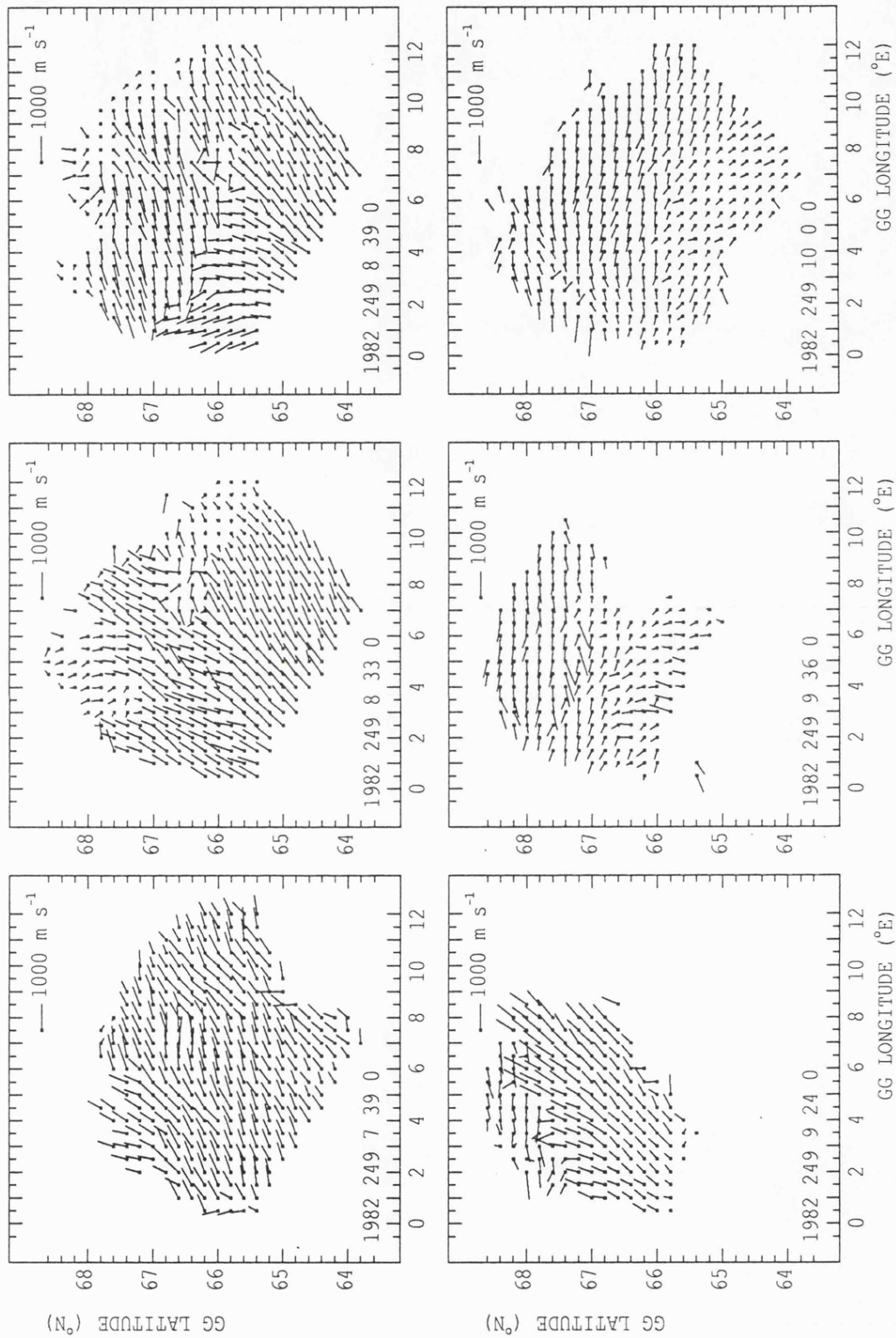


FIGURE 6.14. Sequence of SABRE spatial plots for the morning of 6 September, 1982.

of westward flows entering from the north-east, and by 8:39 UT the westward flows are established in over half the viewing area (position 2), with regions of eastward flow and northward flow confined to the south and the west, respectively. The equatorward edge of the westward flow incursion, which crosses the viewing area from the north-west to the south-east, presumably delineates the boundary of the polar cap. At 9:24 UT, the westward incursion is retreating into the north-west corner of the SABRE field of view, while the majority of the observed flows are directed eastward with a strong northward component. By 9:36 UT, the flows are predominantly westward. At 9:24 and 9:36 UT, the viewing area is probably on opposite sides of the morning cleft, or 'throat', between the dawn cell and the dusk cell (position 3 in Figure 6.13) and the loss of backscatter in the equatorward portion of the field of view for both these times is consistent with the increasing width of the throat with decreasing latitude. By 10:00 UT, the flows are strongly westward throughout the viewing area, which is in agreement with position 4 on Figure 6.13.

Some of the changes in flow direction observed by SABRE occur too rapidly to be explained by the rotation (with the Earth) of the viewing area under a static convection pattern. In particular, the observations of Figure 6.14 indicate that while at 8:33 UT (6 September, 1982) SABRE observes westward flows just at the north-east edge of the field of view, only 6 minutes later (8:39 UT), in which time the viewing area has moved a mere  $1.5^\circ$  in geographic longitude, the westward flows occupy over half of the area. The RTV plot (Figure 6.1) indicates that the westward flow region actually appeared in the poleward edge of the SABRE latitude range from about 8:10 UT, and was confined there until approximately 8:30 UT when, comparatively suddenly, it commenced its rapid equatorward penetration. This must be a temporal variation of the pattern, and an examination of the IMF data (Figure 6.2) suggests two possible triggering mechanisms. Until the data gap at 9:30 UT, the  $B_z$  component exhibits

significant variability. Any change in  $B_z$  is expected to change the dayside merging rate, leading to an expansion or contraction of the polar cap boundary. An expansion of the polar cap could explain the rapid equatorward advance of the westward flow incursion at ~8:30 UT, 6 September, 1982. The equally rapid poleward retreat of the westward incursion on 16 November, 1984 at ~7:50 UT might be due to a contraction of the polar cap.

The sudden reconfiguration of the cusp flow pattern by a change in the polarity of  $B_y$  offers an alternative mechanism for the temporal variations of the flows observed by SABRE. For example, the rapid appearance of westward flow in the poleward half of the SABRE viewing area on 6 September, 1982, shortly after 8:30 UT, correlates (allowing for the ~ 35 minute time delay between ISEE-3 and SABRE) with the return of  $B_y$  to a strongly positive value ( $> 10$  nT) at about 8:00 UT, after a brief interval when  $B_y$  was ~ -5 nT. This suggests that, as the result of the sudden IMF change, the sense of the azimuthal flows in the cusp reversed direction, with a reconfiguration of the large scale pattern from the morphology for  $B_y < 0$  to that for  $B_y > 0$  (Figure 6.12) on a time scale of only a few minutes. This is consistent with the Alfvén travel time between the merging site at the magnetopause and the ionosphere. Southwood (1987) points out that the net motion of a given flux tube requires the redistribution of differential stresses along its length. The agent of this redistribution is a MHD (Alfvén) wave, which carries the information regarding plasma motions at the magnetopause down to low (ionospheric) altitudes.

## 6.6 Summary

Evidence has been presented which indicates that under certain conditions SABRE can determine the morphology and temporal variability of the magnetic

merging process at the dayside magnetopause. The signatures of both a positive and a negative  $B_y$  modulated cusp flow pattern have been observed by SABRE and these are consistent with theoretical predictions (Cowley, 1981) and empirical models derived from satellite measurements (Heelis, 1984). However, in some cases the details of the observations cannot be interpreted in terms of purely spatial variations in the large scale convection pattern, but indicate the occurrence of significant temporal variations which are probably directly triggered by fluctuations in the IMF.

The present investigation confirms the sensitivity of the dayside convection flow morphology to the behaviour of the azimuthal component of the IMF. While  $B_y$  governs the configuration of the cusp flow pattern,  $B_z$  determines its latitudinal location. On the basis of the case studies presented above, the most important requirement for cusp flows to appear in the SABRE latitude range ( $61.5^\circ$ – $66.5^\circ$  N, geomagnetic) is probably that  $B_z < -10$  nT.

## CHAPTER 7

### NIGHTSIDE CONVECTION FLOWS

#### 7.1 Introduction

The gross features of the convection flow pattern for a southward directed IMF are well established. By contrast, the structure of the pattern during northward IMF conditions remains the subject of great controversy. The statistical investigations of Chapters 4 and 5 indicate that convection flows are much less likely to appear within the viewing area after the IMF turns north (see Figures 4.10 and 5.2). Also, dayside convection flows are observed by SABRE far less frequently than are nightside flows. Consequently, SABRE measurements of positive  $B_z$  convection flows are confined to the nightside sector of the pattern. The interpretation of such observations is complicated by the much higher probability of substorm effects on the nightside.

Two case studies of nightside convection flows during northward IMF are presented. For both of these,  $B_z$  was in excess of 10 nT, and the geomagnetic conditions were appreciably more disturbed in one case than the other. In order to highlight the anomalous nature of the measured northward IMF convection flows, a study is first described for conditions of strongly southward IMF (with  $B_z$  in the range -5 to -10 nT), when the convection pattern displayed a typical two cell structure.

#### 7.2 Observations During Southward IMF

SABRE observations are presented here for 2 March (day 61), 1983. This day

has been chosen because SABRE observed strong flows throughout the 24 hour period. There exists in the SABRE data base only one other day (5 February, 1983) during which the large scale convection pattern was sufficiently expanded over a 24 hour interval for this to be the case. It is, therefore, not surprising that 2 March, 1983 was a day on which geomagnetic conditions were highly disturbed. The average value of  $D_{st}$  for the day was  $-101$  nT and the mean value of  $K_p$  was 6. Despite this, the observed flows are reasonably smooth with relatively little turbulence, and the two cell structure of the convection pattern is very well defined. The study is further enhanced by the availability of STARE data for the whole interval.

Figure 7.1 illustrates the convection flow velocities observed by SABRE for the time interval 18:00 to 24:00 UT, 2 March, 1983. The flow direction is predominantly westward, until the arrival in the field of view of the Harang discontinuity between 20:20 and 20:30 UT. Thereafter, the flow is directed eastward. The structure of the Harang discontinuity itself, in which eastward flows associated with the westward electrojet penetrate from the equatorward edge instead of the poleward edge of the viewing area, is the only unusual feature of the convection pattern on this day. However, in the STARE latitude range the discontinuity has a very typical structure. The disparity in the observations from the two different systems is attributable to either a temporal variation (the local time separation between the centres of the two viewing areas is about an hour) or a spatial variation, suggesting the existence of a 'kink', at about  $66^\circ$  N geomagnetic, in the boundary between the convection cells. The ISEE-3 plasma measurements indicate that the spacecraft was in the magnetospheric tail for most of the period 12:00 to 24:00 UT, 2 March, 1983, although short intervals of data, when the spacecraft was apparently sampling solar wind plasma, suggest that  $B_z$  was approximately  $-5$  nT. During the first half of the day (00:00 to 12:00 UT), for which both the SABRE/STARE and

SABRE IRREGULARITY DRIFT VELOCITY

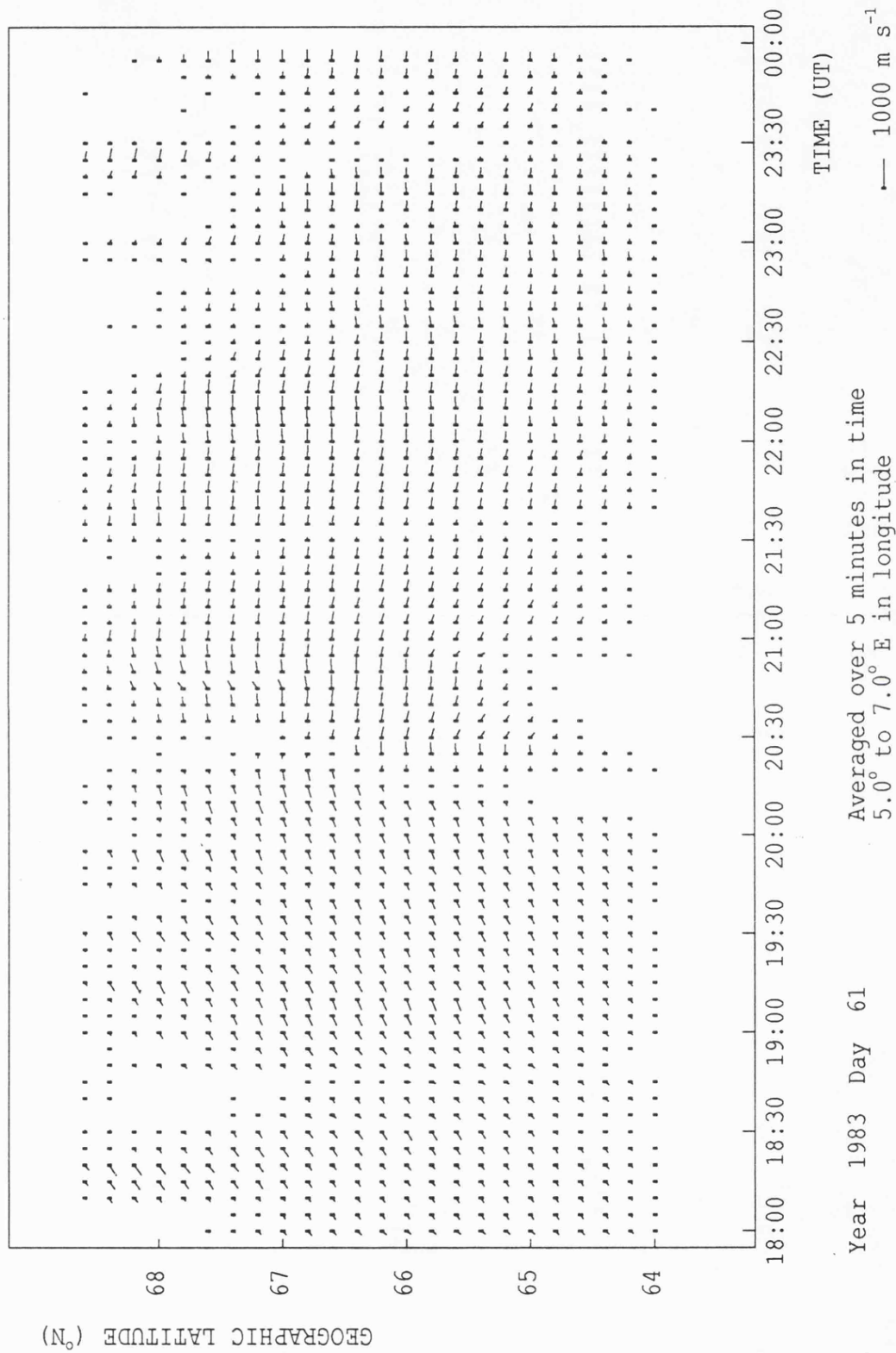
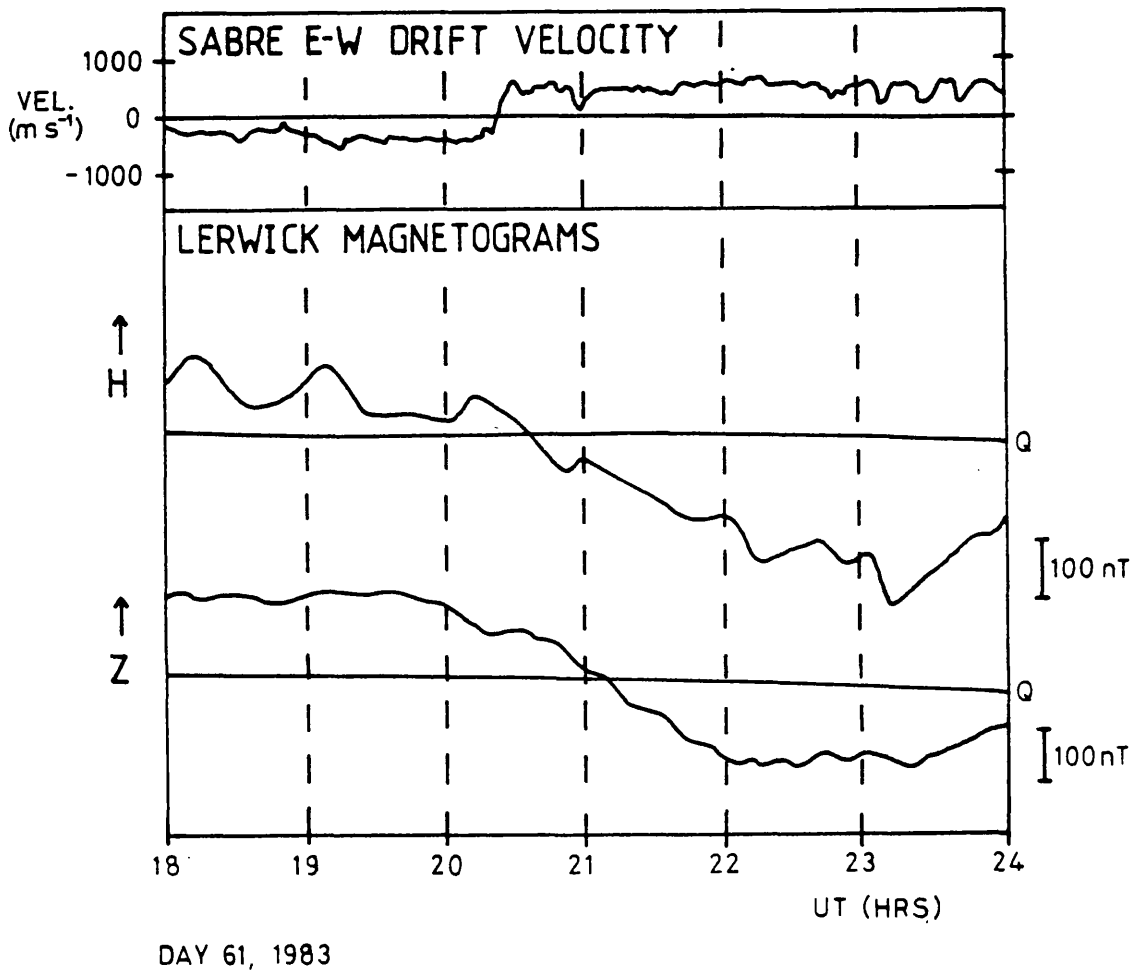


FIGURE 7.1. SABRE flow velocity observations for 2 March, 1983, 18:00 to 24:00 UT when  $B_z \sim -5$  nT.

ISEE-3 measurements have been described in the previous chapter,  $B_z$  averaged  $-10$  nT (Figure 6.5). The average value of  $B_y$  was  $\sim -5$  nT during the evening of 2 March and this may offer a possible explanation for the anomalous structure of the Harang discontinuity observed by SABRE, since the latter is consistent with the negative  $B_y$  induced asymmetry in the discontinuity predicted by Cowley (1981)

The simple structure of the pre-midnight convection pattern indicated by the SABRE observations, with smooth westward flows reversing at  $\sim 20:20$ – $20:30$  UT to regular eastward flows, is supported by Lerwick (geographic coordinates  $60.0^\circ$  N,  $1.2^\circ$  W) magnetometer data. The H and Z magnetic perturbations for the interval 18:00 to 24:00 UT are presented, along with the east-west velocity component measured by SABRE at  $66^\circ$  N,  $6^\circ$  E geographic, in Figure 7.2. The quiet day magnetic levels are also indicated. The magnetometer measurements suggest that the electrojets were intense but comparatively steady and that the Harang discontinuity crossed the Lerwick meridian between 20:40 (as measured by H) and 21:00 UT (as measured by Z). This is in agreement with the SABRE observations, since the Lerwick site is located about 30 minutes west in local time from the centre of the SABRE viewing area.

The clear definition of the two cell structure over the whole of the 2 March, 1983, 0–24 hour period is demonstrated in Figure 7.3, which is an annular plot of combined SABRE and STARE measurements providing a latitudinal coverage of  $64^\circ$ – $72^\circ$  N (geographic), with colour coding for the flow directions. The evening and the morning discontinuities are located almost 4 hours before midnight and noon (UT), respectively. The positive  $B_y$  modulation effect near the morning reversal, which was described in the previous chapter, is clearly visible as a wedge of westward flow around 7:00 UT, in the poleward half of the combined SABRE/STARE viewing area. Also, there is evidence in the SABRE latitude range for the presence of a pulsation event(s) between about 12:00 and 16:30 UT, although this class of



**FIGURE 7.2.** East-west component of the drift velocity measured by SABRE at 66° N, 6° E geographic, with the H and Z components of the geomagnetic field measured at Lerwick (geographic coordinates 60.0° N, 1.2° W), for 18:00 to 24:00 UT, 2 March, 1983. The curves denoted by Q indicate the quiet day levels of H and Z.

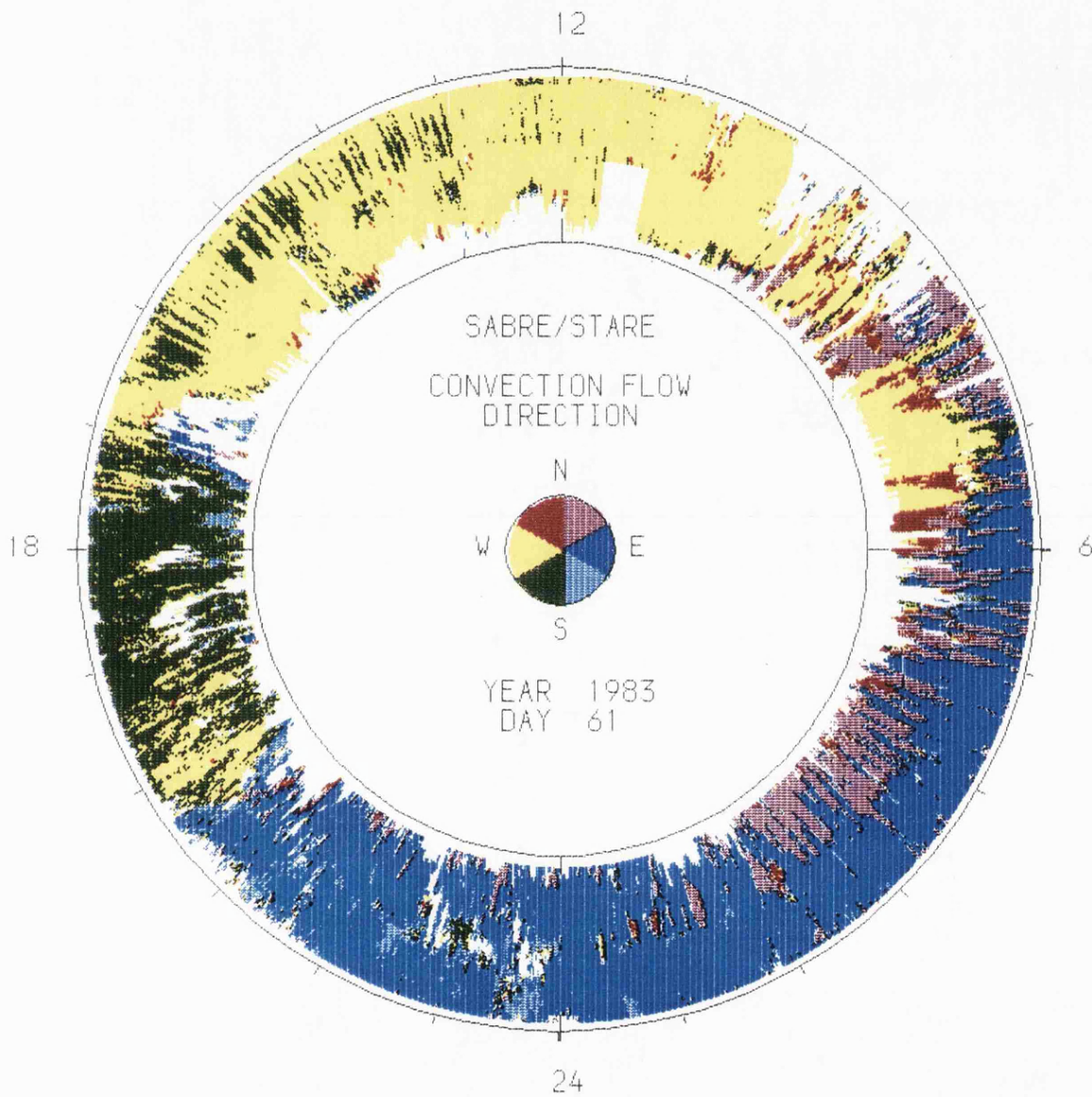


*FIGURE 7.3. SABRE/STARE colour annular plot for 00:00 to 24:00 UT, 2 March, 1983, when  $B_z \ll 0$ . The configuration of the auroral convection flows in a two cell pattern is apparent.*

phenomenon is beyond the scope of the present investigation.

### 7.3 Observations During Northward IMF

When  $B_z$  is strongly positive, low altitude satellites observe sunward directed flow in the polar cap whose magnitude increases as IMF  $B_z$  increases (section 2.4.4). These observations have been interpreted as evidence for the reconfiguration, during northward IMF, of the usual two cell pattern into a four cell structure (Figure 2.14). This consists of two very high latitude cells driven by reconnection and two cells at lower latitudes generated by viscous interaction. The observations indicate that the polar cap cells change their relative sizes according to the sign of  $B_y$  (Potemra et al., 1984).  $B_y$  is not expected to affect the viscous cells since these are not connected to the IMF.

A second model for the convection flow patterns during strong northward IMF conditions has been proposed, in which the convection electric field can become irregular at scale sizes of the order of 10-100 km, while the gross features of the normal two cell pattern remain (Heppner, 1973; Heppner and Maynard, 1987). At present, this does not have as wide support as the four cell model, but will nonetheless be considered in greater detail later in the discussion.

#### 7.3.1 Observations for 4-5 February, 1983

The investigation described in this and the next two sections (7.3.2 and 7.3.3) is concerned with SABRE radar observations of the nightside convection flows on 4-5 February 1983. Plasma and magnetometer data from the ISEE-3 spacecraft, which was located in the solar wind some  $220 R_E$  downstream from the Earth, indicate that the flow speed was very large and that the IMF exhibited a strong northward component.

The SABRE measurements for the period 4 February, 21:00 UT to 5

February, 3:00 UT are presented in Figure 7.4. 5 minute average convection flow velocities, for the geographic latitude range  $64.0^{\circ}$  to  $68.6^{\circ}$  N, in the longitudinal interval  $5^{\circ}$ - $7^{\circ}$  E, are plotted as a function of time. Figure 7.4 indicates that the flows do not correspond to the normal two cell structure. Until 22:15 UT the flows were predominately eastward, with a period of south-west directed flow between 21:30 and 21:50 UT. From 22:45 to 1:20 UT the flows were almost exclusively westward, except for the interval 23:30-23:45 UT when they were directed south-east. At 1:30 UT the flows turned east again, this direction being consistent with a normal two cell pattern, followed at 2:00 UT by a 10 minute period of predominately southward flow. Thereafter the flow direction remained eastward. Evidence for this sequence of flow reversals is present in the Lerwick magnetometer data.

STARE data provides further evidence for the sequence of flow reversals described above. The SABRE and STARE data are combined in Figure 7.5 as a colour annular plot covering the geographic latitude range  $64^{\circ}$ - $72^{\circ}$  N, for the interval from 4 February, 16:00 UT to 5 February, 4:00 UT. The flow directions indicated by the two systems are in general agreement, with the exception of the observation by STARE of predominantly northward flows between about 20:00 and 20:30 UT and between 22:00 and 22:45 UT, which is unusual for the nightside sector where normally only east, west and southward flows are expected. The obvious high degree of flow structure illustrated in Figure 7.5 is in striking contrast to the simple two cell pattern for southward IMF (Figure 7.3).

An examination of the  $D_{st}$  and  $K_p$  indices confirms the highly disturbed nature of the geomagnetic conditions during this period, with  $D_{st}$  reaching  $-150$  nT and  $K_p$  exceeding a value of 7. In addition, a period of strongly enhanced flows were observed by SABRE and also by STARE, following a sudden storm commencement (ssc) at 16:15 UT (McDiarmid and Nielsen, 1987a). Radar observations are not presented here for the interval prior to 2100 UT since

SABRE IRREGULARITY DRIFT VELOCITY

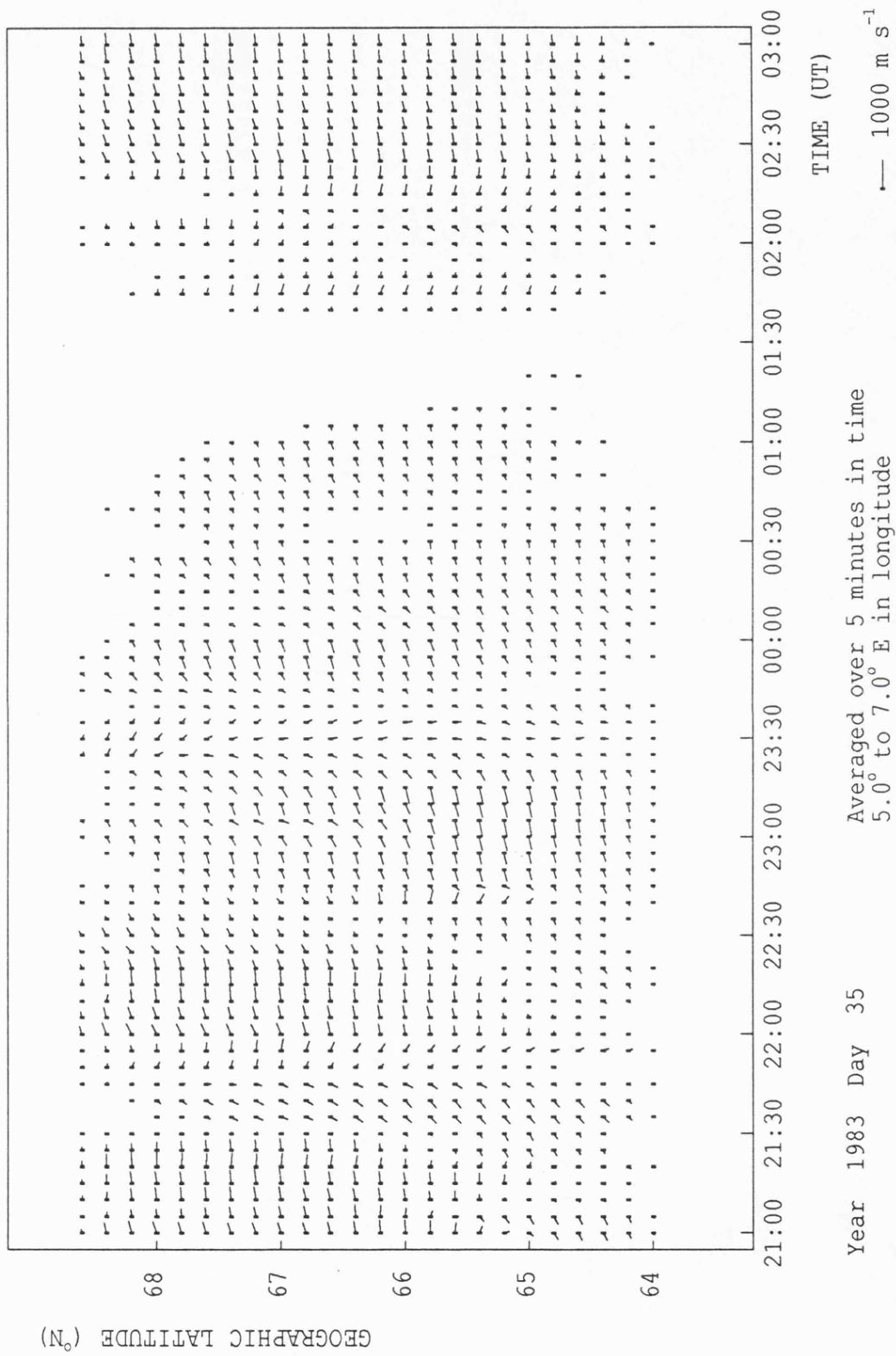
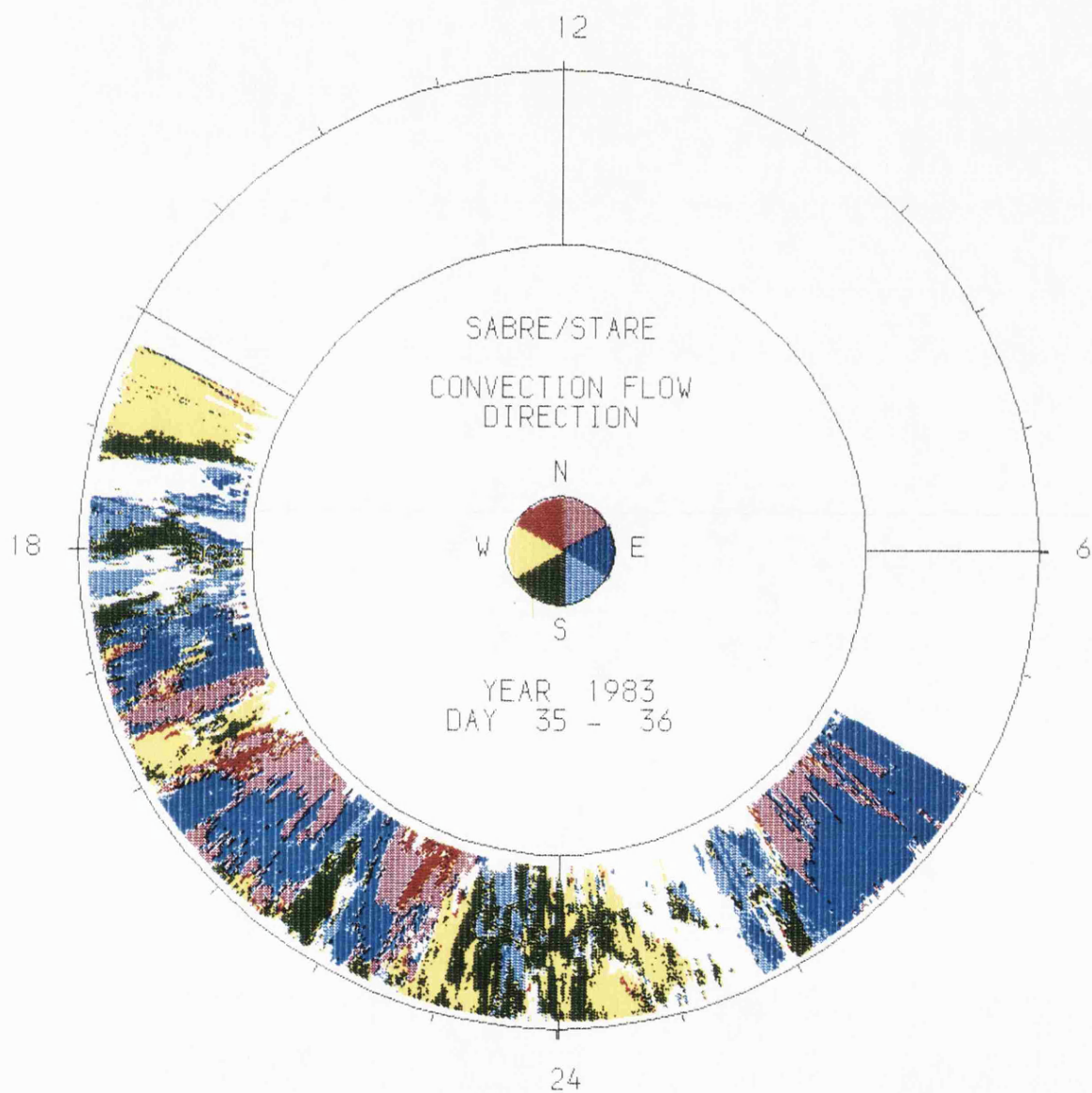


FIGURE 7.4. SABRE flow velocity observations for 4 February, 1983, 21:00 UT to 5 February, 03:00 UT, when  $B_z > 10$  nT.



*FIGURE 7.5. SABRE/STARE colour annular plot for 16:00 UT, 4 February to 04:00 UT, 5 February, 1983, when  $B_z \gg 0$ . The auroral convection flows are highly structured and inconsistent with a two cell pattern.*

there is a large data gap in the ISEE-3 measurements for this period, making a comparison with solar wind parameters impossible.

The solar wind parameters were measured by the ISEE-3 spacecraft, which was located tailward of the Earth, at approximately GSE  $X = -220$ ,  $Y = 15$ ,  $Z = -11 R_E$ . The ISEE-3 particle data reveal that the spacecraft was in the southern tail lobe prior to 16:30 UT. At that time the plasma density increased by a factor of 30, the temperature dropped by a factor of 4-5 and the flow speed increased to  $500 \text{ km s}^{-1}$ . These changes are characteristic of a crossing of the spacecraft from the tail into the magnetosheath. At about 16:45 UT the flow speed increased further to over  $1000 \text{ km s}^{-1}$ . This is believed to be the signature of the interplanetary shock which caused the ssc observed in the ionosphere at 16:15 UT.

One minute resolution ISEE-3 particle and magnetometer data, for the period 4 February, 21:00 UT to 5 February, 3:00 UT, are reproduced in Figure 7.6. From 21:30 UT to 3:00 UT, the plasma density and temperature were almost constant at about  $10 \text{ cm}^{-3}$  and  $5 \times 10^5 \text{ K}$  respectively and the flow speed averaged  $900 \text{ km s}^{-1}$ . These data are characteristic of very fast solar wind plasma. The magnitude of the magnetic field attained values in excess of 30 nT and the azimuthal angle of the IMF indicates that the field direction was largely in the negative Y direction ( $\phi > 180^\circ$  or  $\phi < 0^\circ$ ) except for the periods from about 22:40 to 23:10 UT and 23:45 to 0:20 UT when  $B_Y$  was positive. The average value of the polar angle corresponds to northward IMF ( $0^\circ < \theta < 90^\circ$ ), until the abrupt change in  $B_Z$  from approximately +25 nT to about -12 nT at 2:00 UT.

Since ISEE-3 was located  $220 R_E$  tailward of the Earth, in order to compare the spacecraft measurements of the solar wind with the SABRE convection flows, an estimate of the time delay between the two observing points is required. Assuming a solar wind velocity of  $900 \pm 100 \text{ km s}^{-1}$  during the interval 21:30, 4 February to 1:30 UT, 5 February, the time delay is given by

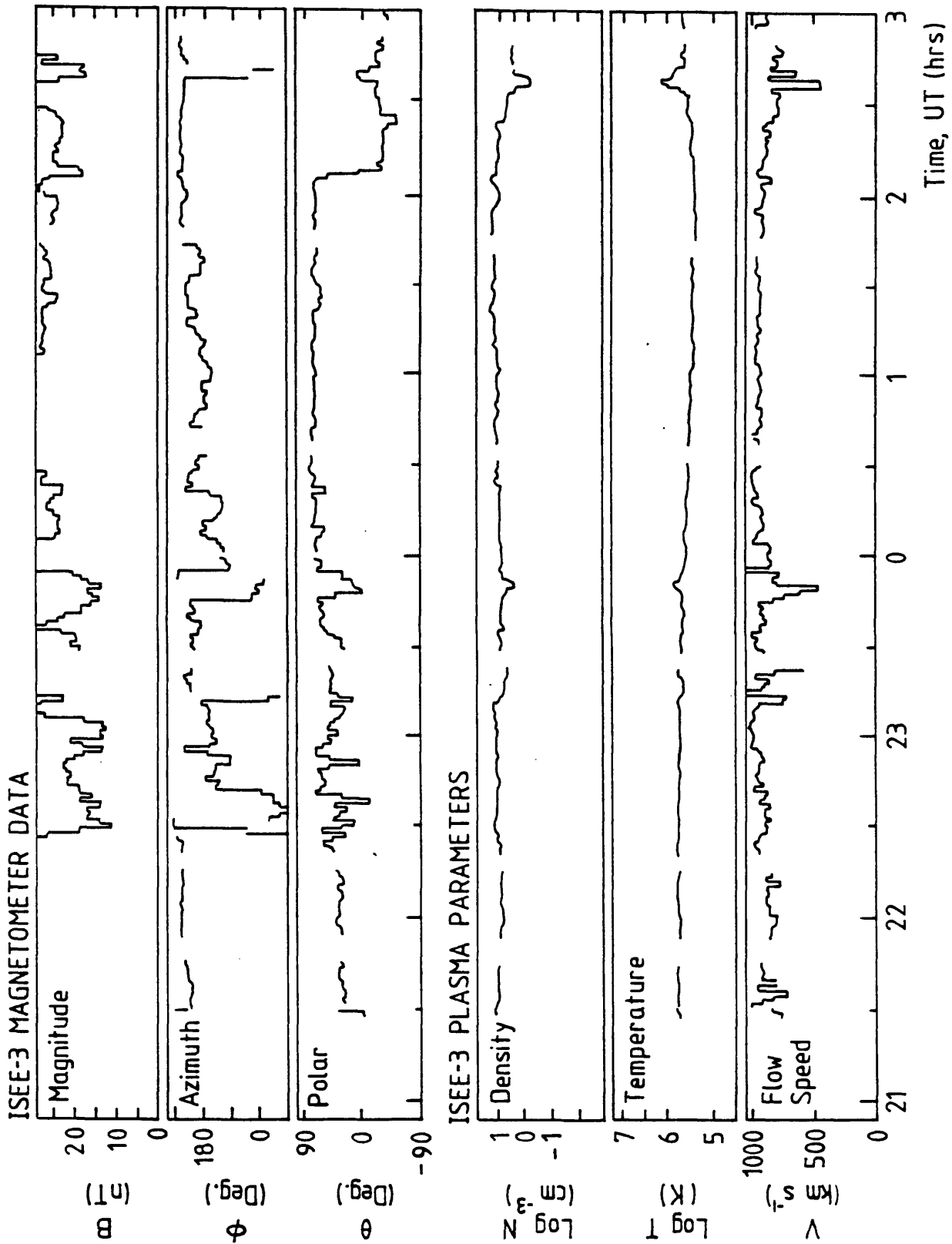


**FIGURE 7.6.** 1 minute resolution ISEE-3 data for the period 4 February, 1983, 21:00 UT to 5 February, 03:00 UT. The upper three panels depict the magnitude, azimuth angle and polar angle of the IMF and the lower three panels the logarithm of the density, the logarithm of the temperature and the bulk flow speed.

$$\tau = -220 R_E / (900 \pm 100 \text{ km s}^{-1}) = -26 \pm 3 \text{ mins}$$

The time delay between the onset of the ssc at 16:15 UT and the rapid increase in solar wind speed to  $> 1000 \text{ km s}^{-1}$  observed by the satellite at 16:45 UT, supports the above estimate. Therefore, assuming a time delay of between 25 and 30 minutes, the anomalous westward flow observed by SABRE between 22:45 UT, 4 February and 1:20 UT, 5 February, occurred when the IMF was very strongly northward. The return to 'normal' eastward flow occurred 25 minutes before ISEE-3 detected the abrupt southward turning of the IMF.

### 7.3.2 Four cell interpretation

The observations of Bythrow et al. (1985) and Heelis et al. (1986) indicate that, for strong northward IMF, the nightside portion of the polar cells are extremely structured, with turbulent and weak ionospheric flows being driven by an irregular reconnection process in the plasma sheet. In addition, four cell models predict that these reconnection cells exist at very high latitudes, poleward of  $75^\circ$  invariant latitude (eg. Rasmussen and Schunk, 1987). Thus, the associated flows should have been well to the north of the SABRE viewing area on 4-5 February, 1983. However, the westward flows measured by SABRE between 22:45 and 1:20 UT are comparatively strong and steady. A possible explanation is that the flows observed by SABRE are not driven by reconnection but arise from an unusually strong viscous interaction process.

The SABRE observations are nonetheless difficult to interpret in terms of any existing multi-cell models for northward IMF, since none of them predicts strong and steady antisunward flows as far south as SABRE in this local time sector. However, as  $B_z$  becomes increasingly positive, it is likely that the viscous cells grow, because the fraction of the magnetopause with closed field lines exposed to the magnetosheath increases (Crooker, 1980). This may offer a possible explanation in view of the

exceptionally large positive value of  $B_z$  and the very high solar wind flow speed. In this case, the SABRE data suggest that the SABRE viewing area rotated through the poleward edge of both dusk and dawn 'viscous' cells, viewing tailward flows.

To test the validity of this idea, the observations that would be expected for a radar rotating under the poleward edge of these cells in the time sector for which  $B_z$  was north are considered. Figure 7.7 depicts such a traversal through a schematic four cell pattern. This pattern is highly idealised with no account being made of any displacement of the nightside reversal from midnight to earlier local times. It is clear that the flow direction is at first east (position 1 on the diagram), but then turns west (position 3) after the passage through the Harang discontinuity. Near the flow reversal (position 2) flows which have significant southward components are expected, with the flow magnitudes becoming very small within the discontinuity itself. A radar looking further to the north (like STARE) might probe the equatorward edge of the reconnection cells, in which case the expected time development of the flow pattern would be firstly eastward, rotating through north, to westward.

When this scenario is compared with the actual SABRE measurements (Figures 7.4 and 7.5), the gross convection flow patterns are consistent with the model, assuming a displacement of the discontinuity of about 80 minutes from midnight to earlier local times. In addition, the possibility that, until 1:30 UT, 5 February, the STARE viewing area was actually within the high latitude reconnection cells would explain the interval of northward flow between 22:00 and 22:45, 4 February, as a region of sunward flow into the polar cap (the feature coloured red in Figure 7.5). There are, however, a number of discrepancies between the above model and the observations.

Firstly, there is a short period of about 20 minutes of primarily southward flow approximately one hour before the principal east-west flow

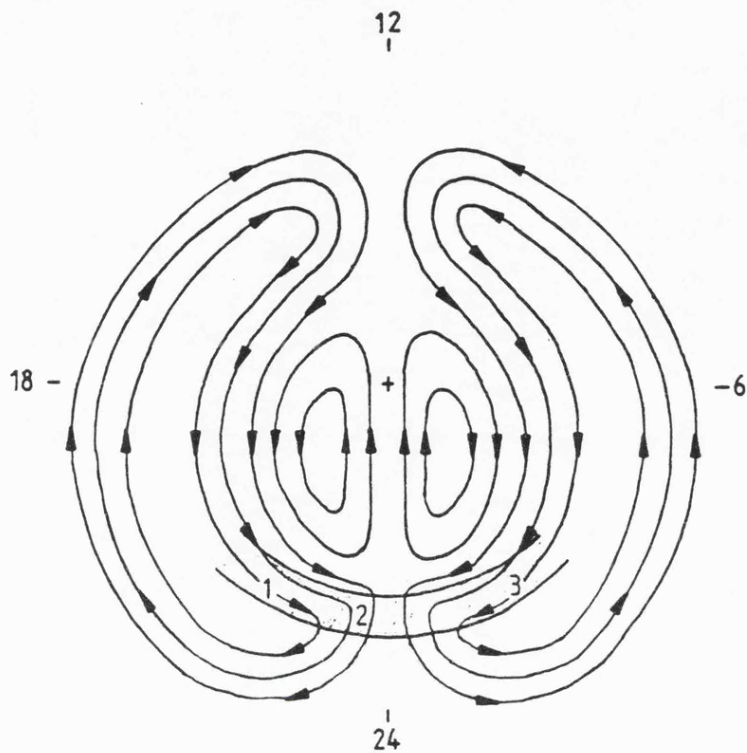


FIGURE 7.7. Schematic diagram suggesting the path taken by the SABRE viewing area through an idealised four-cell convection pattern.

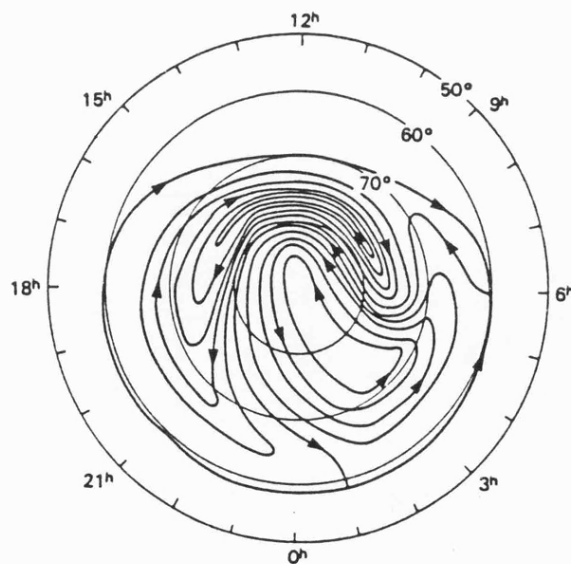


FIGURE 7.8. Convection electric field model after Heppner and Maynard (1987) for negative  $B_y$  and strongly positive  $B_z$ .

reversal at 22:15-22:45 UT. The southward region could be associated with the reversal itself, especially if there was a 'kink' in the dusk cell which allowed SABRE to view first eastward flows, then southward flows associated with the turning of the cell from an antisunward to a sunward flow direction, and subsequently a return to eastward flow on the poleward edge of the cell.

Secondly, the principal eastward to westward flow reversal is very abrupt (occurring in less than 5 minutes), with no evidence of the low electric fields normally associated with the boundaries between convection cells (Nielsen and Greenwald, 1979). This could also be explained in terms of a traversal of the poleward edge of the viscous cell pattern by the viewing area, so that SABRE observed a 'narrow' Harang discontinuity rather than the 'open throat' of low electric fields normally present at the equatorward edge of the discontinuity.

Thirdly, a further short period of southward flow is observed to commence at about 23:30 UT. An examination of the IMF data suggests that this might be associated with a temporary drop of the  $B_z$  component to almost zero, which was detected by the ISEE-3 spacecraft some 20 minutes later. The effect of such a change in IMF conditions could be to enhance the formerly weak reconnection process for a short time. This would allow newly opened flux tubes to convect over the poles in an antisunward direction and in the noon-midnight meridian, producing southward flows in the midnight region of the high latitude ionosphere. This process could also explain the brief southward flow at 2:00 UT.

So far, the discussion has concentrated on an explanation of the gross features of the observations in terms of purely spatial variations in an expanded and temporally stable four cell convection pattern. Alternatively, a sequence of periods of eastward flow and anomalous westward flow, interspersed with comparatively short intervals of southward flow, could arise from temporal variations. Specifically, this

interpretation would require successive expansions and contractions of the convection pattern, with the SABRE viewing area remaining near the Harang discontinuity edge of the dawn cell. SABRE would then observe westward flows for an expanded system and eastward flows for a contracted system. While the system changed from one state to the other, southward flows would be expected.

### 7.3.3 Two cell interpretation

There is the alternative possibility that the SABRE observed flows for 4-5 February, 1983 are not due to a four cell pattern, but rather a highly deformed and temporally variable two cell structure. Heppner and Maynard (1987) reject the concept of multi-cell convection patterns and have proposed, instead, an empirical model for northward IMF which is a rotationally twisted distortion of the 'normal' two cell pattern. Their model for negative  $B_y$  and strongly positive  $B_z$  is reproduced in Figure 7.8. Under conditions of southward IMF, the normal two cell model predicts that as magnetic activity increases, the magnetic local time (MLT) sector of the Harang discontinuity shifts toward the evening hours (Zi and Nielsen, 1982). Heppner and Maynard found no such relationship for northward IMF, and indeed discovered that for  $K_p > 4$ , the Harang discontinuity occurred after 1:00 MLT at the lower latitude boundary of the flow system. Therefore, the west-east flow reversal observed at about 1:30 UT (~3:00 MLT), interpreted above as the signature of a reversion from a four cell pattern to a two cell pattern triggered by the southward turning of the IMF, could alternatively be explained as a simple traversal of the Harang discontinuity, between the dusk and the dawn cell of the pattern depicted in Figure 7.8. The 30 minute interval of very low electric fields, which separates the westward flow from the eastward flow, would tend to support this suggestion.

A further interesting feature of the Heppner and Maynard model is that,

for the geomagnetic and IMF conditions of the present case, it predicts a low-latitude convection boundary which is equatorward of the SABRE field of view. The model may also offer a more satisfactory explanation for the east-west flow reversal between 22:15 and 22:45 UT and the interval of southward flow between 23:30 and 23:45 UT observed by SABRE. An examination of the azimuthal angle of the IMF indicates a correlation between the east-west flow reversal and a change in the polarity of the  $B_y$  component of the IMF from positive to negative detected by ISEE-3 some 30 minutes later. The 23:30-23:45 UT interval of southward flow corresponds to a period during which  $B_y$  turned positive again. These correlations may be interpreted in terms of the  $B_y$  dependence of the local time position of the Harang discontinuity. Both magnetometer (Rodger et al., 1984) and SABRE studies (section 5.3.2) have indicated that a positive (negative) value of  $B_y$  moves the Harang discontinuity to earlier (later) times. The east-west flow reversal could then be explained if the Harang discontinuity shifted rapidly from the west, entering the viewing area at about 22:15 UT, to bring the SABRE field of view completely into the eastward electrojet (westward flow) by about 22:45 UT. An examination of a sequence of high temporal resolution (20 s) SABRE spatial plots, an example of which is illustrated in Figure 7.9 for 22:33 UT, indicates that the westward flow developed from the equatorward edge of the viewing area. Normally, as the SABRE field of view rotates under a temporally stable convection pattern, the Harang discontinuity is characterised by the penetration of eastward flow from the poleward edge of the viewing area (section 5.4). The instantaneous pattern observed at 22:33 UT (Figure 7.9) is highly complex. Regions of eastward flow and southward flow in the north are separated from areas of eastward and westward flow in the south by a diagonally aligned band in which there is no backscatter.

Spatial plots for the interval of southward flow from 23:30 to 23:45 UT reveal that the flow direction actually rotated gradually from west to

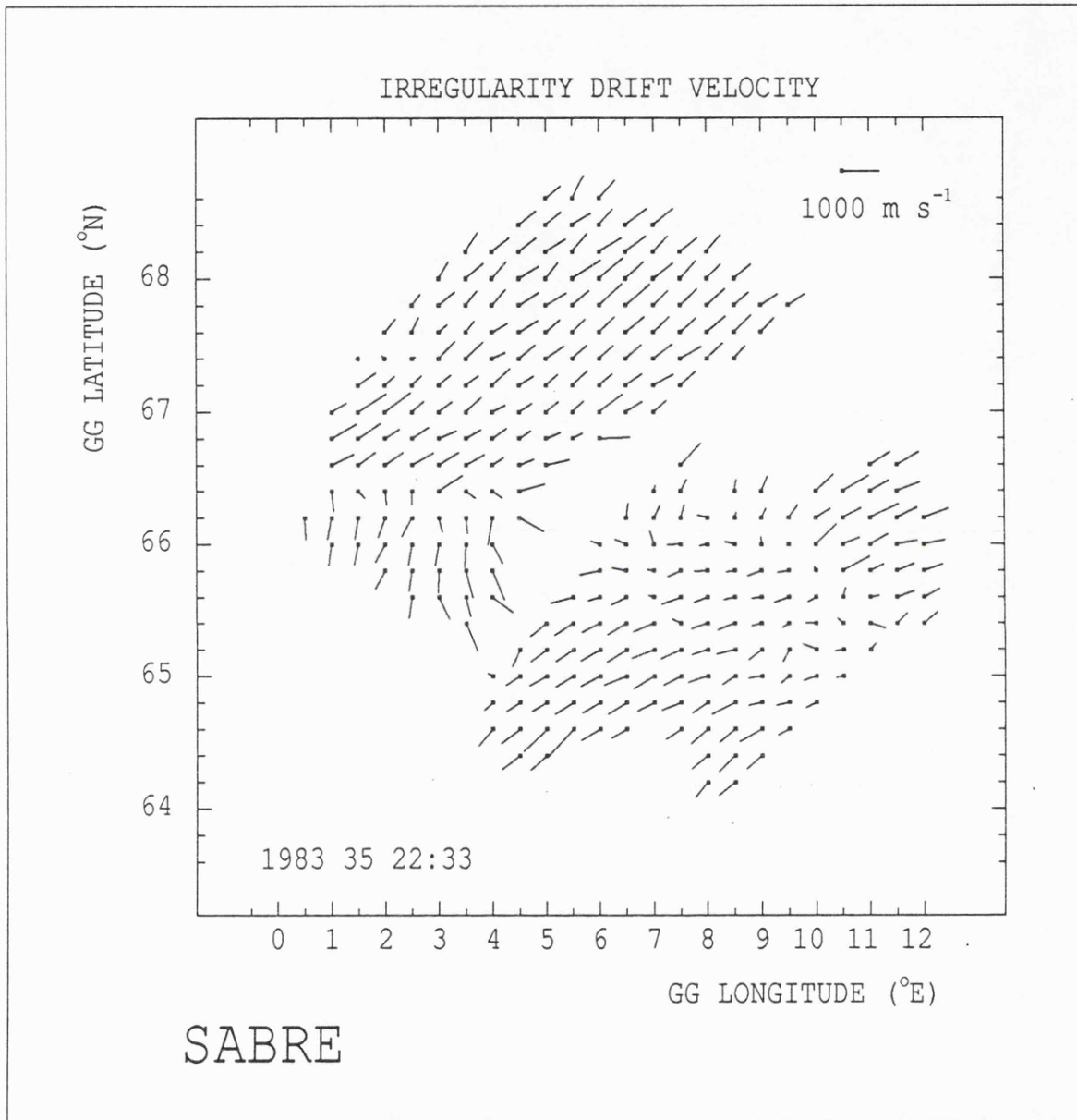


*FIGURE 7.9. SABRE flow velocity observations as a function of latitude and longitude for 4 February, 1983, 22:33 UT. The temporal resolution is 20 s.*

south and then west again, suggesting that when  $B_y$  turned positive, the Harang discontinuity edge of the dusk cell approached the SABRE viewing area from the east and then retreated when  $B_y$  turned negative again. This supposition is supported by the spatial flow pattern observed at 23:38 UT (Figure 7.10), in which the flows steadily changed direction from south-west in the equatorward edge of the viewing area, to southward in the middle, and finally to south-east in the poleward boundary. However, at several times throughout the midnight sector, a very considerable degree of structure existed in the flow pattern (Figure 7.9), and in particular strong velocity shears were frequently observed. This complicates attempts to interpret the SABRE measurements in terms of a simple model. In addition, there is no obvious mechanism in terms of the Heppner model for the period of south-westward flow between 21:30 and 21:50 UT, since it does not appear to correlate with any IMF variation.

#### 7.3.4 Observations for 25 March, 1983

There is one other day, 25 March (day 84), 1983, in which strong nightside convection flows observed by SABRE have been identified as an interval of intensely northward IMF. At this time, the ISEE-3 spacecraft was located at approximately GSE  $X = -100$ ,  $Y = -14$ ,  $Z = 4 R_E$ , and was thus in the vicinity of the far tail. The abrupt increase in the measured flow velocity from 200 to 500  $\text{km s}^{-1}$ , and the equally sudden density enhancement of about 2 to 8 particles  $\text{cm}^{-3}$  at 20:30 UT (Figure 7.11), are indicative of the crossing of ISEE-3 from the tail region into the solar wind, where it remained except for a short interval around 2300 UT, when it was swept temporarily back into the tail. Assuming a solar wind velocity of  $500 \pm 100 \text{ km s}^{-1}$  during the interval 20:30-24:00 UT, the time delay which must be applied to compare the satellite measurements with the SABRE observations is given by

$$\tau = -100 R_E / (500 \pm 100 \text{ km s}^{-1}) = -21 \pm 4 \text{ mins}$$

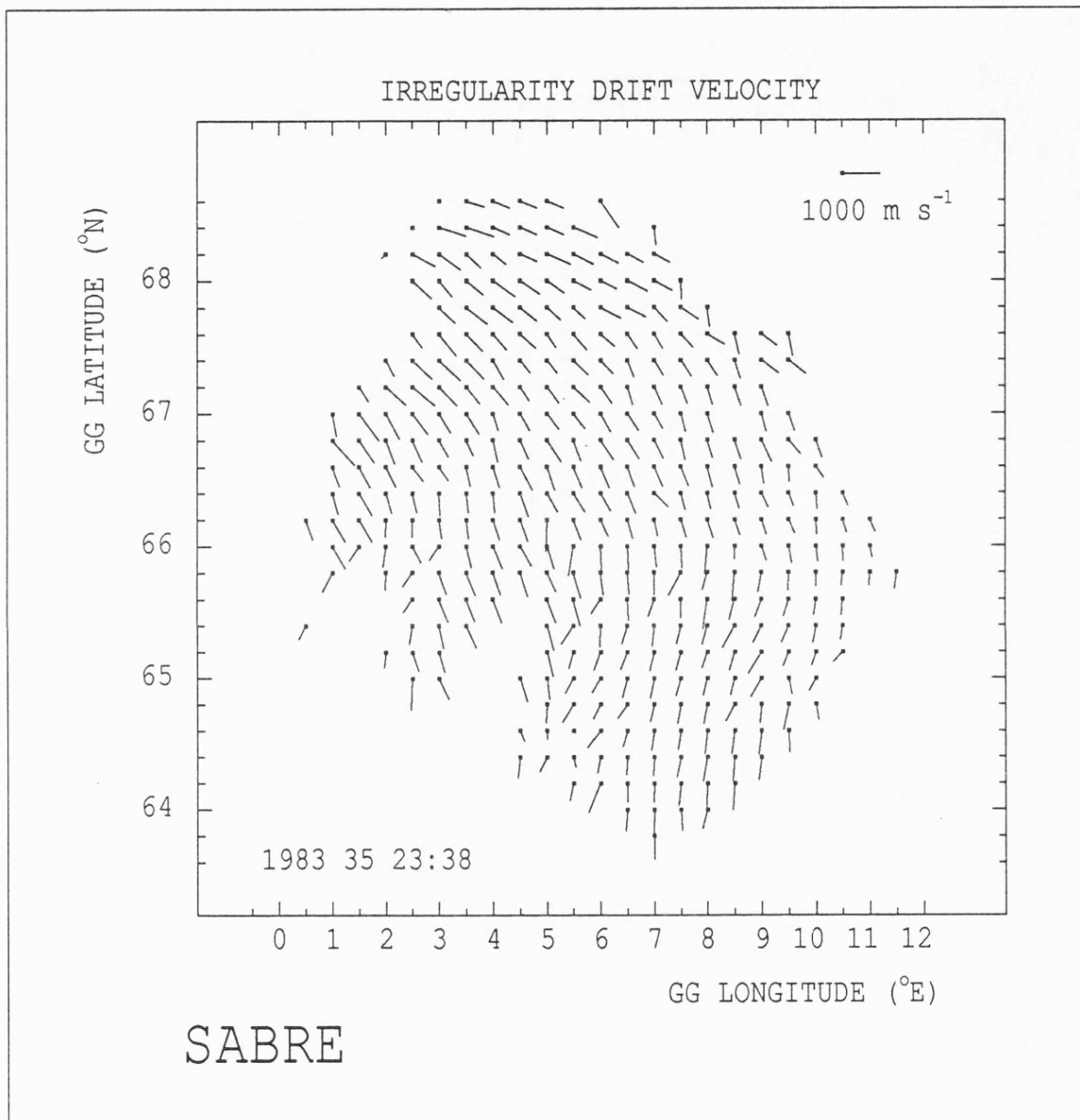
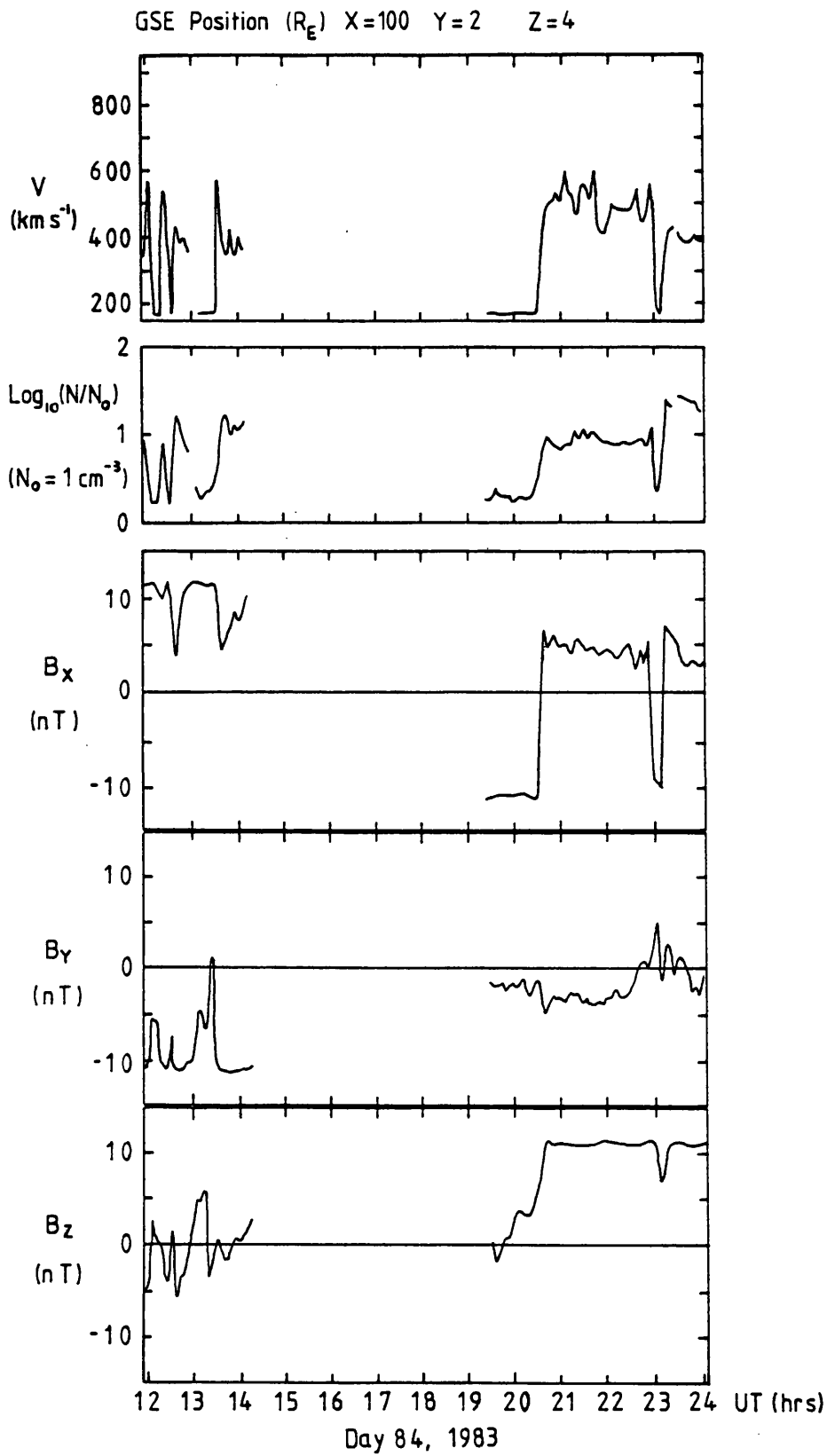


FIGURE 7.10. Same as Figure 7.9 for 4 February, 1983, 23:38 UT.



**FIGURE 7.11.** ISEE-3 plasma and magnetic field data for the interval 12:00 to 24:00 UT, 25 March, 1983.

The magnetometer data from the ISEE-3 spacecraft indicate that the IMF exhibited a strong northward component, with  $B_z$  in excess of 10 nT.  $B_x$  was in the range 2 to 5 nT and  $B_y$  was between -5 and 0 nT. At approximately 22:50 UT, the density of the solar wind plasma, which had been  $\sim 8$  particles  $\text{cm}^{-3}$ , began to rise, and by about 23:15 UT (after the brief excursion of the satellite back into the magnetosphere) the density had attained a value of  $\sim 25$  particles  $\text{cm}^{-3}$ .

The SABRE measurements for the period 25 March, 19:00 UT to 26 March, 1:00 UT are presented in Figure 7.12, which illustrates the 5 minute average convection flow velocities, as a function of geographic latitude, for the longitudinal interval  $5^\circ$ - $7^\circ$  E. The flow direction is purely westward until approximately 23:30 UT, when there are the first indications of eastward flows developing from the poleward edge of the viewing area. Between about 22:00 and 23:00 UT, there is a significant increase in the strength of the flows, and this could be associated with the increase by a factor of about 3 in the solar wind particle density detected by ISEE-3 at  $\sim 23:00$  UT. The gradual turning at approximately 23:30 UT of the convection flow direction from west, through south, to east, which is illustrated more clearly in the sequence of spatial plots for 23:20 to 23:49 UT (Figure 7.13), is consistent with the arrival in the SABRE field of view of the edge of the dusk cell just prior to the appearance of the Harang discontinuity. The evidence for this supposition is not conclusive since 10 minutes later, the backscatter disappeared, although the persistence of westward flow until at least 23:30 UT ( $\sim 1:15$  MLT) does place a lower limit on the Harang discontinuity occurrence time.

The investigation in chapter 5 suggested that for SABRE  $T_{HD}$  is seldom later than about 22:30 UT, even for very quiet conditions, and yet the value of  $K_p$  of 4+ for the 21-24 hour UT interval indicates that geomagnetic conditions were moderately disturbed. An examination of the AE index for the evening of 25 March, 1983 demonstrates that there was intense substorm

SABRE IRREGULARITY DRIFT VELOCITY

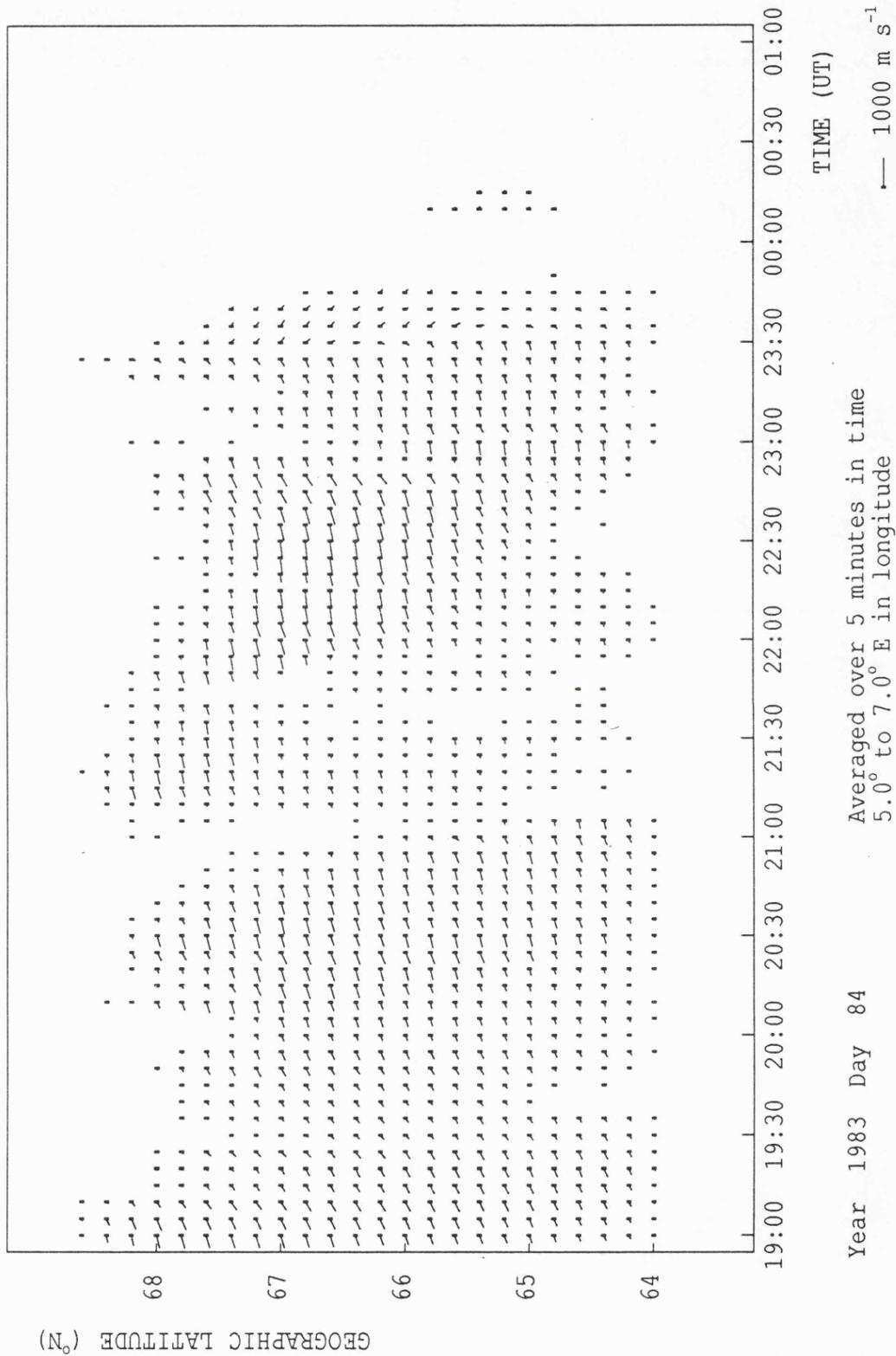


FIGURE 7.12. SABRE flow velocity observations for 25 March, 1983, 19:00 UT to 01:00 UT, when  $B_z > 10$  nT.

SABRE IRREGULARITY DRIFT VELOCITIES

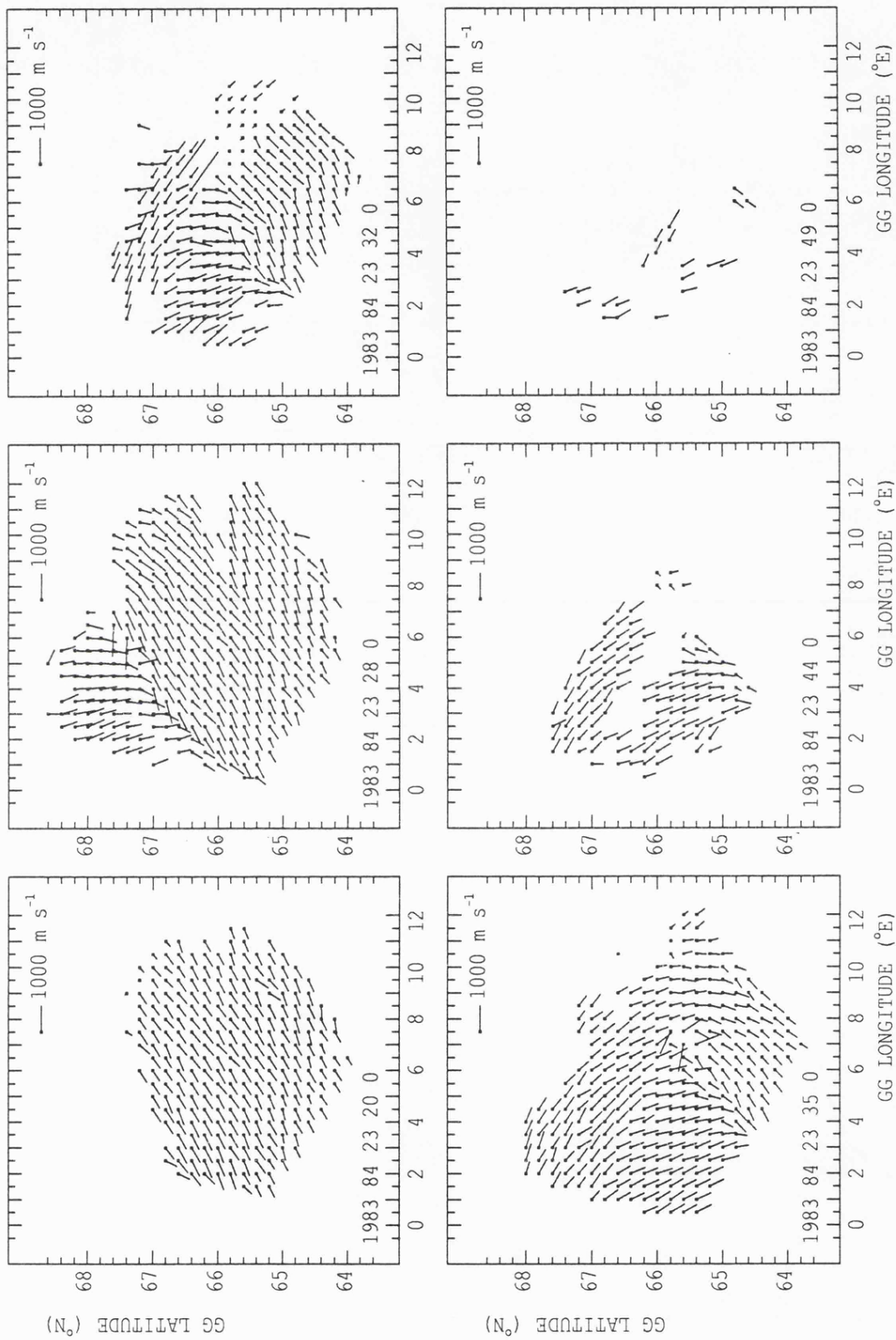


FIGURE 7.13. Sequence of SABRE spatial plots (flow velocities as a function of latitude and longitude) for 23:20 to 23:49 UT, 25 March, 1983.

activity earlier on, with AE peaking at approximately 1400 nT at 19:45 UT, although activity decreased rapidly thereafter, so that the average value of AE for the interval 21:00 to 24:00 UT was only about 100 nT.

The observed flows for this day, which are far less turbulent than for the previous example (4-5 February, 1983), could be explained either in terms of the four cell model by a traversal of the equatorward edge of the dusk viscous cell, or equally well by the Heppner and Maynard (1987) model. In particular, the latter predicts the post-midnight occurrence of the Harang discontinuity for strongly positive  $B_z$  and negative  $B_y$ .

#### 7.4 Summary

Two case studies of auroral nightside ionospheric convection flows, observed by SABRE during very strongly northward IMF, have been presented. Under this condition, a four cell pattern with a boundary well poleward ( $\sim 75^\circ$  N geomagnetic latitude) of the SABRE viewing area is normally predicted. In contrast to this simple model, on 4-5 February, 1983, SABRE observed intense and anomalously directed flows which persisted until the IMF turned south. Thereafter, the measured flows are consistent with a return of the convection pattern to the usual two cell system. It appears that existing four cell models do not extend to very large positive values of  $B_z$  and extremely high solar wind flow speeds. A crude modification of the four cell model, involving the expansion of the viscous cells into the latitude range covered by SABRE, may explain the major characteristics of the flow observations but not the short time scale ( $< 30$  minutes) features. In particular, the convection flows seem to be very sensitive to short term variations in the orientation of the IMF, which is difficult to explain if the observed flows are driven by the viscous interaction mechanism. Consequently, an attempt has been made to interpret the observations in terms of a rotationally twisted two cell pattern driven by reconnection.

This model is rather more successful in explaining the observations, especially the apparent correlation between the ionospheric flows and the  $B_y$  component of the IMF. However, neither of the two models appear to offer a complete and self consistent interpretation of the measurements.

On 25 March, 1983, the observed convection flows are much less turbulent, although the IMF conditions ( $B_z > 10$  nT) are similar to those of 4-5 February, 1983. Consequently, it is much easier to interpret the 25 March observations in terms of a simple, temporally stable model. An explanation based on the traversal of the equatorward edge of the dusk viscous cell assumes that the pattern was contracted relative to the flow system for 4-5 February, 1983. The difference in the characteristics of the flows observed on the two different days may be due to the fact that on 4-5 February the solar wind velocity was exceptionally high ( $\sim 900$  km s<sup>-1</sup>) whereas on 25 March the velocity had a fairly typical value ( $\sim 500$  km s<sup>-1</sup>).

In conclusion, the Heppner model is probably better able to account for the SABRE observations than the four cell model, which is unsatisfactory even after substantial modifications. Low altitude polar orbiting satellites have produced many important results, but attempts to infer two dimensional maps of the large scale convection pattern for strongly northward IMF from the one dimensional profiles which satellites provide, may have led to incorrect conclusions regarding the coupling mechanism under these conditions. To establish the solar wind-magnetosphere coupling mechanism for such very extreme interplanetary conditions requires more extensive convection flow observations for positive  $B_z$  by systems which have large spatial coverages in both the auroral zone and the polar cap.

## CHAPTER 8

### CONCLUSIONS

#### 8.1 Introduction

This thesis describes an experimental investigation of the solar wind-magnetosphere-ionosphere coupling mechanism by means of SABRE and STARE observations of the high latitude ionospheric convection flow pattern. The coherent auroral radar technique is particularly suitable for this type of study, because of its excellent temporal and spatial resolution. The ability to distinguish between spatial and temporal changes provides important advantages over satellite and ground based magnetometer and incoherent radar techniques for observing the convection pattern. In addition, the timespan and continuity of the SABRE data base has been vital to the success of the statistical approaches adopted in some parts of the study.

#### 8.2 Principal results

It has been established that the backscatter intensity measured by the coherent auroral radar technique is a useful parameter for geophysical studies, indicating the strength of the solar wind-magnetosphere interaction and providing information on the structure of the solar current sheet. The backscatter power exhibits a strong long term dependence on the solar wind flow velocity, but is modulated in the short term by the  $B_z$  component of the IMF (Chapter 4). This empirical result is explained in the context of current models of the magnetospheric interaction with the

interplanetary medium and by relating it to a new theory of the radar backscatter mechanism (Robinson et al., 1987). Strong long term periodicities are found in the backscatter data which suggest that the two sector structure of the solar wind is a more prevalent feature than has been previously indicated by investigations employing geomagnetic indices.

A statistical study of the convection flows measured by SABRE provides IMF dependent empirical models of the convection pattern at sub-auroral latitudes (Chapter 5). The results are consistent with the control by  $B_z$  of the latitudinal extent of the large scale convection pattern and there is clear evidence of a  $B_y$  dependent asymmetry in the structure of the Harang discontinuity. The sense of the asymmetry is consistent with the theory of Cowley (1981), but at variance with the empirical model of Burch et al. (1985).

High spatial resolution, two dimensional maps of the ionospheric projection of the dayside magnetic merging process, for both polarities of IMF  $B_y$ , are presented for the first time (Chapter 6). With their large simultaneous spatial coverages, the SABRE and STARE systems provide the unparalleled facility to resolve temporal and spatial variations in the cusp flow pattern. The occurrence of the ionospheric footprint of the cusp at SABRE latitudes is rare, requiring very strongly southward IMF conditions. The structure of the observed flows is temporally highly variable, but can be interpreted in terms of  $B_y$  dependent models of the dayside flow pattern.

Two examples of strong nightside flows measured by SABRE during intense northward IMF conditions ( $B_z > 10$  nT) indicate that the convection pattern can have a much larger latitudinal extent than predicted by established reconnection mechanisms for positive  $B_z$  (Chapter 7). In one case, the structure of the observed flow pattern is very difficult to explain in terms of the four cell model for northward IMF which has previously been proposed to explain observations by low altitude satellites of sunward flow

in the polar cap (eg. Reiff and Burch, 1985). The SABRE observations are rather easier to interpret in terms of a rotationally distorted 2 cell pattern for positive  $B_z$  (Heppner and Maynard, 1987). However, a high degree of temporal variability must be invoked in order to explain the observations in terms of either model.

These investigations have clearly demonstrated that SABRE is a powerful tool for ionosphere-magnetosphere research. A number of new results have been obtained and suggestions are now made for further studies based on the work already completed.

### 8.3 Suggestions for further work

There are indications in the spectra of the Wick backscatter intensities (Chapter 4) of the presence of the semiannual and annual variations. Assuming that the Wick radar continues in operation for several more years, it should be possible to investigate these changes further. In addition, it will be interesting to test the ionospheric response to changes in the stability of the solar current sheet structure over the solar cycle. For an ascending phase of the solar cycle, when the current sheet structure is expected to become increasingly chaotic, the  $T_s$  and  $T_s/2$  peaks in the power spectrum of the backscatter intensity data should reduce in strength and possibly become spread compared with the present result. A detailed investigation of these long term changes is required.

The statistical study of the relationship between SABRE measured convection flows and the IMF (Chapter 5) relied on 1 hour averages of the latter. This investigation could be greatly enhanced if long intervals of IMF data with a temporal resolution which approached that of SABRE (eg. 1 minute) were to become available. Given the fast response times (a few minutes) of the ionospheric flows to changes in the IMF, this would significantly improve the correlations. In addition, if sufficient STARE

data were combined with SABRE in the statistical data base, the latitudinal coverage of the empirical models could be doubled.

The comprehensive investigation of cusp flows (Chapter 6) observed by SABRE in the geomagnetic latitude range  $61^{\circ}$ – $66^{\circ}$  N should be repeated for STARE. Since STARE observes a higher latitude range ( $64^{\circ}$ – $69^{\circ}$  N, geomagnetic) of the convection pattern and the STARE data base is approximately the same size, the number of cusp events should be larger. SABRE and STARE only observe cusp flows for high levels of geomagnetic activity. In the longer term, therefore, the cusp flow pattern should be investigated for a range of geomagnetic and interplanetary conditions. This would require a poleward extension ( $> 69^{\circ}$  N, geomagnetic) of the SABRE/STARE latitudinal range by the construction of a similar system at higher latitudes.

The latter suggestion is equally applicable to the study of the large scale convection pattern for strongly northward IMF, since the observations presented in Chapter 7 are extremely rare due to the statistically low probability of flows appearing in the SABRE viewing area for  $B_z > 10$  nT. One dimensional profiles measured by satellites and ground based incoherent systems tend to give ambiguous results. Detailed two dimensional maps of the convection pattern of the type provided by SABRE and STARE are essential in order to resolve the controversy over the structure of the pattern for northward IMF.

There are a number of current and proposed international collaborative studies of the solar terrestrial interaction, which aim to quantify the energy transferred and the global ionospheric response to a given solar wind/magnetosphere input. Some of these studies involve both theoretical and empirical modelling, together with global monitoring of the ionosphere-magnetosphere system. SABRE is capable of making an important contribution to such programmes and already plays a major role in SUNDIAL (Chapter 4). Future SUNDIAL campaigns and other programmes such as the

World Ionosphere Thermosphere Study (WITS) and the Global Ionosphere Thermosphere Coupling And Dynamics (GITCAD) study will also involve SABRE.

Future spacecraft missions, which are planned as part of the International Solar Terrestrial Physics programme (ISTP), include the Solar and Heliosphere Observatory (SOHO) and Cluster. SOHO will be placed between the Sun and the Earth at the sunward libration point ( $\sim 200 R_E$  upstream of the Earth), to make high resolution solar spectroscopy, helioseismology and solar wind measurements. The Cluster mission will consist of four spacecraft, equipped to make field and plasma measurements of the magnetosphere, which will occupy a high inclination elliptic Earth orbit. These spacecraft, in conjunction with ground based diagnostics of the upper atmosphere such as SABRE, will monitor each element in the causal chain which starts at the surface of the sun and leads, via the solar wind, to the magnetosphere and finally to the ionosphere and the lower atmosphere.

#### 8.4 Concluding remarks

The coherent radar technique provides a powerful tool for a wide range of auroral zone studies. Improvements are now being made to the experimental technique (e.g. the development of SADIE to measure the height of the backscatter) which in the future will enable more detailed studies of both the plasma physics and the geophysics of the auroral region to be undertaken.

## Appendix A: Spectral analysis techniques

Power spectrum analysis is a valuable tool for identifying the fundamental periodicities in a time series, since the periodicities appear as quite sharp peaks, rising above a continuous noise background in the spectral curves. Lines with high signal to noise ratios are likely to correspond to real physical mechanisms. Techniques which are commonly employed for the processing of geophysical signals include Fourier analysis and the maximum entropy method.

### A1 Fourier analysis

The power spectral density function or auto-spectrum of a time series of data provides a frequency domain description of the data. It represents the contribution to the total variance in the signal of components at a given frequency. The Fourier transform of a continuous function of time  $x(t)$  is a complex function of frequency ( $f$ )

$$X(\omega) = \int_{-\infty}^{\infty} x(t) e^{-i\omega t} dt = A(\omega) - iB(\omega) \quad (\text{A1.1})$$

where  $\omega = 2\pi f$ . The auto spectrum is then defined as

$$P(\omega) = |X(\omega)|^2 = A(\omega)^2 + B(\omega)^2$$

Real digital data consists of a series of samples of  $x(t)$ . Time is therefore quantised and the integration in Equation (A1.1) becomes a summation over a finite length of data. The discrete Fourier transform of  $x(t)$  is

$$X_n = (1/N) \sum_j x_j \exp(-i2\pi j n/N)$$

Because  $X_n$  is symmetric about zero, an  $N$  point series in the time domain transforms to an  $N/2$  point series in the frequency domain. A data length of  $T$  days produces spectral estimates with a frequency spacing of  $1/T$  cycles/day. If the sampling interval is  $\Delta t (=T/N)$ , then the maximum frequency which can be investigated is  $1/2\Delta t$  (the Nyquist frequency).

In the present study, a Fast Fourier Transform (FFT) routine from the NAG library on the SABRE analysis Prime 750 computer was employed. The FFT algorithm calculates discrete Fourier coefficients very efficiently, by eliminating repetition in parts of the calculation and so reducing the number of operations from  $N^2$  to  $N\log_2 N$ .

#### A2 Smoothing techniques

The discrete nature of the data makes it impossible to recognise harmonic components whose frequencies are not integer multiples of the frequency spacing. The power at such a component is therefore distributed over a range of frequencies, giving rise to a spreading of the spectral peaks termed 'leakage'. In addition, a finite data set is effectively operated upon by a rectangular window and this also leads to leakage. Applying a cosine bell to the data has the effect of 'rounding off' the edges of the data set. With this method the first  $\beta\%$  (in time) of the data set is transformed by the following expression

$$x_j^* = x_j \cdot \cos[100j\pi/(2\beta.N) - \pi/2]$$

and the last  $\beta\%$  with

$$x_j^* = x_j \cdot \cos[100(N-j)\pi/(2\beta.N) - \pi/2]$$

The middle  $(100-2\beta)\%$  of the data set is unchanged. In the present analysis, a value of 10% was chosen for  $\beta$ .

Leakage may also be reduced by employing a triangular data window (Hanning window) on all the elements of the series, either in the time domain or the frequency domain. In this thesis, the window consisted of a 5 point running mean, incorporating weights of  $(1/9, 2/9, 3/9, 2/9, 1/9)$ . The technique is equivalent to the application of a low pass filter which removes high frequencies corresponding to periods of less than 5 days.

### A3 The maximum entropy method

The maximum entropy method (MEM) is usually considered to be superior to Fourier analysis for the identification of spectral lines when a limited set of data is available (Villante and Francia, 1986, and references therein) particularly since, in contrast to the Fourier method, the frequency resolution of an MEM spectrum does not depend on the length of the data. A detailed account of the technique is given in Ulrych and Bishop (1975), and the computer programme employed in the present study was derived from this paper. A listing of the programme is available at Leicester.

MEM consists of two independent steps. The first of these is the so-called Burg technique which determines a prediction error filter (PEF) with  $m$  weights which, when run in both directions over the  $M$  data points, minimises the mean square prediction error. Since the data are being used to predict later (or earlier) values of the data, the method is also called autoregressive. The second step employs the  $m$  prediction error coefficients in an expression to estimate the power spectral density by maximising the entropy or information content of the available data, subject to constraints. The technique produces smooth spectra which may provide very accurate determinations of the period of a variation. MEM nonetheless suffers from several disadvantages, principally that the smoothness and stability of the maximum entropy spectrum is very sensitive to the choice of the ratio  $m/M$  (de Meyer and de Vuyst, 1982).

References

- Akasofu, S. -I., 1964, *Planet. Space Sci.* 12, 273.
- Akasofu, S. -I., 1974, *Space Sci. Rev.* 16, 617.
- Akasofu, S. -I., 1977, *Physics of Magnetospheric Substorms*, D. Reidel, Dordrecht, Netherlands.
- Akasofu, S. -I., 1981, *Space Sci. Rev.*, 28, 121.
- Akasofu, S. -I., and Fry, C. F., 1986, *Planet. Space Sci.* 34, 77.
- Akasofu, S. -I., Yasuhara, F., and Kawasaki, K., 1973a, *Planet. Space Sci.* 21, 2232.
- Akasofu, S. -I., Perreault, P. D., Yasuhara, F., and Meng, C. -I., 1973b, *J. Geophys. Res.* 78, 7490.
- Alcaydé, D., Caudal, G., and Fontanari, J., 1986, *J. Geophys Res.* 91, 233.
- Alexeev, I. I., 1986, *J. Geomag. Geoelectr.* 38, 1199.
- Alfvén, H., 1977, *Rev. Geophys. Space Phys.* 15, 271.
- André, D., 1983, *J. Geophys. Res.* 88, 8043.
- Armstrong, J. C., and Zmuda, A. J., 1970, *J. Geophys. Res.* 75, 7122.
- Arnoldy, R. L., 1971, *J. Geophys. Res.* 76, 5189.
- Arora, B. R., and Rangarajan, G. K., 1981, *J. Geophys. Res.* 86, 3369.
- Axford, W. I., and Hines, C. O., 1961, *Can. J. Phys.* 39, 1433.
- Baker, D. N., Hones, E. W., Jr., Payne, J. B., and Feldman, W. C., 1981, *Geophys. Res. Lett.* 8, 179.
- Baker, D. N., Zwickl, R. D., Bame, S. J., Hones, E. W., Jr., Tsurutani, B. T., Smith, E. J., and Akasofu, S. -I., 1983, *J. Geophys. Res.* 88, 6230.

Baker, D. N., Bame, S. J., Belian, R. D., Feldman, W. C., Gosling, J. T., Higbie, P. R., Hones, E. W., Jr., McComas, D. J., and Zwickl, R. D., 1984, *J. Geophys. Res.* **89**, 3855.

Baker, D. N., Bargatze, L. F., and Zwickl, R. D., 1986, *J. Geomag. Geoelectr.* **38**, 1047.

Baker, D. N., Anderson, R. C., and Zwickl, R. D., 1987, *J. Geophys. Res.* **92**, 71.

Bame, S. J., Asbridge, J. R., Felthouser, H. E., Glore, J. P., Hawk, H. L., and Chaves, J., 1978, *IEEE Trans. Geosci., GE-16*, 160.

Banks, P. M., Doupnik, J. R., and Akasofu, S. -I., 1973, *J. Geophys. Res.* **78**, 6607.

Baumjohann, W., 1983, *Adv. Space Rev.* **2**, 55.

Baumjohann, W., and Glassmeier, K. H., 1984, *Planet. Space Sci.* **32**, 1361.

Baumjohann, W., Pellinen, R. J., Opgenoorth, H. J., and Nielsen, E., 1981, *Planet. Space Sci.* **29**, 431.

de la Beaujardière, O., Wickwar, V. B., and Kelley, J. D., 1985, *Geophys. Res. Lett.* **12**, 461.

Berko, F. W., 1973, *J. Geophys. Res.* **78**, 1615.

Berko, F. W., Hoffman, R. A., Burton, R. K., and Holzer, R. E., 1975, *J. Geophys. Res.* **80**, 37.

Bevington, P. R., 1969, *Data Reduction and Error Analysis for the Physical Sciences*, McGraw-Hill, New York.

Birkeland, K., 1908, *The Norwegian Aurora Polaris Experiment, 1902-1903*, Vol. 1, Aschoug, Christiana, Norway.

Buneman, O., 1963, *Phys. Rev. Lett.* **10**, 285.

Burch, J. L., 1972, *J. Geophys. Res.* **77**, 6696.

Burch, J. L., 1973, *Radio Sci.* 8, 955.

Burch, J. L., 1979, *Space Sci. Rev.*, 23, 449.

Burch, J. L., Reiff, P. H., Menietti, J. D., Heelis, R. A., Hanson, W. B., Shawhan, S. D., Shelley, E. G., Sugiura, M., Wiemer, D. R., and Winningham, J. D., 1985, *J. Geophys. Res.* 90, 1577.

Burlaga, L. F., 1983, *Rev. Geophys. Space Phys.* 21, 363.

Burke, W. J., and Doyle, M. A., 1986, *J. Geomag. Geoelectr.* 38, 1115.

Burke, W. J., Kelley, M. C., Sagalyn, R. C., Smiddy, M., and Lai, S. T., 1979, *Geophys. Res. Lett.* 6, 21.

Burrage, M. D., 1986, *Auroral Radar Aspect Angles*, Ionospheric Physics Group Technical Report No. 41, University of Leicester.

Burrage, M. D., Waldock, J. A., Jones, T. B., and Nielsen, E., 1985, *Nature* 316, 133.

Burton, R. K., McPherron, R. L., and Russell, C. T., 1975, *J. Geophys. Res.* 80, 4204.

Bythrow, P. F., Burke, W. J., Potemra, T. A., Zanetti, L. J., and Lui, T. Y., 1985, *J. Geophys. Res.* 90, 5319.

Caan, M. N., McPherron, R. L., and Russell, C. T., 1977, *J. Geophys. Res.* 82, 4837.

Cauffman, D. P., and Gurnett, D. A., 1971, *J. Geophys. Res.* 76, 6014.

Chapman, S., 1918, *Proc. Roy. Soc.* A95, 61.

Chapman, S., and Ferraro, V. C. A., 1932, *Terr. Magn.* 37, 147.

Chapman, S., and Bartels, J., 1940, *Geomagnetism*, Clarendon Press, Oxford, U. K..

Clauer, C. R., McPherron, R. L., Searls, C., and Kivelson, M. G., 1981, *Geophys. Res. Lett.* 8, 915.

Courtillot, V., Le Mo  el, J. L., and Mayaud, P. N, 1977, *J. Geophys. Res.*, 82, 2641.

Cowley, S. W. H., 1973, *Radio Sci.* 8, 903.

Cowley, S. W. H., 1981, *Planet. Space Sci.* 29, 79.

Cowley, S. W. H., 1982, In *The Physical Basis of the Ionosphere in the Solar-Terrestrial System*, p. 4-1, AGARD, Neuilly-sur-Seine, France.

Cowley, S. W. H., 1984, In *Proc. Conf. Achievements of the IMS, 26-28 June, 1984*, ESA SP-217, Graz, Austria.

Cowley, S. W. H., 1986, *J. Geomag. Geoelectr.* 38, 1223.

Crooker, N. U., 1979, *J. Geophys. Res.* 84, 951.

Crooker, N. U., 1980, *J. Geophys. Res.* 85, 575.

Delouis, H., and Mayaud, P. N.; 1975, *J. Geophys. Res.* 80, 4681.

Dungey, J. W., 1961, *Phys. Rev. Lett.* 6, 47.

Eastman, T. E., Hones, E. W. Jr., Bame, S. J., and Asbridge, J. R., 1976, *Geophys. Res. Lett.* 3, 685.

Eather, R. H., 1985, *J. Geophys. Res.* 90, 1569.

Eather, R. H., Mende, S. B, and Weber, E. J, 1979, *J. Geophys. Res.* 84, 3339.

Fairfield, D. H., and Cahill, L. J., 1966, *J. Geophys. Res.* 71, 155.

Farley, D. T., 1963, *J. Geophys. Res.* 68, 5083.

Farley, D. T., 1985, *J. Atmos. Terr. Phys.* 47, 729.

Farley, D. T., Ierkik, H. M., and Fejer, B. G., 1981, *J. Geophys. Res.* 86, 1569.

Fedder, J. A., and Lyon, J. G., 1987, *Geophys. Res. Lett.* 14, 880.

Fejer, D. T., and Kelley, M. C., 1980, *Rev. Geophys. Space Phys.* 18, 401.

Feldman, W. C., Asbridge, J. R., Bame, S. J., Montgomery, M. D., and Gary, S. P., 1975, *J. Geophys. Res.* 80, 4181.

Feldstein, Y. I., 1963, *Geomagn. Aeron.* 3, 183.

Fenimore, E. E., Asbridge, J. R., Bame, S. J., Feldman, W. C., and Gosling, J. T., 1978, *J. Geophys. Res.* 83, 4353.

Foster, J. C., Banks, P. M., and Doupnik, J. R., 1982, *J. Geophys. Res.* 87, 7513.

Frandsen, A. M. A., Connor, B. V., Van Amersfoort, J., and Smith, E. J., 1978, *IEEE Trans. Geosci., GE-16*, 195.

Friis-Christensen, E., and Wilhjelm, J., 1975, *J. Geophys. Res.* 80, 1248.

Friis-Christensen, E., Lassen, K., Wilhjelm, J., Wilcox, J. M., Gonzalez, W., and Colburn, D. S., 1972, *J. Geophys. Res.* 77, 3371.

Galeev, A. A., Coroniti, F. V., and Ashour-Abdalla, M., 1978, *Geophys. Res. Lett.* 5, 707.

Gosling, J. T., Asbridge, J. R., Bame, S. J., and Feldman, W. C., 1976, *J. Geophys. Res.* 81, 5061.

Gosling, J. T., Asbridge, J. R., Bame, S. J., Feldman, W. C., Paschmann, G., Sckopke, N., and Russell, C. T., 1982, *J. Geophys. Res.* 87, 2147.

Greenwald, R. A., Ecklund, W. A., and Balsley, B. B., 1975, *J. Geophys. Res.* 80, 3635.

Greenwald, R. A., Weiss, W., Nielsen, E., and Thomas, N. R., 1978, *Radio Sci.* 13, 1021.

- Harang, L., 1946, *J. Geophys. Res.* 51, 353.
- Hasegawa, M., 1940, In *Trans. Washington Meeting, IUGGATME, Bull.* 11, 311, A. H. R. Goldie (ed.), Edinburgh.
- Heelis, R. A., 1979, In *Magnetospheric Boundary Layers*, B. Battrick (ed.), p.175, ESA SP-148, Noordwijk, Netherlands.
- Heelis, R. A., 1984, *J. Geophys. Res.* 89, 2873.
- Heelis, R. A., Hanson, W. B., and Burch, J. L., 1976, *J. Geophys. Res.* 81, 3803.
- Heelis, R. A., Reiff, P. H., Winningham, J. D., and Hanson, W. B., 1986, *J. Geophys. Res.* 91, 5817.
- Heppner, J. P., 1972a, *Geophys. Publ.* 29, 105.
- Heppner, J. P., 1972b, *Planet. Space Sci.* 20, 1475.
- Heppner, J. P., 1972c, *J. Geophys. Res.* 77, 4877.
- Heppner, J. P., 1973, *Radio Sci.* 8, 933.
- Heppner, J. P., 1977, *J. Geophys. Res.* 82, 1115.
- Heppner, J. P., and Maynard, N. C., 1987, *J. Geophys. Res.* 92, 4467.
- Hill, T. W., 1983, In *Solar-Terrestrial Physics*, R. L. Carovillano and J. M. Forbes (eds.), p. 261, D. Reidel, Dordrecht, Netherlands.
- Holt, J. M., Wand, R. H., Evans, J. V., and Oliver, W. L., 1987, *J. Geophys. Res.* 92, 203.
- Holzer, R. E., and Slavin, J. A., 1982, *J. Geophys. Res.* 87, 2558.
- Holzworth, R. H., and Meng, C. -I., 1975, *Geophys. Res. Lett.* 2, 377.

Hones, E. W., Jr., Baker, D. N., Bame, S. J., Feldman, W. C., Gosling, J. T., McComas, D. J., Zwickl, R. D., Slavin, J. A., Smith, E. J., and Tsurutani, B. T., 1984, *Geophys. Res. Lett.* 11, 5.

Horwitz, J. L., and Akasofu, S. -I., 1977, *J. Geophys. Res.* 82, 2723.

Horwitz, J. L., Doupnik, J. R., and Banks, P. M., 1978, *J. Geophys. Res.* 83, 1463.

Iijima, T., and Potemra, T. A., 1976, *J. Geophys. Res.* 81, 2165.

Iijima, T., Fujii, R., Potemra, T. A., and Saflekos, N. A., 1978, *J. Geophys. Res.* 83, 5595.

Iijima, T., Potemra, T. A., Zanetti, L. J., and Bythrow, P. F., 1984, *J. Geophys. Res.* 89, 7441.

Kamide, Y., 1982, *Space Sci. Rev.* 31, 127.

Kamide, Y., Burch, J. L., Winningham, J. D., and Akasofu, S. -I., 1976, *J. Geophys. Res.* 81, 698.

Kamide, Y., Ahn, B. -H., Akasofu, S. -I., Baumjohann, W., Friis-Christensen, E., Kroehl, H. W., Maurer, H., Richmond, A. D., Rostoker, G., Spiro, R. W., Walker, J. K., and Zaitsev, A. N., 1982, *J. Geophys. Res.* 87, 8228.

Kawasaki, K., Akasofu, S. -I., Yasuhara, F., and Meng, C. -I., 1971, *J. Geophys. Res.* 76, 6781.

King, J. H., 1982, In *The IMS Source Book*, Russell, C. T. and Southwood, D. J. (ed.), American Geophysical Union, Washington D. C..

Koehler, J. A., Sofko, G. J., and Mehta, V., 1985, *Radio Sci.* 20, 689.

Kokubun, S., McPherron, R. L., and Russell, C. T., 1977, *J. Geophys. Res.* 82, 74.

Leont'yev, S. V., and Lyatskiy, W. B., 1974, *Planet. Space Sci.* 22, 811.

- Maeda, K., Tsuda, T., and Maeda, H., 1963, Rpt. Ionosph. Space Res. 17, 147.
- Mansurov, S. M., 1969, Geomag. Aeronom. 9, 622.
- Matsushita, S., and Trotter, D. E., 1980, J. Geophys. Res. 85, 2357.
- Matsushita, S., and Xu, W. Y., 1982, J. Geophys. Res. 87, 8241.
- Mazaewa, K., 1976, J. Geophys. Res. 81, 2289.
- McDiarmid, D. R., and Nielsen, E., 1987a, J. Geophys. Res. 92, 159.
- McDiarmid, D. R., and Nielsen, E., 1987b, J. Geophys. Res. 92, 4449.
- McDiarmid, I. B., Burrows, J. R., and Wilson, M. D., 1978, J. Geophys. Res. 83, 5753.
- McPherron, R. L., Russell, C. T., and Aubry, C. T., 1973, J. Geophys. Res. 78, 313.
- McPherron, R. L., Terasawa, T., and Nishida, A., 1986, J. Geomag. Geoelectr. 38, 1089.
- Meng, C. -I., 1980, In Dynamics of the Magnetosphere, S. -I. Akasofu (ed.), p. 23, D. Reidel, Dordrecht, Netherlands.
- Meng, C. -I., 1983, J. Geophys. Res. 88, 137.
- de Meyer, F., 1986, J. Atmos. Terr. Phys. 48, 115.
- de Meyer, F., and de Vuyst, A., 1982, Ann. Géophys. 38, 61.
- Mozer, F. S., 1984, Geophys. Res. Lett. 11, 135.
- Mozer, F. S., and Serlin, R., 1969, J. Geophys. Res. 74, 4739.
- Mozer, F. S., Gonzalez, W. D., Bogott, F., Kelley, M. C., and Schutz, S., 1974, J. Geophys. Res. 79, 56.

- Murayama, T., Aoki, T., Nakai, H., and Hakamada, K., 1980, *Planet. Space Sci.* 28, 803.
- Nagata, T., and Kokubun, S., 1962, *Rep. Ionosph. Res. Japan* 16, 256.
- Ness, N. F., 1964, *J. Geophys. Res.* 69, 3531.
- Nielsen, E., and Greenwald, R. A., 1979, *J. Geophys. Res.* 84, 4189.
- Nielsen, E., and Schlegel, K., 1983, *J. Geophys. Res.* 88, 5745.
- Nielsen, E., and Schlegel, K., 1985, *J. Geophys. Res.* 90, 3498.
- Nielsen, E., Whitehead, J. D., Hedberg, L. A., and Jones, T. B., 1983, *Radio Sci.* 18, 230.
- Nishida, A., 1968, *J. Geophys. Res.* 73, 5549.
- Nishida, A., 1971, *Planet. Space Sci.* 19, 205.
- Park, C. G., 1976, *J. Geophys. Res.* 81, 168.
- Perreault, P., and Akasofu, S. -I., 1978, *Geophys. J. Roy. Astron. Soc.* 54, 547.
- Potemra, T. A., Zanetti, L. J., Bythrow, P. F., and Lui, A. T. Y., 1984, *J. Geophys. Res.* 89, 9753.
- Primdahl, F., and Bahnsen, A., 1985, *Ann. Geophys.* 3, 57.
- Rasmussen, C. E., and Schunk, R. W., 1987, *J. Geophys. Res.* 92, 4491.
- Ratcliffe, J. A., 1972, *An Introduction to the Ionosphere and the Magnetosphere*, Cambridge University Press, Cambridge.
- Reiff, P. H., 1983, In *Solar-Terrestrial Physics*, R. L. Carovillano and J. M. Forbes (eds.), p. 493, D. Reidel, Dordrecht, Netherlands.
- Reiff, P. H., and Burch, J. L., 1985, *J. Geophys. Res.* 90, 1595.

- Reiff, P. H., Spiro, W., and Hill, T. W., 1981, *J. Geophys. Res.* 86, 7639.
- Rishbeth, H., and Garriot, O. K, 1969, *Introduction to Ionospheric Physics*, Academic Press, New York.
- Robinson, T. R., 1986, *J. Atmos. Terr. Phys.* 48, 417.
- Robinson, T. R., 1987, Private communication.
- Robinson, T. R., and Honary, F., 1987, In Prep..
- Robinson, T. R., Waldock, J. A., Burrage, M. D., and Jones, T. B., 1988, *Annales Geophysicae*, In Press.
- Rodger, A. S., Cowley, S. W. H., Brown, M. J., Pinnock, M., and Simmons, D. A., 1984, *Planet. Space Sci.* 32, 1021.
- von Rosenvinge, T. T., 1982, In *The IMS Source Book*, Russell, C. T. and Southwood, D. J. (ed.), American Geophysical Union, Washington D. C..
- Rostoker, G., 1983, *J. Geophys. Res.* 88, 6981.
- Rostoker, G., and Fälthammer, C. -G., 1967, *J. Geophys. Res.* 72, 5853.
- Rostoker, G., Lam, H. -L., and Hume, W. D., 1972, *Can. J. Phys.* 50, 544.
- Rostoker, G., Mareschal, M., and Samson, J. C., 1982, *J. Geophys. Res.* 87, 3489.
- Ruohoniemi, J. M., and Moorcroft, D. R., 1985, *Radio Sci.* 20, 719.
- Russell, C. T., and McPherron, R. L., 1973, *J. Geophys. Res.* 92, 92.
- Russell, C. T., and Elphic, R. C., 1979, *Geophys. Res. Lett.* 6, 33.
- Russell, C. T., Chappel, C. R., Montgomery, M. D., Neugebauer, M., and Scarf, F. L., 1971, *J. Geophys. Res.* 76, 6743.
- Sandholt, P. E., Egeland, A., Holtet, J. A., Lybekk, B., Svenes, K., Asheim, S., and Deehr, C. S., 1985, *J. Geophys. Res.* 90, 4407.

Schwenn, R., 1981, *Advance Space Res.* 1, 3.

Scourfield, M. W. J., and Nielsen, E., 1981, *J. Geophys. Res.* 86, 681.

Siscoe, G. L., 1982, *J. Geophys. Res.* 87, 5125.

Siscoe, G. L., 1983, In *Solar-Terrestrial Physics*, R. L. Carovillano and J. M. Forbes (eds.), p. 11, D. Reidel, Dordrecht, Netherlands.

Southwood, D. J., 1987, *J. Geophys. Res.* 92, 3207.

Starkov, G. V., Oksman, J., Uspensky, M. V., and Kustov, A. V., 1983, *J. Geophys.* 52, 49.

Stern, D. P., 1973, *J. Geophys. Res.* 78, 7292.

Sudan, R. N., 1983, *J. Geophys. Res.* 88, 4853.

Svalgaard, L., 1968, Pap. 6. Dansk. Meteorl. Inst. Geophys. Charlottenlund, Denmark.

Svaalgaard, L., 1973, *J. Geophys. Res.* 78, 2064.

Thomas, E. C., 1988, Private communication.

Thomas, E. C., and Jones, T. B., 1988, In Prep..

Vasyliunas, V. M., 1983, In *Solar-Terrestrial Physics*, R. L. Carovillano and J. M. Forbes (eds.), p. 243, D. Reidel, Dordrecht, Netherlands.

Villante, U., 1975, *Planet. Space Sci.* 23, 723.

Villante, U., and Francia, P., 1986, *Ann. Geophysicae* 4, 75.

Villante, U., Francia, P., and Vellante, M., 1983, *Ann. Geophysicae* 1, 277.

Ulrych, T. J., and Bishop, T. N., 1975, *Rev. Geophys. Space Phys.* 13, 183.

Uspensky, M. V., Pellinen, R. J., Baumjohann, W., Starkov, G. V., Nielsen, E., Sofko, G., and Kailaa, K. U., 1983, *J. Geophys.* 52, 40.

Waldock, J. A., Jones, T. B., and Nielsen, E., 1984, *Planet. Space Sci.* 32, 837.

Waldock, J. A., Jones, T. B., and Nielsen, E., 1985, *Radio Sci.* 20, 709.

Wolf, R. A., 1983, In *Solar-Terrestrial Physics*, R. L. Carovillano and J. M. Forbes (eds.), p. 303, D. Reidel, Dordrecht, Netherlands.

Zi, M., and Nielsen, E., 1982, *J. Geophys. Res.* 87, 5202.

Zi, M., Nielsen, E., Hanson, W. B, and Potemra, T. A., 1987, *J. Geophys. Res.* 92, 3417.

Zmuda, A. J., and Armstrong, J. C., 1974, *J. Geophys. Res.* 79, 2501.

Zmuda, A. J., Martin, J. H., and Heuring, F. T., 1966, *J. Geophys. Res.* 71, 5033.

RADAR STUDIES OF  
HIGH LATITUDE CONVECTION FLOWS

MARK DAVID BURRAGE

ABSTRACT

Studies of the electrodynamics of the high latitude ionosphere contribute to the understanding of the coupling between the solar wind, magnetosphere and upper atmosphere. This thesis describes an experimental investigation of high latitude E-region convection flows carried out with the Sweden And Britain auroral Radar Experiment (SABRE). The ionospheric observations have been related to satellite measurements of the interplanetary medium and hence interpreted in terms of models of solar wind-magnetosphere-ionosphere coupling processes.

A close relationship has been established between various solar wind parameters and the daily mean SABRE backscatter intensity, a quantity which is rarely employed in geophysical studies. Empirical IMF-dependent models of the convection flows observed by SABRE are developed and statistical studies of the occurrence time of the Harang discontinuity are presented. High spatial resolution, two dimensional maps of the ionospheric projection of the dayside merging region, for both polarities of the azimuthal component of the IMF, are obtained for the first time. Two examples of strong nightside convection flows observed throughout the SABRE latitude range indicate that the convection flows may penetrate at least as far south as  $61.5^{\circ}$  N, geomagnetic latitude, during strongly northward IMF.

The study indicates that, in the long term, the structure of the solar wind can be deduced from the mean backscatter intensity measured by a SABRE radar. In addition, the azimuthal component of the IMF exerts a crucial influence on the convection flows observed by SABRE in the cusp region. This effect is not confined to the noon sector but is also apparent in the vicinity of the Harang discontinuity. In general, the convection pattern exhibits a dependence on the north-south component of the IMF consistent with established reconnection mechanisms. However, there is evidence that existing models are insufficient to explain the anomalous convection flows observed under conditions of strongly northward IMF.